ISSN number 0971 - 9709

IGU
Promoting Earth System Sciences

The Journal of Indian Geophysical Union

A SCI Journal

Impact Factor (2025) 0.2

AN OPEN ACCESS BIMONTHLY JOURNAL OF IGU

VOLUME 30, ISSUE 3, MAY, 2026

PUBLISHED BY
Indian Geophysical Union, NGRI Campus, Uppal Road, Hyderabad- 500 007
Telephone: 91-4027012739, 27012332; Telefax:+91-04-27171564
Email: jigu1963@gmail.com, website: http://iguonline.in/journal/

The Journal with six issues in a year publishes articles covering
Solid Earth Geosciences; Marine Geosciences; and Atmospheric, Space and Planetary Sciences.

The Journal is supported by CSIR-NGRI & MoES, Govt. of India

Annual Subscription
Individual Rs -1000/- per issue and Institutional Rs- 5000/- for six issues
Payments should be sent by DD drawn in favour of "The Treasurer, Indian Geophysical Union", payable at Hyderabad,
Money Transfer/NEFT/RTGS (Inter-Bank Transfer), Treasurer, Indian Geophysical Union, State Bank of India, Habsiguda Branch,
Habsiguda, Uppal Road, Hyderabad- 500 007
A/C: 52191021424, IFSC Code: SBIN0020087, MICR Code: 500002318, SWIFT Code: SBININBBHO9.
For correspondence, please contact, Hon. Secretary, Indian Geophysical Union, NGRI Campus, Uppal Road,
Hyderabad - 500 007, India; Email: igu123@gmail.com; Ph: 040 27012332

ISSN: 0257-7968 (Clarivate Analytics)
ISSN: 0971-9709 (NISCAIR)
Approved as bimonthly ESCI journal by Clarivate Analytics
Cited in Indian Citation Index (ICI), New Delhi
Evaluated by NISCAIR, New Delhi
UGC Approved Journal

CONTENTS

Editorial

J. Ind. Geophys. Union, 30(3) (2026), 148-155
https://doi.org/10.71122/JIGU.30(3)2026.0016

Seismic imaging of coal seams and structural features: A prerequisite for CO_2 sequestration studies in the Raniganj Basin, India

Shaik Nasif Ahmed[1,2], Pankaj Kumar[1,2]*, Saqib Zia[1,2], Prince Saini[1,2], Ajay Malkoti[1,2], Nimisha, A. G.[1], P. Pavan Kishore[1], A. K. Routa[1], K. Dhanam[1], D. Mysaiah[1], K.N.S.S.S. Srinivas[1], K. Satish Kumar[1,2], M.Srihari[1], Rajib Dhar[3], H.V.S. Satyanarayana[1], Jyotirmoy Mallik[4] and Nimisha Vedanti[1,2]

[1]CSIR-National Geophysical Research Institute, Hyderabad-500007, India
[2]Academy of Scientific and Innovative Research (AcSIR), Ghaziabad-201002, India
[3]Essar Oil and Gas Exploration and Production Limited, Durgapur-713212, India
[4]Indian Institute of Science Education and Research Bhopal, Bhopal-462066, India
*Corresponding author: pankajk.ngri@csir.res.in

ABSTRACT

This study presents an integrated seismic and well-based characterization of the eastern Raniganj Basin, India, aimed at imaging coal seams and delineating subsurface structural features, which are essential for evaluating geological CO_2 sequestration potential. Multiple geophysical datasets, including legacy 2D seismic, high resolution 3D seismic, and 2D multicomponent (2D-3C) seismic data, were analyzed and calibrated using lithological information from drilled wells. The 3D seismic data from the northeastern part of the basin image shallow coal horizons, characterized by laterally continuous and predominantly flat lying reflectors, indicating a structurally less disturbed subsurface. In contrast, seismic interpretation in the southeastern part of the basin, based on conventional 2D and 2D-3C datasets, reveals multiple coal seams, stratigraphic boundaries, and subtle structural features, such as gentle monoclines and minor normal faults. Based on the integrated seismic analysis, the southeastern Raniganj Basin exhibits geological characteristics that are favourable for further evaluation of CO_2 sequestration potential compared to the northeastern sector. However, the presence of interpreted fault systems highlights the need for detailed investigations including high-resolution seismic imaging and fault seal analysis, to assess structural continuity and long-term containment integrity. The study establishes a preliminary understanding of the geological framework of the eastern Raniganj Basin that can be further strengthened by integrating high-resolution seismic data with other datasets to quantitatively evaluate storage capacity and long-term containment integrity.

Keywords: CO_2 sequestration, Coal seams, Seismic imaging, Subsurface structure, Raniganj Basin (India)

INTRODUCTION

Global industrialization and rapid urban expansion have led to a sustained increase in energy demand, which continues to be met predominantly by fossil fuels. While these energy resources have supported economic development, their extensive utilization has resulted in a significant rise in atmospheric CO_2 concentrations, contributing to climate change (Metz et al., 2005; Vedanti et al., 2025). This growing environmental concern, combined with the need for reliable energy, has intensified interest in cleaner and more sustainable energy solutions. In this context, geological carbon sequestration has emerged as a promising mitigation strategy (Pandey et al., 2016; Vedanti, 2026). Among various storage options, coal formations offer the additional advantage of enhanced coalbed methane recovery (ECBM), enabling simultaneous greenhouse gas mitigation and energy production (Bachu, 2008; Gale and Freund, 2001).

The Raniganj Basin (Figure 1), a sub-basin of the Damodar Valley, is of significant geological and historical importance as the birthplace of India's coal industry (Gee, 1932; Dutta, 2002). Geological investigations in the basin date back over two centuries, with formal coal mining initiated in 1774 (Varma et al., 2015). Owing to its extensive coal-bearing successions and long history of resource exploitation, the basin has attracted sustained interest in coal-bed methane and other unconventional resources. The presence of coal-based thermal power plants and ongoing coalbed methane production by commercial operators such as Great Eastern Energy Corporation Limited (GEECL) and Essar Oil and Gas Exploration and Production Limited (EOGEPL), has further motivated interest in evaluating the basin for CO_2 storage (Vedanti et al., 2020). However, safe and effective carbon sequestration in coal formations requires a detailed understanding of the subsurface geological conditions, including coal seam continuity, fault systems, and structural configuration.

Previous studies have established the regional stratigraphic and structural framework of the Raniganj Basin (Gee, 1932; Dutta, 2002; Mendhe et al., 2018; Satyanarayana et al., 2020; Satyavani et al., 2021). Multiple studies have documented the presence of several coal horizons with variable depth and thickness within the Raniganj and Barakar Formations (Ghosh, 2002; Chatterjee and Pal, 2010; Mishra et al., 2016). For instance, Mohanty et al. (2018) identified a total of nine coal horizons (R-I to R-IX) in the Raniganj Formation and seven coal horizons (I to VII) in the Barakar Formation, whereas Chattaraj et al. (2019) reported ten coal horizons (R-I to R-X) within the Raniganj Formation. These variations reflect the complex depositional and tectonic evolution of the basin.

Structurally, the basin is characterized by numerous faults, sub-basins, basement highs, and intrusive bodies (Gee, 1932; Ghosh, 2019). Intra-basinal faulting has resulted in the development of multiple structural compartments, with

spatial variability in fault trends. Earlier studies have also highlighted significant heterogeneity in subsurface structural configurations, including the presence of distinct sub-basins in the western-central and southeastern regions (Verma et al., 1980; Ghosh et al., 1993; Kumar, 2006; Ghosh, 2019).

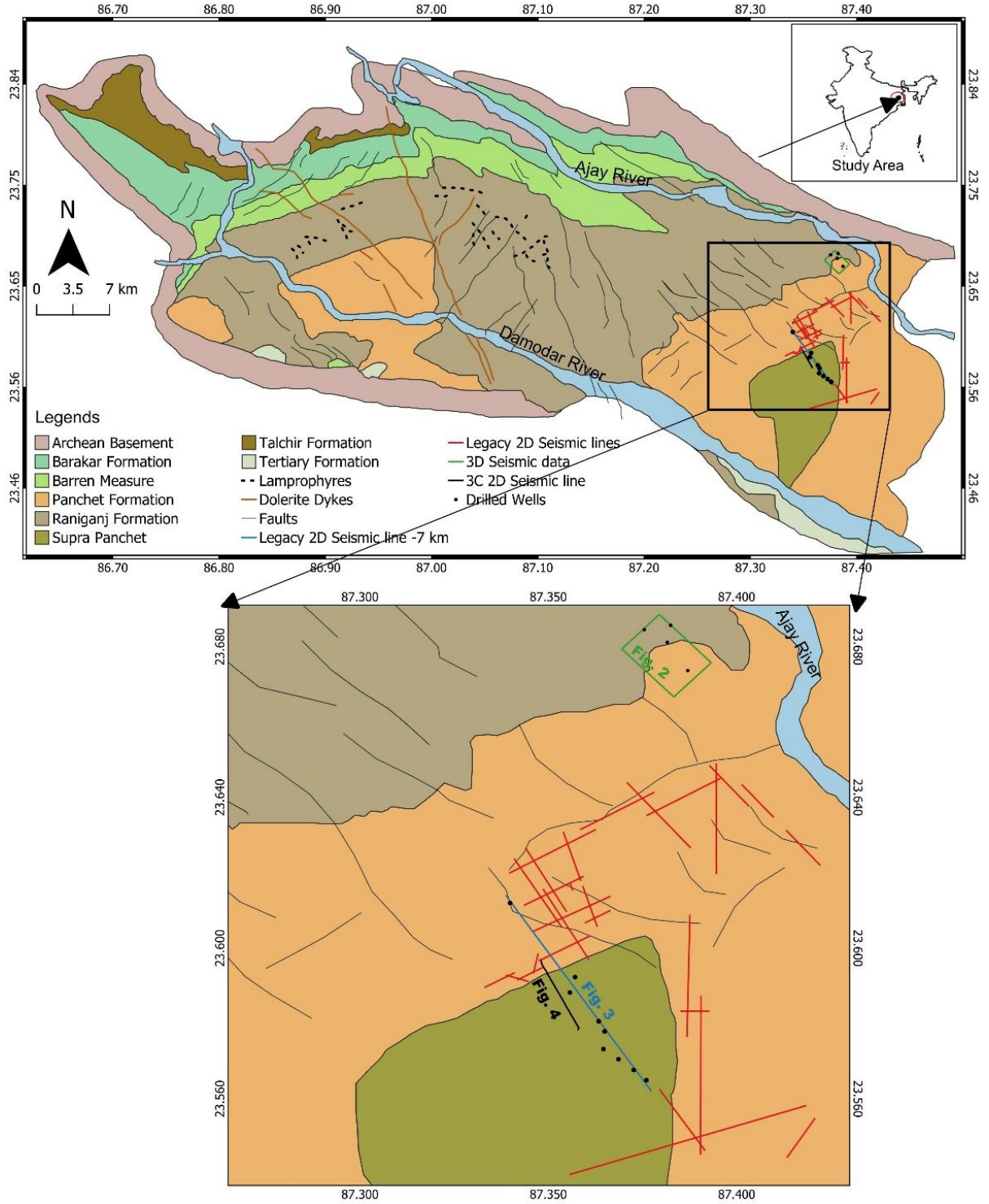

Figure 1. Geological map of the Raniganj Basin, India (modified after Murthy et al., 2010; Mohanty et al., 2018; Bandyopadhyay et al., 2020). The map highlights the locations of 2D seismic survey lines and 3D seismic data coverage

Despite these extensive investigations, subsurface information in the eastern Raniganj Basin remains limited. Uncertainties persist in imaging thin coal seams and identifying subtle fault systems, primarily due to sparse well control and limited seismic coverage. The present study addresses these gaps through a multi-dataset seismic analysis using 2D, 3D, and multicomponent (2D-3C) seismic data. The objectives are to delineate coal seams, identify structural discontinuities, and refine the regional subsurface structural framework. The results provide an improved geological understanding of coal seam distribution and structural features, forming a basis for subsequent, more detailed evaluations of CO_2 sequestration potential.

GEOLOGY OF THE RANIGANJ BASIN

Raniganj Basin is the easternmost intra-cratonic rift basin of the Damodar Valley, covering an area of approximately 1900 km² (Gee, 1932; Mendhe et al., 2018; Ghosh, 2019). The basin exhibits a semi-elliptical, elongated geometry, bounded by the Ajay River to the north and the Damodar River to the south. It is developed over a Precambrian crystalline basement composed predominantly of quartz, feldspar, and biotite (Ghosh, 2002). The sedimentary succession rests unconformably on this basement and comprises the Talchir, Barakar, Barren Measures, and Raniganj Formations, collectively representing the Lower Gondwana (Permian) sequence. These are overlain by Upper Gondwana formations (Panchet to Supra-Panchet, Triassic-Lower Cretaceous) (Fox, 1931; Mishra et al., 2016).

The Talchir Formation forms the basal unit and consists mainly of glacio-lacustrine and fluvio-glacial deposits. It is overlain by the Barakar Formation, which is characterized by sandstones, conglomerates, carbonaceous shales, and multiple coal seams, deposited in braided to fluvio-lacustrine alluvial environments (Ghosh, 2002; Mishra et al.,2016). The overlying Barren Measures Formation is a non-coal-bearing unit comprising organic-rich shales (Varma et al., 2015; Mendhe et al., 2018). The Raniganj Formation conformably overlies the Barren Measures and comprises fine-grained, micaceous sandstones, shales, and several well-developed coal seams. Structurally, the Raniganj Basin is faulted down towards the south and west, with the southern boundary defined by a series of echelon faults. The dip of the strata generally ranges between 5° and 10° (Varma et al., 2015). The geological map of the study area is shown in Figure 1.

DATA AND METHODOLOGY

This study utilizes multiple seismic and well datasets to delineate coal seams and subsurface structural features in the eastern part of the Raniganj Basin (Figure 1). The seismic database comprises (i) Legacy 2D seismic data consisting of sixteen profiles acquired in 2007 from the south-eastern part of the basin. The survey employed an impulsive explosive source of 2.5 kg, with a receiver spacing of 10 m and a sampling interval of 0.5 ms, (ii) 3D seismic data covering an area of 2.4 km² in the north-eastern part of the basin, acquired in 2018. The survey parameters include a shot spacing of 10 m, a receiver spacing of 5 m, a sampling interval of 0.5 ms, and a frequency bandwidth of 10-150 Hz, (iii) 2D multicomponent (2D-3C) seismic data, acquired in 2022 along a 2.38 km long profile in collaboration with Essar Oil and Gas Exploration and Production Limited (EOGEPL). This represents the first multicomponent seismic acquisition conducted in Indian coalfields. The acquisition employed a sampling interval of 1 ms, receiver spacing of 20 m, and shot spacing of 10 m, enabling the recording of both compressional (P-wave) and shear (S-wave) responses. (iv) Litholog data from eleven drilled wells were employed for calibration and interpretation. In addition, a density log obtained from one well was also used to support seismic interpretation.

All the seismic datasets were processed and interpreted using a standard workflow designed to enhance data quality and ensure reliable structural and stratigraphic imaging. Pre-processing steps included geometry definition, amplitude recovery, and spherical divergence correction to compensate for energy decay with depth. Predictive deconvolution and band-pass filtering were applied to suppress noise and improve temporal resolution. Velocity analysis was performed using semblance to develop stacking velocity models. These models were subsequently used for normal moveout correction and common midpoint stacking. Post-stack time migration was performed to improve reflector positioning and enhance structural continuity. The processed seismic data were then converted from time to depth using interval velocities derived from stacking analyses and calibrated with available well information. The interpretation of seismic and well data yielded a refined structural and stratigraphic framework for the eastern Raniganj Basin. This framework provides an improved basis for understanding coal seam distribution and structural configurations, supporting future and more detailed evaluations of CO_2 sequestration studies.

RESULTS

Seismic imaging of the northeastern Raniganj Basin

Two mutually perpendicular time-migrated seismic sections (Figure 2) from the 3D seismic survey in the Rangamati

Block located in the northeastern Raniganj Basin, are presented to see the lateral variations in geological structures in different directions. The results display laterally continuous and predominantly flat-lying reflections with minimal structural dip. The overall reflection pattern suggests a relatively stable and weakly deformed subsurface, with no clearly resolvable major faults or large-scale structural discontinuities within the imaged interval. A prominent high-amplitude reflection is observed at a two-way travel time of approximately 0.2 s. This reflector is characterized by a strong acoustic impedance contrast interpreted as a coal seam. Correlation with well-log and available core data confirms that this reflector corresponds to a coal seam approximately 6 m thick, occurring at a depth of ~300 m (Figure 2). Lithological interpretation based on well data indicates that the Raniganj Formation begins at a depth of ~60 m and has an overall thickness of approximately 256 m in the study area. This interpretation is consistent with previous studies, including Shaik et al. (2025), which reported multiple coal seams in the Rangamati Block.

Seismic imaging of the southeastern Raniganj Basin

Seismic results from the southeastern part of the Raniganj Basin are presented using both conventional 2D seismic and multicomponent (2D-3C) seismic datasets to delineate coal seams and subsurface structures. A depth-scaled seismic section along a ~7 km long 2D seismic line oriented in a NW-SE direction (location shown in Figure 1) is presented in Figure 3. The shallow portion of the section, up to approximately 400 m, was muted due to high noise levels. Below this depth, multiple subsurface reflectors are observed, with stratigraphic layering becoming more distinct between depths of ~600 and ~1200 m. Reflections within this interval exhibit improved continuity and amplitude coherence. High-amplitude, high-contrast reflectors are interpreted as coal seams and are validated through correlation with well-log data and stratigraphic markers (Figure 3). Based on well control, the Raniganj Formation is identified at depths of approximately 600-700 m, with a thickness ranging from ~ 500 to 700 m along the profile. The Barren Measures Formation occurs at depths of ~1100-1400 m; however, its base could not be mapped due to limited seismic penetration. Structurally, the reflectors define a broad southeast-dipping monocline. Individual coal seams (Seams 1, 2, and 3) are separated by non-coaly interbeds of sandstone or shale. The reflectors deepen towards the central part of the seismic section (offsets ~1-3.5 km) and become shallower towards the flanks, suggesting a broad antiform-synform geometry with superimposed minor undulations. Several small-scale normal faults are interpreted, locally affecting the reflector continuity.

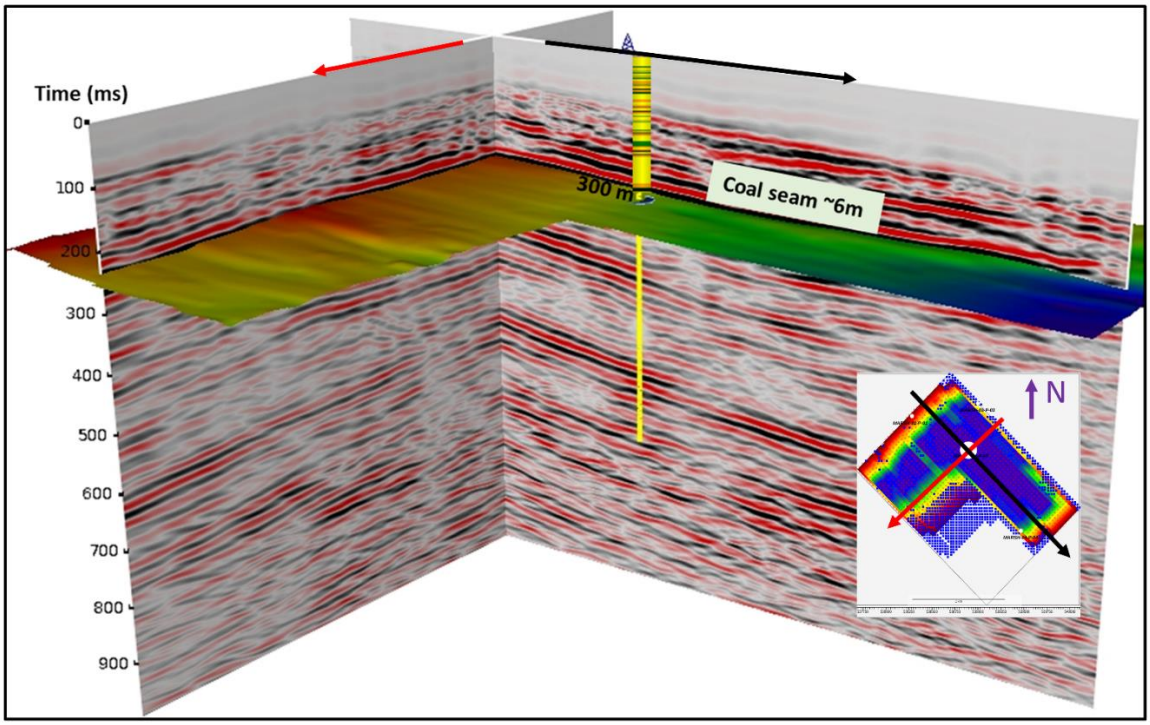

Figure 2. Two mutually perpendicular time-migrated seismic sections from the 3D seismic survey. High-amplitude reflections near 0.2 s indicate strong acoustic impedance contrast, interpreted as coal seams and confirmed by the litholog of the drilled well.

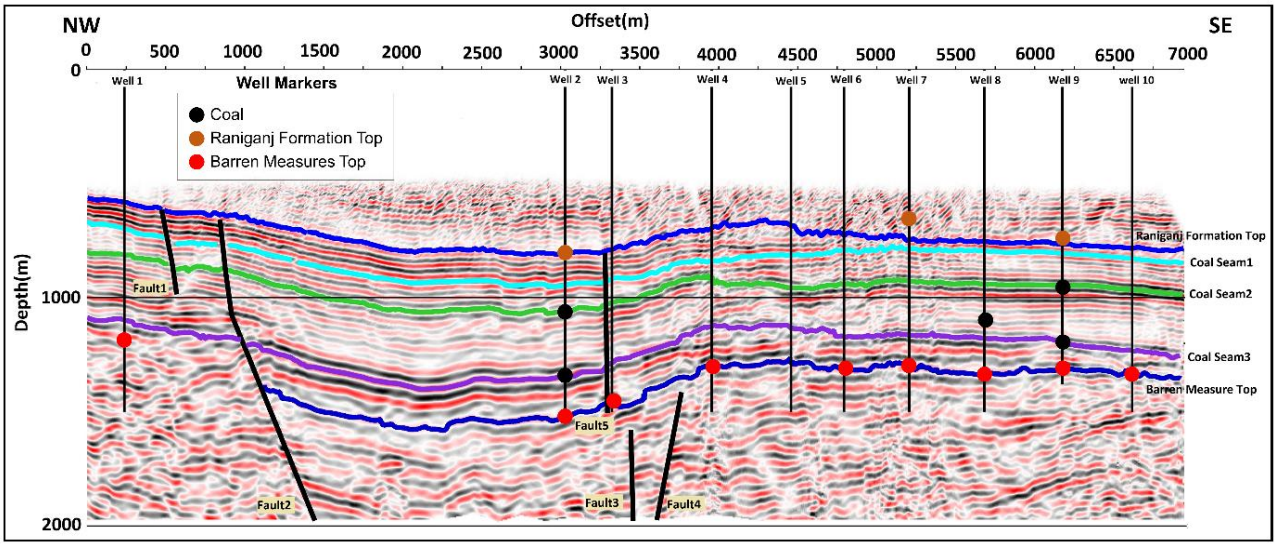

Figure 3. A depth-scaled seismic section showing the presence of coal seams, minor faulting, and broadly folded layers

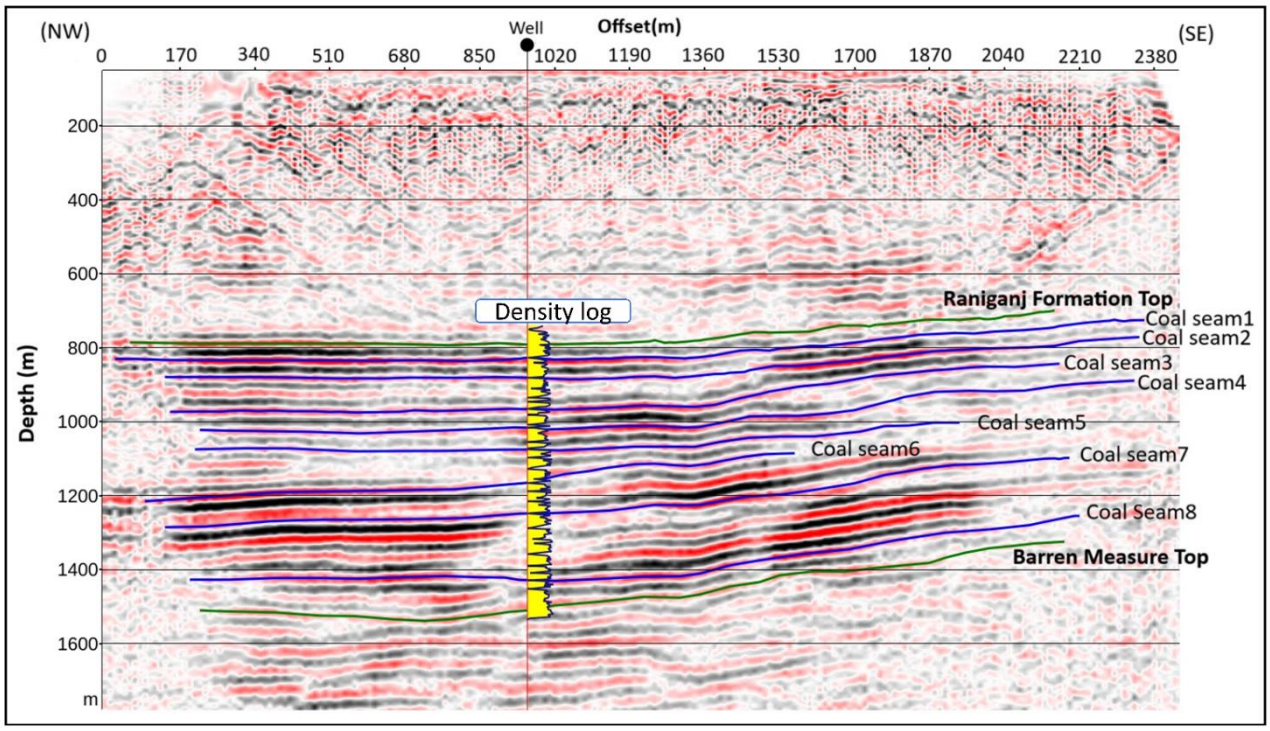

Figure 4. Depth-scaled seismic section along a 2D profile in the Raniganj (East) block showcasing distinct reflectors. High-amplitude contrast suggests the presence of coal layers that are validated with the density log data of a drilled well.

A depth-scaled seismic section derived from the 2D-3C seismic data along a ~2.4 km long NW-SE-oriented profile (location shown in Figure 1) in the southeastern part of the basin is presented in Figure 4. This section exhibits distinct amplitude variations associated with lithological contrasts, particularly within coal-bearing intervals. We used density log data from a borehole located along the seismic profile to identify coal seams as it is characterized by low-density signatures (Figure 4). Correlation between seismic and density -log data confirms the presence of multiple coal seams. The well data indicate six major coal seams, each ~3 m thick, and several thin coal seams (~1-2 m). However, only eight coal seams could be confidently interpreted on the seismic section due to resolution limitations. The Raniganj

Formation occurs at a depth of ~700 m in the southeastern part of the profile and deepens to ~800 m towards the northwest, indicating a gentle northwestward dip. The formation exhibits a thickness of ~600-700 m along the profile. The Barren Measures Formation is encountered at depths of ~1350 to 1500 m and displays a structural configuration similar to the overlying Raniganj Formation.

DISCUSSION

Subsurface structures in the eastern Raniganj Basin

The combined interpretation of 2D, 3D, and multicomponent seismic datasets reveal significant spatial variability in subsurface structural architecture across the eastern Raniganj Basin. The northeastern sector, particularly the Rangamati Block, is characterized by shallow coal seams associated with laterally continuous, sub-horizontal reflectors and minimal structural deformation. Although previous studies **(**Chatterjee and Pal, 2010; Sen et al., 2016; Ahmed et al., 2025**)** have reported shallow coal occurrence in this region, constraints on the detailed structural framework have remained limited. The present results indicate that coal horizons within the Rangamati Block, are laterally continuous and exhibit negligible structural disruption over the extent of the 3D seismic survey (~2.4 km^2). However, this interpretation is spatially restricted to the surveyed area, and structural variations beyond this extent cannot be ruled out.

In contrast, the southeastern part of the basin exhibits deeper coal horizons and a comparatively more complex structural configuration, as evidenced by gentle monoclines, broad antiform-synform geometries, and small-scale normal faults. Sen et al. (2016) have documented relatively deeper coal seams in the central and southern sectors of the eastern Raniganj Basin, and highlighted significant depth variability based on litholog data from multiple wells. Earlier geological interpretations **(**Verma et al., 1980; Ghosh et al., 1993; Kumar, 2006**),** proposed the existence of a sub-basin in this region, commonly referred to as the Durgapur sub-basin. The observed depth variations and structural geometries in the present study are consistent with earlier interpretations and suggest the presence of a basin-like structural configuration or a sub-basin in the study area. Recent findings by Bandyopadhyay et al. (2025**)** further support the presence of gentle deformation and faulting within coal-bearing sequences.

Overall, the results indicate the coal seams in the northeastern sector are shallow, laterally continuous, and structurally less disturbed, whereas those in the southeastern sector occur at greater depths and exhibit increased structural variability. These observations are consistent with earlier studies (Ghosh, 2002; Sen et al., 2016; Ghosh, 2019), which report systematic deepening of coal seams away from basin margins and towards structurally depressed regions. For instance, Sen et al. (2016) reported coal seams at relatively shallower depths (~450 m) near the basin margins, compared to deeper occurrences (~650 m) towards the basin interior. Similarly, Ghosh (2002, 2019**)** demonstrated that coal seams tend to be thicker and deeper in the central part of the basin, while thinning or terminating toward the margins.

Implications for CO_2 sequestration potential

The observed variations in burial depths and structural configurations across the eastern Raniganj Basin have important implications for evaluating CO_2 sequestration potential. In the northeastern region, coal seams occur at relatively shallow depths, which are generally considered less favourable for long-term CO_2 storage due to insufficient pressure–temperature conditions, and the possibility of leakage to surface or interaction with shallow groundwater systems. Previous CCS studies suggest that effective CO_2 sequestration in coal seams typically requires burial depths exceeding 800 m to ensure supercritical CO_2 conditions and enhanced storage efficiency (White et al., 2005; Bachu, 2008).

In contrast, the southeastern sector is characterized by deeper coal-bearing horizons and thicker stratigraphic successions, which are more consistent with conditions generally considered suitable for CO_2 storage. However, the presence of interpreted fault systems and structural heterogeneities introduces uncertainty regarding subsurface continuity and potential fluid migration pathways. These factors necessitate careful evaluation of fault seal integrity, caprock effectiveness, and geomechanical stability prior to any site-specific assessment of CO_2 storage feasibility.

The results demonstrate the utility of seismic data for delineating coal seams and resolving subsurface structural features relevant to CO_2 storage feasibility. At the same time, limitations in resolving thin coal seams highlight the need for advanced approaches such as seismic inversion, full-waveform inversion, and joint geophysical-petrophysical modelling. Overall, the southeastern Raniganj Basin exhibits geological characteristics that warrant further detailed investigations for CO_2 sequestration. Future studies should integrate seismic-derived structural models with coal petrophysical properties, adsorption characteristics, and in-situ stress characterization to enable a robust assessment of storage capacity and long-term containment integrity.

CONCLUSIONS

This study presents a multi-dataset seismic analysis of coal seams and subsurface structures in the eastern Raniganj Basin, supported by well data, with implications for geological CO_2 sequestration. The key findings are as follows.

1. The combined analysis of 3D, 2D, and 2D-3C seismic data, calibrated with well logs and core information, enables reliable delineation of coal seams, formation boundaries, and structural features relevant to subsurface characterization.

2. The northeastern part of the basin is characterized by laterally continuous and weakly deformed coal-bearing sequences, whereas the southeastern part exhibits deeper coal horizons associated with gentle monoclines and minor faulting, indicating spatial variability in structural conditions.

3. Based on the observed variations in seam continuity, burial depth, and structural configuration, the southeastern Raniganj Basin exhibits geological characteristics that warrant further detailed evaluation for CO_2 sequestration. However, the presence of interpreted fault systems necessitates additional investigations, including assessments of fault-seal integrity and caprock effectiveness, before confirming its suitability for long-term CO_2 storage.

Acknowledgement

The authors are thankful to the Director for his support and permission to publish this work. We are grateful to the NGRI seismic team for acquiring seismic data in multiple phases for various projects. The authors acknowledge all the project partners, including CSIR-CIMFR, CMPDI, and EOGEPL. The datasets used in this study were acquired for the projects: GAP-673, HCP-48, and NCP-0010. SNA acknowledges the Department of Science and Technology (DST), New Delhi, Government of India, for providing the INSPIRE fellowship (IF190159), which supported this research as a part of his doctoral studies.

Author credit statement

Conceptualization: Shaik Nasif Ahmed, Pankaj Kumar, Saqib Zia, Prince Saini, Ajay Malkoti, and Nimisha Vedanti. Data acquisition: Ajay Malkoti, P Pavan Kishore, Alok Kumar Routa, D Mysaiah, K N S S S Srinivas, Sri Hari, Saqib Zia, Shaik Nasif Ahmed, and Nimisha Vedanti. Writing original draft: Shaik Nasif Ahmed, Pankaj Kumar, and Prince Saini. Formal analysis: Shaik Nasif Ahmed, Prince Saini, Pankaj Kumar, Nimisha Anna G, P Pavan Kishore, and K Dhanam. Review: Nimisha Vedanti, Jyotirmoy Mallik, H V Satyanarayana, and K Sathish umar. Resources: Nimisha Vedanti, Rajib Dhar, and H V Satyanarayana. Funding acquisition: H V Satyanarayana and Nimisha Vedanti. Supervision: Nimisha Vedanti.

Data availability

Data is available at CSIR-NGRI and will be shared on request.

Compliance with ethical standards

No conflict of interest, and authors adhere to copyright norms.

References

Ahmed, S. N., Routa, A. K., Kumar, P. and Vedanti, N., 2025. Attenuation of Ground Roll in Seismic Data Using Model-Based Inversion and Genetic Algorithm. J. Geol. Soc. India, 101(10), 1572-1577.

Bachu, S., 2008. CO2 storage in geological media: Role, means, status and barriers to deployment. Prog. Energy Combust. Sci., 34(2), 254-73.

Bandyopadhyay, K., Mallik, J. and Ghosh, T., 2020. Dependence of fluid flow on cleat aperture distribution and aperture–length scaling: a case study from Gondwana coal seams of Raniganj Formation, Eastern India. Int. J. Coal Sci. Technol., 7(1), 133-146.

Bandyopadhyay, K., Mallik, J., Suman, S., Dhar, R., Shaik, N. A. and Vedanti, N., 2025. Field scale coal permeability modeling and sweet-spotting using seismic attributes. Int. J. Coal Sci. Technol., 12(1), Article 89.

Chatterjee, R. and Pal, P. K., 2010. Estimation of stress magnitude and physical properties for coal seam of Rangamati area, Raniganj coalfield, India. Int. J. Coal Geol., 81(1), 25-36.

Chattaraj, S., Mohanty, D., Kumar, T., Halder, G. and Mishra, K., 2019. Comparative study on sorption characteristics of coal seams from Barakar and Raniganj formations of Damodar Valley Basin, India. Int. J. Coal Geol., 212, 103202.

Dutta, P., 2002. Gondwana lithostratigraphy of peninsular India; Gondwana Res., 5(2), 540-553.

Fox, S.C.S., 1931. The Gondwana system and related formations. Government of Indian Central Publication Branch.

Gale, J. and Freund, P., 2001. Coal-bed methane enhancement with CO2 sequestration worldwide potential. Environ. Geosci., 8(3), 210-217.

Gee, E.R., 1932. The geology and coal resources of the Raniganj Coalfield. Government of India, Central Publication Branch.

Ghosh, D., Das, L. K., Ghatak, T. K., Saha, D. K. and Bose, R. N., 1993. Morphotectonic configuration of cratonic Gondwana depocentres of eastern India. Tectonophysics, 223(3-4), 423-438.

Ghosh, S.C., 2002. The Raniganj coal basin: an example of an Indian Gondwana rift. Sediment. Geol., 147(1-2), 155-76.

Ghosh, S.C., 2019. Nature of boundary and other faults in Raniganj Gondwana rift basin. In Developments in

Structural Geology and Tectonics (Vol. 4, pp. 33-44). Elsevier. https://doi.org/10.1016/B978-0-12-815218-8.00005-4

Kumar, J., 2006. Integrated modelling of Durgapur Depression (Damodar Basin). In 6th International Conference & Exposition on Petroleum Geophysics (pp. 26-29).

Mendhe, V.A., Mishra, S., Varma, A.K., Kamble, A.D., Bannerjee, M., Singh, B.D., Sutay, T.M. and Singh, V.P., 2018. Geochemical and petrophysical characteristics of Permian shale gas reservoirs of Raniganj Basin, West Bengal, India. Int. J. Coal Geol., 188, 1-24. https://doi.org/10.1016/j.coal.2018.01.012

Metz, B., Davidson, O., De Coninck, H.C., Loos, M. and Meyer, L., 2005. IPCC special report on carbon dioxide capture and storage. Cambridge: Cambridge University Press.

Mishra, S., Mendhe, V.A., Kamble, A.D., Bannerjee, M., Varma, A.K., Singh, B.D. and Pandey, J.K., 2016. Prospects of shale gas exploitation in Lower Gondwana of Raniganj coalfield (West Bengal), India. J. Palaeoscience, 65(1-2), 31-46.

Mohanty, D., Chattaraj, S. and Singh, A.K., 2018. Influence of coal composition and maturity on methane storage capacity of coals of Raniganj Coalfield, India. Int. J. Coal Geol., 196, 1-8. https://doi.org/10.1016/j.coal.2018.06.016

Murthy, S., Chakraborti, B. and Roy, M.D., 2010. Palynodating of subsurface sediments, Raniganj Coalfield, Damodar Basin, West Bengal. J. Earth Syst. Sci., 119(5), 701–10.

Pandey, O.P., Vedanti, N. and Ganguli, S.S., 2016. Some Insights into Possible CO_2 Sequestration in Subsurface Formations beneath Deccan Volcanic Province of India. J. Indian Geophys. Union, Spl. Volume, 1, pp. 20-25

Satyanarayana, H.V., Mendhe, V.A., Lochan, R., Singh, P.K., Kalpana, M.S., Patil, D.J., Mysaiah, D., Seshunarayana, T., Singh, H., Kumar, J., Singh, K.K. and Mishra, V.K., 2020. Shale gas potentiality evaluation of the Damodar Basin of India (S and T Project Report by CSIR-NGRI, CSIRCIMFR, CMPDI). Ministry of Coal, Government of India.

Satyavani, N., Uma, V., Kishore, P.P., Srinivas, K.N.S.S.S., Mysaiah, D., Dhanam, K., Srinivas, G.S., Satyanarayana, H.V.S. and Vedanti, N., 2021. Geophysical exploration of unconventional hydrocarbons; J. Geol. Soc. India, 97(10), 1274-1279.

Sen, S., Das, N. and Maiti, D., 2016. Facies analysis and depositional model of late Permian Raniganj formation: Study from Raniganj coal bed methane block. J. Geol. Soc. India, 88(4), 503-516.

Shaik, N.A., Khanna, M. and Vedanti, N., 2025. Quantifying the potential of the Raniganj Basin for shale gas exploration and CO2 sequestration using a deep learning framework; J. Pet. Explor. Prod. Technol., 15(4), 1-17. https://doi.org/10.1007/s13202-025-01978-w

Varma, A.K., Hazra, B., Mendhe, V.A., Chinara, I. and Dayal, A.M., 2015.Assessment of organic richness and hydrocarbon generation potential of Raniganj basin shales, West Bengal, India. Mar. Pet. Geol., 59, 480-490. https://doi.org/10.1016/j.marpetgeo.2014.10.003

Vedanti, N., 2026. Underground energy storage in India: A geoscientific imperative for energy security and the net-zero transition. J. Indian Geophys. Union, 30(2), 86-88.

Vedanti, N., Tripathi, P., Dwivedi, S.K. and Das, D., 2025. Chlorophaeite-linked low velocity and high seismic attenuation in Deccan LIP basalts and scope for CO2 sequestration. The Leading Edge. 44(10), 804-810.

Vedanti, N., Vadapalli, U. and Sain, K., 2020. A brief overview of CBM development in India; Proc. Indian Natl. Sci. Acad., 86(1) 623-629. DOI: 10.16943/ptinsa/2020/49799

Verma, R. K., Bandyopadhyay, T. K. and Mukhopadhyay, M., 1980. Gravity Field, Structure and Tectonics of the Raniganj Coalfield-Three Dimensional Model. J. Geol. Soc. India, 21(3), 117-127.

White, C.M., Smith, D.H., Jones, K.L., Goodman, A.L., Jikich, S.A., LaCount, R.B., DuBose, S.B., Ozdemir, E., Morsi, B.I. and Schroeder, K.T., 2005. Sequestration of carbon dioxide in coal with enhanced coalbed methane recovery a review. Energy & Fuels, 19(3), 659-724.

Received on: 12-01-2026; Revised on: 23-03-2026; Accepted on: 26-03-2026

J. Ind. Geophys. Union, 30(3) (2026), 156-170
https://doi.org/10.71122/JIGU.30(3)2026.0017

Tectonic implications and seismicity triggering during the 2015 Nepal earthquake sequence

Ankush Kumar Ruhela[1*], J. Das[1], S.C. Gupta[1] and Sonu Devi[2]
[1]Department of Earthquake Engineering, Indian Institute of Technology Roorkee, Roorkee-247667, India
[2]Department of Mathematics, Birla Institute of Technology and Science Pilani, Pilani-333031, India
[*]Corresponding author: aruhela@eq.iitr.ac.in

ABSTRACT

An earthquake of M_w 7.8, having an epicenter 80 km northwest of Kathmandu, struck the Pokhara region in central Nepal, causing widespread damage. After 16 days, a second earthquake with a magnitude of M_w 7.3 followed the mainshock. The focal mechanism solution and the distribution of aftershocks indicate that the earthquake occurred on an oblique thrust fault, oriented in a NW-SE direction. In this study, we estimated statistical seismological parameters, including the spatial fractal dimension D-value, the aftershocks temporal decay p-value, the b-value of the G-R relationship, and coseismic stress modelling to analyze the tectonic implications and triggering during this sequence. The sequence had aftershocks of greater magnitude because of the large asperities within the rupture zone, as indicated by the determined b-value of 0.89, which shows that the mainshock struck in a highly stressed zone. The high decay of aftershock activity indicated by the high p-value of 1.10, is likely an indication of a higher value of the surface heat flow. In the fault zone, high heat results in shortened stress relaxation time. A spatial fractal dimension value (D-value) of 2.14, indicates a random spatial distribution and a source of a two-dimensional plane filled with fractures. Using the slip model, the estimated coseismic coulomb stress shows a butterfly-like distribution, and the majority of aftershocks occur in the positive coulomb stress zone. This implies that the majority of aftershock activity has been caused by the transfer of positive coulomb stress as a result of the mainshock's coseismic slip. This also validates that the Nepal earthquake raised the possibility of a large aftershock that occurred on 12 May 2015. For future seismic hazard assessments and risk mitigation in Nepal and the adjacent areas, the estimated results of this study may be helpful.

Keywords: Static earthquake triggering, Coulomb failure function, b-value, Omori law, Spatial fractal dimension, Nepal earthquake.

INTRODUCTION

Two of the most fundamental physical parameters controlling the earthquake process are the level of stress and its temporal variation (Deng and Sykes, 1997). Tectonic loading and stress variations from previous events, particularly from large earthquakes or other local shocks, have an impact on each event. It appears that the seismicity rate changes, and that the rate on one fault influences the probability of earthquakes on another (Scholz, 1990). Seismicity relies significantly on earthquake interaction, which produces clusters, aftershocks, and earthquake sequences. One interaction criterion that offers a more detailed and precise explanation of earthquake occurrence is coulomb stress transfer. This study employs two approaches: the initial strategy relies on the immediate correlation between stronger earthquakes and subsequent smaller ones, while the latter approach considers the long-term connections between larger earthquakes. These coulomb stress variations are estimated using information on the slip of the source fault. The fundamental idea is that, on receiver faults, movement in the elastic crust provides a tensorial stress disturbance that needs to be divided into shear and normal components. If the normal stress decreases in the compressive direction and the shear stress increases in the slip direction, then future events are more likely to occur. An earthquake can thus enhance or suppress events, depending on their location and orientation. Viewed in this light, aftershocks are simply sites of seismicity rate increase, occurring where the stress has increased. Sites of seismicity rate decrease, or where the rate was higher before the earthquake than after, might logically be called ‘antishocks’, because antishocks precede rather than follow the mainshock. Dynamic coulomb stress changes can sometimes be a factor of magnitude greater than static stress changes as a result of the seismic waves stimulated by earthquakes. The dynamic stresses are positive in time everywhere because they oscillate. Since every site has been shaken, there should be no stress shadows or anti-shocks. The final fault offset determines the static coulomb stress changes, which are constant and independent of the rupture process. Compared to the dynamic stress change, it decreases with distance from the source significantly more rapidly.

Strong qualitative relationships between static stress changes and the locations of ensuing events, such as the pair of aftershocks and mainshocks, have been observed in numerous investigations. After the 1992 (M_w 7.3) Landers earthquake, Stein et al. (1994) made the public aware of this connection. Lesser events in the years before had raised stress at the lander focus and along a considerable portion of its rupture length, as the analyst of that analysis showed, and the number of aftershocks occurred in areas of enhanced stress. In order to compare the geographic distribution of the ΔCFF transmitted by the three megathrust earthquakes (the 2011 Tohoku-Oki M_w 9.1, the 2010 Chile M_w 8.8, and the 2004 Sumatra-Andaman M_w 9.0) with the distribution of their aftershocks, Miao and Zhu (2012) assumed that optimally orientated faults would serve as receiver faults. They concluded that there was insufficient evidence to support the idea that changes in coulomb stress, boosted the subsequent activity. The percentage of aftershocks that happened in the positively stressed areas after the earthquakes in Chile,

Sumatra-Andaman, and Tohoku-Oki was 47.6%, 49.8%, and 47%, respectively. They declared that the static triggering theory functioned fairly for these two major intraplate earthquakes (the 2008 Wenchuan and the 1999 Chi-Chi earthquake, respectively), with over 85% of the aftershocks having positive ΔCFF values. Many studies have utilized this model to estimate changes in static stress for various regions, including the Himalaya (Bayrak et al., 2013; Ishibe et al., 2017; Parija et al., 2021).

In order to provide insight into the seismotectonic characteristics of the study area, a statistical evaluation of the aftershock data was conducted (b-value of the Gutenberg-Richter relation, p-value of the modified Omori law, and D-value, the fractal dimension). In addition, an attempt has been made to test the triggering hypothesis, which states how coseismic stress transfer from significant events, affects the subsequent seismicity. This study involves the investigation of the correlation of static stress changes, which are associated with the Nepal earthquake of 2015, with smaller events (aftershocks). Computation has been performed in an elastic half-space due to the slip of a rectangular fault, assuming a shear modulus of 3.2×10^5 bars and a Poisson ratio of 0.25. **Figure 1** shows the fault plane solutions of the Nepal earthquake and its major aftershock, with corresponding aftershocks used in the present work.

REGIONAL TECTONICS AND SEISMICITY

The tectonics of Nepal and the surrounding areas are quite complicated. Situated in the seismically active region of the central Himalaya, Nepal has previously experienced a number of moderate to large/great earthquakes. The collision between the Indian and Eurasian plates produced the Himalaya and numerous thrusts. Four longitudinal tectono-stratigraphic regions have been identified within the Himalayan region: (1) Sub-Himalaya, (2) Lesser Himalaya, (3) Higher Himalaya, and (4) Tethys Himalaya. Several north-dipping thrust faults known as the Main frontal thrust (MFT), Main boundary thrust (MBT), and Main central thrust (MCT) constitute the principal tectonic features of the Nepal Himalaya (Gansser, 1964). It is believed that these thrusts diverge from the main basal detachment of the Himalayan thrust belt, the Main Himalayan Thrust (MHT). The underthrusting of the Indian lithosphere beneath Tibet and the Himalaya is concentrated below this region. In addition, Nepal, adjoining Sikkim and Bhutan, has a concentration of several transverse folds and faults. Along the river Arun, the Arun anticline stretches across eastern Nepal. The Kunchandzangha Dharan bazar syncline, the Sunkoshi anticline, the Trisuli anticline, the Tila anticline, and the Karnali anticline in Nepal are other transverse folds in the region (Nakata, 1989).

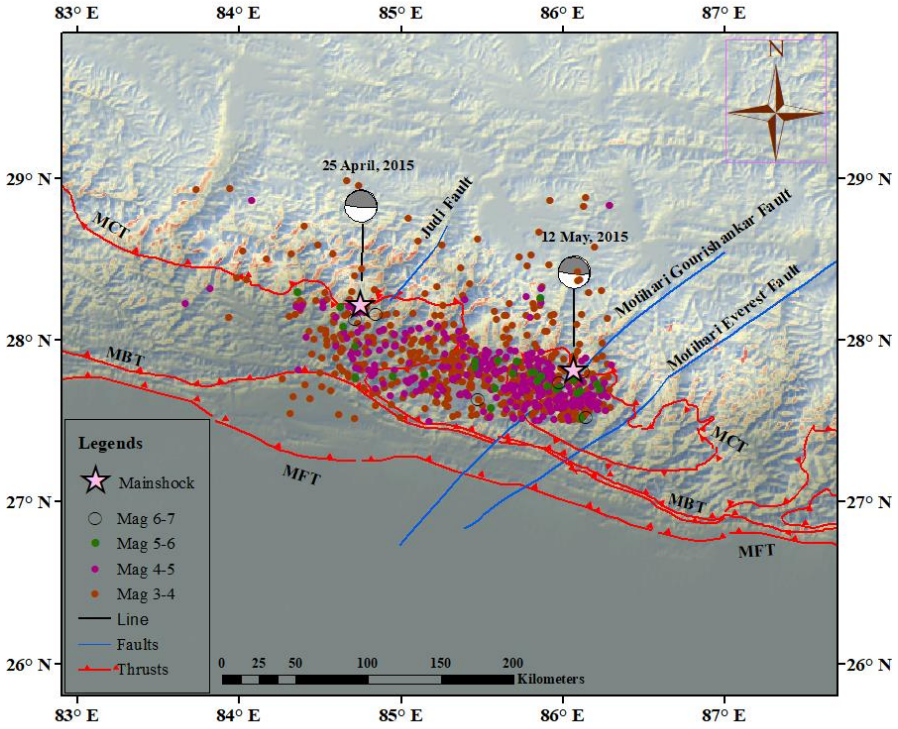

Figure 1. Map showing the fault plane solutions of the Nepal earthquake and its major aftershock with the corresponding aftershocks (circle). MFT-Main frontal thrust, MBT-Main boundary thrust, MCT-Main central thrust. Tectonic features are from Seismotectonic Atlas of India and its Environs by GSI, 2000, along with SRTM-DEM.

Other faults in eastern and central Nepal are the Judi fault, the Motihari-Gaurishanker fault, and the Motihari-Everest fault. Major transverse structures in the Ganga Basin are the Patna fault in Bihar and the Monghyr-Saharsa ridge further south. The regional plate tectonics model has certain limitations, but thrusting is frequently indicated in focal solutions of earthquakes in the Himalaya (Tandon and Srivastava, 1975; Ni and Barazangi, 1984). Remarkably, different MHT geometries have been proposed for central and western Nepal (Pandey et al., 1999). Whereas the latter consists of several smaller ramps, the former is characterised as a single huge ramp located 100 km from the MFT.

Nepal has suffered greatly since ancient times due to earthquakes. Based on paleoseismic data, the earliest known major earthquake in central Nepal is estimated to have occurred in 1100 (Lave et al., 2005). Following 1900, there were 5 or 6-magnitude earthquakes in 1902, 1906, 1909, 1918, 1926, and 1927 (Tandon and Srivastava, 1974). On August 27, 1916, a major earthquake (M 7.5) struck during this time, causing all of the homes in Dharachula to fall. On January 15, 1934, the greatest earthquake (M_w 8.1) struck the Bihar-Nepal region, resulting in a significant loss of life (about 10,000) and extensive property destruction. This earthquake caused large-scale liquefaction in the Bihar lowlands near the Ganga river (Dunn et al., 1939). Buildings were damaged, and there were gaping fractures in the ground along with landslides and ground ruptures due to an earthquake of magnitude 6.5 that struck Kapkote, approximately 110 km away from Almora, on December 28, 1958. This earthquake was correlated with a thrust event. Among the numerous earthquakes that struck Nepal between 1960 and 1990, the magnitude 6 earthquakes that struck in 1966 and 1980 significantly damaged Dharachula and the surrounding areas. According to Srivastava and Gautam (1987), the focal mechanism of these earthquakes revealed thrust faulting that was consistent with the local tectonics. In addition to causing damage to hundreds of dwellings and 721 fatalities in Nepal and 282 fatalities in Bihar, the August 21, 1988, earthquake (M: 6.8) had a huge focal depth of 57 km. This earthquake's focal mechanism revealed strike-slip faulting with a thrust component (Srivastava and Rao, 1991). It was linked to the Monghyr-Saharsa ridge. Major damage was also produced in eastern Nepal, reaching as far as Kathmandu, by the Sikkim earthquake of September 18, 2011 (M_w 6.9), which had a focal depth of 52 km. According to Harvard, this earthquake also displayed strike-slip motion along nodal planes parallel to the Tista and Kunchandzanga lineaments. These are thought to be caused by the region's lake deposits amplifying seismic waves.

A microearthquake study conducted in eastern Nepal revealed a cluster of earthquakes along the border of Sikkim and a concentration of earthquakes along the front of the Himalayan arc, with a seismic gap between longitudes 87.3°N and 87.7°E (Monsalve et al., 2006). In the upper and lower crust, the active zone of microseismicity that stretches from Kunchandzanga to MFT, exhibits thrust, normal, and strike-slip faulting, however, strike-slip faulting predominates near or below Moho. The continental collision is absorbed by strike-slip earthquakes at the Moho in the Himalaya at depths of more than 60 km (Torre et al., 2007).

NEPAL EARTHQUAKE

Nepal is a landlocked nation in South Asia, with a population of almost 3 crore people living in its 147,516 square km region. The largest metropolis and capital city of Nepal is Kathmandu. Situated in a bowl-shaped valley in central Nepal, encircled by four major mountains (Shivapuri, Phulchowki, Nagarjun, and Chandragiri), Kathmandu city is at an elevation of about 1400 meters. The city has been subjected to numerous moderate-intensity earthquakes and approximately one catastrophic earthquake of a higher magnitude every century.

On April 25, 2015 (UTC 06:11:25, local time 11:56 a.m.), a strong earthquake (M_w 7.8) with an epicenter 80 km northwest of Kathmandu struck the Pokhara district in central Nepal. It was the largest and most destructive earthquake in the region since the 1934 Bihar-Nepal earthquake. About 20,000 people were injured in addition to over 8500 fatalities in Nepal. The earthquake rupture moved from deep to shallow sections of the shallowly dipping fault plane, and from west to east, causing strong shaking in Kathmandu and the adjacent municipalities. Deaths also took place in Tibet and India, while damage spread to Bangladesh and Bhutan. Most deaths were reported from the Kathmandu Valley, which has previously seen significant devastation from numerous earthquakes. The recent earthquake destroyed several historic sites in the Kathmandu Valley, including Bhaktapur Durbar Square and Kathmandu Durbar Square (Martin et al., 2015). Two significant aftershocks were recorded; the first (M: 6.6) happened shortly after the first, and the second (M: 6.9) happened around 24 hours later, the following day, resulting in additional house damage and panic. An avalanche on Mount Everest that claimed the lives of at least 19 people, was caused by the earthquake, and another avalanche in Langtang Valley left about 250 people missing. After 16 days, on May 12, 2015, at 12:50 p.m. local time, the largest aftershock (M_w 7.3) struck the Kodari region northeast of Kathmandu in eastern Nepal (Namche Bazar). Its secondary aftershock sequence gave another large

aftershock of magnitude 6.2 about 32 minutes later. In Nepal and India, these shocks resulted in further fatalities and injuries. The Global Centroid Moment Tensor (GCMT) favours a nodal plane with strike 293^0, dip 7^0, and rake 108^0, and the preliminary finite-fault model from the U.S. Geological Survey National Earthquake Information Center (NEIC) shares an identical solution (strike 295^0, dip 10^0, and rake 107^0). The hypocenter depth is 15 km, indicating the earthquake occurred on the MHT. Large occurrences have frequently occurred on this fault (Ambraseys and Douglas, 2004). According to Ader et al. (2012), the GPS-derived convergence rate between South Tibet and India varies from 17.8 ± 0.5 mm/yr to 20.5 ± 1 mm/yr from central and eastern Nepal to western Nepal. Due to the significant moment deficit accumulating on the MHT within Nepal, it has been proposed that if all of the moment is released seismically, the fault might host a great earthquake.

STATISTICAL CHARACTERISTICS OF THE AFTERSHOCK SEQUENCE

Several statistical models have been developed to explain seismic properties in time, space, size of earthquakes, and aftershock sequence (Bath, 1965; Drakatos and Latoussakis, 1996). The key features examined in seismic sequences are, the frequency-magnitude distributions, the decay rate of aftershocks (modified Omori law), and the fractal dimension. Since aftershock sequences can provide information regarding earthquake nucleation and the physical properties of the materials at a fault zone where slip occurs, there has been a significant rise in attention to aftershock sequences in recent years (Frohlich, 1987). The physical characteristics of the Nepal earthquake are examined using widely recognized and often-used empirical and statistical methods. For intent, the aftershocks reported by ISC during the period April 25, 2015 - December 31, 2015, have been considered, in an area bounded within 27.5°N-29°N and 83.5°E-86.5°E.

FREQUENCY–MAGNITUDE SCALING RELATIONSHIP

The most often used parameter for assessing the size of an earthquake is its magnitude. The statistically significant range for a collection of earthquakes is incredibly challenging. An empirical formula

$$\log_{10} N = a - bM \qquad \text{----------(1)}$$

is referred to as the Ishimoto and Lida (1939) relation in the east and the Gutenberg and Richter (1944) relation in the west that define the distribution of earthquakes concerning magnitude. This relationship has been verified for both regional and global seismicity in several seismic zones across the globe (Riznichenko, 1959). For a significant location and time period, equation (1) provides the number of earthquakes N of magnitude M, where a and b are constants. The degree of seismicity in the area is represented by the parameter a. It is dependent upon the dimension of the location, the frequency of earthquakes that have happened there, the maximum seismic magnitude, and the time period. A measure of the potential to characterize stress in the area is the parameter b, which is the slope of the earthquake magnitude and frequency plot. Typically, the b-value varies from 0.6 to 1.5 with a global mean of roughly 1. A b-value of more than 1.0 suggests an area of crustal heterogeneity and low stress, while a value of less than 1.0 implies crustal homogeneity and high stress (Wiemer and Wyss, 2002). In this study, the b-value is estimated using ZMAP (version 6.0) software (Wiemer, 2001).

The assembly of the earthquake catalogue is a prerequisite for estimating b-values. There are two ways to determine b-values,

(i) Least Square (LS) Method
(ii) Maximum Likelihood Estimation (MLE)

The b-value was derived by the maximum likelihood estimation method using the formulation following Utsu (1965), which is given as,

$$b = \log e / M_a - (M_c - \Delta M/2) \qquad \text{----------(2)}$$

Where ‘e’ reflects a constant, M_a signifies the mean magnitude, M_C indicates the minimum magnitude from magnitude completeness, and ΔM is the binding dimension of the collection (Aki, 1965). It is believed that the MLE approach has greater confidence level than the LS approach. A linear trend may be seen in the LS approach when an illustration of earthquake magnitude versus the total collection of earthquakes is examined. The b-value of that location can be determined by measuring the gradient of the trend line. An inherent drawback of this approach is that larger magnitudes have a greater impact on the value than smaller ones. The size of the zone and the earthquake density both affect b-value map resolution; that is, a high-resolution map is produced by a small zone with a high earthquake density. The minimal number of earthquakes per zone for the computation of b-values was determined to be 50, taking into account the above consideration and the number of epicentres in the collection.

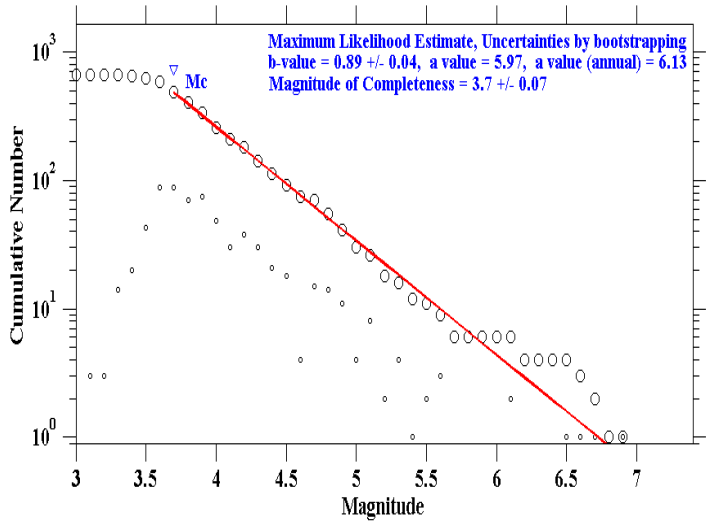

Figure 2. Plot showing the b-value estimation from the frequency-magnitude distribution ($\log_{10}$ N = a-bM) for the Nepal earthquake sequence.

The magnitude of completeness (M_c) for the Nepal sequence was estimated to be equal to 3.7 ± 0.07 (Figure 2) from the maximum curvature method (Woessner and Weimer, 2005). The errors in the parameters have been employed using the bootstrapping method of Efron and Tibshirani (1993). The a and b-values for this sequence were estimated to be equal to 5.97 and 0.89 ± 0.04, respectively. It should be noted that the b-value is less than the worldwide mean value of 1.0, suggesting that the Nepal sequence has substantial differential crustal stress in the regime and aftershocks of greater magnitude.

TEMPORAL DECAY OF AFTERSHOCKS

The following equation provides an empirically acceptable description of the temporal distribution of aftershocks using the modified Omori law (Utsu et al., 1995)

$$n(t) = \frac{K}{(c+t)^P} \qquad \text{----------(3)}$$

where n(t) is the rate at which aftershocks occur, t is the time after the mainshock, and K, p, and c are empirical constants. This law can be considered a sophisticated relaxing process that takes place after the mainshock and is an expression of temporal correlations in the aftershock sequence. The productivity of aftershocks, or the total number of events in a sequence, determines the constant K, while the rate of activity in the earliest portion of the sequence determines the constant c. The inability to correctly detect minor aftershocks in the early stages of the sequence has an impact on the parameter c. The slope of the double-logarithmic plot of the number of aftershocks per unit of time and the time following the mainshock, represents the constant p, which characterizes how steeply the aftershocks decay.

The most significant of these three parameters is p, a decay parameter that fluctuates between 0.6 and 1.8 (Wiemer and Katsumata, 1999) or between 0.5 and 1.8 (Olsson, 1999). This variation could be caused by the crustal heat flow in the source volume or the tectonic conditions of the region, including temperature, stress, and structural heterogeneity. The values of constant K, p, and c in equation (3) for the Nepal sequence are estimated using the maximum likelihood approach, as shown in Figure 3. This sequence was estimated to have a p-value of 1.10 ± 0.03, which is greater than the global p-value of 1.0. High aftershock activity decay is revealed by the high p-value for the Nepal sequence. Bowman (1997) mentioned that in the Australian aftershock region, the temporal decrease of aftershock activity demonstrates the stress dissipation over time. Kisslinger and Jones (1991) proposed that higher temperatures shorten the stress relaxation times by correlating high p-values with high heat flow values for California. The high surface heat flux in the epicentral zone of the Nepal sequence is responsible for the high decay rate of aftershock activity. Short stress relaxation time in the fault zone is caused by high surface heat flux.

SPATIAL FRACTAL DIMENSION (D_s)

The spatial fractal dimension (Ds) is used to analyze the spatial clustering of earthquakes. It suggests that spatial clustering decreases with decreasing fractal dimensions and vice versa. For fractal analysis, this study employed the correlation integral method. According to Grassberger and Procaccia (1983), the correlation integral of the distribution of N earthquakes is,

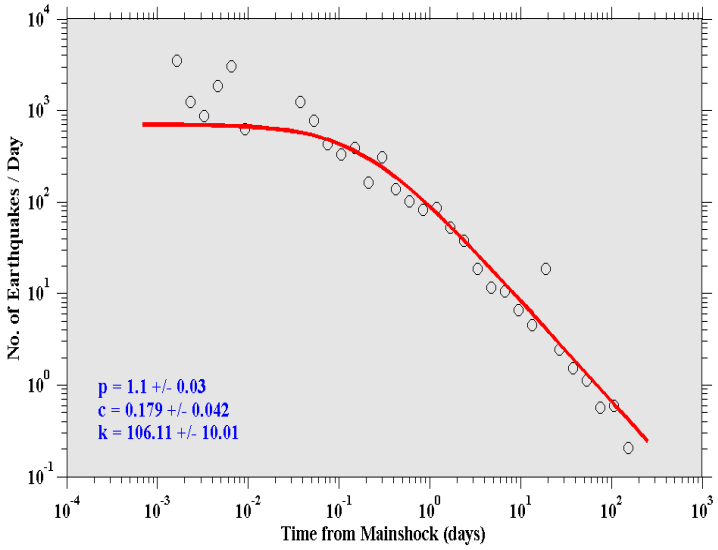

Figure 3. Graph showing the occurrence rate of aftershocks as a function of time after the mainshock. The modified Omori law was fitted with respect to K, c, and p parameters.

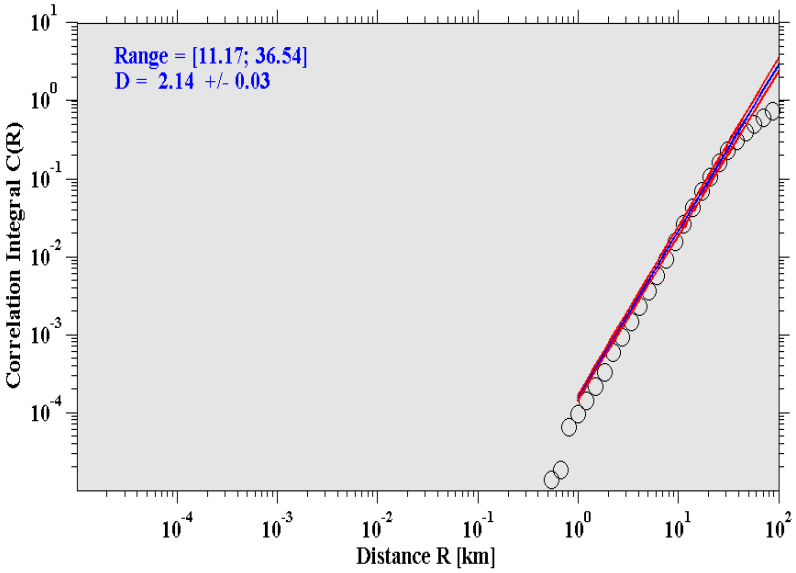

Figure 4. Graph showing the fractal dimension (Ds) of the aftershock distribution. Solid circles show the data for which the best fit is performed for the computation of the D-value.

$$C(R) = \frac{2N_{R<r}}{N(N-1)} \qquad \text{----------(4)}$$

where N (R<r) is the number of event pairs separated by a distance R smaller than r. If the distribution is fractal, then,

$$C(R) \sim r^{D_S} \qquad \text{----------(5)}$$

where Ds is the spatial fractal dimension. The slope of the best-fitted straight line in the log-log plot of C(R) versus r can be used to determine the fractal dimension of a spatial distribution of earthquakes. The heterogeneity of the fractured material is associated with the fractal dimension of the spatial distribution of hypocenters (DeRubeis et al., 1993; Dimitriu et al., 1993). A Ds-value near 0 can be interpreted as all events clustering into one point, near 1 denoting the dominance of line sources, near 2 denoting the filling up of the planar fractured surface, and near 3 denoting the filling up of a crustal volume by earthquake fractures (Khattri, 1995).

Based on the double-logarithmic plot of the correlation integral and distance between the hypocenter **(**Figure 4), we calculated the spatial fractal dimension for the Nepal sequence, which came out to be 2.14 ± 0.03. The events are dispersed randomly along the two-dimensional fault plane that is being filled up by fractures, according to the Ds-value of about 2. One could conclude that this value indicates the approach of a two-dimensional region. Numerous researchers have extensively examined the relationship between the fractal dimension, Ds, and b-value (Wyss et al., 2004; Yadav et al., 2011, 2012). The relationship between these two factors was initially noted by Aki (1981) as D = 3b / c, where c ≈ 1.5 is the scaling constant between the logarithm of a moment and the magnitude of an earthquake (Kanamori and Anderson, 1975). In this study, with Ds = 2.14 and b = 0.89, we found that c = 1.25, which agrees with the aforementioned statements and validates the relationship between the b-value and the fractal dimension.

COULOMB STRESS MODELLING

The subjective movement and tension can be calculated based on the seismic dislocation standard and the assumption that the earth is a homogeneous, isotropic, elastic medium. Variations in the Coulomb failure function (ΔCFF) for a given fault plane and slip direction define variations in stress (King et al., 1994; King and Cocco, 2001; Freed, 2005).

$$\Delta CFF = \Delta\tau + \mu(\Delta\sigma_n + \Delta P) \quad \text{---------(6)}$$

Here, Δτ represents the change in shear stress in the direction of slip, $\Delta\sigma_n$ represents the normal stress change (positive for compressive direction or extension), μ represents the friction coefficient, and ΔP represents the change in pore pressure. The effective normal stress is altered by pore fluid pressure over the failure plane. When the rock stress is altered more quickly than the fluid pressure. By using the Skempton coefficient, P may be connected to normal stress $\Delta P = -B\Delta\sigma_n$, where B varies between 0 and 1.

$$\Delta CFF = \Delta\tau + \mu(\Delta\sigma_n - B\Delta\sigma_n) \quad \text{----------(7)}$$

$$\Delta CFF = \Delta\tau + \mu'\Delta\sigma_n \quad \text{-----------(8)}$$

Here, the effective friction coefficient is denoted by $\mu' = \mu(1-B)$. The ΔCFF is specified on the particular failure plane, also known as the target fault. When ΔCFF is positive, earthquakes tend to occur, and it suppresses the occurrence of earthquakes when ΔCFF is negative.

While the cumulative stress is greater than the ΔCFF induced by an earthquake, numerous seismic activities show that an increase in coulomb stress of more than 0.01 MPa appears to be adequate to trigger occurrences. It is a very surprising fact since an earthquake causes very high stress drops. However, the co-seismic stress increases associated with one earthquake, do not always imply that they are sufficient to cause a second earthquake in a region that was previously stress-free. According to Papadimitriou and Sykes (2001), this suggests that the stresses at the location of the second earthquake were previously close enough to failure that the first earthquake might trigger the second by increasing the coulomb stress and pushing it into the regime of failure. To estimate coulomb stress changes, one needs to know the precise form and focal mechanism of the target fault where stress perturbations are resolved. Usually, two approaches are employed. The first one assigns the strike, dip, and rake angles of the target fault by linking stress variations to a specific faulting mechanism. This method can be used to study a region with a compatible tension field or large source faults with well-known fault processes. This suggests that the slip direction and the fault process are used as guiding variables in the stress interaction simulations. When employing this method, active blind faults are ignored. The second one relies on figuring out the coulomb failure function on planes that are appropriately oriented. Instead of determining the strike, dip, and rake angles of the target faults in this case, we must determine the moment and direction of the principal axes of the regional stress field. These planes approach the tectonic stress in the stress distant field, but they are not guided according to regional trends in the stress close field. If the heterogeneity of the regional stress field is not adequately taken into account, earthquakes with distinct focal processes that occur in a complex regional stress field may result in large errors.

MODEL PARAMETERS AND EARTHQUAKE RUPTURE DATABASE

Though intriguing, subsequent events in zones of increasing stress do not demonstrate that the stress from the mainshock affected seismicity in any way, since seismic activity may have been common in these locations even before the mainshock. Sites exhibiting both an increasing and decreasing seismicity rate are noted after a major shock. An earthquake can therefore either promote or inhibit subsequent occurrences, depending on where and how they are oriented. When this perspective is taken, ensuing events are only spots where the seismic activity has increased and consequently occurs. Sites with a drop in seismicity activity or where it was stronger prior to the earthquake than it was afterwards could reasonably be referred to as anti-shocks because they occur before the mainshock. The fault rupture area and slip are two important characteristics required for the model application. The slip distribution is not uniform along a fault, but one is interested in its average value as well as the fault area expressing the main rupture. Consequently, we computed both of these values as a function of the magnitude M_w of the

significant earthquake using the scaling laws proposed by Wells and Coppersmith (1994). The range of values for μ' is taken from 0.1 to 0.8. While a low friction value is preferred for strike-slip faults with considerable cumulative slip, a high value of μ' has been taken into account for thrust faults and strike-slip faults with little cumulative slip. Because of the significant cumulative slip and the possibility of high pore pressure, the value of μ' for subduction zones will probably be an intermediate value (Toda et al., 2011). **Table 1** shows the information on the source parameters of the earthquakes with magnitude M_w that occurred in the study region. The coseismic displacement of the earthquakes has been considered for stress modelling, and their rupture models are given in **Table 2**, which is used in the study for calculation.

RESULTS

The rupture plane has a dimension of about length 166.52 km and a width of 57.41 km, as estimated by Wells and Coppersmith (1994) for the earthquake that occurred on 25 April 2015. These scaling laws are widely used empirical relationships that link earthquake magnitude to fault rupture dimensions. They are especially important in seismology, hazard analysis and engineering when estimating earthquake size from fault geometry. The up-dip and down-dip ends of the rupture area lie at a depth of 15 km and 21.05 km. The reverse slip and right lateral slip are estimated as 1.86 m and 0.59 m, respectively. According to Lin and Stein (2004), the effective coefficient of friction is assumed to be 0.4. For this analysis, the aftershock data from the International Seismological Centre have been used. We addressed the co-seismic stress variations from the 2015 mainshock simultaneously with ΔCFF imposed by the inter-seismic storing of around 8 months, considering that this particular earthquake occurred onto the Optimally Oriented Plane and a thrust faulting mechanism is likely to have caused it. The co-seismic stress changes have been modelled along with regional seismicity from April 2015 to December 2015 for the Nepal earthquake of 25 April 2015.

Table 1. Source parameters of the earthquakes that occurred in the study region.

S. No.	Events			Moment mag. (M_w)	Nodal plane 1			Nodal plane 2			Source
	Year	Month	Day		Strike	Dip	Rake	Strike	Dip	Rake	
1.	2015	04	25	7.8	295°	10°	108°	96°	79°	87°	USGS
	2015	05	12	7.3	312°	11°	127°	94°	81°	83°	
2.	2015	04	25	7.9	293°	7°	108°	95°	83°	88°	Harvard
	2015	05	12	7.2	312°	11°	127°	94°	81°	83°	

Table 2. Rupture database of the earthquakes that occurred in the study region.

S. No.	Year	Month	Date	Focal depth (Km)	Lat ($°_N$)	Long ($°_E$)	Updip depth (km)	Downdip depth (km)	Length (km)	Width (km)	Reverse slip (m)	Right lateral slip (m)
1.	2015	04	25	15	28.23	84.75	15	21.05	166.52	57.41	1.86	0.59
2.	2015	05	12	18.5	27.82	86.07	18.5	24.56	76.90	31.81	1.07	0.81

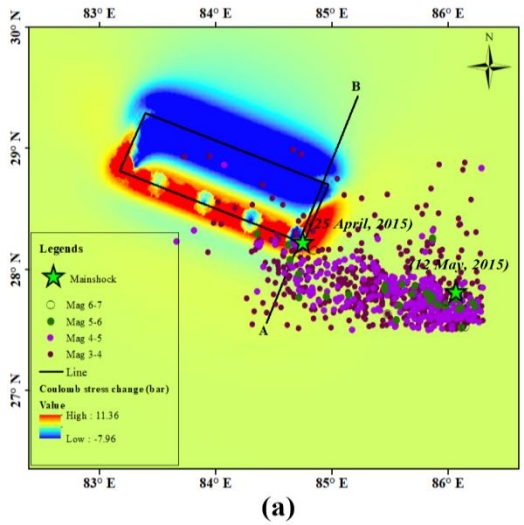

(a)

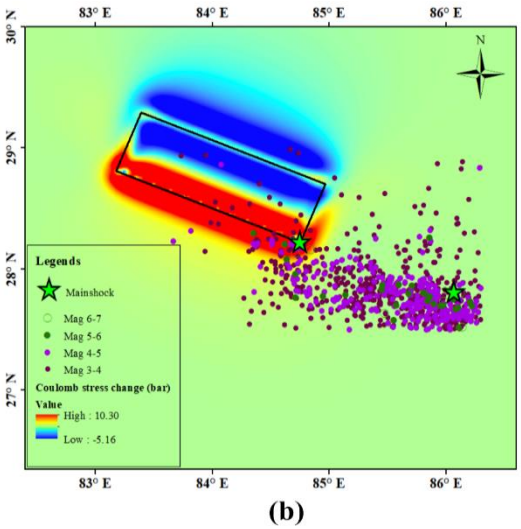

(b)

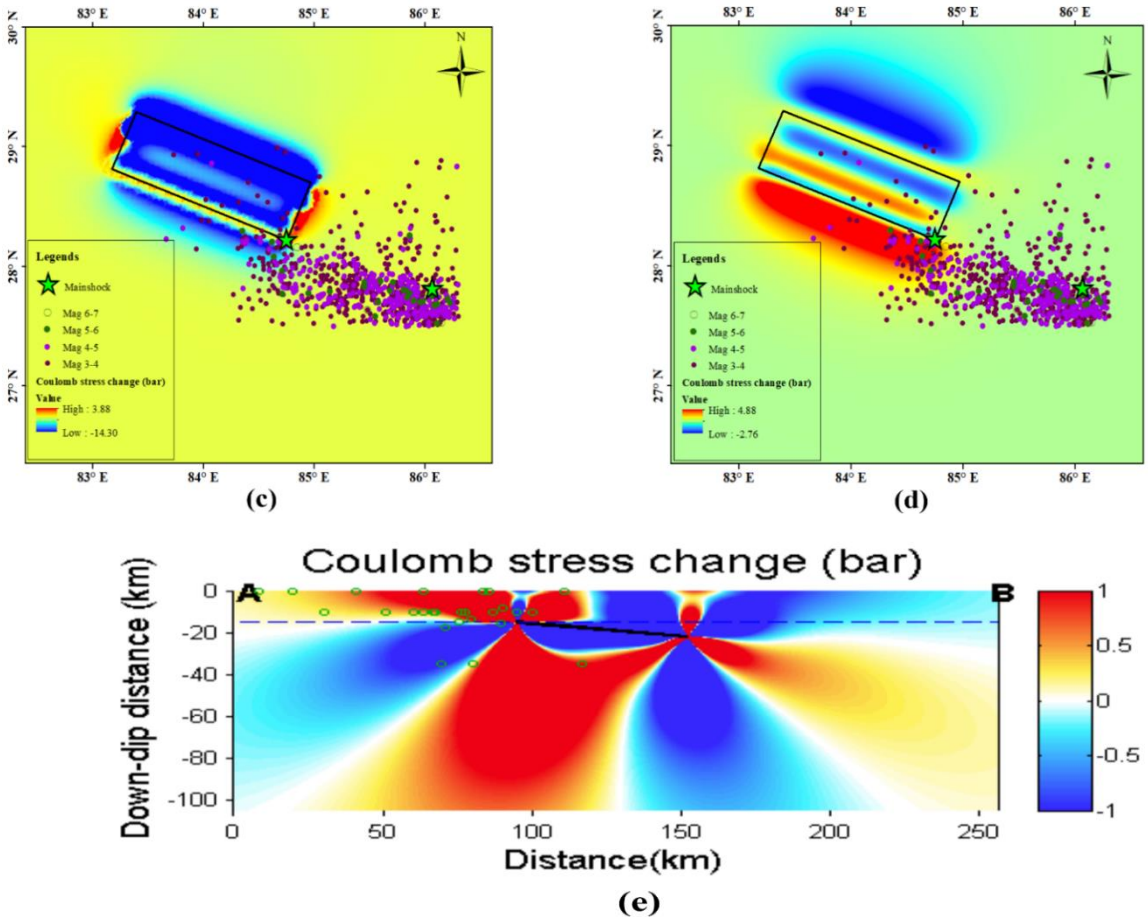

Figure 5. Nepal earthquake of April 25, 2015, Coulomb stress analysis resolved onto ideally oriented planes with a thrust-faulting mechanism for the value of 0.4 effective coefficient of friction. **(a)** Co-seismic stress variations estimated at the depth 15 km (the focus of the earthquake), **(b)** Co-seismic stress variations estimated at the depth 10 km (above the focus), **(c)** Co-seismic stress variations estimated at the depth 20 km (below the focus), **(d)** Co-seismic stress variations estimated at the depth 0 km (on the surface), **(e)** Cross-section of stress variations estimated up to 100 km depth along the profile AB shown in Figure 5(a).

The estimated horizontal distribution of static stress at 15 km depth (Figure 5a) shows the high stress of 11 bar in the NW and NE sides, and low stress of -7.9 bar along the north side of the fault. At 10 km depth, high stress is dominant in the NW and the south side of the fault with a value of 10 bar (Figure 5b). At 20 km depth, high stress is dominant in the NE and NW sides of the fault with a value of 3.88 bar (Figure 5c). The stress values decrease at the surface and are distributed in high and low stress lobes, with values ranging from 5 bar to -2.76 bar (Figure 5d). Major high-stress regions are along the SW and west side, and it is small towards the NW side of the fault at the surface. Low stress regions are in the north side of the fault, showing stable regions. There is less correlation between aftershocks with bright zones (red-coloured area), respectively. The cross-sectional view (Figure 5e) of coulomb stress observed along the profile AB, as shown in Figure 5a, is a vertical cross-section rather than a spatial cross-section. This explains why the cross-sectional view shows fewer aftershocks. It shows an increase in coulomb stress below the up-dip end of the fault up to 100 km depth, suggesting that this may trigger an intermediate earthquake in this region. The two lobes of increased coulomb stress above the up-dip end of the fault can trigger the earthquake at shallow depth and may result in some secondary effects. Two lobes of high coulomb stress are observed at the down-dip end, but smaller than the low-stress lobes. A shallow earthquake may trigger at the down-dip end.

The rupture plane has a dimension of about length 76.90 km and a width of 31.81 km, as estimated by Wells and Coppersmith (1994) for the earthquake that occurred on 12 May 2015. The up-dip and down-dip ends of the rupture area lie at a depth of 18.5 km and 24.56 km. The reverse slip and right lateral slip are estimated as 1.07 m and 0.81 m, respectively. Here, we have taken both earthquake models simultaneously. The estimated horizontal distribution of static stress at different depths is shown Figure 6a-d. From Figure 6d, it can be concluded that there is a maximum

correlation of aftershocks with bright zones (red-coloured area). The findings indicate that maximum aftershocks have occurred in the vicinity of the epicenter of the subsequent event. This also concludes that the major aftershock on 12 May 2015 was caused by the Nepal earthquake that occurred on 25 April 2015.

We additionally examined how friction variation affected the triggering effect shown in Figure 7 (a-d) and Figure 8 (a-d). We repeat our analysis for two additional values (0.2 and 0.8), holding the shear modulus and Poisson's ratio the same. There are variations to varying degrees among the promoted aftershocks for different values, but the concentration of aftershocks with bright zones is still higher. For the value (μ'-0.8), high stress of 9 bar is estimated in the NW and NE sides of the fault compared to stress changes for value (μ'-0.2) at a depth of 20 km (Figure 7c-8c). The triggered events are more than the events that lie in the inhibited regions. Consequently, the variation in the effective coefficient of friction value has a positive influence on the static triggering effect.

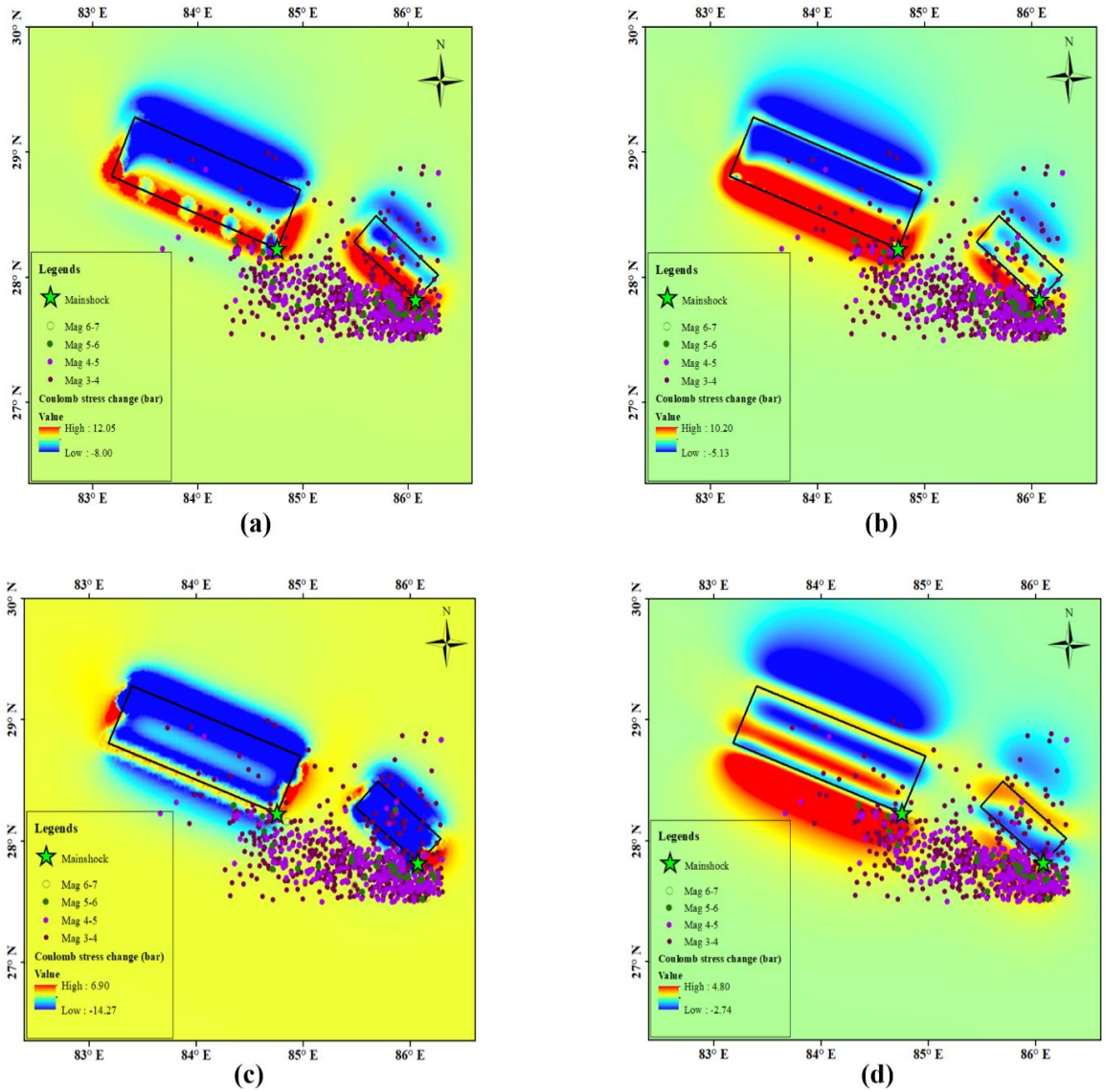

Figure 6. Nepal earthquake of April 25, 2015, together with the major aftershock that occurred on 12 May 2015, Coulomb stress analysis resolved onto ideally oriented planes with a thrust-faulting mechanism for the value of 0.4 effective coefficient of friction, **(a)** Co-seismic stress variations estimated at the depth 15 km (the focus of the earthquake), **(b)** Co-seismic stress variations estimated at the depth 10 km (above the focus), **(c)** Co-seismic stress variations estimated at the depth 20 km (below the focus), **(d)** Co-seismic stress variations estimated at the depth 0 km (on the surface).

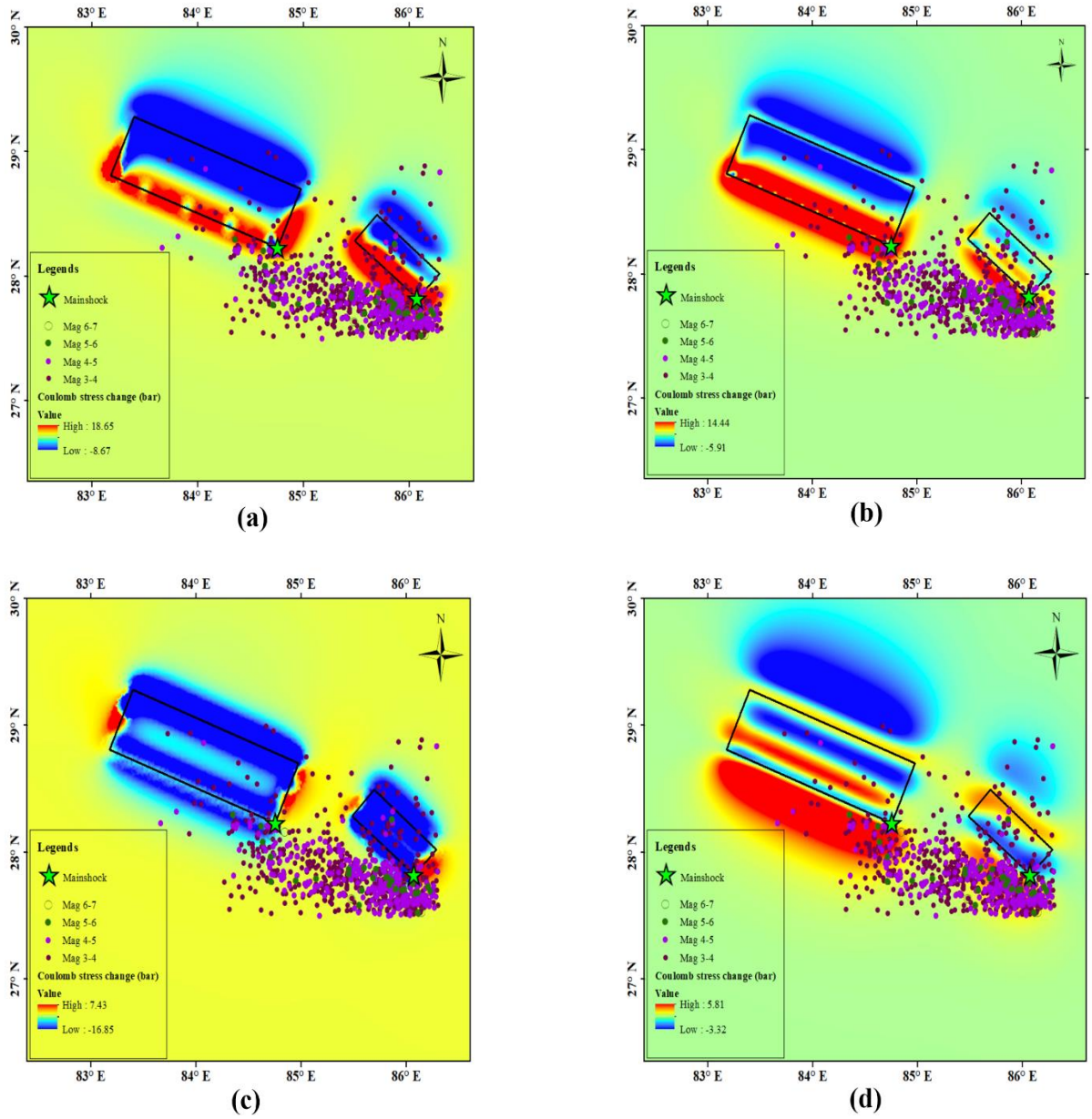

Figure 7. Nepal earthquake of April 25, 2015, together with the major aftershock that occurred on 12 May 2015, Coulomb stress analysis resolved onto ideally oriented planes with a thrust-faulting mechanism for the value of 0.2 effective coefficient of friction, **(a)** Co-seismic stress variations estimated at the depth 15 km (the focus of the earthquake), **(b)** Co-seismic stress variations estimated at the depth 10 km (above the focus), **(c)** Co-seismic stress variations estimated at the depth 20 km (below the focus), **(d)** Co-seismic stress variations estimated at the depth 0 km (on the surface).

DISCUSSION AND CONCLUSIONS

Using statistical methods and stress modelling, the seismotectonic properties and sequential seismicity triggering during the 2015 Nepal earthquake sequence have been examined. For this purpose, seismological parameters such as the b-value, relationship between magnitude of mainshock and largest aftershock (modified Bath's law), p-value, and D-value have been used to analyze the seismic properties of the region using aftershock data from the ISC catalogue during the period April 25, 2015 - December 31, 2015. The Nepal sequence exhibited the complexity of present-day tectonics. The source fault of the Nepal earthquake is oriented towards the NW-SE direction. The spatial distribution of aftershocks that occurred on the fault rupture plane, and the occurrence of aftershock activity towards SE of the rupture, suggests that these shocks have been triggered by coseismic slip of the mainshock fault.

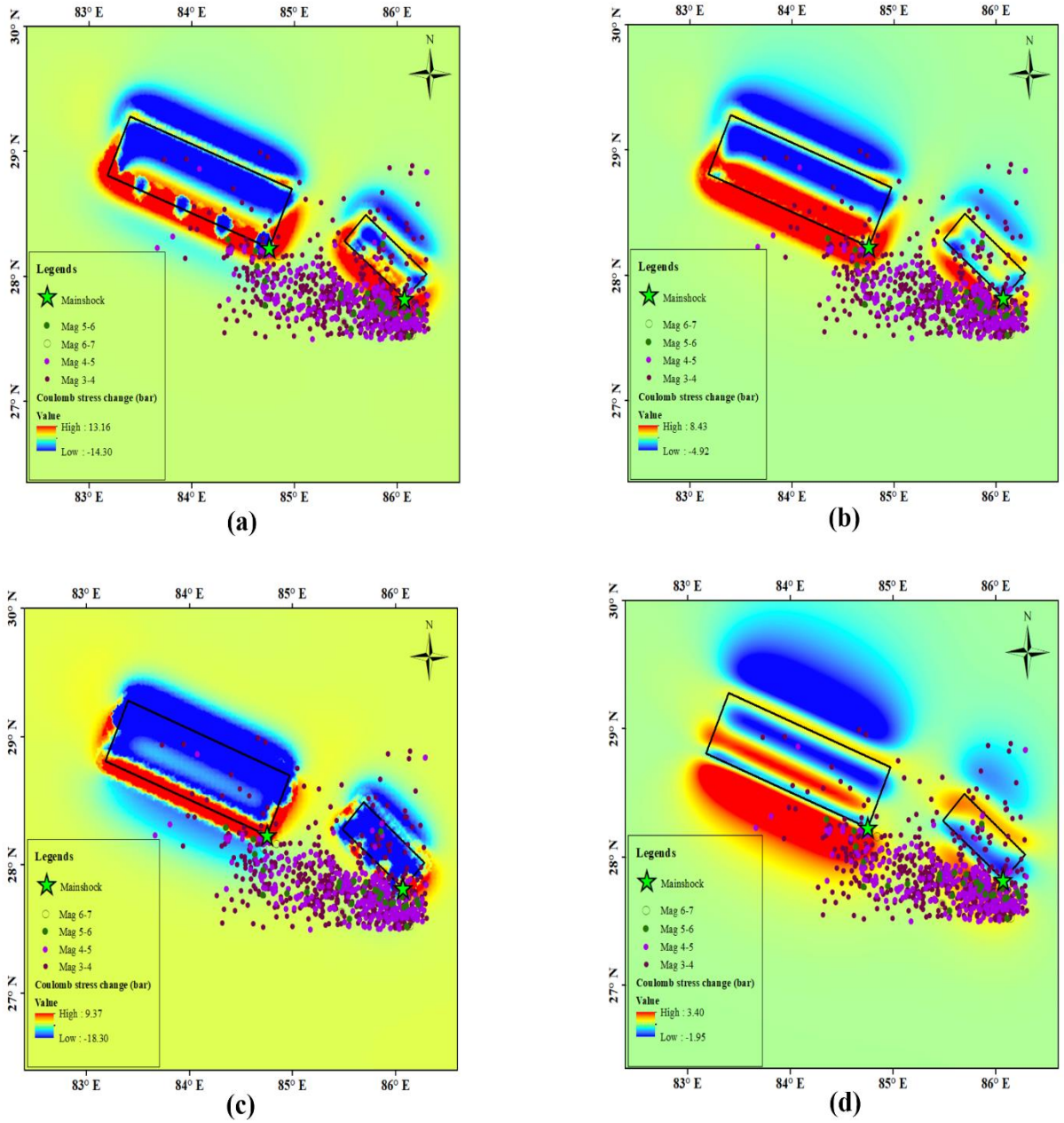

Figure 8. Nepal earthquake of April 25, 2015, together with the major aftershock that occurred on 12 May 2015, Coulomb stress analysis resolved onto ideally oriented planes with a thrust-faulting mechanism for the value of 0.8 effective coefficient of friction, **(a)** Co-seismic stress variations estimated at the depth 15 km (the focus of the earthquake), **(b)** Co-seismic stress variations estimated at the depth 10 km (above the focus), **(c)** Co-seismic stress variations estimated at the depth 20 km (below the focus), **(d)** Co-seismic stress variations estimated at the depth 0 km (on the surface).

The statistical properties of the Nepal earthquake sequence have been analysed and correlated with present tectonics. The creation of substantial aftershock activity in a short period of time confirms the overall estimated low b-value (0.89) for this earthquake sequence, which indicates that the region is exhibiting high differential stress and lesser heterogeneities. Larger-size aftershocks that occurred as a result of the presence of large-size asperities in the rupture zone are likewise correlated with the low b-value. This is further supported by Irmak et al. (2012), who found that a large slip in the epicentral region could be associated with a substantial asperity. Tiwari et al. (2025) also observed low b-values ranging from 0.68 to 0.93 for Nepal and the eastern Himalayan region. The relationship between the magnitude

of the mainshock and its largest aftershock for this sequence has been studied on the basis of the modified Bath law. The ratio of the magnitude of the largest aftershock and mainshock is calculated as 0.93, which is rather high, implying heterogeneous rock mass within the seismogenic volume. Similar characteristics are also observed by Shcherbakov et al. (2005) for the January 17, 1994, Northridge earthquake. The fact that the p-value is close to the typical estimate of 1.10 indicates that the earthquake occurred in a region that is tectonically active and that the stress dissipation time is shorter. The estimated fractal dimension (Ds) of 2.14 indicates that fractures are filling up the rupture that propagated in the two-dimensional plane. The mainshock originated in a section of the rock mass that was highly strained and fractured, according to the estimated seismological parameters above. We investigated coulomb stress models for the Nepal earthquake (M_w 7.8) that occurred in the central Nepal Himalaya. The hypothesis that the occurrence of one earthquake is related to another can be supported by testing the model of coulomb stress variations in the research region. In terms of variations in static coulomb stress, the triggering of earthquakes has been thoroughly explained. The coseismic stress increases linked to one earthquake, however, do not always suggest that they are sufficient to trigger a second earthquake in a previously stress-free area. This implies that the stresses at the site of the second earthquake are formerly sufficiently close to failure that the first earthquake can induce the second one by delivering a positive increase in coulomb stress, causing it to enter the regime of failure.

The Nepal earthquake, which has increased the maximum number of future incidents, fits well with the static triggering model. The triggering effect is still satisfactory by changing the effective coefficient of friction values of the mainshock for the Nepal earthquake. The promoted aftershocks are highly concentrated in the bright zones (red-coloured area). It is observed that the cumulative static stress changes from the mainshock triggered a population of subsequent aftershock activity. The occurrence of aftershock activity at the south-eastern end of the mainshock rupture, could be interpreted as a result of end effects of slip propagation or as the site of additional fault slip. This validates the postulation of earthquake triggering in this sequence. It is also concluded that the major aftershock (12 May, 2015) was caused by the Nepal mainshock.

Acknowledgments

The authors are grateful to the organizations and individual sections that provided the data and information used in the present study. The authors express their gratitude to the Department of Earthquake Engineering, IIT Roorkee, for providing the data and research facilities. The authors are appreciative of their support.

Author credit statement

Ankush Kumar Ruhela and Sonu Devi have done the formal analysis and research work using ZMAP6.0 software. The Coulomb stress modelling in this study has been performed using the Coulomb3.2 software. J. Das supervised the methodology of the whole research work. J. Das and S.C. Gupta have helped in the planning and execution of the manuscript. All the named authors provided critical feedback on data interpretation and supported the improvement of the manuscript.

Data Availability

The data used in the study were sourced from the International Seismological Center (ISC).

Compliance with ethical standards

The authors declare that there are no known financial conflicts of interest or personal relationships that could have influenced the work presented in the paper. They adhere to copyright norms.

References

Ader, T., Avouac, J., Lyon-Caen, H., Bollinger, L., Galetzka, J., Genrich, J., Thomas, M., Chanard, K., Sapkota, S.N. and Liu-Zeng, J., 2012. Convergence rate across the Nepal Himalaya and interseismic coupling on the main Himalayan thrust: implications for seismic hazard. J. Geophys. Res., 117, B04403.

Aki, K., 1965. Maximum likelihood estimate of b in the formula logN= a-bM and its confidence limits. Bull. Earthq. Res. Inst., University of Tokyo, 43, 237–239.

Aki, K., 1981. A probabilistic synthesis of precursory phenomena. In: Symposium, D.W., Richards, P.G. (Eds.), Earthquake Prediction: An International Review. AGU, Washington, DC, pp. 566–574.

Ambraseys, N. N. and Douglas, J., 2004. Magnitude calibration of north Indian earthquakes. Geophys. J. Int., 159, 165-206.

Bath, M., 1965. Lateral inhomogeneities in the upper mantle. Tectonophysics 2, 483–514.

Bayrak, Y., Yadav, R. B. S., Kalafat, D., Tsapanos, T. M., Çınar, H., Singh, A. P., Bayrak, E., Yilmaz, S., Ocal, F. and Koravos, G., 2013. Seismogenesis and earthquake triggering during the Van (Turkey) 2011 seismic sequence. Tectonophysics, 601, 163-176.

Bowman, J. R., 1997. A seismicity precursor to a sequence of Ms 6.3-6.7 midplate earthquakes in Australia. Pure Appl. Geophys., 149, 61–78.

Deng, J. and Sykes, L. R., 1997. Evolution of the stress field in southern California and triggering of moderate-size earthquakes: A 200-year perspective. J. Geophys. Res.: Solid Earth, 102(B5), 9859-9886.

DeRubeis, V., Dimitriu, P., Papadimitriou, E. and Tosi, P., 1993. Recurrent patterns in the spatial behaviour of Italian

seismicity revealed by the fractal approach. Geophys. Res. Lett., (20/18), 1911–1914.

Dimitriu, P. P., Papadimitriou, E. E., Papazachos, B. C. and Tsapanos, T. M., 1993. Global study of the distribution of earthquakes in space and in time by the fractal method. In: Proc. 2nd Congress Hellenic Geophysics Union, vol. 1. May 5–8, Florina, pp. 164–174.

Drakatos, G. and Latoussakis, J., 1996. Some features of aftershock patterns in Greece. Geophys. J. Int., 126, 123–134.

Dunn, J. A., Auden, J. B., Ghosh, M. N., Roy, S. C. and Wadia, D.N., 1939. The Bihar-Nepal earthquake of 1934. Mem. Geol. Survey India, 73,183-391.

Efron, B. and Tibshirani, R., 1993. An Introduction to the Bootstrap. Monographs on Statistics and Applied Probability, vol. 57. Chapman and Hall/CRC, New York.

Freed, A. M., 2005. Earthquake triggering by static, dynamic, and postseismic stress transfer. Annual Rev. Earth Planet. Sci., 33, 335-367.

Frohlich, C., 1987. Aftershocks and temporal clustering of deep earthquakes. J. Geophys. Res., 92, 13,944–13,956.

Gansser, A., 1964. The Geology of the Himalaya. London: Interscience Publishers.

Grassberger, P. and Procaccia, I., 1983. Characterization of strange attractors. Phys. Rev. Lett., 50, 346–349.

GSI, 2000. Geological Survey of India, Seismotectonic atlas of India and its environs.

Gutenberg, R. and Richter, C. F., 1944. Frequency of earthquakes in California. Bull. Seism. Soc. Am., 34, 7507-7514

Irmak, T. S., Doğan, B. and Karakaş, A., 2012. Source mechanism of the 23 October 2011Van (Turkey) earthquake (Mw = 7.1) and aftershocks with its tectonic implications. Earth, Planets and Space. http://dx.doi.org/10.5047/eps.2012.05.002.

Ishibe, T., Ogata, Y., Tsuruoka, H. and Satake, K., 2017. Testing the Coulomb stress triggering hypothesis for three recent megathrust earthquakes. Geosci. Lett., 4(1), 1-11.

Ishimoto, M. and Lida, K., 1939. Observations of earthquakes registered with the microseismograph constructed recently. Bull. Earthq. Res. Inst., University of Tokyo 17, 443–478.

Kanamori, H. and Anderson, D. L., 1975. Theoretical basis of some empirical relations in seismology. Bull. Seism. Soc. Am., 65, 1073–1095.

Khattri, K. N., 1995. Fractal description of seismicity of India and inferences regarding earthquake hazard. Curr. Sci., 69, 361–366.

King, G. C. P. and Cocco, M., 2001. Fault interaction by elastic stress changes: New clues from earthquake sequences. Adv. Geophys., 44, pp. 1-VIII.

King, G. C., Stein, R. S. and Lin, J., 1994. Static stress changes and the triggering of earthquakes. Bull. Seism. Soc. Am., 84(3), 935-953.

Kisslinger, C. and Jones, L. M., 1991. Properties of aftershocks in southern California. J. Geophys. Res., 96, 11947–11958.

Lave, D., Yule, S., Sapkota, S., Basant, C., Madden, M., Attal, M. and Pandey, R., 2005. Evidence for a great medieval earthquake (1000 A.D) in the central Himalaya, Nepal. Science, 307, 1302-1305.

Lin, J. and Stein, R. S., 2004. Stress interaction in thrust and subduction earthquakes. J. Geophys. Res., http://dx.doi.org/10.1029/2003JB002607.

Martin, S. S., Hough, S. E., Bilham, R. and Hung, C., 2015. Ground motions from the 2015 M_w 7.8 Gorkha Nepal earthquake constrained by a detailed assessment of macroseismic data. Seismolog. Res. Lett., 86(6), 1524-1532.

Miao, M. and Zhu, S., 2012. A study of the impact of static Coulomb stress changes of megathrust earthquakes along the subduction zone on the following aftershocks. Chinese J. Geophys., 55(5), 539-551.

Monsalve, G., Sheelan, A., Sehuoke, Pelkum, V., Rajaure, S., Pandey, M. R. and Wu, F., 2006. Seismicity and one-dimensional velocity structure of the Himalayan collision zone: earthquakes in the crust and upper mantle. J. Geophys. Res., 111, B10301.

Nakata, T., 1989. Active faults of the Himalayas of India and Nepal. Geol. Soc. Am. Spect., 232, 243-264.

Ni, J. and Barazangi, M., 1984. Seismotectonics of the Himalayan collision zone: geometry of the underthrusting Indian plate beneath the Himalaya. J. Geophys. Res., 89, 1147-1163.

Olsson, R., 1999. An estimation of the maximum b-value in the Gutenberg–Richter relation. J. Geodynam., 27 (4–5), 547–552.

Pandey, M. R., Tandukar, R., Avouac, J. P., Vergne, J. and Heritier, T., 1999. Seismotectonics of the Nepal Himalaya from a local seismic network. J. Asian Earth Sci., 17, 703-712.

Papadimitriou, E. E. and Sykes, L. R., 2001. Evolution of the stress field in the northern Aegean Sea (Greece). Geophys. J. Int., 146(3), 747-759.

Parija, M. P., Kumar, S., Tiwari, V. M., Biswal, S., Biswas, A. and Velliyidathu, A., 2021. Coulomb stress modelling and seismicity in the Western Himalaya, India since 1905: implications for the incomplete ruptures of the Main Himalayan thrust. Tectonics, 40(9), doi.org/10.1029/2020TC006204.

Riznichenko, J. V., 1959. On quantitative determination and mapping of seismic activity Annali Di Geofisica, 12: 227–37.

Scholz, C. H., 1990. The mechanics of earthquakes and faulting. Cambridge University Press, pp. 439.

Shcherbakov, R., Turcotte, D. L. and Rundle, J. B., 2005. Aftershocks statistics. Pure Appl. Geophys., 162, 1051-1076.

Srivastava, H. N. and Gautam, U. P., 1987. Spatio-temporal variations of seismicity preceding earthquakes of 1966 and 1980 near India Nepal border. In: Proc. Seminar on Geophysics and Environment, Jan 22-23, Hyderabad (India): Indian Geophysical Union.

Srivastava, H. N. and Rao, P. C. S., 1991. Seismicity patterns associated with earthquakes of August 1988 near Manipur, Burma and Bihar, Nepal regions. Bull. Indian Soc. Earthq. Tech., 28, 13-22.

Stein, R. S., King, G. C. and Lin, J., 1994. Stress triggering of the 1994 M= 6.7 Northridge, California earthquake by its predecessors. Science-New York, Washington, 1432-1435.

Tandon, A. N. and Srivastava, H. N., 1974. Earthquake occurrence in India. Meerut: Sarita Prakashan, p. 1-44.

Tandon, A. N. and Srivastava, H. N., 1975. Focal mechanism of some recent Himalayan earthquakes and regional plate tectonics. Bull. Seism. Soc. Am., 65, 963-969.

Tiwari, R. K., Subedi, A., Parajuli, D., Dharel, S., Neupane, A. and Subedi, H., 2025. Regional patterns of seismic b-values variations in the Himalayan region (71.6 E-95.5 E and 37.5 N-26.6 N). J. Seismic Exploration, 34(1), 1-11.

Toda, S., Lin, J. and Stein, R. S., 2011. Using the 2011 Mw 9.0 off the Pacific coast of Tohoku Earthquake to test the Coulomb stress triggering hypothesis and to calculate faults brought closer to failure. Earth Planets Space, 3(7):725–730. doi:10.5047/eps.2011.05.010.

Torre, T. L., De la, Monsalve, G., Sheehan, A. F., Sapkota, S. and Wu, F., 2007. Earthquake processes of the Himalayan Collision zone in eastern Nepal and the Southern Tibetan Plateau. Geophys. J. Int., 171, 718-738.

Utsu, T., 1965. A method for determining the value of b in a formula logN = a – bM, showing the magnitude frequency for earthquakes. Geophys. Bull., Hokkaido University, 13, 99–103.

Utsu, T., Ogata, Y. and Matsuura, R. S., 1995. The centenary of the Omori formula for a decay law of aftershock activity. J. Phys. Earth, 43, 1–33.

Wells, D. L. and Coppersmith, K. J., 1994. New empirical relationships among magnitude, rupture length, rupture width, rupture area, and surface displacement. Bull. Seism. Soc. Am., 84(4), 974-1002.

Wiemer, S., 2001. A software package to analyze seismicity: ZMAP. Seism. Res. Lett., 373–382.

Wiemer, S. and Katsumata, K., 1999. Spatial variability of seismicity parameters in aftershock zones. J. Geophys. Res., 104, 13135–13151.

Wiemer, S. and Wyss, M., 2002. Spatial and temporal variability of the b-value in seismogenic volumes: an overview. Adv. Geophys., 45, 259–302.

Woessner, J. and Wiemer, S., 2005. Assessing the quality of earthquake catalogues: estimating the magnitude of completeness and its uncertainty. Bull. Seism. Soc. Am., 95 (2), 684–698.

Wyss, M., Sammis, C. G., Nadeau, R. M. and Wiemer, S., 2004. Fractal dimension and b-value on creeping and locked patches of the San-Andreas fault near Parkfield, California. Bull. Seism. Soc. Am., 94, 410–421.

Yadav, R. B. S., Papadimitriou, E. E., Karakostas, V. G., Shanker, D., Rastogi, B. K., Chopra, S., Singh, A. P. and Santosh, K., 2011. The 2007 Talala, Saurashtra, western India earthquake sequence: tectonic implications and seismicity triggering. J. Asian Earth Sci., 40 (1), 303–314.

Yadav, R. B. S., Gahalaut, V. K., Chopra, S. and Shan, B., 2012. Tectonic implications and seismicity triggering during the 2008 Baluchistan, Pakistan earthquake sequence. J. Asian Earth Sci., 45, 167-178.

Received on: 09-12-2024 ; Revised on: 04-02-2026; Accepted on: 15-02-2026

J. Ind. Geophys. Union, 30(3) (2026), 171-183
https://doi.org/10.71122/JIGU.30(3)2026.0018

Geophysical mapping east of Closepet Granite in Eastern Dharwar Craton for inferring geology and structure

Santosh Yadav* and Abir Deogharia
Geological Survey of India, Hyderabad- 500 068, India
*Corresponding author: santosh.yadav@gsi.gov.in

ABSTRACT

An integrated gravity and magnetic survey was carried out over the eastern margin of the Closepet Granite in the Eastern Dharwar Craton (EDC), southern India, to delineate concealed structural trends and crustal configuration. Ground gravity measurements were acquired using a Scintrex CG-5 gravimeter with DGPS elevation control, and magnetic total field data were collected using a proton precession magnetometer. Bouguer gravity anomalies were computed using standard free-air and Bouguer corrections ($\rho = 2.67$ g/cm³), while the magnetic data were corrected for diurnal variations and the IGRF (epoch 2015). The datasets were processed using minimum curvature gridding and Fourier domain filters including analytical signal, tilt derivative, and Reduction to Equator (RTE). Spectral analysis, Euler deconvolution, and joint gravity–magnetic modelling were carried out to constrain source geometry and depth. The Bouguer gravity anomaly map exhibits a total relief of ~33 mGal (–95 to –62 mGal) and reveals a prominent N–S trending gravity high in the central part of the study area. This feature is characterized by steep gradients along its eastern margin and comparatively gentle gradients to the west, suggesting asymmetric geometry. Spectral analysis of gravity data identifies three principal depth levels at approximately 6 km, 3 km, and 1.5 km, indicating a layered upper crustal structure. Euler depth solutions corroborate these estimates and suggest deeper-seated sources in the northern part, compared to the south. The gravity high is interpreted as a laterally extensive three-dimensional crustal body and is considered to represent the probable subsurface extension of the Ramagiri Schist Belt. Associated gravity lows are attributed to lower-density granitic intrusions and structural depressions. Magnetic data, after RTE transformation, reveal dominant E–W to NW–SE trending features, superimposed on the N–S structural fabric. Spectral depths from magnetic data (4.5 km, 3 km, and 1.5 km) indicate that the deepest gravity source lacks significant magnetic susceptibility contrast, suggesting a weakly magnetic basement. Analytical signal and tilt derivative maps clearly delineate structural boundaries and dyke-like intrusions. Euler solutions further constrain shallow magnetic sources aligned along E–W and NW–SE trends. Further, the Joint gravity–magnetic modelling along a 76 km AA′ (N–S) profile, constrained by spectral depths, Euler solutions, geological information, and measured density and susceptibility values, confirms presence of a deep N–S trending density-controlled body and relatively shallow magnetically controlled intrusions. Spatial correlation between structural intersection zones and known corundum occurrences suggests additional prospective targets.

Keywords. Eastern Dharwar Craton, Closepet granite, gravity-magnetic, Indian shield

INTRODUCTION

The Dharwar Craton of Peninsular India, comprises Archean greenstone belts ranging in age from 3.4 to 2.7 Ga, intruded by extensive granitic bodies during later tectono-magmatic events. The craton is broadly divided into the Western Dharwar Craton (WDC) and Eastern Dharwar Craton (EDC) by ~2518 Ma Closepet Granite (Naqvi and Rogers, 1987; Jayananda et al., 2000; Ramakrishnan and Vaidyanadhan, 2008). Compared to WDC, EDC contains smaller and discontinuous greenstone belts. Subsequent Proterozoic dyke intrusions modified the crustal architecture after granitic emplacement, resulting in present-day surface exposures dominated largely by the Peninsular Gneissic Complex (PGC) and granitic terrains.

Extensive gravity and magnetic surveys have been conducted in the region to delineate subsurface geological structures and lithological variations. The Geological Survey of India (GSI) carried out geophysical investigations in multiple phases (Kailasam et al., 1974; Khare and Nagabhushanam, 1984; Chayanulu et al., 1989; Kesavamani et al., 1994), primarily focusing on localized areas of 1–2 km extent. The present survey covers a large area with higher data density using advanced geophysical instruments. Bouguer gravity anomalies and magnetic total field anomalies were computed from the acquired data. To enhance structural interpretation, derivative maps such as the first vertical derivative and horizontal gradient maps were generated. These derivative maps amplify short-wavelength anomalies and sharpen anomaly gradients, thereby enhancing the shallow subsurface features. The first vertical derivative, highlights near-surface sources by suppressing deeper regional effects, while horizontal gradient maps delineate lateral density and susceptibility contrasts by emphasizing maxima along structural boundaries. Consequently, faults, dyke intrusions, lithological contacts and structural discontinuities, can be identified more clearly from these enhanced gradients. The processed gravity and magnetic data sets were integrated to examine spatial correlations between density and magnetic susceptibility contrasts. Joint gravity–magnetic modeling was then performed to constrain the geometry of subsurface bodies and propose a plausible geological configuration for the study area.

GEOLOGY SETTING

Geochronologically, Archean Sargur group and Peninsular Gneissic Complex (PGC) forms bottom followed by Dharwar Supergroup (Archean-Lower Proterozoic) and then Closepet granite and dykes of Proterozoic age (Geology Map Degree sheet 57G by Cartography Division, GSI, Hyderabad

1994). The geology map of the study region is shown in Figure 1. The Sargur group of rocks mostly occur as N-S trending narrow enclaves within the vast PGC. Lithologically, this group comprises hornblende schist, amphibolite, ultramafic schist, chlorite schist, pyroxene granulite and quartzite, while the PGC consist migmatite, grey granite and gneissic granite. The Dharwar Supergroup is represented by meta-sedimentary and meta-volcanic rocks. They are folded, sheared and faulted. The Closepet granite ranges in width from 15 to 26 Km and is regarded generally as of magmatic origin. Most of the basic dykes are of dolerite composition and cut across the above formations in two major trends namely N-S to NNW-SSE and E-W to ENE-WSW. Quartz veins are seen throughout the area. Overall, the area is covered by PGC and grey granite. The later intrusions are seen in the form of dykes.

SURVEY LAYOUT AND METHODOLOGY

The study area is bounded by 13°15′ N to 14°00′ N and 77°15′ E to 78°00′ E, covering Survey of India topo sheets 57G/5, 57G/6, 57G/7, 57G/9, 57G/10, 57G/11, and 57G/13. Gravity and magnetic observations were acquired along available metaled roads, fair-weather roads, and cart tracks, achieving an average station density of approximately one station per 2.5 sq. km. The instruments used for the geophysical survey include a Scintrex CG-5 gravimeter for gravity measurements, a Leica DGPS (GS10 sensor with CS10 controller) for precise elevation and positional control, and a GEM Systems Proton Precession Magnetometer (Model TM-16) for total magnetic field measurements.

Gravity drift correction was performed using local base stations established near field camps. These local bases were connected to the primary gravity base at Hindupur I.B., established by the Geophysics Division of the Geological Survey of India (GSI), which is tied to the Survey of India Pendulum Station at Guntakal I.B., ensuring regional consistency and accuracy. Bouguer gravity anomalies were computed by subtracting theoretical gravity (calculated using the International Gravity Formula 1980) from observed gravity values. Free-air and Bouguer corrections were then applied, assuming a standard crustal density of 2.67 g/cm^3. Similarly, total magnetic field (TF) anomalies were obtained by subtracting the International Geomagnetic Reference Field (IGRF, epoch 2015) from the drift-corrected observed magnetic field values.

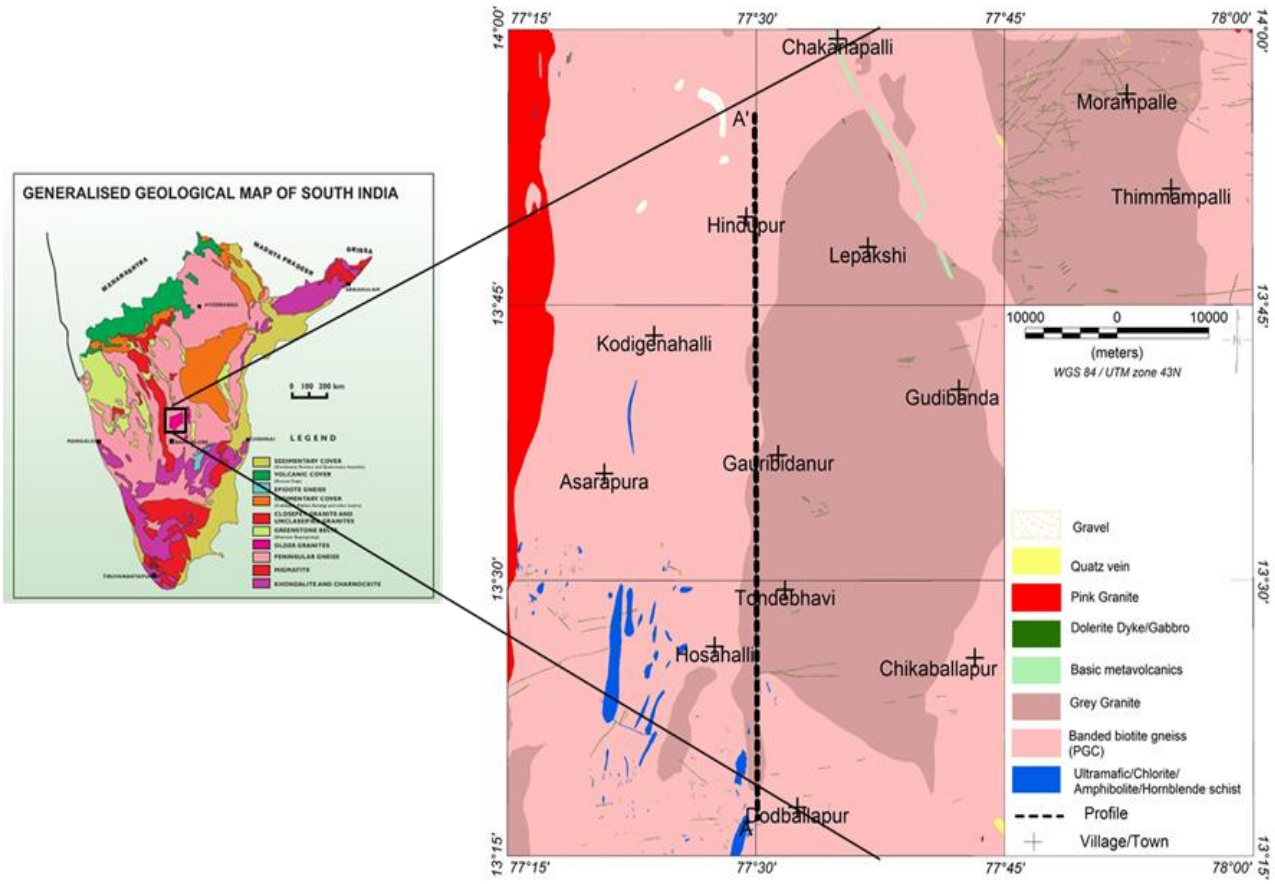

Figure 1. Location map of the study area and regional geology

Data processing was carried out using Geosoft software (version 8.3). Both gravity and magnetic datasets were gridded using the minimum curvature algorithm with a grid cell size of 1500 m. The MAGMAP module was employed to apply Fourier domain filters to the gridded data. Filters such as Analytical Signal (Nabighian, 1984), Tilt Derivative (Miller and Singh 1994), and Reduction to the Equator (Leu, 1982) were applied for enhanced structural interpretation. The analytical signal amplitude highlights the edges of magnetized or density-contrasting bodies and attains maxima directly over the causative source, independent of magnetization direction. It is expressed as:

$$A(x,y) = \sqrt{\left(\frac{dT}{dx}\right)^2 + \left(\frac{dT}{dy}\right)^2 + \left(\frac{dT}{dz}\right)^2} \qquad (1)$$

where A(x,y) is the analytical signal amplitude and T represents the observed potential field (gravity or magnetic anomaly).

The Tilt derivative gives high over the source irrespective of its magnitude of response and its zero contour marks the boundary of source. It is expressed as

$$TDR = tan^{-1}\left(\frac{\frac{dT}{dz}}{\sqrt{\left(\frac{dT}{dx}\right)^2 + \left(\frac{dT}{dy}\right)^2}}\right) \qquad (2)$$

where TDR is tilt derivative and T is potential field. Reduction to the equator is used in low magnetic latitudes to center the peaks of magnetic anomalies over their sources. It causes features normal to the declination direction to blow up due to the strong amplitude correction. Radially Averaged Power Spectrum (RAPS) which gives ln (power) vs wavenumber K and depth estimate vs wave number K, is calculated using Magmap module (Spector and Grant, 1970). It is a relation between power spectrum and depth values of ensembles expressed as,

$$P(w) = A\exp(-2|w|h) \qquad (3)$$

$$\text{after taking logarithm,} \quad \ln\big(P(w)\big) = -2|w|h + A \quad (4)$$

where P(w) is power spectrum, A is constant, w is wavenumber and h is depth of source. Thus, the slope gives the depth of source. The GM-SYS module is used for profile modelling to create a geologic model and test its accuracy by comparing the model's gravity and magnetic response to observed measurements (Talwani and Heirtzler, 1964). The average values of density and susceptibility of different lithology is used for modelling. The profile is chosen along the N-S direction cutting magnetic anomalies and along the inferred schist extension. Euler solutions were obtained using Euler 3D module in Geosoft (Reid et al., 1990). The equation is iterated over the given window size and depths are obtained in given depth tolerance limit. The equation is

$$(x - x_o)\frac{\partial T}{\partial x} + (y - y_o)\frac{\partial T}{\partial y} + (z - z_o)\frac{\partial T}{\partial z} = N(F - T) \quad (5)$$

where T is field at (x, y, z) from source at position (x_o, y_o, z_o), N is structural index which defines the dimensions of source and F is total field. The original grid is re-grided to 500 m interval and appropriate windows size and structural index have been chosen to obtain optimum solutions falling on major linear reported in this this area. The structural index (SI) is chosen 0.2 and window size is 20 with depth tolerance of 5% for gravity data and structural index (SI) is chosen 1.5 and window size is 20 with depth tolerance of 5% for magnetic data.

A total of 112 samples is collected from the surveyed area for which density and susceptibility measurements have been carried out. The susceptibility of samples was measured using Dual Frequency Susceptibility Meter of Bartington make with an accuracy of 0.1 CGS units. Density measurements were carried out with electronic balance of Afcoset with an accuracy of 0.001. The measured value of density and susceptibility is tabulated in Table 1.

Table 1. Measured physical properties of samples from the studied region

Rock type	No. of samples	Density (g/cm^3)		Magnetic susceptibility range in CGS units (x 10^{-6})
		Range	Average	
Dolerite	17	2.60-3.0	2.98	25-4023
Quartz	15	2.32-2.78	2.60	0-308
Granodiorite	4	2.64-2.73	2.68	4.5-2056
Granite	51	2.3-2.81	2.57	1-940
Mafic	7	2.96-3.36	3.07	20-1800
Gabbro	4	2.54-3.02	2.84	7-830
Amphibolite	3	2.98-3.02	2.95	18-30
Epidote	3	2.71-3.02	2.85	12-725
Basalt	7	2.70-3.04	2.96	46-744

RESULTS

The physical properties of collected rock samples are quite useful in gravity and magnetic data analysis. In fact, the contrast between these physical properties gives rise to anomalies, which we analyze. Thus, an idea of density and susceptibility variation in an area is effective in interpretations of gravity and magnetic data. The granite which constitutes a major portion of exposed surface has variation in density 2.3-2.81 g/cm^3 and susceptibility 1-940 x 10^{-6} CGS. Similarly, granodiorite 2.64-2.73 and 4.5-2056 x 10^{-6} CGS, and diorite 2.60-3.0 and 25-4023 x 10^{-6} CGS. Samples from Quartz veins have shown density variation of 2.32-2.78 g/cm^3 and susceptibility of 0-308 x 10^{-6} CGS. Other samples are from mafic source which have higher density and susceptibility. It can be seen that most of study area has granite, which are associated with dolerite dykes or mafic intrusions.

Bouguer Gravity Anomaly

The Bouguer gravity anomaly map, contoured at an interval of 1 mGal, is shown in Figure 2. The anomaly values range from –95 mGal to –62 mGal, exhibiting a total relief of approximately 33 mGal across the study area. Based on the anomaly pattern and amplitude, several distinctive features are identified: a prominent central high (GH1), a gravity low in the northern part (GL1), a comparatively less prominent high in the eastern sector (GH2), and moderate amplitudes elsewhere. The feature GH1 is characterized by closely spaced contours along its eastern margin, indicating a steep gradient, whereas the western side shows a comparatively gentler gradient. The amplitude of GH1 gradually decreases northward, and the anomaly appears discontinuous along the north–south direction. In the northernmost part of the area, a noticeable change in anomaly trend is observed. Pinching and swelling of contours along the margins of GH1, suggest structural complexity or segmentation of the causative body. The eastern high (GH2) is marked by widely spaced contours and a gentle gradient, with a predominant E–W trend. Both GH1 and GH2 occur over the exposures of PGC and grey granite. These gravity highs are interpreted to be associated with subsurface high-density material. A localized swelling of GH1 near Tondebhavi extends across the Closepet Granite, suggesting subsurface continuity of the high-density body beneath the granitic cover. Between GH1 and GH2, a major gravity low extends up to Tondebhavi. The northern low (GL1) exhibits a contrast of approximately 10 mGal relative to the surrounding background and shows maximum amplitude contrast in the northern part, which progressively decreases southward.

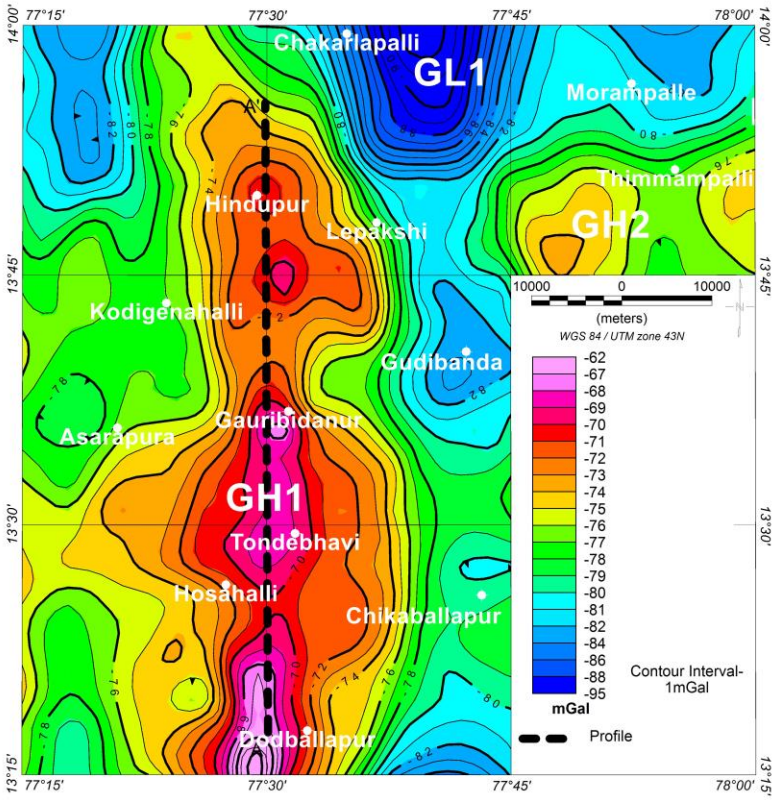

Figure 2. Bouguer gravity anomaly map of the studied region located east of Closepet granites

Derivative maps and Euler deconvolution of Bouguer gravity anomaly

The tilt derivative of the Bouguer gravity anomaly, shown in Figure 3, enhances the edges of density contrasts. In the tilt derivative map, the zero-contour delineates the boundaries of causative sources, thereby clearly defining structural edges. A prominent N–S trending feature corresponding to GH1 is observed, with evident pinching and swelling along its extent. An additional E–W trending source is delineated in the eastern part, corresponding to GH2. Euler deconvolution was applied to estimate the depth to source and structural configuration. The depth solutions were classified into three categories: less than 1000 m, 1000–3000 m, and greater than 3000 m. The solutions indicate comparatively greater depths along the eastern boundary of GH1 than along its western margin, consistent with the broader anomaly gradient observed on the Bouguer map. Furthermore, depth estimates in the northern part are generally higher than in the southern part, which correlates with the broader anomaly character and reduced gradient observed northward, suggesting deeper-seated sources in that region. The spatial distribution of Euler solutions shows a dominant N–S alignment in the central part, with minor discontinuities, while an E–W alignment is evident in the eastern sector, consistent with the trends observed in both the Bouguer anomaly and tilt derivative maps.

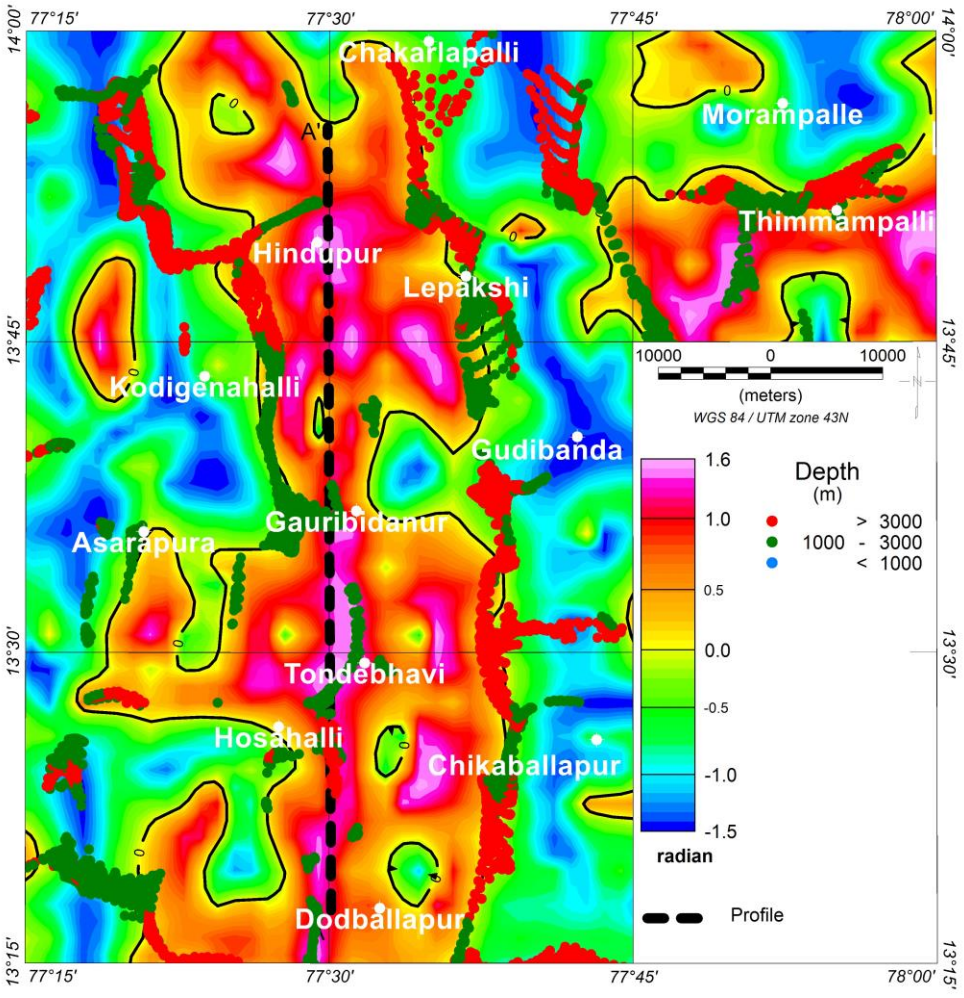

Figure 3. Euler solutions on Tilt derivative of Bouguer gravity anomaly

Total magnetic field anomaly

Magnetic anomalies in low latitudes are generally bipolar in nature because the Earth's magnetic field has a low inclination in such regions. At low magnetic inclinations, the inducing geomagnetic field is nearly horizontal. As a result, magnetized bodies produce anomalies with adjacent positive and negative lobes rather than a single symmetric peak. The shape and polarity of the anomaly therefore depend strongly on the orientation, dip, strike, and magnetization direction of the causative body. To facilitate interpretation, the Reduction to Equator (RTE) filter was applied to the total magnetic field anomaly data. RTE corrects the anomaly for the effect of low magnetic inclination and shifts the anomaly closer to the causative source, thereby simplifying its geometry. The RTE magnetic anomaly map, contoured at 25 nT interval, is shown in Figure 4. The northern part of the map is characterized by high-amplitude anomalies. The southern part shows moderate to low amplitudes, while the eastern part is dominated by relatively low-amplitude anomalies. The general structural trends vary from E–W to NW–SE. Alternate high and low anomalies are observed from Dodballapur to Hindupur. A dominant low-amplitude anomaly with large wavelength is observed near Thimmanpalli, indicating a deeper or broader source. A strong bipolar anomaly is present near Hindupur. Smaller bipolar anomalies with lower amplitude and shorter wavelength are observed near Gudibanda and north of Chikkaballapur.

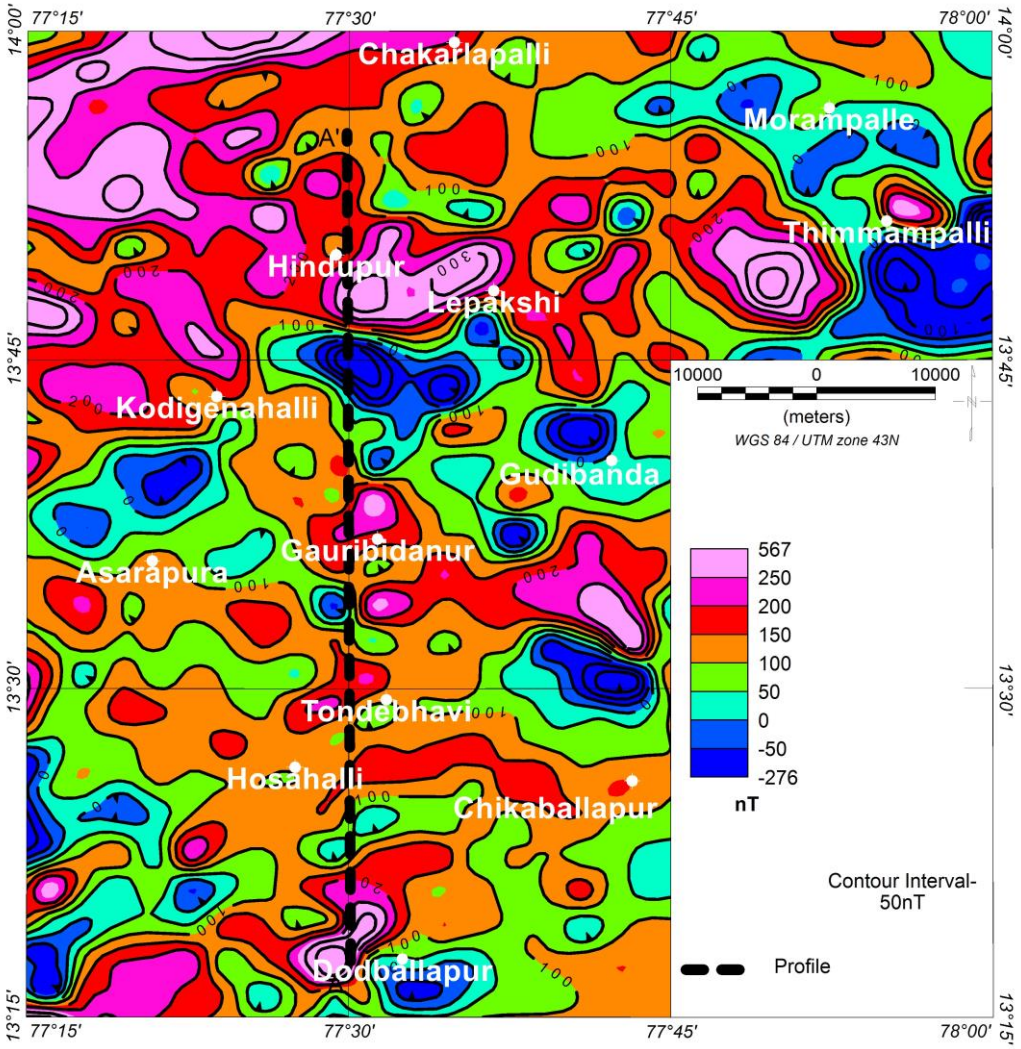

Figure 4. RTE of magnetic total field anomaly

Derivative maps and Euler deconvolution of magnetic total field anomaly

The analytical signal map of the magnetic anomaly is shown in Figure 5. It combines the horizontal and vertical derivatives of the magnetic field and produces a peak directly over the causative body, independent of magnetization direction. As a result, bipolar anomalies appear as single highs on the analytical signal map. A prominent N–S trending feature is observed in the central part of the map.

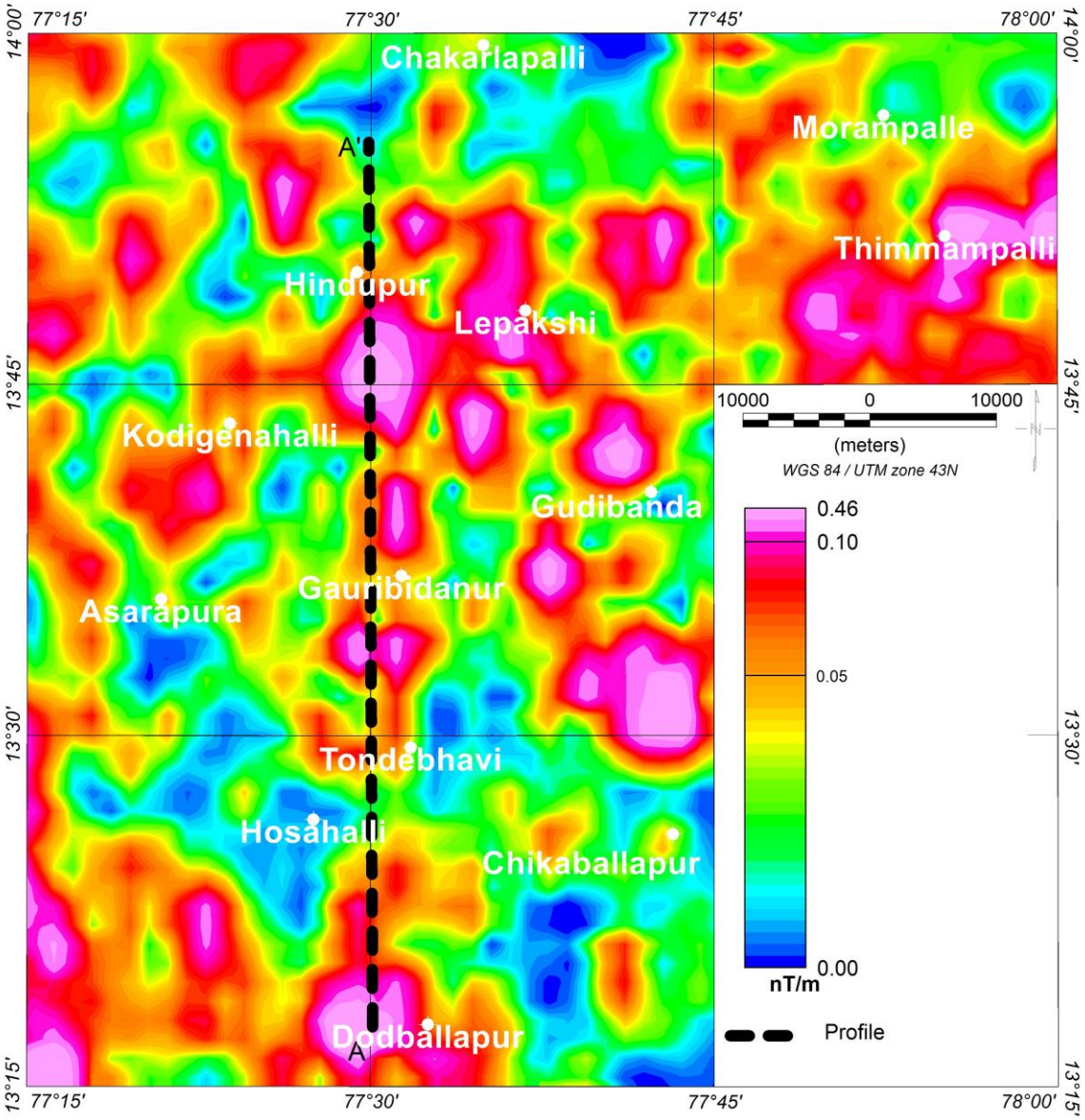

Figure 5. Analytical signal map of total magnetic field anomaly. A-A′ is the location of modelled profile

The tilt derivative map is shown in Figure 6. The tilt derivative enhances source boundaries and highlights both high- and low-amplitude anomalies. The zero contour of the tilt derivative marks the edges of magnetic sources. On this map, E–W and NW–SE trending features are clearly delineated.

Euler deconvolution was applied to estimate the depth to magnetic sources, assuming a contact model. The depth solutions were classified into three ranges: less than 1000 m, 1000–3000 m, and greater than 3000 m. The solutions corresponding to E–W trending features mostly fall within the depth range of 1000–3000 m. These solutions align well with the source boundaries identified on the tilt derivative map. The large-wavelength anomaly near Thimmanpalli and the prominent bipolar anomalies near Hindupur and Dodballapur show depth solutions greater than 3000 m, indicating deeper-seated sources.

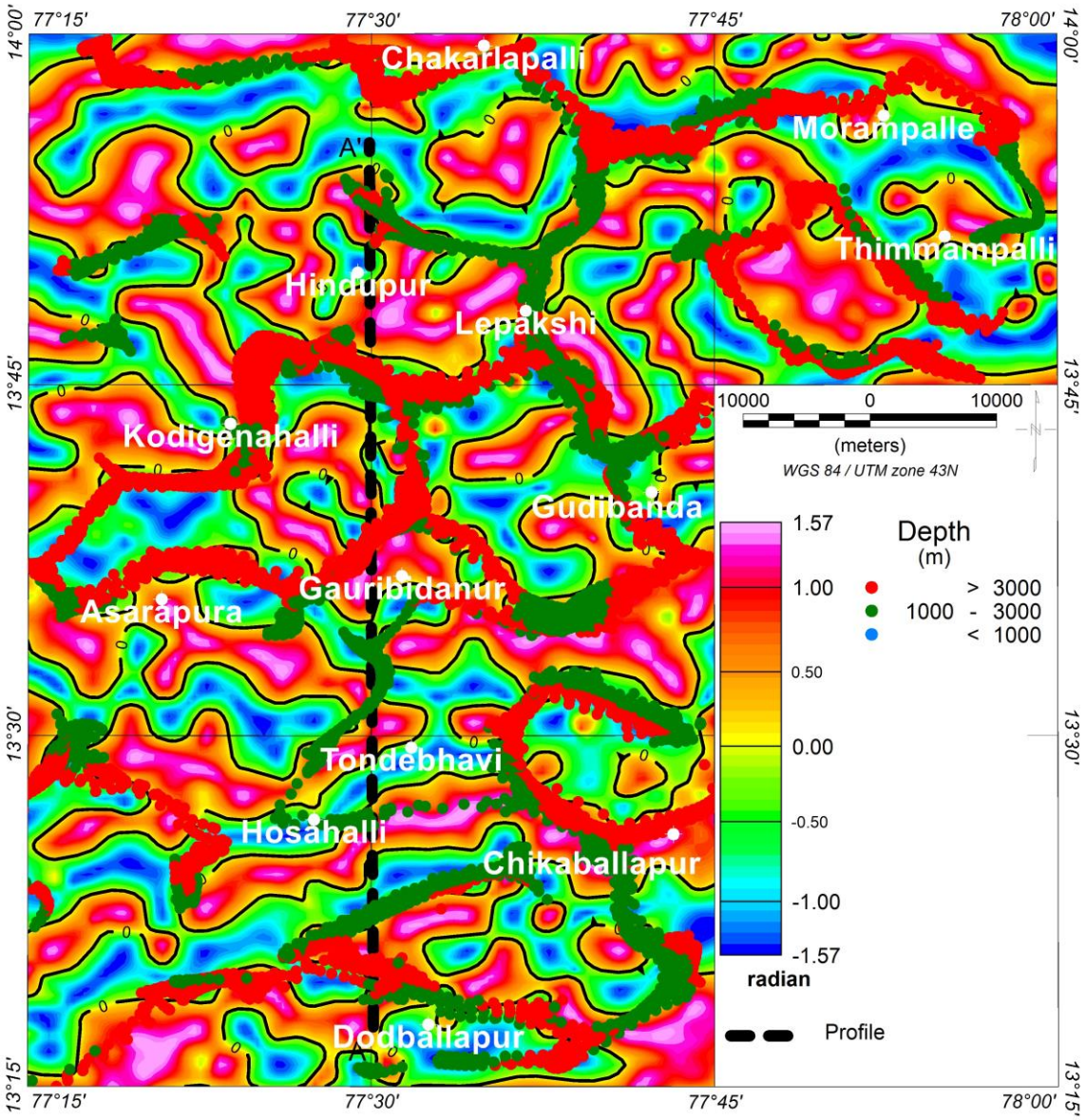

Figure 6. Euler solutions on tilt derivative of magnetic anomaly

Spectral analysis of gravity and magnetic data

The radially averaged power spectra of the gravity and magnetic data are shown in Figure 7. Based on the slopes of the linear segments of the spectra, three distinct source depth levels are identified for each dataset. For the gravity data, the estimated average depths are approximately 6 km, 3 km, and 1.5 km. For the magnetic data, the corresponding depths are approximately 4.5 km, 3 km, and 1.5 km. The deepest magnetic source (4.5 km) is shallower than the deepest gravity source (6 km). This difference suggests that the deeper basement contributing to the gravity anomaly does not possess significant magnetic susceptibility contrast and is therefore weakly magnetic or non-magnetic in nature. As a result, it is clearly resolved in gravity data but not in magnetic data. The intermediate (3 km) and shallow (1.5 km) depth levels are common to both gravity and magnetic spectra. This indicates that these layers have both density and magnetic susceptibility contrasts, enabling their detection by both methods. These depth levels likely correspond to major lithological interfaces or structurally controlled zones within the upper crust.

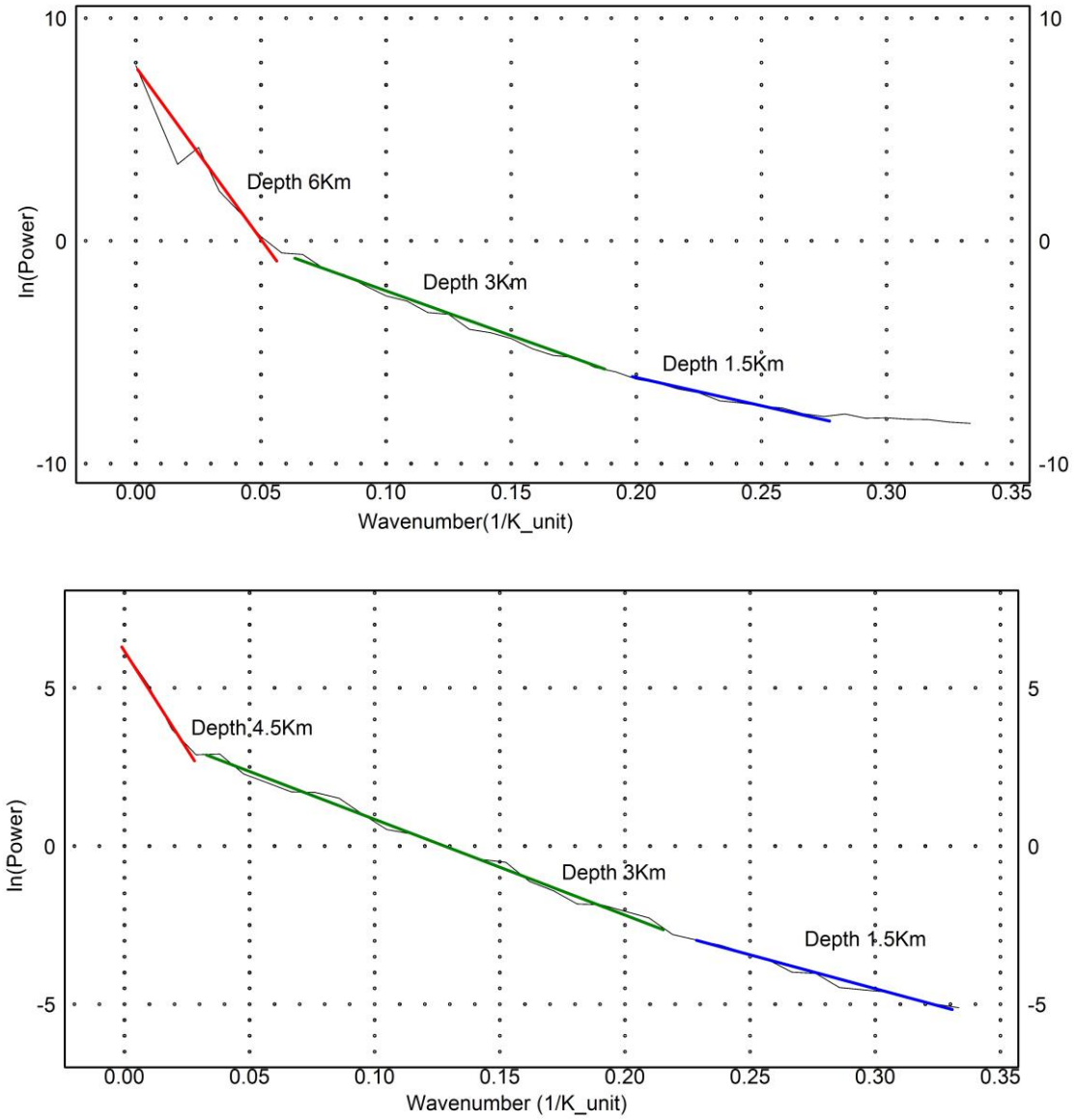

Figure 7. Radially averaged power spectrum of gravity data as shown in top figure and magnetic data, in bottom figure

Joint gravity and magnetic modelling

The gravity anomaly map shows a prominent N–S trending feature, whereas the magnetic anomaly map reveals several E–W trending features in the central part of the study area. Therefore, a N–S oriented profile was selected (shown as AA′ in all maps) for crustal modelling in order to intersect the major gravity high and crosscut the dominant magnetic trends. Modelling of potential field data inherently suffers from non-uniqueness, as a given anomaly can be explained by different combinations of source geometry, depth, and physical properties. To reduce this ambiguity, joint gravity and magnetic modelling was carried out so that both density and magnetic susceptibility constraints act simultaneously on the model. The modelling approach adopted here is primarily forward modelling, because the objective is to construct a geologically plausible crustal section constrained by known geological information, measured physical properties, and independent depth estimates. The model was constrained using: (i) Euler deconvolution depth solutions, (ii) Spectral analysis depth estimates, (iii) Measured density and magnetic susceptibility values of rock samples, and (iv) Surface geological information.

Forward modelling was performed using GM-SYS (Geosoft version 8.3). The deeper crustal layers below the modelled section were assigned standard default parameters. Based on regional geology and spectral depth estimates, major lithological layers were incorporated into the model (Figure 8). The model was iteratively adjusted to achieve a satisfactory fit between observed and calculated gravity and magnetic anomalies. After obtaining a reasonable forward model consistent with geological constraints, minor parameter adjustments were carried out using the joint inversion routine available in GM-SYS. This inversion was used only to refine the model parameters and not to generate an unconstrained solution. Thus, the approach consists of constrained forward modelling followed by limited inversion refinement.

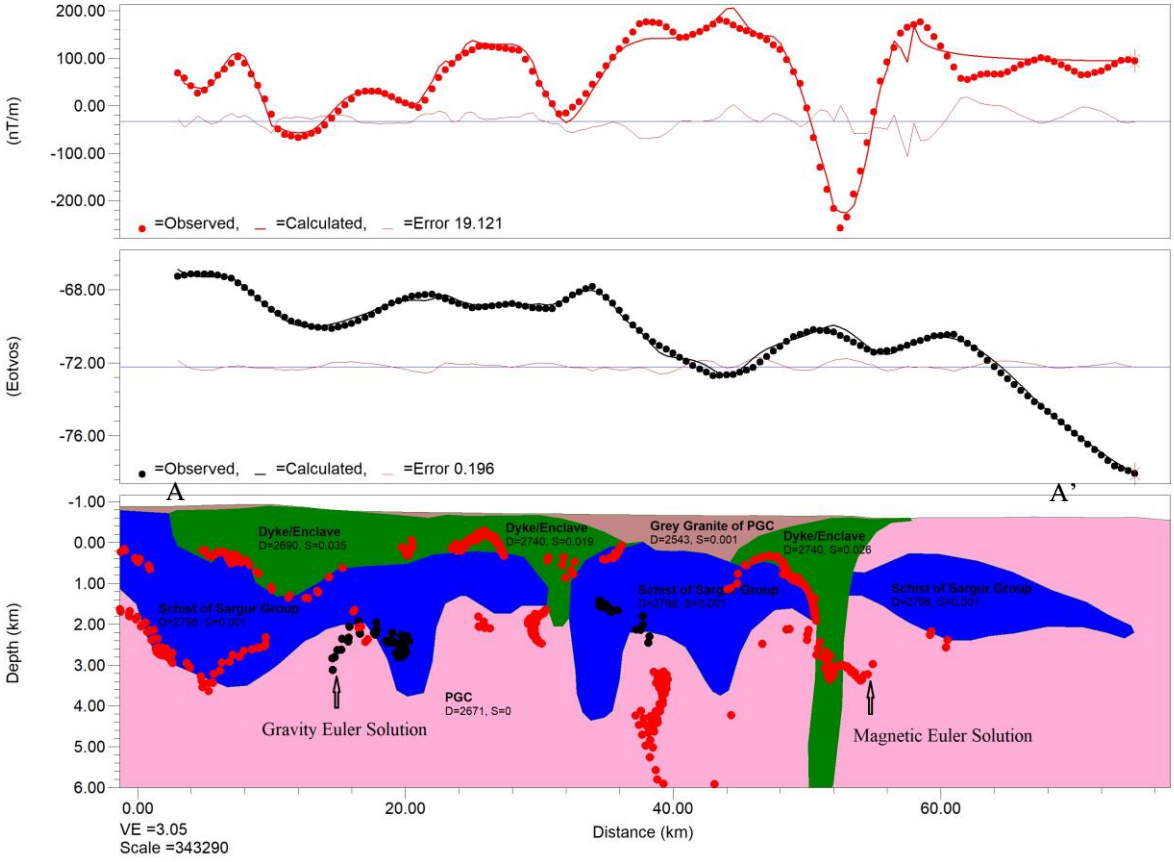

Figure 8. Joint gravity and magnetic modelling along the N-S Profile AA′

Model geometry and model interpretation

The selected profile is approximately 76 km long and oriented in the N–S direction. Based on Euler depth solutions and spectral analysis, a modelling depth of about 6 km was considered appropriate for the upper crustal section. Euler depth solutions from both gravity and magnetic datasets were incorporated into the model as geometric constraints. The gravity anomaly shows relatively gentle gradients in the southern part and steeper gradients toward the north. The overall gravity amplitude decreases northward, suggesting either reduction in density contrast or increasing depth of the causative body. The southern gravity high is modelled as a schistose or mafic-rich litho-unit with a density of approximately 2820 kg/m³ and magnetic susceptibility of about 0.001 SI. Overlying or intruding this unit are comparatively lower-density litho-units with densities of approximately 2670 kg/m³, 2720 kg/m³, and 2457 kg/m³. These units exhibit susceptibility contrasts relative to the underlying unit, producing higher-frequency magnetic anomalies. The variations in magnetic response along the profile correlate with changes in lithology and susceptibility contrast. Around 40 km along the profile, a gravity low associated with a broad magnetic high suggests granitic intrusion, consistent with lower density and variable magnetic properties. Near 50 km, a sharp magnetic low coinciding with a gravity high indicates the possible presence of a basic intrusion within the host rock, characterized by higher density but contrasting magnetic properties. Toward the northern end of the profile, the gravity anomaly decreases sharply, which may indicate thinning or pinching of the high-density body. In this region, the magnetic anomaly approaches background levels, suggesting minimal susceptibility contrast between adjacent litho-units.

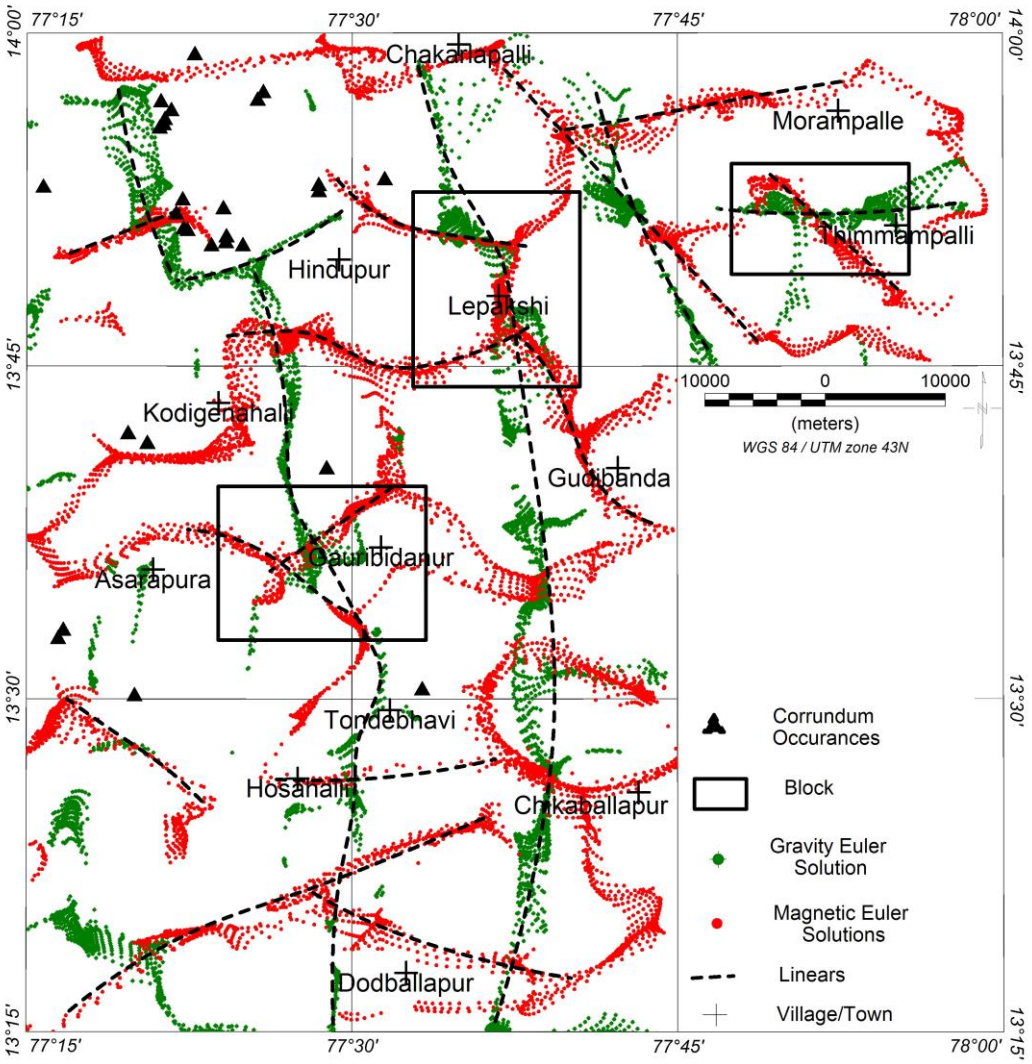

Figure 9. Inferred structural map of the studied region, lying east of the Closepet granite in EDC.

CONCLUSIONS

Integrated analysis of gravity and magnetic data over the eastern margin of the Closepet Granite in the Eastern Dharwar Craton (EDC) has provided important constraints on the subsurface structural framework of the area **(**Figure 9**).** Following conclusions are drawn from the present study

1. The Bouguer gravity anomaly reveals a prominent N–S trending gravity high in the central part of the study area. Considering its geometry, amplitude, and spatial continuity, the causative source is interpreted as a laterally extensive, three-dimensional (3D) crustal body, rather than a simple two-dimensional (2D) structure. The anomaly characteristics and its continuity suggest that this gravity high represents the possible subsurface extension of the Ramagiri Schist Belt.
2. Derivative maps and Euler deconvolution results consistently delineate this N–S trending body and provide depth constraints supporting its crustal-scale nature. The relatively weak magnetic response of this large N–S structure suggests limited magnetic susceptibility contrast, consistent with schistose lithology. However, superimposed short-wavelength magnetic anomalies along the same trend, indicate localized susceptibility variations, possibly due to minor intrusions or compositional heterogeneity.
3. In contrast, the magnetic data prominently display E–W to NW–SE trending features. These features are interpreted as relatively shallow, structurally controlled bodies, likely related to dyke activity. The tilt derivative and analytical signal maps clearly demarcate these trends, confirming their structural significance. The gravity response associated with these features is comparatively subdued, suggesting that they are primarily controlled by magnetic susceptibility contrast rather than density contrast.
4. The integrated interpretation indicates the coexistence of: (i) A major N–S trending, deep-seated 3D density-controlled body (probable Ramagiri Schist Belt extension), and, (ii) Relatively shallow E–W to NW–SE trending magnetic features associated with dyke intrusions. The cross-cutting relationship between these N–S and E–W/NW–SE trends, indicate multiple tectono-magmatic phases in the region, reflecting a complex structural evolution. Euler depth solutions from both gravity and magnetic datasets were compared with known corundum occurrences (Geology Map, Degree Sheet 57G; GSI, 1994). One known occurrence in the northwestern part coincides with a structural intersection zone identified from geophysical analysis. Based on this spatial association, three additional structurally controlled intersection zones are identified as potential targets for similar mineralization.

Acknowledgements

The authors are grateful to the Director General, Geological Survey of India (GSI), for providing logistical support during the field survey, laboratory facilities for physical property measurements, and permission to publish this work. The authors sincerely thank Shri N. V. S. Murthy, Superintending Geophysicist, GSI, for his valuable guidance, constructive suggestions, and continuous supervision throughout the study. The authors also express their gratitude to Shri Satish Chandra Triparthy, Deputy Director General & Regional Head (SR), GSI, Hyderabad, for his support during the field season and for his valuable inputs in the interpretation of geophysical anomalies. The study was carried out as part of an internal project of the Geological Survey of India. No external funding was received.

Author credit statement

Santosh Yadav carried out field data acquisition, data processing, interpretation of gravity and magnetic data, preparation of figures, and drafting of the manuscript. Abir Deogharia contributed to conceptualization of the study, supervision, interpretation of results, and critical review and editing of the manuscript.

Data availability

The gravity and magnetic datasets used in this study were acquired under an internal project of the Geological Survey of India (GSI). The data are available with GSI and can be made accessible upon reasonable request, subject to the data sharing policies and approval of the Geological Survey of India. Physical property measurement data generated during the study are included in Table 1.

Compliance with ethical standards

The authors declare that they have no conflict of interest and adhere to copyright norms.

References

Chayanulu, A. Y. S. R., Murthy, V. V. S., and Singh, R. K., 1989. Report on regional gravity and magnetic survey and detailed geophysical surveys, Anantapur District, Andhra Pradesh. Geological Survey of India, Field Season 1985–86 (Unpublished report).

Jayananda, M., Moyen, J. F., Martin, H., Peucat, J. J., Auvray, B. and Mahabaleswar, B., 2000. Late Archaean (2550–2520 Ma) juvenile magmatism in the Eastern Dharwar Craton, southern India: Constraints from geochronology, Nd–Sr isotopes, and whole-rock geochemistry. Precamb. Res., 99, 225–254.

Kailasam, L. N., Chayanulu, A. Y. S. R. and, Mathew, M. P.,1974. Report on gravity-cum-magnetic investigations in Anantapur and Kurnool districts, Andhra Pradesh, and Ballari District, Karnataka. Geological Survey of India, Field Season 1971–73 (Unpublished report).

Kesavamani, M., Venkateswarlu, M. and, Rajini Kumar, M., 1994. Report on regional gravity and magnetic investigations over a portion of Eastern Group of Greenstone Belts of Andhra Pradesh and Karnataka and detailed I.P., resistivity and magnetic surveys in Konapuram–Kanaganapalli block of Ramagiri Greenstone Belt, Anantapur District, Andhra Pradesh. Geological Survey of India, Field Season 1993–94 (Unpublished report).

Khare, A. C. and, Nagabhushanam, K., 1984. Progress report on magnetic, electrical resistivity and gravity surveys in Kalyandurg–Jonnagiri belt, Anantapur and Kurnool districts, Andhra Pradesh. Geological Survey of India, Field Season 1979–80 (Unpublished report).

Leu, L. (1982) Use of Reduction-to-the-Equator Process for Magnetic Data Interpretation. Geophysics, 47, 445

Miller, H. G. and, Singh, V., 1994. Potential-field tilt A new concept for location of potential-field sources. J. App. Geophys., 32, 213–217.

Nabighian, M. N., 1984. Toward the three-dimensional automatic interpretation of potential-field data via generalized Hilbert transforms. Geophysics, 49, 780–786.

Naqvi, S. M. and Rogers, J. J. W., 1987. Precambrian Geology of India. Oxford Monographs on Geology and Geophysics. Oxford University Press.

Ramakrishnan, M. and Vaidyanadhan, R 2008. Geology of India, Volume 1. Geological SocietyofIndia. pp.994.

Reid, A. B., Allsop, J. M., Granser, H., Millett, A. J. and Somerton, I. W., 1990. Magnetic interpretation in three dimensions using Euler deconvolution. Geophysics, 55, 80–91.

Spector, A. and Grant, F. S., 1970. Statistical models for interpreting aeromagnetic data. Geophysics, 35, 293–302.

Talwani, M. and Heirtzler, J. R., 1964. Computation of Magnetic Anomalies Caused by Two-Dimensional Bodies of Arbitrary Shape. In G. A. Parks (Ed.), Computers in the Mineral Industries, Part 1 (pp. 464-480). Stanford Univ. Publ., Geological Sciences 9.

Received on: 04-04-2024; Revised on: 25-02-2026; Accepted on: 26-02-2026

J. Ind. Geophys. Union, 30(3) (2026), 184-193
https://doi.org/10.71122/JIGU.30(3)2026.0019

On the pre-seismic effects of VLF electric field anomalies on the atmosphere corresponding to major shallow seismic events (M = 5.1 - 6.4, depth < 29 km) occurring in India and nearby countries

Ashwani Yadav and Raj Pal Singh*
Department of Physics, GLA University, Mathura-281406, (U.P.), India
*Corresponding Author: rp.singh@gla.ac.in

ABSTRACT

Observation of horizontal component of VLF electric field data are going on at 3.012 kHz frequency since 24 March 2011 at Mathura station (27.49° N, 77.67° E) by employing a horizontal antenna for investigating the effects of earthquakes. Bulk of the VLF data recorded is analysed using Quartile-based statistical analysis, covering the months of June–July 2015 and February, March and May 2016 in the light of 14 seismic events (M = 5.1 - 6.4, depth < 29 km) that took place in India and countries lying in a circular radius of 1270 km from Chaumuhan, Mathura observatory. Anomalous amplitude enhancements in VLF data were noticed, 1-27 days ahead the onset of the earthquakes that are considered in the present study. Moreover, pre-seismic anomalous amplitude enhancements were found to vary from 0.8 mV to 31.3 mV, and the percentage range of these enhancements varies from 0.95% to 86.22%. The unusual VLF amplitude intensifications are also explored in reference to spurious sources, which include geomagnetic and lightning activities, local building noises, radiations of power lines, and instrumental errors. It is found that the unusual amplitude enhancements are not connected with said sources, excluding the 4 cases of amplitude augmentations with the magnetic storms. To explore the association of VLF amplitude enhancements and their precursory times with earthquakes, probabilities for the pairs of magnitude with VLF amplitude enhancements and precursory time, and focal depth with VLF amplitude enhancements and precursory time, are calculated. Probable values for the aforesaid pairs comes to 84.96%, 88.61%, 81.94% and 92.33% respectively, which are significant and show a correlation of amplitude enhancements and their precursory time with the seismic events. Possible mechanisms for the origin of VLF electric field radiations and their propagation to long distances, are discussed briefly in terms of chemical and acoustic gravity wave channels. Further, following the model given by Sharma and Singh (2022), an attempt has been made to justify the observed VLF amplitude enhancements related to earthquakes using electromagnetic channel.

Keywords: VLF electric field, Horizontal antenna, Seismic events, Atmosphere, ∑Kp data, Mathura observatory (India)

INTRODUCTION

Gokhberg et al. (1982) first recorded an unusual increase in the intensity of electromagnetic radiations approximately 1 hour prior to onset of the earthquake (M = 6.1) on 25 September 1980 in central Japan, employing a ground-based receiver of peak frequency 81 kHz. Subsequently, dedicated scientific efforts were initiated in many countries to detect electromagnetic effects of earthquakes, taking their precursory nature into account using ground and satellite-based methods (Zhao et al., 2020; Biswas et al., 2023; Calderon et al., 2025). Laboratory experiments involving fracturing of rock samples have provided several evidences for the association of electromagnetic waves with earthquakes (Panfilov, 2014; Gao et al., 2024). Studies by Hayakawa (2016), Pulinets and Ouzounov (2018), Arneva and Cordaro (2019), Conti et al. (2021), Pulinets et al. (2022), Zeigarnik et al. (2022), and Hayakawa (2025) provide a detailed account of recent findings obtained in the field of Seismo-electromagnetics.

Among many ground-based methods developed so far for the observation of electromagnetic effects of earthquakes, monitoring of VLF electric field on ground and in atmosphere has also drawn the attention of several researchers. Using this method, Zhang et al. (1988) observed the VLF pre-earthquake electromagnetic radiations using horizontal antenna at the Jiangsu station in China and they found anomalous variations in it, a few days to several weeks before the Liyang earthquake (M = 6.0), Heze earthquake (M = 5.9), and South yellow sea earthquake (M = 6.2) that occurred on 9 July 1979, 7 November 1983 and 21 May 1984 respectively. Singh et al. (2003) noted unusual enhancements in VLF electric field (frequency, f = 3 kHz) data, 3 hours before the onset of the Chamoli earthquake (M = 6.8) in the Chamoli district of India, while Fujinawa et al. (2013) recorded pulse-like VLF signals with different waveforms, 6 days before the seismic event (M = 9.0) in Tohoku, Japan using almost similar type of borehole antenna in case of both the seismic events. Employing satellite-based VLF receiving antenna, several important findings in relation to precursory nature of seismo-electromagnetic radiations are reported in the recent past (Zhima et al., 2020; Salikhov et al., 2025).

Motivated by the findings of earlier researchers in the field of seismo-electromagnetics and precursory characteristics of electromagnetic radiations, observation of amplitude of horizontal component of seismogenic VLF electric field data at the frequency f = 3.012 kHz has started at Chaumuhan, Mathura since 24 March 2011 using a horizontal antenna of length 5.85 m for exploring the influence of these emissions in the atmosphere. In this paper, VLF electric field data monitored in horizontal antenna, are analysed using Quartile analysis for the periods of June and July 2015 and February, March, and May 2016 to explore the influence of 14

earthquakes (M ≥ 5.1, depth < 29 km) which occurred in India and its nearby countries within the circular region of radius 1270 km taking Mathura observatory as center. In addition to this, effects of other possible spurious sources such as lightning activity, magnetic storms, local building noises, and instrumental errors in the VLF data of the horizontal antenna are also explored.

EXPERIMENTAL SETUP

Figure 1 shows the block diagram of the experimental setup at the Mathura observatory for monitoring VLF electric field data associated with earthquakes. It comprises a horizontal antenna which is installed between two vertical poles of GI pipes at a height of 18 m horizontally in air using two insulators on both sides of the poles at the roof of double storied building of the central library of GLA University, Chaumuhan, Mathura city in India, located in a rural area where urban electromagnetic noises are very low. This antenna is made up of copper wire with a length of 5.85 m and diameter 2 mm. The reason for taking the said length and diameter is that at this length (5 ~ 6 m) and diameter (~2 mm), antenna provides best signal-to-noise ratio, mechanical stability, and impedance matching. At higher lengths and diameters, antennae offer poor impedance matching and pickup more local noises while at lesser lengths and diameters (length < 5 m, diameter < 1 mm), they offer more thermal noises and hence their efficiency is reduced (Rozhnoi et al., 2004). One more terminal is provided, which is a naked copper wire, placed 3 m below the ground. Natural voltage developed on the antenna is observed to be 0 - 5 mV under normal conditions. The antenna is connected to a Personal Computer (PC) via an amplifier (gain 26 dB), band pass filter (peak frequency = 3.012 kHz, bandwidth ~ 550 Hz), and notch filter (notch frequency = 50 Hz). The VLF emissions emanated either from a seismic or non-seismic source, may interact with the horizontal antenna and hence may perturb the natural voltage induced in it, which is amplified and filtered at 3.012 kHz. These analog signals are converted into digital signals employing A/D converter and then recorded on a PC round the clock. The signal-to-noise ratio of the antenna setup is 10.5. The reason for selecting the frequency 3.012 kHz as peak frequency is that power line radiations dominate at lower frequencies, and at higher frequencies, attenuation enhances as the frequency increases. To remove the influence of power line radiations on the VLF data recorded, filtered signals obtained from band pass filter are fed to notch filter. Further, the differential amplifiers are used to reduce the effect of power line signals on the VLF data because the common noises affecting the VLF data are rejected by them, and only the difference of the electric potential developed in horizontal antenna and grounded electrode is amplified.

EARTHQUAKE AND MAGNETIC STORM DATA

Earthquakes data are collected from website: http//neic.usgs.gov maintained by United States Geological Survey (USGS) for the period of observations to investigate the influence of electromagnetic waves related to seismic events on the VLF data recorded using horizontal antenna. To investigate the effect of geomagnetic activity on the VLF data, magnetic storm data are collected from the website: https://wdc.kugi.kyoto-u.ac.jp taken care of by World Data Centre, Kyoto, Tokyo, Japan.

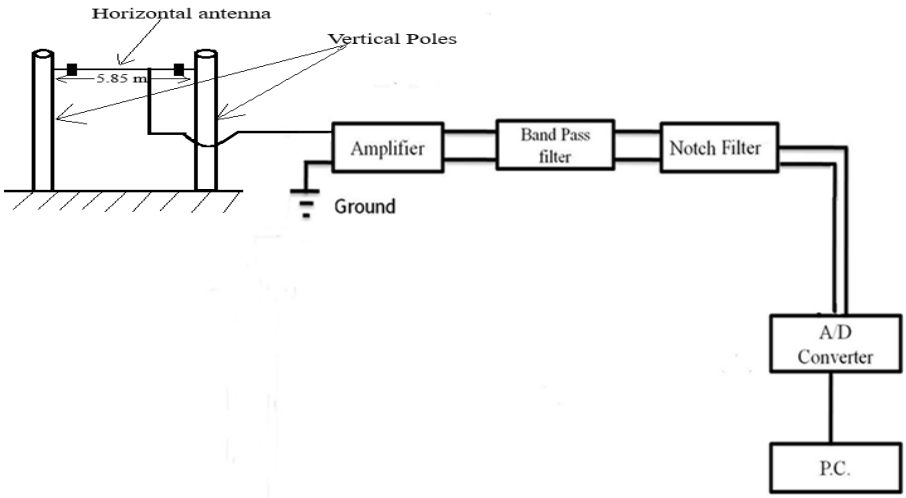

Figure 1. Experimental setup installed at Mathura observing station for the monitoring horizontal component of seismogenic VLF electric emissions.

EARTHQUAKE LOCATIONS AND POSITION OF OBSERVING STATION

The map of India and the surrounding countries are shown in Figure 2. Locations of 14 shallow major earthquakes (red solid circles) that took place in India (Assam), China, Pakistan, Nepal, and Tajikistan during June and July 2015, February, March, and May 2016, and the Mathura observatory (green triangle) are shown in the map. The rest of the details of the seismic events, which include date and time of occurrence, magnitude, latitude, longitude, focal depth, and their distances from Mathura station are mentioned in Table 1.

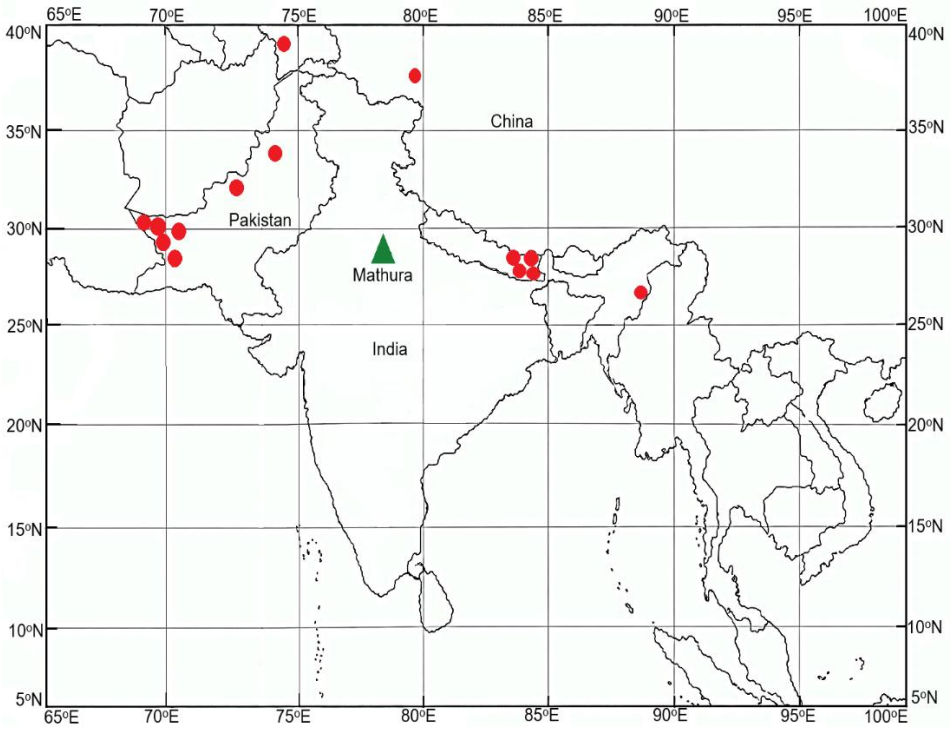

Figure 2. The map of India and nearby countries, showing the locations of earthquakes (red circles) and Mathura station (green triangle).

Table 1. Details of earthquakes (M ≥ 5.1, depth < 29 km) that took place in India, China, Pakistan, Nepal and Tajikistan during 2015 and 2016 within a circular region of 1270 km from the Mathura observing site.

Date of Earthquake	Time of occurrence (LT)	Latitude (^{0}N)	Longitude (^{0}E)	Magnitude (M)	Depth (Km)	Distance of earthquake eepicentres (in km) from Mathura
28-06-2015	01:05:28	26.64 ^{0}N	90.41 ^{0}E	5.1	26	1264
02-07-2015	07:18:24	34.45 ^{0}N	73.71 ^{0}E	5.3	10	860
03-07-2015	01:07:47	37.46 ^{0}N	78.15 ^{0}E	6.4	20	1109
15-07-2015	11:25:59	27.33 ^{0}N	65.99 ^{0}E	5.3	10	1152
24-07-2015	20:59:54	33.86 ^{0}N	73.19 ^{0}E	5.1	17.03	827
03-08-2015	13:16:03	27.40 ^{0}N	65.91 ^{0}E	5.3	28.57	1159
05-02-2016	16:20:11	27.88 ^{0}N	85.34 ^{0}E	5.2	23.53	756
21-02-2016	18:10:00	27.96 ^{0}N	84.70 ^{0}E	5.1	16.72	693
18-03-2016	16:11:00	38.02 ^{0}N	72.41 ^{0}E	5.6	10	1269
21-03-2016	14:48:51	27.77 ^{0}N	66.10 ^{0}E	5.6	10	1139
13-05-2016	06:59:32	30.66 ^{0}N	66.42 ^{0}E	5.2	10	1147
13-05-2016	07:01:10	30.66 ^{0}N	66.39 ^{0}E	5.5	10	1150
22-05-2016	01:48:48	28.45 ^{0}N	87.53 ^{0}E	5.4	9.36	973
22-05-2016	02:05:54	28.55 ^{0}N	87.48 ^{0}E	5.1	4.44	969

It is to be noted that only those shallow major earthquakes ($M \geq 5.1$, depth < 29 km) are examined in this study that took place in India and its nearby countries in the months of June, July (2015), and February, March, May (2016) in a radius of 1270 km from Mathura observatory. The reason for taking into account the shallow and large magnitude earthquakes ($M \geq 5.1$, depth < 29 km) is that considerable electric field is generated in case of such earthquakes in the atmosphere/ionosphere through electromagnetic, acoustic and gravity wave and chemical channels.

PROCESSING OF VLF DATA

As discussed before, horizontal antenna has been installed at Chuamuhan, Mathura observing station to record the horizontal component of VLF electric field radiations and night time (19:00 – 05:00 hr) VLF data recorded by using this antenna have been used for analysis. The root mean square value of the VLF data are estimated for each day applying the relation, $A = \sqrt{\frac{d_1^2 + d_2^2 + d_3^2 + \ldots\ldots\ldots}{n}}$, where d_1, d_2, d_3..... are the values of VLF data points observed at the time interval of one second and n is the number of data points recorded during the time interval for which the VLF data are processed. It is important to mention here that during day hours, electromagnetic and electrical noises are more prominent (Sharma et al., 2020), which may interact with the horizontal antenna and hence may perturb the VLF data recorded by using it. To eliminate the effect of these emissions on the VLF data recorded in horizontal antenna, only the nighttime VLF data are considered, as mentioned earlier.

To investigate the effect of 14 earthquakes VLF data are analysed using Quartile-based analysis. In this technique, the moving median (S) of the VLF data is estimated using 15 days VLF data just before the day of occurrence of the earthquakes. The reason for considering 15 days VLF data for estimating moving median is that 15 days window is long enough to average over the fluctuations due to geomagnetic and lightning activities, etc., but not so longer that precursory anomalies get absorbed into background, and the shorter windows could be embedded with these noises (Tatsuta et al., 2015; Hayakawa, 2025). Then, the deviation for 16th day observed VLF data from the calculated median (S) is computed. Finally, applying the formulae UB = S+1.5(UQ-S) and LB = S-1.5(S-LQ), upper and lower bounds (UB and LB) are computed, where LQ and UQ are lower and upper quartiles, respectively. The enhancement in VLF data above the upper bound on a day shows anomalous enhancement on that day, and this day is known as an anomalous/disturbed day.

RESULTS AND DISCUSSION

Digital recording of VLF data (frequency = 3.012 kHz) at sampling frequency of 1 sample/sec is continued at Mathura observing station employing a horizontal antenna since 24 March 2011 for studying the effect of earthquakes on it. The mean value of the VLF data for each day is computed by using the method as discussed before. For identifying the effect of seismic or non-seismic sources on the VLF data, its daily values are plotted (by solid green colour curves with solid circles) between the upper and lower bounds obtained from quartile analysis (by solid red and dashed blue colour straight lines with solid squares respectively) for the months of June, and July 2015, February, March, and May 2016 and results obtained are shown in Figures 3a and 3b. Discontinuities in the curves indicate unavailability of the VLF data due to power failure.

From Figures 3a and 3b, it is clear that the daily VLF data recorded are much above the upper limit on 1-7, 13, 14, 18, 27, 30 June 2015, 4, 6, 26, 28, July 2015, 5-9, 12, 18 February 2016, 1-3, 5-7, 12, 19, 20 March 2016, and 11, 15, 18, 22, 26, 27, May 2016. These unusual enhancements in VLF data may be due to magnetic storms, local lightning activity, local building noises, instrumental inaccuracy, and earthquakes. These unusual enhancements will be verified in view of the said sources, and attempt will be made to identify which one of the aforesaid sources is more liable for the unusual VLF amplitude enhancements.

The VLF data observed in horizontal antenna may be perturbed by the magnetospheric electric field originating during the course of a storm, as noticed in earlier studies (Lakshmi et al., 1997; Singh et al., 2009). Daily variation of $\sum$Kp for every month is demonstrated just below the daily variation of VLF data of that month (by solid pink colour curve with crosses) to explore the effect of storms on the VLF data. It is worthwhile to mention here that in earlier studies, it is considered that the days with $\sum Kp < 30$ are called magnetically calm days, and the days on which $\sum Kp \geq 30$ are known as magnetically disturbed days (Singh et al., 2024). Looking at daily variation of $\sum$Kp data shown in Figures 3a and 3b, it is obvious that on 8, 14, 22-25 June 2015, 5, 11, 13, 23 July 2015, 16-19 February 2016, 6, 7, 11, 15-17 March 2016, and 2, 8, 9 May 2016, are magnetically disturbed days as on these days $\sum$Kp values are 30 or more.

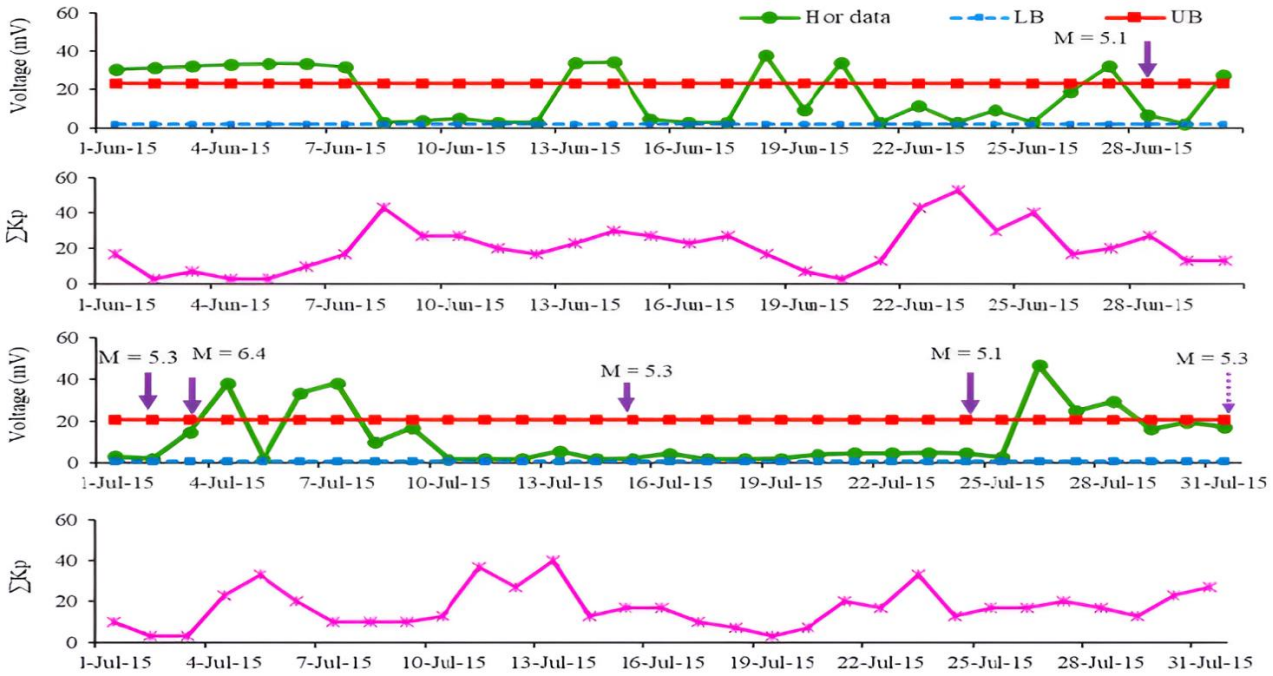

Figure 3 a. Daily variation of horizontal component of VLF electric field emissions (marked by solid green colour curves with solid circles) for June 2015 and July 2015. Solid and dashed horizontal lines (by red and blue colours with solid squares respectively) show upper and lower bounds in the top panel of each month. Downward arrows (shown by purple colour) indicate the day and magnitude of earthquakes considered. Daily variation of ∑Kp is shown in the bottom panel of each month (by solid pink colour curve with crosses).

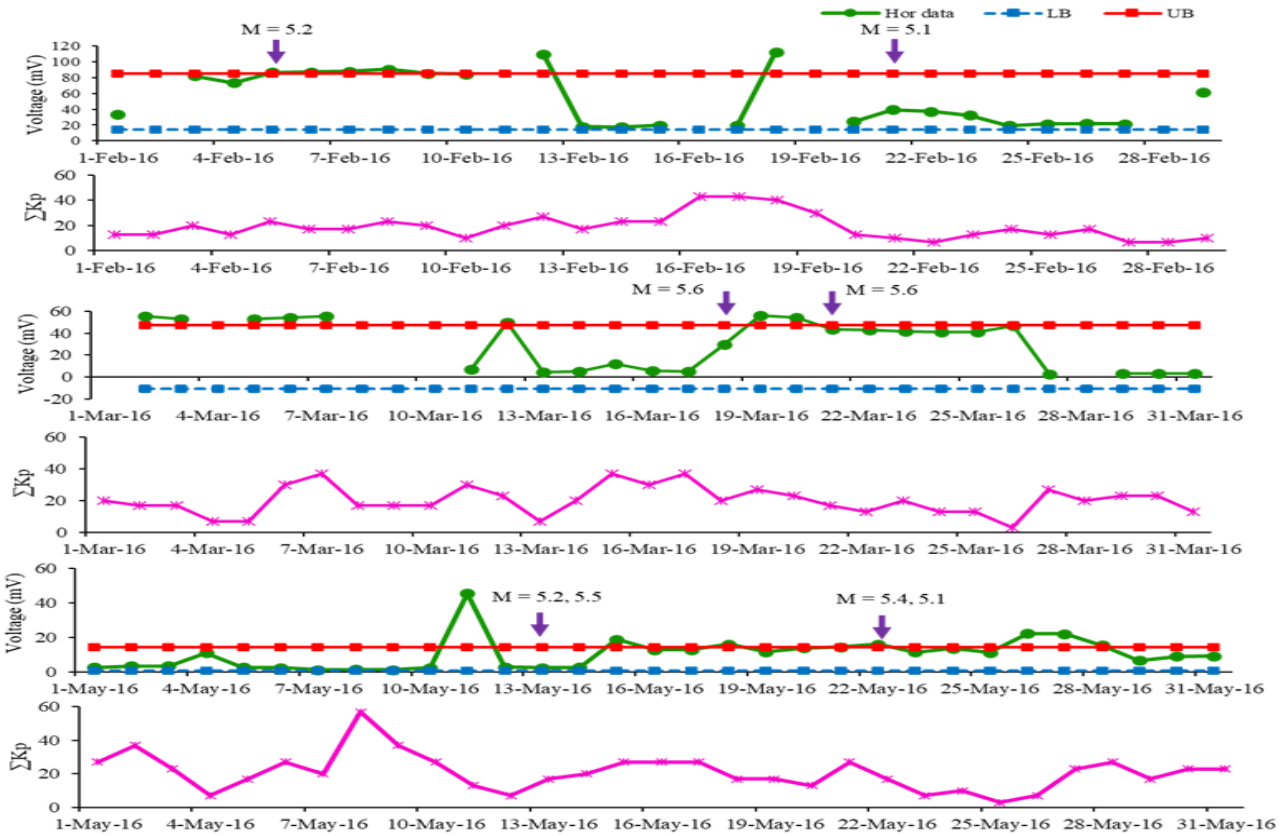

Figure 3b. Same as Fig. 3(a) but for February 2016, March 2016, and May 2016.

The days of VLF amplitude enhancements do not match with days of magnetic storms, excluding the 4 cases of magnetic storms that happened on 14 June 2015, 18 February 2016, 6-7 March 2016, for which the values of ∑Kp were 30, 40, 30, and 37, respectively. Thus, VLF amplitude enhancements seen on the aforesaid days may not be attributed to storms except for 4 cases of enhancements on 14 June 2015, 18 February 2016, and 6-7 March 2016. The cause for not affecting the VLF data due to magnetic storms is that the time-varying electric field originated by these storms is too weak. Details for VLF electric field being weak can be found in Sharma et al. (2020) and Sharma and Singh (2020).

Lightning activity that happens in atmosphere may perturb the voltage produced in the horizontal antenna as electromagnetic emissions emanated during this activity interact with it and may alter the potential difference induced in it. But from recent studies, wherein the influence of lightning on the VLF data recorded at frequencies 3kHz and 3.012 kHz is examined, it is found that the lightning phenomenon does not perturb the VLF data (Sharma et al., 2020). The possible causes for this are, (a) weak electromagnetic radiations corresponding to frequency 3.012 kHz are emanated during lightning phenomena and hence the energy associated with them is less (rest of the large amount of energy emitted is associated with the radiations of other frequencies f = 0.01Hz─10^6 Hz, except f = 3.012 kHz, which are not being recorded at the observing site), which they dissipate on the way during their interaction with the particles of medium prior to arriving at the Mathura observatory. Source and cavity transfer function showing highest strength of signals having frequencies nearly 7 kHz and 300 kHz for the farthest and nearest sources, respectively, also supports the said observations (Meloni et al., 2015), (b) being a short-lived phenomenon, the time interval of its occurrence is very low (10^{-3} Sec). For picking up the response of lightning activity, the sampling frequency of recording the VLF data should be 10^3 Hz while in our case it is merely 1 Hz, (c) findings are in good agreement with model suggested by Bruce and Golde (1941) in which intensity of lightning strokes of various frequencies was estimated and it was found that it is 2×10^{-6} volt/m for the radiations of frequency 3 kHz, which is too low to the sensitivity of the antenna (2.4 mV), and (d) No impact of lightning strokes on the VLF data is noted in many other studies (Fujinawa et al., 2011; Fujinawa et al., 2013). In view of earlier findings and the reasonings discussed above, it can be concluded that the enhancements noted in VLF electric field data on the days mentioned before may not be due to lightning activity. Moreover, possibilities of influencing the VLF electric field data from power line emissions and building noises may be ruled out on account of employing the notch filter (50 Hz) and differential amplifiers in the experimental setup, and taking night-time data into account. In addition to this, instrumental errors may not be liable for unusual VLF amplitude augmentations observed on various days, as mentioned before. If it were the case, erroneous VLF data would have produced during the entire period of observations.

As abrupt intensification in VLF amplitude data observed in horizontal antenna on the days mentioned before are not associated with geomagnetic and lightning activities, power line emissions, local buildings noises, and instrumental errors, the amplitude augmentation seen on these days may be owing to earthquakes ($M \geq 5.1$, depth < 29 km) occurred in India, Pakistan, China, Nepal, Tajikistan during the periods of observations. Among 39 cases of unusual enhancements, 4 are found to be related to the geomagnetic storms, and the remaining 35 are related to the seismic events. Out of the total 35 cases of intensification in VLF data related to earthquakes, 3 cases are co-seismic, and the remaining 32 are pre-seismic. The ranges of pre-seismic VLF amplitude enhancements in June, July 2015, February, March, and May 2016 are 4.28 -14.6 mV, 8.89 - 26.3 mV, 0.8 - 27.3 mV, 2.51 - 11.1 mV, and 1.88 - 31.3 mV respectively and the ranges of percentage enhancements in it in the said months are 8.43% ─ 62.8%, 43.24% ─ 86.22%, 0.95% ─ 32.71%, 5.33% ─ 23.62%, 13.29% ─ 57.4% respectively. The overall range of pre-seismic VLF amplitude enhancements is 0.8 mV ─ 31.3 mV, and the percentage precursory enhancements in it varied between 0.95% ─ 98.67%. Co-seismic VLF amplitude enhancements are found to vary from 1.96 - 30.6 mV, and percentage enhancements in it are found to lie between 2.31% ─ 72.45%.

In order to find out the precursory time of the VLF amplitude enhancements for the earthquakes considered in this study, it is necessary to relate these enhancements to the earthquakes. For this, we looked at the top panel of Figure 3a and unusual variations are seen beyond the upper bound on 1-7, 13-14, 18, 20, 27 June 2015, which may be the precursory signatures of the earthquake (M = 5.1) in Basugaon, Assam, India on 28 June 2015 and precursory period of this quake (M = 5.1) ranges between 1-27 days. Similar precursory enhancements were also seen on 30 June 2015 for the earthquakes of 2, 3 July 2015 with precursory time 1-2 days; enhancements on 4, 6, 7 July 2015 for the earthquakes of 15, 24 July 2015 with precursory duration 8-20 days; amplitude enhancements on 26-28 July 2015 for the earthquake of 3 August 2015 with precursory time interval 6-8 days; enhancements on 6-9, 12 February 2016 for the quake of 21 February 2016 with the precursory time interval 9-15 days; VLF amplitude enhancements on 1-5 and 12 March 2016 for the seismic

event of 18 March 2016 with the precursory time 6-17 days; amplitude enhancements on 20 March 2016 for the earthquake of 21 March 2016 with precursory time 1-20 days; enhancements on 11 May 2016 for the earthquakes (M = 5.2, 5.5) of 13 May 2016 with precursory time 2 days; enhancements on 15, 18 May 2016 for the earthquakes (M = 5.4, 5.1) of 22 May 2016 with precursory time interval 4-7 days and the enhancements on 26, 27 May 2016 are the after effects of these earthquakes. The overall precursory time lies between 1-27 days for all the earthquakes, while the post-effects are noticed within 4-5 days in the case of two earthquakes.

It is reasonable to mention here that the earthquake (M = 5.3) of 3 August 2015 which occurred in Khuzdar, Pakistan is shown in 3rd panel of Figure 3a on 31 July 2015 as the VLF data for this month (i.e. August 2015) are not available with us due to equipment failure and same is shown by a dashed arrow for distinguishing it from others. The reason for considering this earthquake is that it has a precursory effect, and hence its details are included in Table 1. Further, for the earthquake (M = 5.2) which occurred on 5 February 2016, no precursory effect could be observed because of the unavailability of VLF data of January 2016 and the initial days of February 2016. Due to this reason, it is not considered in Table 2. However, it is shown in Figure 3b.

In order to ascertain correlation of VLF amplitude enhancements with the seismic events considered, pairs of magnitude with VLF amplitude enhancements and precursory times and focal depth with VLF amplitude enhancements and precursory times are formed as depicted in Table 2, and the probabilities for the association of observed amplitude augmentations and precursory days with the seismic events considered are estimated by adopting t-test. It is reasonable to discuss here that those VLF amplitude enhancements and precursory time intervals are taken into account, which yield the maximum probability for their association with the earthquakes considered in this study, and the rest of the values are ruled out.

From the results of computation shown in this table, it is clear that the probabilities for the correlation between the VLF amplitude intensifications and precursory times with the earthquakes are 84.96%, 81.94%, 88.16%, and 92.33%, respectively, which are significant for the geophysical observations like this. Thus, the VLF amplitude intensifications and the precursory times noted are correlated with the earthquakes.

To discriminate pattern of VLF electric field variations belonging to earthquakes as recorded in the horizontal antenna on a disturbed day from those observed on a routine day, temporal variations of the VLF data of both the anomalous day (15/05/2016) and a routine day (15/05/2016) for a time period of 10 minutes from 19:00:00 to 19:10:00 (LT) are plotted in Figure 4 (by solid red and blue colour curves) respectively. The cause for taking the temporal variation into account is that the pattern of variation of electric field could not be investigated from the daily variation of VLF electric field data as represented in Figure 3, owing to its averaging. It is pertinent from the Figure 4 that VLF data are remarkably oscillating with large amplitude on the disturbed day while the same are less varying and have low amplitude on the routine day. The main cause for the increased amplitudes on anomalous day can be described in terms of chemical, acoustic and gravity wave, and electromagnetic channels, whose details are furnished in the next paragraphs.

Table 2. Computational results regarding the probabilities for the pairs of magnitude with VLF amplitude enhancements and precursory time, and focal depth with VLF amplitude enhancements and precursory time.

Magnitude (M)	VLF amplitude enhancements (mV)	Precursory time (days)	Depth (Km)	VLF amplitude enhancements (mV)	Precursory Time (days)
5.1	14.6	15	26	8.22	23
5.3	4.28	2	10	4.28	2
6.4	4.28	3	20	4.28	3
5.3	17.7	8	10	12.9	8
5.1	17.7	17	17.03	12.9	17
5.3	8.89	6	28.57	4.29	6
5.1	24.7	9	16.72	3.03	9
5.6	2.51	6	10	8.26	6
5.6	6.99	1	10	6.99	1
5.2	31.3	2	10	31.3	2
5.5	31.3	2	10	31.3	2
	$p_{(M\text{-}VLF\ amplitude\ enhancements)}$ = 0.8496 or 84.96%	$p_{(M\text{-}PT)}$ = 0.8861 or 88.61%		$p_{(D\text{-}VLF\ amplitude\ enhancements)}$ = 0.8194 or 81.94 %	$p_{(D\text{-}PT)}$ = 0.9234 or 92.34 %

It remains to be described here that in what manner the VLF electric field radiations were created in focal zones of the earthquakes considered and transmitted to the observatory located in Mathura and perturb the VLF data registered in the horizontal antenna. This can be responded to by taking chemical, acoustic and gravity wave, and electromagnetic channels into account (Sorokin et al., 2007; Sanchez and Kherani, 2024; Gao et al., 2025). In case of chemical channel, radon and other gases emanating from the focal regions of the earthquakes reach the atmospheric height. Alpha particles emanated from radon reacts with the molecules present in atmosphere (O_2, N_2, etc.) and produce electrons and ions, while other gases (like CH_4, H_2, CO_2, etc) enhance the efficiency of ion production and modify electron/ion lifetime through their interaction with these ions. Due to variation in concentration of radon released from focal zone owing to variation in stresses there, efficiency of ion production, and variation in electron/ion lifetime, conductivity of atmosphere varies with time (Sorokin et al., 2011).

This results in origin of time-dependent currents from atmosphere to ionosphere. These currents produce electric field varying with time, which is transmitted to the Mathura observing station through $\vec{E} \times \vec{B}$ mechanism, here $\vec{E}$ is seismic electric field, while $\vec{B}$ is magnetic field of earth in ionosphere. A detailed explanation of the chemical channel can be found in Sorokin et al. (2007). In case of acoustic and gravity wave channe, atmospheric oscillations are produced due to variation in pressure, temperature, etc., during preparatory phase of an earthquake. These oscillations couple with ionosphere and cause variation in electron concentration there, leading to emanation of the electric field which reaches the Mathura observatory under the mechanism of $\vec{E} \times \vec{B}$ drift as mentioned before and perturb the voltage induced in the horizontal antenna. Detailed description of this channel is available in Sanchez and Kherani (2024).

In an electromagnetic channel, rocks under varying stresses in focal zones, produce elementary radiators under the phenomenon of microfracturing/piezoelectric effect. These radiators are randomly oriented in space and time and emit electromagnetic waves. These waves may leak to the surface of the earth via special geological formations of reduced conductivity (10^{-8} – 10^{-10} S/m) and then arrive at the Mathura station via earth-ionosphere waveguide and alter the voltage induced in the antenna. Another possibility of arriving at these radiations at the observing station and causing voltage enhancements can be explained following the model of Sharma and Singh (2022). This model suggests that the middle layer of the earth's crust serves as waveguide for electromagnetic radiations produced from the radiators available in the focal zone of earthquakes, and the strength of the electric field incorporated with these emissions at the observing site can be computed by using the relation;

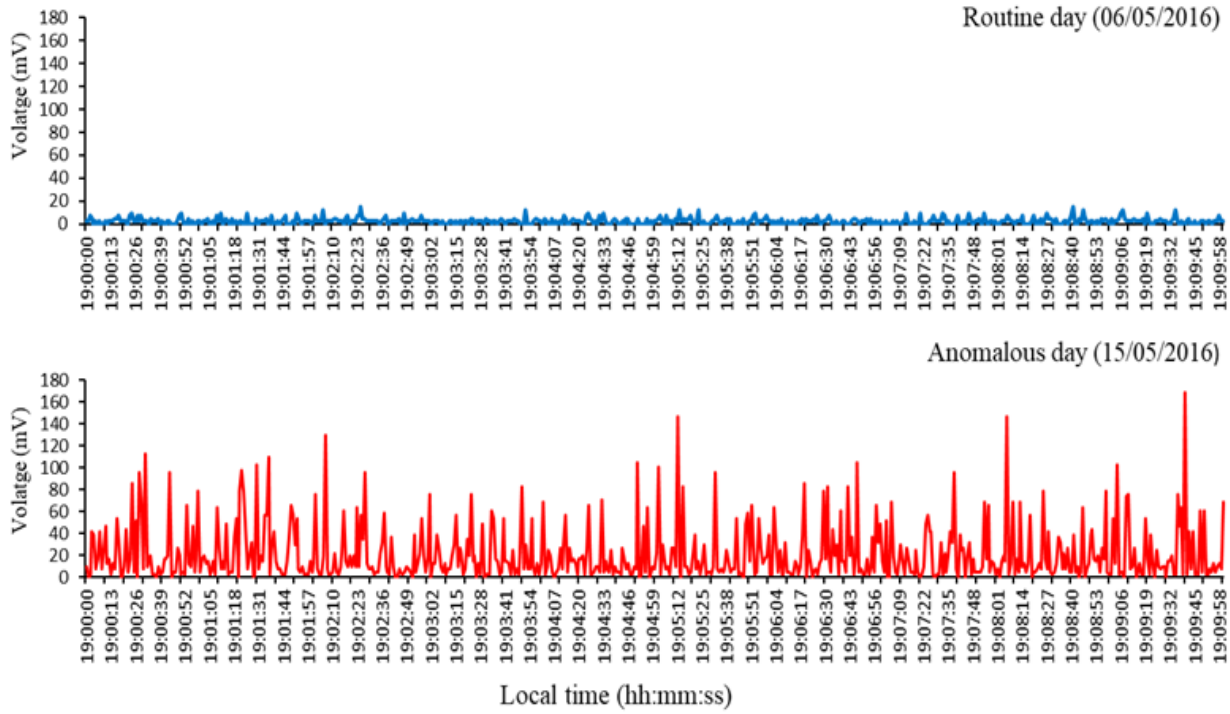

Figure 4. An example for temporal variation of horizontal component of VLF electric field emissions observed in horizontal antenna on a routine day (06/05/2016) and anomalous day (15/05/2016) by solid blue and red colour curves.

$$E_{RMS} = [(ncf^3/2d)^{1/2} \times \{\mu_0 p_0 \pi/(\varepsilon_r)^{1/4} h\}] \exp [-\{(\pi f \sigma_m \mu_0)^{1/2} d\} - (d/2h)\{(\pi f \sigma_m)^{1/2}((\sigma_{b1})^{-1/2} + (\sigma_{b2})^{-1/2})\}] \ldots\ldots\ldots\ldots\ldots\ldots\ldots(1)$$

here, p_0, n, f, d, μ_0, σ_m, ε_r, h, σ_{b1}, σ_{b2}, c stands for dipole moment of each radiator (dipole), number of dipoles in preparation zone, frequency of electromagnetic waves radiated by dipoles, distance at which field received, permeability of free space, conductivity of middle layer of crust, relative permittivity of middle layer of crust, depth of the elementary radiators from earth's surface, conductivity of upper and lower layers of crust, and speed of light respectively.

The values of the various parameters considered to compute the strength of field propagating through middle layer of crust at observing site are: $p_0 = 10^{-14}$ coulomb × meter (Ogawa et al., 1985), n = 4.35×10^{28}, f = 3012 Hz, d = 6.93×10^5 m – 1.269×10^6 m, $\mu_0 = 4\pi \times 10^{-7}$ H/m, $\sigma_m = 10^{-9}$ S/m (Tsarev and Sasaki, 1999), ε_r = 10 (Tsarev and Sasaki, 1999), h = 4.40×10^3 – 2.8570×10^4 m, $\sigma_{b1} = \sigma_{b2}$ = 0.1 Mho/m (for continental crust).

Putting the aforesaid values of various variables in equation (1), the range of electric field received at Mathura observatory comes out to be 2.53×10^{-4} – 4.12×10^{-3} V/m. The strength of the electric field produced corresponds to anomalous VLF amplitude enhancements beyond the upper bound (0.8 mV- 31.3 mV), range 1.37×10^{-4} – 5.53×10^{-3} V/m, which is quite close to the theoretical range of the electric field for the frequency of 3012 Hz at which VLF data is recorded. This ascertains that the theoretical estimations carried out are consistent with the experimental observations. Thus, the proposed model for the possible underground propagation of seismogenic emissions seems to be plausible.

CONCLUSIONS

The VLF electric field data observed in horizontal antenna at the Mathura observatory are analysed statistically for the months of June–July 2015 and February, March, and May 2016 to explore the impact of earthquakes which occurred within the circular region of radius 1270 km, from Mathura. Main results are summarised below.

1. Anomalous amplitude enhancements beyond the upper bound are observed in VLF electric field, 1-27 days before the occurrence of the seismic events (M ≥ 5.1, depth < 29 km) in India and its nearby countries.
2. Unusual VLF amplitude enhancements are found to vary between 0.8 mV and 31.3 mV, and the range of percentage enhancements in it is 0.95% - 86.22%.
3. The observed amplitude anomalies are not correlated with magnetic storms, lightning phenomenon, radiations of power lines, building noises, and instrumental inaccuracy, excluding cases of amplitude intensification associated with geomagnetic storms.
4. Probabilities for the pairs of magnitude with VLF amplitude enhancements and precursory time, and focal depth with VLF amplitude enhancements and precursory time are calculated, which are found 84.96%, 88.61%, 81.94%, and 92.33%, respectively, for these pairs which being sufficiently large, showing a strong connection between amplitude enhancements and their precursory times with the seismic events considered.

Acknowledgements

Authors are indebted to the Ministry of Earth Sciences, Government of India, New Delhi, for furnishing the financial assistance in the form of project: MOES/PO (Seismic)/1(16)/2008. Thanks also to the World Data Centre, Kyoto, Japan, and the United States Geological Survey (USGS), for providing the magnetic storm (∑Kp) and seismic event data, respectively.

Author credit statement

Ashwani Yadav: Data curation, methodology, data analysis, design of figures. Raj Pal Singh: Conceptualization, writing original draft and editing.

Data availability

Horizontal component of VLF electric field data used in this study are obtained by using a horizontal antenna installed at Mathura observatory, which is available to us.

Compliance with ethical standards

The authors declare that they have no conflict of interest and adhere to the copyright norms.

REFERENCES

Aravena, V.P. and Cordaro, E.G., 2019. A review and upgrade of the lithospheric dynamics in context of the seismo-electromagnetic theory. Nat. Hazards Earth Syst. Sci., 19, 1639–1651.

Biswas, S., Kundu, S., Sasmal, S., Politis, D.Z., Potirakis, S.M. and Hayakawa, M., 2023. Pre-seismic perturbations and their inhomogeneity as computed from ground- and space-based investigation during the 2016 Fukushima earthquake. J. Sensors, 2023, 1-23. https://doi.org/10.1155/2023/7159204

Bruce, C.E.R. and Golde, R.H., 1941. The lightning discharge. J. Institution of Electrical Eng., 88, 487-505.

Calderon, C.M., Shiokawa, K., Santolik, O., Kurita, S., Keika, K., Connors, M., Schofild, I., Hanzelka, M. and Kurth, W.S., 2025. Simultaneous ground-satellite observations of ELF/VLF emissions generated by a strong magnetospheric compression. Earth, Planets and Space, 77, 1-18.

Conti, L., Picozza, P. and Sotgiu, A., 2021. A critical review of ground-based observations of earthquake precursors. Frontiers in Earth Sci., 9, 1-30.

Fujinawa, Y., Takahashi, K., Noda, Y., Iitaka, H. and Yazaki, S., 2011. Remote detection of the electric field change induced at the seismic wave front from the start of fault rupturing. Int. J. Geophys., 2011, 1-11. https://doi.org/10.1155/2011/752193

Fujinawa, Y., Noda, Y., Takahashi, K., Kobayashi, M., Takamatsu, K. and Natsumeda, J., 2013. Field detection of microcracks to define the nucleation stage of earthquake occurrence. Int. J. Geophys., 2013, 1–18. https://doi.org/10.1155/2013/651823

Gao, Q., Ma, L., Liu, W., Khan, N.M., Alarifi, S.S., Sazid, M., and Inqiad, W.B., 2024. Method for rock fracture prediction and early warning: Insight from fusion of multi-physics field information. Heliyon, 10(10), 1-15.

Gao, X., Shu, L., Ma, Z., Tian, P., Pan, L., Zhang, H. and Yang, S., 2025. An investigation of pre-seismic ionospheric TEC and acoustic–gravity wave coupling phenomena using BDS GEO measurements: a case study of the 2023 Jishishan Ms6.2 earthquake. Remote Sens., 17, 1-26.

Gokhberg, M.B., Morgunov, V.A., Yoshino, T. and Tomizawa, I., 1982. Experimental measurement of electromagnetic emissions possibly related to earthquakes in Japan. J. Geophys. Res., 87(B9), 7824-7828.

Hayakawa, M., 2016. Earthquake prediction with radio techniques. Wiley and Sons.

Hayakawa, M., 2025. Review of sub-ionospheric VLF/LF radio signals for the study of seismogenic lower-ionospheric perturbations. Atmosphere, 16, 1-40.

Lakshmi, D.R., Veenadhari, B., Dabas, R.S. and Reddy, B.M., 1997. Sudden post-midnight decreases in equatorial and F region electron densities associated with severe magnetic storms. Ann. Geophys., 15, 306-313.

Meloni, A., Bianchi, C., Mele, G. and Palangio, P., 2015. Background electromagnetic noise characterisation: The role of external and internal earth sciences. Ann. Geophys., 58, 1-10.

Ogawa, T., Oike, K. and Miura, T., 1985. Electromagnetic radiations from rocks. J. Geophys. Res., 90, 6245-6249.

Panfilov, A.A., 2014. The results of experimental studies of VLF–ULF electromagnetic emission by rock samples due to mechanical action. Nat. Hazards Earth Syst. Sci., 14, 1383–1389.

Pulinets, S. and Ouzounov, D., 2018. The possibility of earthquake forecasting: learning from nature, Bristol: IOP Publishing.

Pulinets, S.A., Ouzounov, D., Karelin, A.V. and Boyarchuk, K., 2022. Earthquake precursors in the atmosphere and ionosphere. Springer Nature.

Rozhnoi, A., Solovieva, M.S., Molchanov, O.A. and Hayakawa, M., 2004. Middle latitude LF (40 kHz) phase variations associated with earthquakes for quiet and disturbed geomagnetic conditions. Phys. Chem. Earth, 29, 589–598.

Salikhov, N., Shepetov, A., Pak, G., Nurakynov, S., Ryabov, V. and Zhukov, V., 2025. Seismogenic effects in variation of the ULF/VLF emission in a complex study of the lithosphere–ionosphere coupling before an M6.1 earthquake in the region of northern Tien Shan. Geosciences, 15, 1-17.

Sanchez, S.A. and Kherani, E.A., 2024. A New Analytical simulation code of acoustic-gravity waves of seismic origin and rapid co-seismic thermospheric disturbance energetics. Atmosphere, 15, 1-14.

Sharma, S. and Singh, R.P., 2020. Effect of VLF electric field emissions related to shallow earthquakes ($M \geq 4.5$) in Nepal on atmosphere. J. Indian Geophys. Union, 24, 32-39.

Sharma, S. and Singh, R.P., 2022. On the propagation of VLF electric field emissions associated with earthquakes in the middle layer of the Earth crust. J. Earth Space Phys., 47, 1–13.

Sharma, S., Singh, R.P., Pundhir, D. and Singh, B., 2020. A multi-experiment approach to ascertain electromagnetic precursors of Nepal earthquakes. J. Atmos. Sol.-Terr. Phys., 197, 1–11.

Singh, R.P., Singh, B., Mishra, P.K. and Hayakawa, M., 2003. On the lithosphere-atmosphere coupling of seismo-electromagnetic signals. Radio Sci., 38, 1065-1075.

Singh, R.P., Kumar, M., Singh, O.P. and Singh, B., 2009. Subsurface VLF electric field emissions associated with regional earthquakes. Ind. J. Radio Space Phys., 38, 220-226.

Singh, R. P., Awasthi, M. and Pundhir, D., 2024. Detection of effects of shallow major earthquakes ($M \geq 5.0$, depth ≤ 30 km) occurred in India, Nepal, and China on ionosphere using statistical approaches. Geomag. Aeronomy, 64, 981-994.

Sorokin, V.M., Yashchenko, A.K. and Hayakawa, M., 2007. Electric field perturbation caused by an increase in conductivity related to seismicity-induced atmospheric radioactivity growth. J. Phys. Chem. B, 1, 644–648.

Sorokin, V.M., Ruzhin, Yu.Ya., Yaschenko, A.K. and Hayakawa, M., 2011. Generation of VHF radio emissions by electric discharges in the lower atmosphere over a seismic region. J. Atmos. Sol.-Terr. Phys., 73, 664–670.

Tatsuta, K., Hobara, Y., Pal, S. and Balkhin, M., 2015. Sub-ionospheric VLF signal anomaly due to geomagnetic storms: a statistical study. Ann. Geophys., 33, 1457–1467.

Tsarev, V.A. and Sasaki, H., 1999. Low frequency seismogenic electromagnetic radiation: how does it propagate in the Earth's crust and where it can be detected? in atmospheric and ionospheric electromagnetic phenomenon associated with earthquakes, Hayakawa, M., Ed., Tokyo: Terra. Science, 383–393.

Zeigarnik, V.A., Bogomolov, L.M. and Novikov, V.A., 2022. Electromagnetic earthquake triggering: Field observations, laboratory experiments, and physical mechanisms—a review. Izvestiya, Phys. Solid Earth, 58(1), 30–58.

Zhang, D., Shengfei, W. and Zhang, N., 1988. Observations and studies of electromagnetic waves during the approaching of earthquakes. Acta Seismologia Sinica, 1(4), 103-112.

Zhao, S., Shen, X.H., Zhima, Z. and Zhou, C., 2020. The very low-frequency transmitter radio wave anomalies related to the 2010 M = 7.1 Yushu earthquake observed by the DEMETER satellite and the possible mechanism. Ann. Geophys., 38, 969–981.

Zhima, Z., Hu, Y., Piersanti, M., Shen, X., Santis, A.D., Yan, R., Yang, Y.Y., Zhao, S., Zhang, Z., Wang, Q., Huang, J. and Guo, F., 2020. The seismic electromagnetic emissions during the 2010 Mw 7.8 northern Sumatra earthquake revealed by DEMETER satellite. Frontiers in Earth Sci., 8, 1-14.

Received on: 27-09-2025; Revised on: 13-03-2026; Accepted on: 18-03-2026

J. Ind. Geophys. Union, 30(3) (2026), 194-201
https://doi.org/10.71122/JIGU.30(3)2026.0020

Interlinkages between air pollution and local weather changes in urban environment: A case study from Alwar, Northwestern India

Vivek Kumar[1], Divya Prakash[1,2*] and Swagata Payra[3]
[1]Department of Civil Engineering, Poornima University Jaipur, 303905, Rajasthan, India
[2]Centre of Excellence in Water and Clean Air, Poornima University Jaipur, 303905, Rajasthan, India
[3]Department of Remote Sensing and Geoinformatics, Birla Institute of Technology Mesra, Ranchi, 835215, Jharkhand, India
*Corresponding author: divya.prakash@poornima.edu.in

ABSTRACT

The air pollution challenge has become a significant environmental and public health issue in the semi-arid urban areas of India. The current study looked at the effect of meteorological factors on the ambient air quality of Alwar, which is a non-attainment city in northwestern India, by examining five years (2018-2022) data of Continuous Ambient Air Quality Monitoring Station (CAAQMS) of the Central Pollution Control Board (CPCB) in Alwar. The parameters of interest are PM_{10}, $PM_{2.5}$, NO_2, SO_2, CO, and O_3. $PM_{2.5}$ concentrations ranged from an annual mean of 40.9-52.1 µg/m^3 and PM_{10} concentrations from 77.5-105.4 µg/m^3; both of which are consistently above the NAAQS. Highest concentrations of particulates were found during winter months with $PM_{2.5}$ concentrations exceeding 90 µg/m^3 under low wind speed/stable atmosphere conditions. The correlation analysis found a negative correlation between PM, NOx and CO; and positive correlation between O_3 and temperature. The drop in pollutants during the 2020 pandemic showed that humans were the dominant contributor to air pollution. Based on these findings, it is concluded that the use of meteorological conditions within air quality management strategies will contribute to improving the air quality in semi-arid urban areas.

Keywords: Urban air pollution, Meteorological parameters, Particulate matter ($PM_{2.5}$, PM_{10}), Seasonal variation, Alwar, Northwestern India

INTRODUCTION

Air is one of the most important components of the biosphere because it provides all living organisms with the ability to live on the planet, as well as sustains life itself. Unfortunately, many factors that are outside the control of nature have created an increase in the amount of contamination found in the air, resulting from the increasing levels of human activity on Earth. It has created significant air pollution, which threatens both human health and ecosystems, as well as the climate. Urbanization, industrialization, and increasing energy use, have significantly reduced air quality, especially in cities. Many of the emissions produced by business industries, automobiles, construction projects, and even the weather conditions where the air is polluted, can lead to very high levels of emission of pollutants like PM, SO_2, NO_x, CO, and hydrocarbons, which impact both the processes related to atmospheric chemistry and global warming.

India has become one of the world's highly polluted nations in the last thirty years and is particularly polluted in the western part of the country and along the Indo-Gangetic Plain. Most of the air pollution in urban India comes from large groups of industries, the number of vehicles in use, an overall lack of urban planning and the burning of both biomass and coal in the home environment. The air pollutants responsible for the majority of urban air pollution in India are found in the form of particulate matter ($PM_{2.5}$ and PM_{10}), but they also transport trace elements and heavy metals, most of which are associated with a variety of illnesses, including respiratory and cardiovascular diseases (Moghadamnia et al., 2017; Li et al., 2018; Kumar et al., 2020, 2023; Rani and Kulshrestha, 2026). In addition, $PM_{2.5}$ frequently contain more harmful metals compared to PM_{10} particles (Kulshrestha et al., 2009; Hsu et al., 2016), and there is a large number of epidemiological studies showing that there is a strong correlation between PM exposure and adverse health effects (Dockery et al., 1993; Cascio et al., 2009; Knol et al., 2009; Hoek et al., 2010; Cassee et al., 2013; Kelly and Fussell, 2015; Gupta and Elumalai 2017). In addition to health impacts, PM also results in decreased visibility, imbalance of the Earth's radiative system and the ability for global climate to remain stable (Dan et al., 2004).

The concentrations of air pollutants are affected by weather because the weather determines how much and how fast these pollutants are released, dispersed, and chemically transformed (Latini et al., 2002; Yang and Wang, 2017). The meteorological parameters that influence accumulation and transport of pollutants include solar radiation, wind speed, temperature and relative humidity; these parameters have a larger impact on semi-arid desert regions (Ma et al., 2025). Due to rapid urbanization of cities like Alwar (Rajasthan), increased vehicle emissions, dust resuspension and the climate, Alwar is becoming increasingly vulnerable to decreased air quality. Alwar has a mixed emissions profile from vehicle, industrial, residential and construction emissions and natural sources of dust due to its proximity to the Aravalli mountain range and also from the Indo-Gangetic Plain. Alwar is more representative of emerging urban centers in NW India, where studies of the relationship between meteorology and pollutant

concentration are lacking. The goal of this research work is to assess the influence of important parameters on the temporal change in ground level ozone (O_3), nitrogen dioxide (NO_2), PM_{10} and $PM_{2.5}$ in Alwar: A semi-arid urban centre of NW India, and how this understanding can be used to assist with informed air quality management and public health protection. The purpose is two-fold: (i) To review the seasonal and inter-annual trends of the common air pollutants in Alwar from 2018-2022, and (ii) to explore the statistical relationships between the pollutant concentrations and the meteorological factors using robust analytics.

STUDY AREA

The study was carried out in Alwar, a fast-expanding urban-industrial area in northeastern Rajasthan, India (Figure 1). Alwar is one of the non-attainment cities of Rajasthan under National Clean Air Program (NCAP). Situated in the semi-arid region, Alwar exhibits diverse seasonal fluctuations and escalating human activity, rendering it an optimal location for examining the interplay between meteorological factors and air quality. This city is characterized by increased human emissions and a semi-arid environment.

DATA AND METHODOLOGY

Air quality data

The Continuous Ambient Air Quality Monitoring Station (CAAQMS) of the Central Pollution Control Board (CPCB) in Alwar, provided data on primary air pollutants, including $PM_{2.5}$, PM_{10}, NO_2, SO_2, CO, and O_3, from January 2018 to December 2022, to investigate the relationship between air quality and meteorological variables.

Meteorological data

Meteorological parameters including relative humidity, temperature, wind speed, wind direction have been obtained from CPCB site. Meteorological parameters data has been compiled into daily, monthly, and seasonal averages, following quality assessments to exclude missing or inaccurate values.

Air Quality Index (AQI)

AQI was computed following CPCB (2014) guidelines using pollutant-specific sub-indices set by the Ministry of Environment, Forests, and Climate Change (MoEFCC). The conclusive AQI result for each day was determined by selecting the maximum pollutant-specific index. The evaluation of the AQI (ranging from 0 to 500) for a specific air pollutant is determined by correlating its concentration with a defined set of air contaminants. The AQI at any time (daily) is typically computed based on the pollutants with the highest Air Quality Index scores among all general air contaminants (Kumari and Jain, 2018).

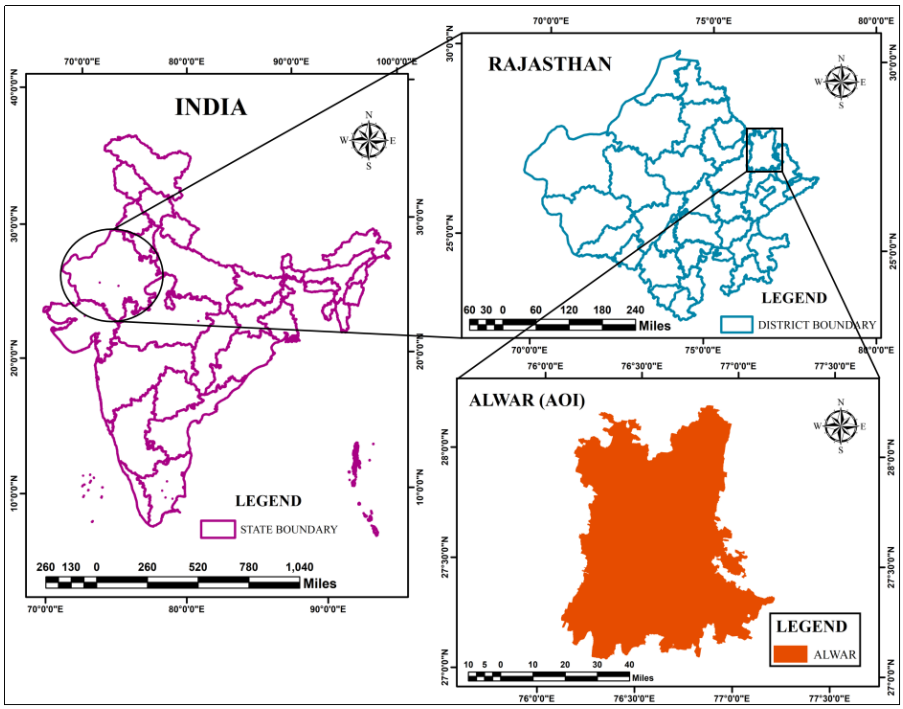

Figure 1. Study area of Alwar located in Northwest India

Statistical analysis

The association between pollutant concentrations and climatic circumstances was examined utilizing statistical techniques, including descriptive statistics and Pearson correlation analysis. The Annual average is derived from the monthly averages, and the monthly averages are derived from daily averages based on hourly averages. Statistical significance was evaluated at $p < 0.05$. All analyses were conducted using Python, IBM SPSS and MS Excel.

RESULTS AND DISCUSSION

Seasonal and interannual variation of pollutants over Alwar

Concentration levels of PM_{10}, $PM_{2.5}$, SO_2, NO_X, CO and O_3 over Alwar, Rajasthan from January 2018 to December 2022 were obtained from CPCB website (https://app.cpcbccr.com/ccr/#/caaqm-dashboard-all/caaqm-landing/data) and Air Quality Index was calculated by the method as described above. Comparison of monthly concentration levels of PM_{10}, $PM_{2.5}$, NO_2 and SO_2 for the period 2018 to 2022 is depicted in **Figures 2**. Comparison of monthly Air Quality Index (AQI) for the period 2018 to 2022 is also depicted in **Tables 1** and **2**.

The Figure 2 illustrates the monthly distribution of PM_{10}, $PM_{2.5}$, NO_2, and SO_2 during 2018-2022. PM_{10} and $PM_{2.5}$ have an observable seasonal variation as they have higher levels of concentration during the winter months. This is due to stable atmospheric conditions, and fewer dispersal opportunities available as well as more emissions. During the monsoon season, PM_{10} and $PM_{2.5}$ have a lower level of concentration than winter because of the wet scavenging process and the improved ventilation throughout that period. There are significant episodic emissions of NO_2, mainly related to vehicle traffic and combustion sources. The increased concentration of NO_2 in winter is attributed to less photo-chemical removal of NO_2 and shallow boundary layers. SO_2 is maintained at a low concentration and has little deviation from that point for the duration of the time frame represented in the graph, which suggests that emissions of SO_2 are controlled and therefore, subject to limited seasonal influences. The figure represents a combination of the influences of emissions and meteorology.

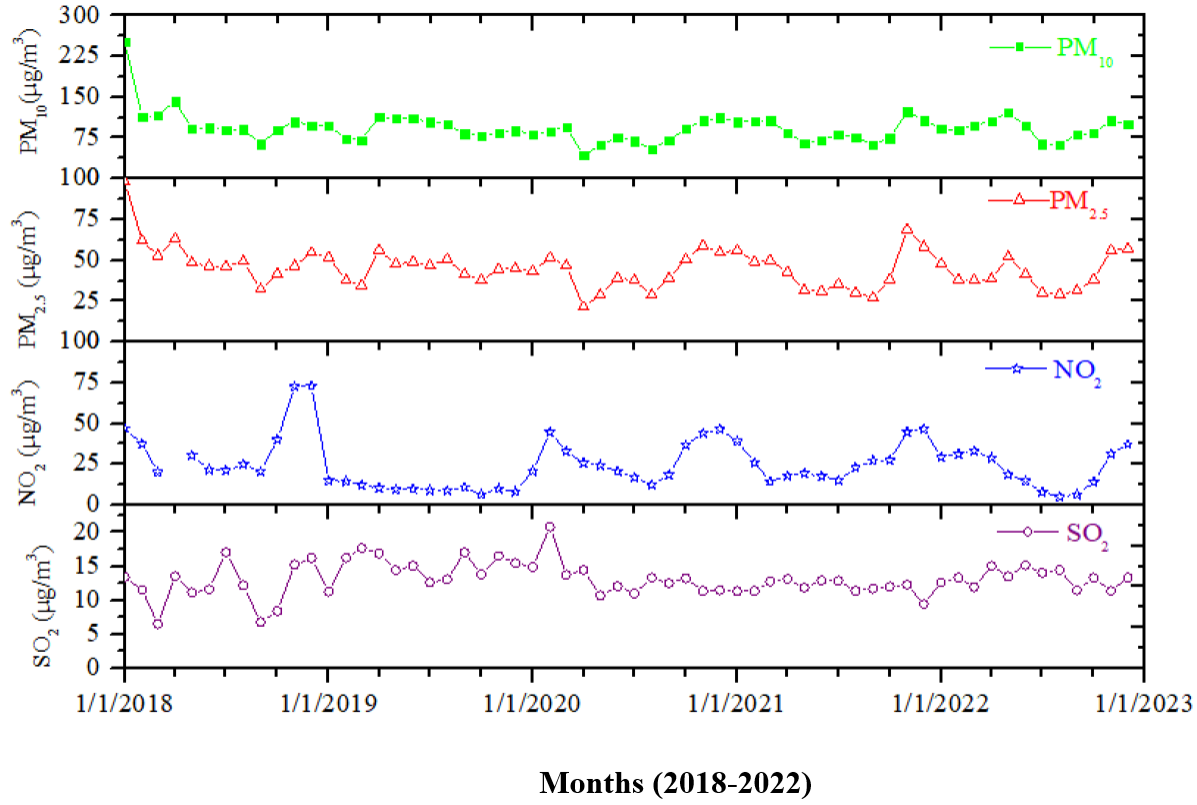

Figure 2. Monthly variation of air pollutants during 2018-2022 over the Alwar region in northwest India

This study also explored the annual concentration of different air pollutant during the study period and compared with the National Ambient Air Quality Standard (NAAQS) of India. It is found that the annual concentration of PM_{10} and $PM_{2.5}$ exceed the NAAQS and considered as non-attainment city of Rajasthan under NCAP. Annual trends of PM_{10}, $PM_{2.5}$, NO_2, and SO_2 concentrations in Alwar, as indicated in Figure 3, reveals wide fluctuations between the years 2018 and 2022. PM_{10}, $PM_{2.5}$, and NO_2 concentrations reached their highest levels in 2018 due to increased emissions from vehicle traffic, resuspension of road dust, construction and demolition activities, industrial activities, and burning of fossil fuels, while SO_2 reached its peak in 2019. This was likely due to increased emissions from power plants, refineries, and industrial sources that produce high levels of sulfur.

The data in Tables 1 and 2 showed the annual air pollutant concentration and AQI, respectively during 2018-2022. From Table 2, the maximum AQI over Alwar was found 219 in the month of January 2018 which represents the poor air quality. The poor air quality may cause breathing discomfort to people with prolonged exposure and discomfort to people with heart disease. It is observed that minimum AQI over Alwar was found 43 in the month of April 2020 which shows the air quality in good category. Most of the time AQI over Alwar was found to be in satisfactory category for all five consecutive years. The air quality is satisfactory category responsible for possible health impact as minor breathing discomfort to sensitive people.

Relationship between meteorological parameters and air pollutant concentration

Meteorology plays a significant role in dispersion or accumulation of air pollutants in the atmosphere. This study explores the relationship between pollutant gases (NO_2 and SO_2) and particulate matter (PM_{10} and $PM_{2.5}$) with temperature and relative humidity during 2018-2022. There are clear seasonal trends for both PM and gas pollutants with increased levels during the winter and post-monsoon months than during the summer and monsoon months. The winter peak concentrations of PM_{10}, $PM_{2.5}$, and NO_2 can mainly be attributed to the stable atmospheric conditions that prevail over Alwar during the winter months, lower boundary layer heights, reduced wind speed, and increased emissions from vehicles and combustion sources, which result in the accumulation of these pollutants. Conversely, the summer and monsoon months generally have lower concentrations of PM_{10}, $PM_{2.5}$, and NO_2 due to the increased mixing of the atmosphere, warmer temperatures, and wet scavenging of pollutants as shown in Figure 4 and 5.

Air temperature displays a distinct annual pattern and has an inverse relationship with PM and NO_2, indicating greater dispersion and photochemical degradation of these pollutants when air temperatures are higher than average. Relative humidity increases with seasonal variability and has a negative relationship to air pollutants due to the potential for humidity to promote the removal of particles and the scavenging of gases. SO_2 appears stable during the study period, indicating localized and closely controlled sources of emissions.

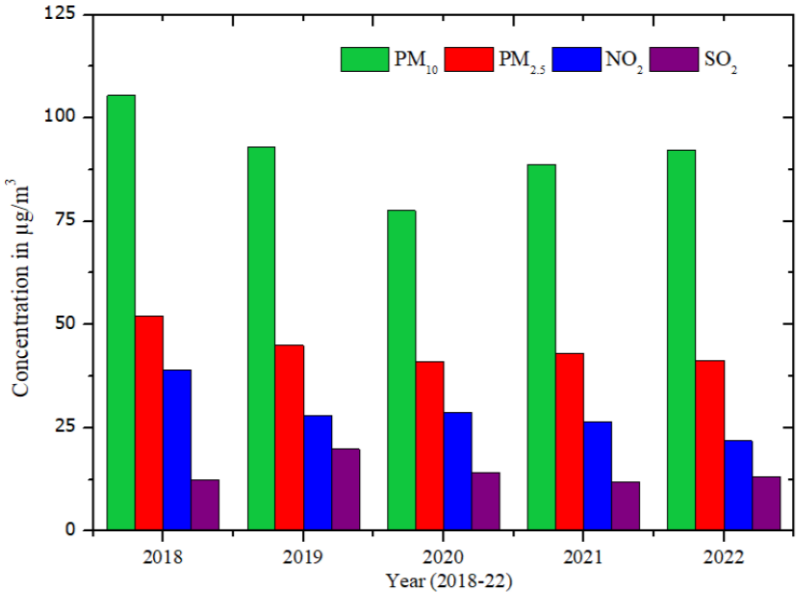

Figure 3. Annual variation of air pollutants over Alwar City in northwest India for the period of 2018-2022

Table 1. Comparison of annual concentration levels of PM_{10}, $PM_{2.5}$, NO_2, and SO_2 for the period 2018 to 2022

S. no.	Year	Pollutants			
		PM_{10}	$PM_{2.5}$	NO_2	SO_2
1	2018	105.4	52.1	37.2	12.4
2	2019	93.1	44.9	10.5	19.8
3	2020	77.5	41.0	28.7	14.0
4	2021	88.8	43.1	26.6	11.7
5	2022	92.2	41.4	21.5	13.1

Table 2. Comparison of monthly variation of AQI over Alwar for the period 2018 to 2022

Month	AQI				
	2018	2019	2020	2021	2022
January	219	220	83	106	93
February	108	288	88	103	89
March	134	298	77	102	97
April	83	294	43	84	103
May	119	264	61	65	114
June	99	271	76	71	95
July	100	242	70	81	65
August	101	243	55	76	62
September	64	290	71	62	82
October	133	250	94	77	84
November	105	282	113	141	118
December	105	273	106	113	109

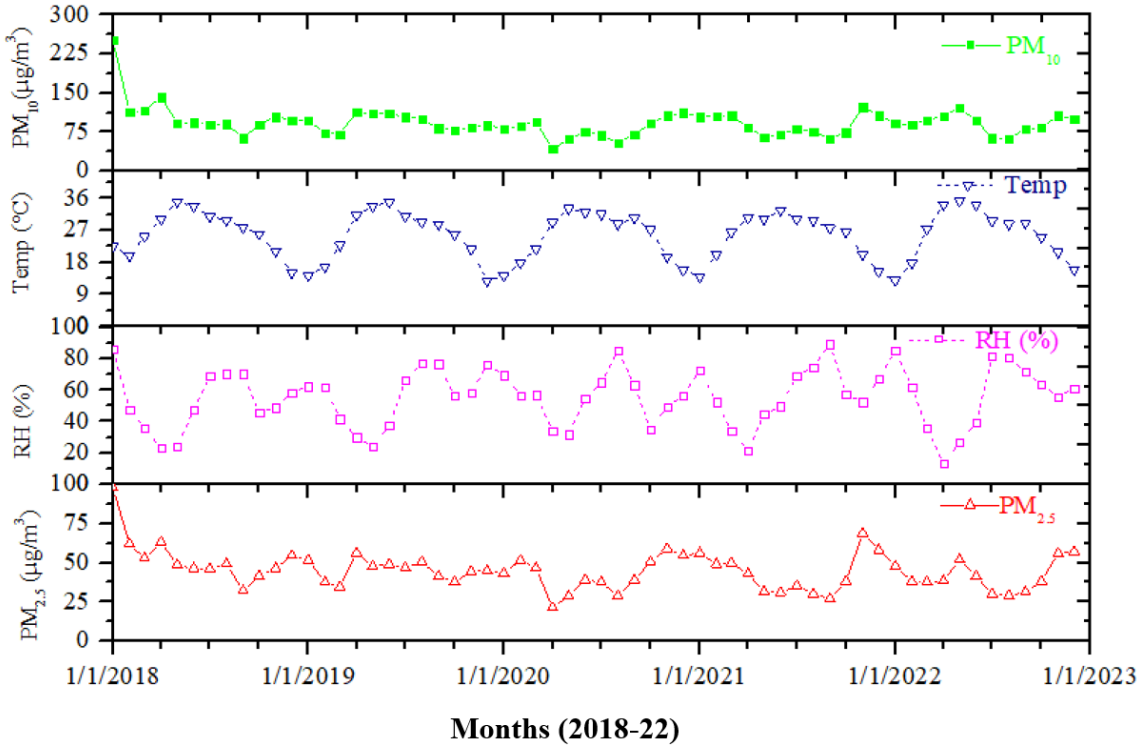

Figure 4. Monthly variation of PM_{10} and $PM_{2.5}$ with temperature and relative humidity at Alwar during 2018-2022.

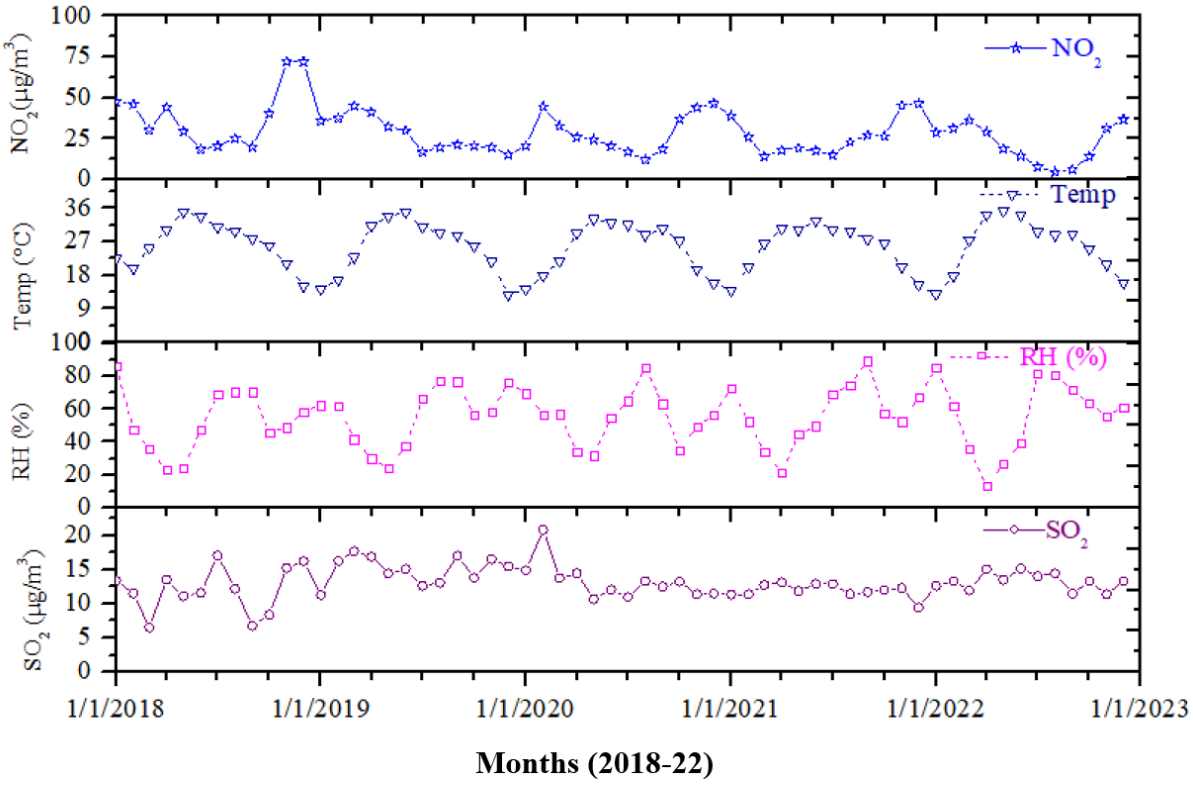

Figure 5. Monthly variation of SO_2 and NO_2 with temperature and relative humidity at Alwar during 2018-2022.

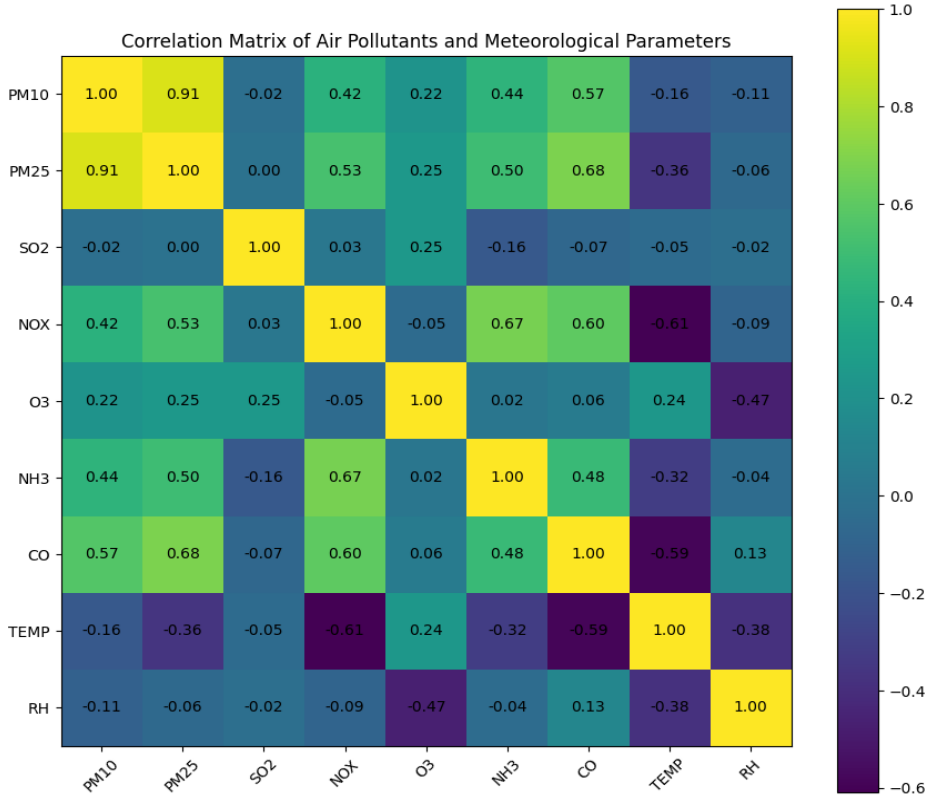

Figure 6. Correlation matrix of air pollutants and meteorological parameters over Alwar during 2018-22

To find out the potential association between the measured near-surface pollutants and surface meteorological parameters, Karl Pearson correlation analysis was conducted using IBM SPSS version 21.0 software. The correlation between air pollutants and meteorological parameters are shown in Figure 6. This matrix shows the very strong correlation (+0.91) between PM_{10} and $PM_{2.5,}$ represent the common origin such as vehicular emissions, road dust and industrial activities (Lee et al., 2006; George et al., 2017; Tomar and Singh, 2023; Gupta et al., 2025). Additionally, there is a moderate level of correlation between particulate matter, NOx, NH_3, and CO as a result of combustion and transportation activities. NOx is positively correlated with NH_3 (r=0.67) and CO (r=0.60), indicating that these pollutants have also been co-emitted from anthropogenic sources.

The temperature has a significantly negative correlation with the NOx (r=-0.61) and CO (r=-0.59), which implies warmer temperatures allow improved dispersion of the pollutants and/or increase photochemical removal of the pollutants. This supports prior studies by Jayamurugan et al. (2013), Kayes et al. (2019), and Das et al. (2021), who found that air quality was consistently improved under various temperature ranges for a variety of locations. Whereas, as noted in Zhang et al. (2006), CO levels tend to increase with varying temperature, suggesting the occurrence of photochemical reactions due to the increased amount of light received, which forms as CO becomes more stable. Ozone has a positive correlation with temperature (r=0.24) while having a negative correlation with relative humidity (r=-0.47) indicating that ozone requires photochemical reactions and is sensitive to moisture. Relative humidity generally has weak to moderate negative correlations with most pollutants, indicating the role of moisture in the removal processes of pollutants. Thus, the results of the correlation matrix indicate that the air quality in the studied area is controlled by the same source of emissions and significantly affected by meteorological conditions.

CONCLUSIONS

The present study investigates the interaction between atmospheric conditions and urban air pollution in Alwar City, a city located in NW India that continuously fails to meet air quality standards. The five years of continuous measurements (2018-2022) of atmospheric air quality data, show large seasonal changes in the concentration of atmospheric pollutants. It was found that concentrations of PM_{10} and $PM_{2.5}$ are very high in the winter months, mainly due to the lack of atmospheric conditions to disperse pollutants (i.e. low wind speeds), and low heights of the boundary layer, as well as an increase in the emissions from human activities (i.e. motor vehicle traffic, resuspended road dust, and burning activities in households). The strong positive correlations between particulate matter, NO_X , and CO during stagnant meteorological conditions suggest that these pollutants share common source emissions and may accumulate to greater concentrations when atmospheric conditions are stagnant. The high relative humidity in Alwar City is related to the increased concentration of particulate matter as a result of the dry climate's role in enhancing resuspension of dust and making it more difficult to scavenge particulate matter through moisture. The large reduction in all pollutant concentrations observed during the period of lockdown because of COVID-19 is compelling evidence of the degree to which the activities of humans have harmed urban air quality in the area.

ACKNOWLEDGEMENT: The authors are thankful to the Rajasthan State Pollution Control Board (RSPCB) Jaipur and Central Pollution Control Board (CPCB) New Delhi for the air quality data used in this study.

Author Credit Statement

Vivek Kumar: Data curation, validation, writing-original draft. Divya Prakash: conceptualization, supervision, visualization, investigation, writing, reviewing and editing. Swagata Payra: visualization, writing-review and editing, supervision.

Data Availability

The air pollutant and meteorological data used in this study can be found at https://app.cpcbccr.com/ccr/#/caaqm-dashboard-all/caaqm-landing/data.

Compliance with Ethical Standards

The authors declare that they have no conflict of interest and adhere to the copyright norms.

REFERENCES

Cascio, W.E., Katwa, L.C., Linn, W.S., Stram, D.O., Zhu, Y., Cascio, J.L. and Hinds, W.C., 2009. Effects of Vehicle Exhaust in Aged Adults Riding on Los Angeles Freeways. In *A25.* Evidence from human studies on the cardiovascular effects of air pollution. Am. Thorac. Soc., A1175.

Cassee, F.R., Héroux, M.E., Gerlofs-Nijland, M.E. and Kelly, F.J., 2013. Particulate matter beyond mass: recent health evidence on the role of fractions, chemical constituents and sources of emission. Inhal. Toxicol., 25(14), 802–812.

CPCB, 2014. Central Pollution Control Board. National Air Quality Index, National AQI Report 2014. https://www.cpcb.nic.in/displaypdf.php?id=bmF0aW9uYWwtYWlyLXF1YWxpdHktaW5kZXgvRklOQUwtUkVQT1JUX0FRSV8ucGRm.

Dan, M.O., Zhuang, G., Li, X., Tao, H. and Zhuang, Y., 2004. The characteristics of carbonaceous species and their sources in PM2.5 in Beijing. Atmos. Environ., 38(21), 3443–3452.

Das, M., Das, A., Sarkar, R., Mandal, P., Saha, S. and Ghosh, S., 2021. Exploring short term spatio-temporal pattern of PM2. 5 and PM10 and their relationship with meteorological parameters during COVID-19 in Delhi. Urban Clim., 39, 100944.

Dockery, D.W., Pope, C.A., Xu, X., Spengler, J.D., Ware, J.H., Fay, M.E., Ferris Jr, B.G. and Speizer, F.E., 1993. An association between air pollution and mortality in six US cities. N. Engl. J. Med., 329(24), 1753–1759.

George, K. V., Patil, D. D., Anil, M. N., Kamal, N., Alappat, B. J. and Kumar, P., 2017. Evaluation of coarse and fine particles in diverse Indian environments. Environ. Sci. Pollut. Res., 24, 3363–3374.

Gupta, A., Srivastava, A.K., Bisht, D.S. and Jhamaria, C., 2025. Long-Term Assessment of Near-Surface Air Pollutants at Jaipur: Source Identifications and Their Association with Surface Meteorology. Pure Appl. Geophys. https://doi.org/10.1007/s00024-025-03895-9

Gupta, S.K. and Elumalai, S.P., 2017. Size-segregated particulate matter and its association with respiratory deposition doses among outdoor exercisers in Dhanbad City, India. J. Air Waste Manag. Assoc., 67(10), 1137-1145.

Hoek, G., Boogaard, H., Knol, A., De Hartog, J., Slottje, P., Ayres, J.G., Borm, P., Brunekreef, B., Donaldson, K., Forastiere, F. and Holgate, S., 2010. Concentration response functions for ultrafine particles and all-cause mortality and hospital admissions: results of a European expert panel elicitation. Environ. Sci. Technol., 44(1), 476-482.

Hsu, C.Y., Chiang, H.C., Lin, S.L., Chen, M.J., Lin, T.Y. and Chen, Y.C., 2016. Elemental characterization and source apportionment of PM10 and PM2.5 in the western coastal area of central Taiwan. Sci. Total Environ., 541, 1139-1150.

Jayamurugan, R., Kumaravel, B., Palanivelraja, S. and Chockalingam, M.P., 2013. Influence of temperature, relative humidity and seasonal variability on ambient air quality in a coastal urban area. Int. J. Atmos. Sci., 2013(1), 264046.

Kayes, I., Shahriar, S.A., Hasan, K., Akhter, M., Kabir, M.M. and Salam, M.A., 2019. The relationships between meteorological parameters and air pollutants in an urban environment. Glob. J. Environ. Sci. Manag., 5(3), 265-278.

Kelly, F.J. and Fussell, J.C., 2015. Air pollution and public health: emerging hazards and improved understanding of risk. Environ. Geochem. Health, 37(4), 631-649.

Knol, A.B., de Hartog, J.J., Boogaard, H., Slottje, P., van der Sluijs, J.P., Lebret, E., Cassee, F.R., Wardekker, J.A., Ayres, J.G., Borm, P.J. and Brunekreef, B., 2009. Expert elicitation on ultrafine particles: likelihood of health effects and causal pathways. Part. Fibre Toxicol., 6(1), 19.

Kulshrestha, A., Satsangi, P.G., Masih, J. and Taneja, A., 2009. Metal concentration of PM2.5 and PM10 particles and seasonal variations in urban and rural environment of Agra, India. Sci. Total Environ., 407(24), 6196-6204.

Kumar, K., Singh, S., Chandra, S. and Kulshrestha, M.J., 2020. Episodic measurements of PM2.5 during crop residue burning and Diwali Periods at Delhi. J. Indian Geophys. Union, 24(4), 40-50.

Kumar, K., Kulshrestha, M.J., and Singh, S., 2023. Influence and distribution pattern of n-Alkanes in PM2.5 and PM10 during odd- even scheme in Delhi, India. J. Indian Geophys. Union, 27(3), 174-184.

Kumari, S. and Jain, M.K., 2018. A critical review on air quality index. Water Sci. Technol., 77, 87–102.

Latini, G., Grifoni, R.C. and Passerini, G., 2002. Influence of meteorological parameters on urban and suburban air pollution. WIT Trans. Ecol. Environ., 53.

Lee, B. K., Lee, H. K. and Lee, O. K., 2006. Analysis of the correlation between particulate matter concentrations and traffic volume in the metropolitan city of Ulsan, Korea. In 2006 International forum on strategic technology (351–353). IEEE.

Li, T., Hu, R., Chen, Z., Li, Q., Huang, S., Zhu, Z. and Zhou, L.-F., 2018. Fine particulate matter (PM2.5): the culprit for chronic lung diseases in China. Chronic Dis. Transl. Med., 4(3), 176-186.

Ma, R., Xia, X., Xue, J., Yao, Y., Xin, A., Song, S., Wang, L. and Li, X., 2025. Impact of meteorological conditions and air pollution on the incidence of carbon monoxide poisoning: a retrospective analysis in northern China. BMC Public Health, 25(1), 2155.

Moghadamnia, M.T., Ardalan, A., Mesdaghinia, A., Keshtkar, A., Naddafi, K. and Yekaninejad, M.S., 2017. Ambient temperature and cardiovascular mortality: a systematic review and meta-analysis. Peer J., 5, p. e3574.

Rani, N. and Kulshrestha, M.J., 2026. Abundance, distribution pattern and health risk assessment of polycyclic aromatic hydrocarbons in size-segregated aerosols during Diwali festival in Delhi (India). J. Indian Geophys. Union, 30(2), 114-121.

Tomar, A. and Singh, C., 2023. Estimation of PM2.5 and PM10 during an intense dust episode over Indian region using satellite data set. In: 2023 IEEE, InGARSS, 1-4.

Yang, Z. and Wang, J., 2017. A new air quality monitoring and early warning system: Air quality assessment and air pollutant concentration prediction. Environ. Res, 1*58*, 105-117.

Zhang, Y., Xie, H. and Chen, G., 2006. Factors affecting the efficiency of carbon monoxide photoproduction in the St. Lawrence estuarine system (Canada). Environ Sci Technol, 40(24), 7771-7777.

Received on: 13-08-2025; Revised on: 08-02-2026; Accepted on: 27-02-2026

J. Ind. Geophys. Union, 30(3) (2026), 202-215
https://doi.org/10.71122/JIGU.30(3)2026.0021

North Atlantic Ocean a visible contributor to Indian summer monsoon rainfall

Vinod Kumar[1*] and M. Satya Kumar[2]
[1]Shyam Bhawan, Ashok Nagar, Road No. 11, Kankarbagh Colony, Patna- 800020, India
[2]6-3-565, Flat No. 301, Akshaya Aparment, Somajiguda, Hyderabad-500082, India
*Corresponding author: vinodmanjusingh@gmail.com

ABSTRACT

Moisture feeding from North Atlantic Ocean saves summer monsoon rainfall over India also during El-Nino, El Nino-Southern Oscillation (ENSO) and Indian Ocean Dipole neutral conditions if cyclonic circulation/flow is observed along North African coast having minimum latitudinal width of 5º south of 25ºN during south west monsoon season. Southern Hemisphere Zonal Westerlies Activity Index (SHZWAI), which had been prepared on the basis of (i) combination of High and Low located along 40ºS between 40ºW-120ºE at 850 hPa geo-potential height or vector wind anomaly fields, (ii) a continuous negative anomaly (Low) from 40ºS-30ºN along 90ºE, (iii) a region of negative anomalies lying to the north of positive anomalies (High) along 40ºS, (iv) a continuous High from 80ºW-150ºW or 120ºW-170ºE, (v) a continuous Low from 80ºW-150ºW or 120ºW-170ºE, and (vi) Cyclonic circulation/trough over Arabian Sea in the anomaly of 850 hPa vector wind observed during April-May of the ensuing monsoon year, has been modified for the quantitative forecast of All India Monsoon Rainfall. By considering cyclonic flow and anti cyclonic flow along North African coast up to 25ºN over the North Atlantic Ocean during April-May for the period of 50 years (1948-1997), a methodology has been developed for modifying the quantitative forecast of All India Monsoon Rainfall with modified Southern Hemisphere Zonal Westerlies Activity Index. Reanalysed NCEP/NCAR (National Centres for Environmental Prediction/National Centre for Atmospheric Research) data of geo-potential height, vector wind fields and relative humidity at 850 hPa geo-potential height and Sea Surface Temperature of North Atlantic Ocean up to 20ºN for the period 1948-2025, have been used in the study. It has been shown that composite anomaly field of vector wind/relative humidity at 850 hPa level for the period April-May from the region bounded by 60ºW-100ºE and equator to 30ºN, are helpful in identifying the conditions that are related to inter-annual variability in All India Monsoon Rainfall .

Key words: Southwest monsoon, North Atlantic Ocean, West coast of North Africa, Vector wind anomaly, Quantitative forecast, Cyclonic flow

INTRODUCTION

Popularity of Long Range Forecast for southwest monsoon rainfall is increasing day by day as people from all walks of life know that a normal rainfall is the life line of our country. As ground water is depleting gradually, deficient rainfall in any parts of our country, creates biggest problem in availability of drinking water not only in cities and towns but also in villages besides affecting agriculture produce and general health of the people due to rise in temperature. Kumar and Satya Kumar (2021) had prepared real time long range forecast of All India Monsoon Rainfall. During 2024 southwest monsoon season, La-Nina conditions were expected from August-September months, but this did not happen till the month of December 2024. Average Sea Surface Temperature for Nino 3.4 was observed as -0.4^{o}C for the combined months of October-November-December (NOAA, 2025). El Nino-Southern Oscillation (ENSO) neutral conditions are present and so was the condition of Indian Ocean Dipole. Even then monsoon rainfall for the monsoon season 2024 (June to September) over the country was recorded as 108% (above normal) of the Long Period Average. During EL-Nino years 1953 (109.9%), 1957 (97.6%), 1958 (109.8%) and 1997 (102.2%) normal/above normal rainfall had been recorded and during La Nina years 1974 (88%) and 1985 (92.9%) deficient and below normal rainfall had been recorded respectively (E-Mausam)**.**

The observed analysis revealed that despite the presence of the same climate drivers, El- Nino and positive Indian Ocean Dipole, in 1997 and 2015, 1997 was a normal monsoon year, whereas 2015 was a below normal monsoon year (86.0%) for the Indian region (Ratna et al., 2024). There are years in which dipole mode events coincide with the strong ENSO events as in 1972 or 1997 (Saji et al., 1999). 1972 was a deficient monsoon year. Attempts have been made to look out for an atmospheric condition, which may further improve the real time Long Range Forecast of All India Monsoon Rainfall prepared by Kumar and Satya Kumar (2021). They had shown that composite anomaly field of geo-potential height/vector wind at 850/700 hPa level for the period April-May from the region bounded by 40ºW-140ºE/80ºW-150ºW-170ºE and 40ºS-30ºN, are helpful in identifying the circulation features that are related to inter-annual variability in All India Monsoon Rainfall. The features identified were: (i) a pair of positive and negative anomalies along 40ºS latitude, (ii) continuous negative anomalies from 40ºS to 30ºN, (iii) region of negative anomalies lying to the north of positive anomalies along 40ºS, (vi) cyclonic circulation/trough over Arabian Sea, and (v) positive/negative anomalies between 80ºW-150ºW-170ºE/40ºS. The semi-permanent subtropical anticyclone over North Atlantic Ocean basin, commonly referred as the “Azores” or the “Bermuda High”, has a major influence on the weather and climate over the eastern United States,

Western Europe and north western Africa (Davis et al., 1997). Sahsmanoglou (1990) showed that the anticyclone migrates in a somewhat elliptical pattern from month to month within an area bounded by 25ºN – 40ºN and 20ºW - 50ºW. In its summer position, the high is centred near Bermuda, and creates a southwest flow of hot tropical air towards the east coast of United States. In summer the Azores-Bermuda high is strongest (1024 hPa, Wikipedia, https://en.wikipedia.org/wiki/Azores_High). The Indian summer monsoon rainfall and the Atlantic Nino peaks during boreal summer (June to August) and have inverse relationship. It is found that Atlantic Nino significantly influences a dipole pattern of rainfall in the north-east and north-western parts of India (Yadav et al., 2018). Strong negative (positive) North Atlantic Oscillation through hemispheric changes in winds and storm tracks lead to tropospheric temperature anomalies over Eureasia. These anomalies decrease (increase), meridional gradient of tropospheric temperature resulting in, below (above) normal monsoon rainfall. A positive Atlantic multidecadal Oscillation (AMO) produces stronger monsoon by producing tropospheric temperature anomaly over Eurasia. It is also associated with enhanced La Nina type Pacific Sea Surface Temperature anomalies that induces stronger regional monsoon Hadley circulation and stronger monsoon (Goswami et al., 2006). The study revealed statistically significant relationship, which are caused by the changes in the position and strength of the Azores High. During the considered normal monsoon years, Azores High and Aleutian low become stronger and the North Atlantic Jet moves northwards (Rajeevan and Sridhar, 2008). Warm Sea Surface Temperature over Eastern Pacific Ocean, corresponds to an overall decrease in Indian Summer Monsoon Rainfall, while warm Sea Surface Temperature anomalies over Indian Ocean (Indian Ocean Basement mode, IOB), corresponds to a decrease in rainfall over the north and increase in rainfall over the south of India.

The central Indian region experienced the most substantial variation in the ENSO - Indian Summer Monsoon Rainfall relationship. This variation corresponds to the variability of the monsoon trough and depressions, strongly influenced by the Pacific Decadal Oscillation and North Atlantic Oscillation, which regulate the relative dominance of the two spatial modes of Indian Summer Monsoon Rainfall (Athira et al., 2023). Ensemble experiments with an atmospheric general circulation model reveal that a positive (warm) Ocean phase of the Atlantic Multidecadal Oscillation increases Indian Summer Monsoon rainfall (Li et al., 2008). The positive Atlantic Multidecadal Oscillation phase characterised by anomalous warm North Atlantic and cold South Atlantic, leads to strong Southeast and East Asian summer monsoons, and late withdrawal of the Indian summer monsoon (Lu et al., 2006).

In this study, Southern Hemisphere Zonal Westerlies Activity Index has been modified with the help of a new parameter called North Atlantic Ocean Index. Cyclonic flow observed south of 25ºN and anti cyclonic flow observed south of 20ºN having at least 5º latitudinal width over North Atlantic Ocean along the west coast of North Africa during April and May at 850 hPa geo-potential height, have been considered for preparation of North Atlantic Ocean Index. Modified Southern Hemisphere Zonal Westerlies Activity Index helps in improving the quantitative Long Range Forecast of All India Monsoon Rainfall also during El Nino-Southern Oscillation (ENSO) and Indian Ocean Dipole neutral years.

DATA AND METHODOLOGY

Data

Plots of composite anomaly of vector wind, relative humidity at 850 hPa level and SST of North Atlantic Ocean for the period April-May and June-September1948-2025, had been prepared using data available on NOAA /Earth System Research Laboratory's website: http://www.esrl.noaa.gov/psd/cgi/bin/data/composite. All India Monsoon Rainfall data from 1948 to 2025 had been collected from IMD's website.

Definition of Southern Hemisphere Zonal Westerlies Activity Index (SHZWAI)

Different features developing in zonal westerlies of Southern Hemisphere during pre-monsoon months of April-May are precursors to development of southwest monsoon over India during June-September. This could be used to prepare quantitative Long Range Forecast on monsoon rainfall in India. For doing quantitative Long Range Forecast, the features have to be quantified. An attempt has been made here to quantify these features by assigning a point, ranging from -2 to 4 to each individual feature in a year called as Southern Hemisphere Zonal Westerlies Activity Index, has been obtained. Southern Hemisphere Zonal Westerlies Activity

Index (=1) corresponds to only one high or a pair of High and weak low/weak High and Low located along 40ºS between 40ºW and120ºE. Southern Hemisphere Zonal Westerlies Activity Index (2) corresponds to a pair of High and Low. The High and Low should have longitudinal and latitudinal width of at least 25º long. and at least 5º lat. respectively.

Table 1. Brief discussion of the features in 850 hPa geo-potential height and vector wind anomaly fields along 40ºS from 40ºW-120ºE/80ºW-170ºE and points (a numerical value) assigned to them

S. No.	Features in 850 hPa geo-potential height or vector wind anomaly fields	Points assigned
1	A pair of H and L. The H and L should have longitudinal and latitudinal width of at least 25º long. and at least 5º lat. respectively.	2
2	Only one H or a pair of H and weak L weak H and L	1
3	Only one L or a pair of weak H and L	0
4	A continuous negative anomaly (L) from 40ºS-30ºN along 90ºE and is also seen from 60ºS	4
5	A continuous negative anomaly from 40ºS-30ºN along 90ºE and is not seen from 60ºS.	1
6	Presence of a region of negative anomalies north of positive anomalies (H), L is seen north of H	2
7	A continuous H from 80ºW-120ºE (horizontal width 140º)	2
8	A continuous H from 80ºW-150ºW or 120ºW-170ºE (horizontal width 70º long. starting from at least 120ºW)	1
9	A continuous H of at least 40º long. horizontal width but less than 70º long. (starting from at least 120ºW)	0.5
10	A continuous L from 80ºW-120ºE (horizontal width 140º).	-2
11	A continuous L from 80ºW-150ºW or 120ºW-170ºE (horizontal width 70º long. starting from at least 120ºW)	-1
12	A continuous L of at least 40º long. horizontal width but less than 70º long. (starting from at least 120ºW)	- 0.5
13	Cycir./Tr over Arabian Sea in anomaly of 850 hPa vector wind for April- May having latitudinal width ≥5º	-1
14	Cycir./Tr over Arabian Sea in anomaly of 850 hPa vector wind for April- May having latitudinal width <5º	-0.5

Legend: H: High, L: Low, Cycir: Cyclonic circulation, Tr: Trough.

Note: Points 0 or less- markedly deficient, 0 to 1 – deficient, 1.5 - below normal, 2.0 but less than 3 - normal, 3 - active normal, 4 - above normal and more than 4 - excess rainfall.

The distance separating them should not be more than 20º long. Southern Hemisphere Zonal Westerlies Activity Index (0) corresponds to only one Low or a pair of weak High and Low. Southern Hemisphere Zonal Westerlies Activity Index for different features has been given under Table 1 (Kumar and Satya Kumar, 2021). Data for a period of 50 years (1948-1997) have been used to find the correlation coefficient between All India Monsoon Rainfall and Southern Hemisphere Zonal Westerlies Activity Index and the regression equation (straight line) relating them. The correlation coefficient is 0.74 which is highly significant. The regression equation relating All India Monsoon Rainfall (AIMR) and Southern Hemisphere Zonal Westerlies Activity Index (SHZWAI) is

$$AIMR=4.4 \times SHZWAI+ 90.4$$

All India Monsoon Rainfall is expressed as % of long period average (100%). The error for the Model Development Period (MDP) is ±4%. India Meteorological Department uses 5 ranges of % departure of All India Monsoon Rainfall for categorization of monsoon: 'Excess' >110% of normal, 'Above Normal' (110-105%), 'Normal' (104-96%), Below Normal (95-90%) and 'Deficient' < 90%. We have split the normal range into two i.e., 'Active Normal' and 'Normal' and have used seven categories (Kumar and Satya Kumar 2021).

North Atlantic Ocean Index (NAOI) parameter and scoring

Cyclonic flow south of 25ºN and anti cyclonic flow south of 20ºN of having at least 5º latitudinal width has been considered for adding points for the new parameter, North Atlamtic Oscillation Index, in the modified Southern Hemisphere Zonal Westerlies Activity Index. As anti cyclone migrates within the area bounded by 25ºN-40ºN/20ºW-50ºW from month to month (Sahsmanoglou, 1990), so anti cyclone observed south of 20ºN has been considered for North Atlantic Oscillation Index. If cyclonic flow is observed south of 25ºN (at least 20º latitudinal width), 0.5 point has been given and for anti cyclonic flow south of 25ºN, -0.5 point has been given. If cyclonic and anti cyclonic flows both are observed south of 25ºN, 0 point has to be given for North Atlantic Oscillation Index. For cyclonic/anti cyclonic flow having latitudinal width less than 20º, 0.25/-0.25 point can be considered for North Atlantic Oscillation Index. Point has to be given only on the basis of cyclonic/anti cyclonic flow observed along the west coast of North Africa**.** On the basis of synoptic situations at 850 hPa vector winds for the year 2025, the points have been given under Southern Hemisphere Zonal Westerlies Activity Index and North Atlantic Oscillation Index (Figure 1).

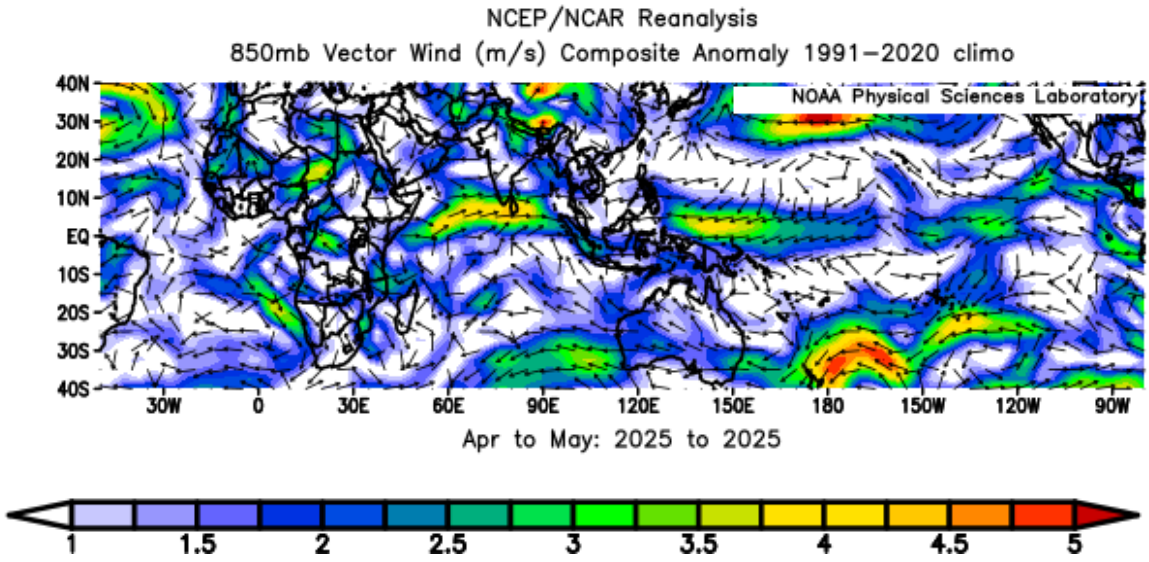

Figure 1. 850 hPa vector wind (meter/second) composite anomaly, Apr-May 2025

A high is located from 020ºE-020ºW/40ºS (anti cyclonic flow) and a low (cyclonic flow) is located north of high between 020ºE-010ºW/25ºS for which 2 points can be given. Another high is located from 060ºE-120ºE/40ºS for which 1 point can be been given. A high is located between 80ºW-150ºW/40ºS for which 1 point can be given. A cyclonic flow is seen between 060ºE-070ºE/10ºN-20ºN over Arabian Sea for which -1.0 point can be given (Figure 1). So, Southern Hemisphere Zonal Westerlies Activity Index comes to 3.0. A cyclonic flow is seen between 5ºN-25ºN along the west coast of North Africa over North Atlantic Ocean for which 0.5 point can be given (Figure 1). Here North Atlantic Oscillation Index value is 0.5. Combining these values total points under modified Southern Hemisphere Zonal Westerlies Activity Index come to 3.5. Putting the value of modified Southern Hemisphere Zonal Westerlies Activity Index (3.5) in the regression equation expected All India Monsoon Rainfall during monsoon season 2025 comes to 105.8 % of Long Period Average, with Model Development Period ± 4%. Actual rainfall recorded during 2025 summer monsoon was 108% (IMD, 2025).

RESULTS AND DISCUSSION

Composite anomaly of 850 hPa vector winds, for June to September from 1948-1975, shows cyclonic flow between 30ºN-20ºN and anti cyclonic flow south of 20ºN, along the west coast of North Africa. Cyclonic flow has been observed between 25ºN-15ºN from 1976-2000 and between 15ºN-10ºN for June-September from 2001-2024 respectively. Westerly component of winds has been observed along 10ºN and 5ºN for June-September from 2001-2024 **(**Figure 2). So, cyclonic flow is an important meteorological parameter observed during June-September between 10ºN-30ºN over Atlantic Ocean along the West coast of North Africa during 77 years period. Cyclonic flow has been observed for composite anomaly of 850 hPa vector winds, for April-May, south of 25ºN along the west coast of North Africa for the period 1948-1975. Anti cyclonic flow has been observed south of 25ºN for the period 1976-2000 and cyclonic flow between 25ºN and 10ºN for the period 2001-2024 for the composite anomaly of 850 hPa vector winds for the period April-May **(**Figure 3**)**. Relative humidity data have been used only for proper identification of cyclonic and anti cyclonic flow. Anomaly of cyclonic and anti cyclonic flow, at 850 hPa geo potential height does not match with the anomaly of relative humidity for their respective regions during a few years, Figure 4 and 5. Cyclonic flow has been observed south of 15ºN (0.25) in the anomaly of vector wind for April-May 1956 (Figure 4) but negative anomaly of relative humidity has been found south of 15ºN along

the west coast of North Africa (Figure 5). As such only on the basis of cyclonic and anti cyclonic flow points for North Atlantic Oscillation Index have been considered. During 1987 anti cyclonic flow had been noticed south of 25ºN, so -0.5 has been given under column 2 in Table 2 and Figure 6**.**

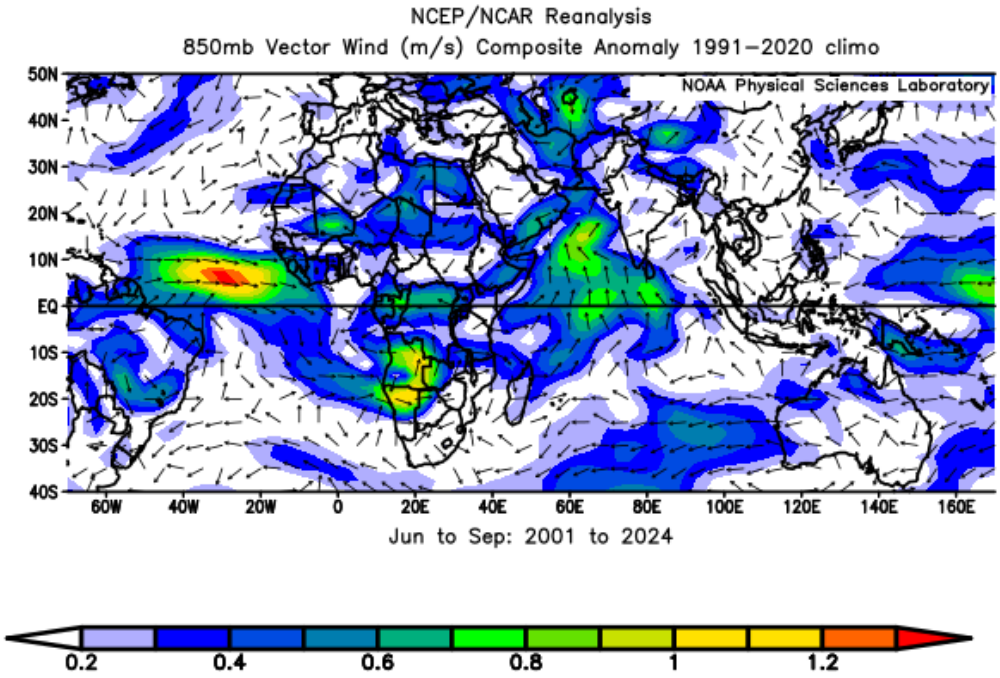

Figure 2. 850 vector wind (meter/second) composite anomaly, Jun-Sep, 2001-2024

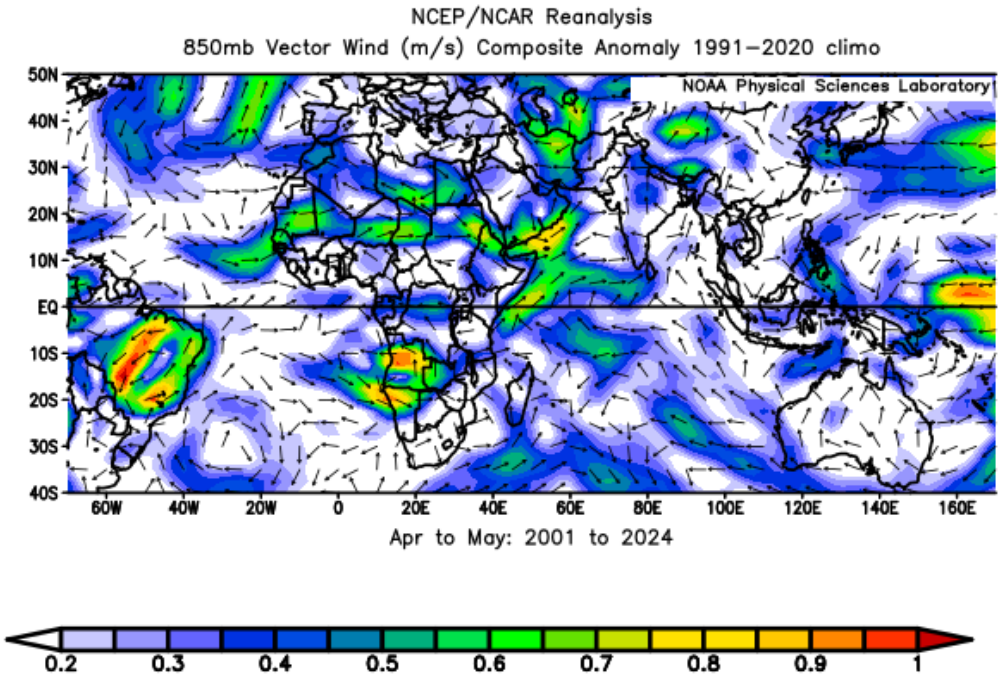

Figure 3. 850 vector wind (meter/second) composite anomaly Apr-May, 2001-2024

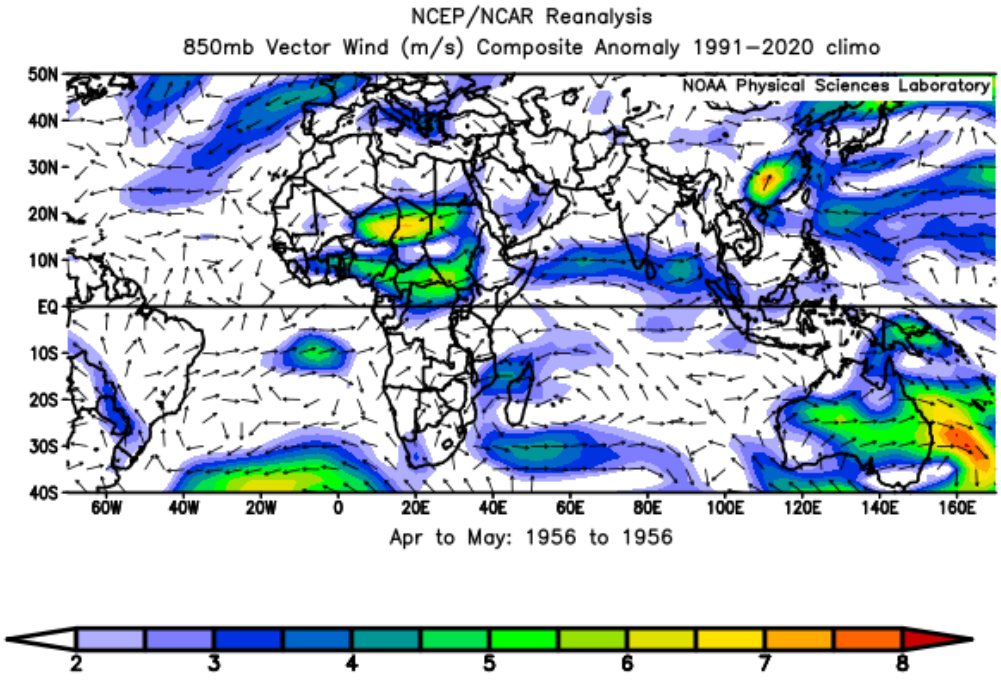

Figure 4. 850 hPa vector wind (meter/second) composite anomaly, Apr-May, 1956

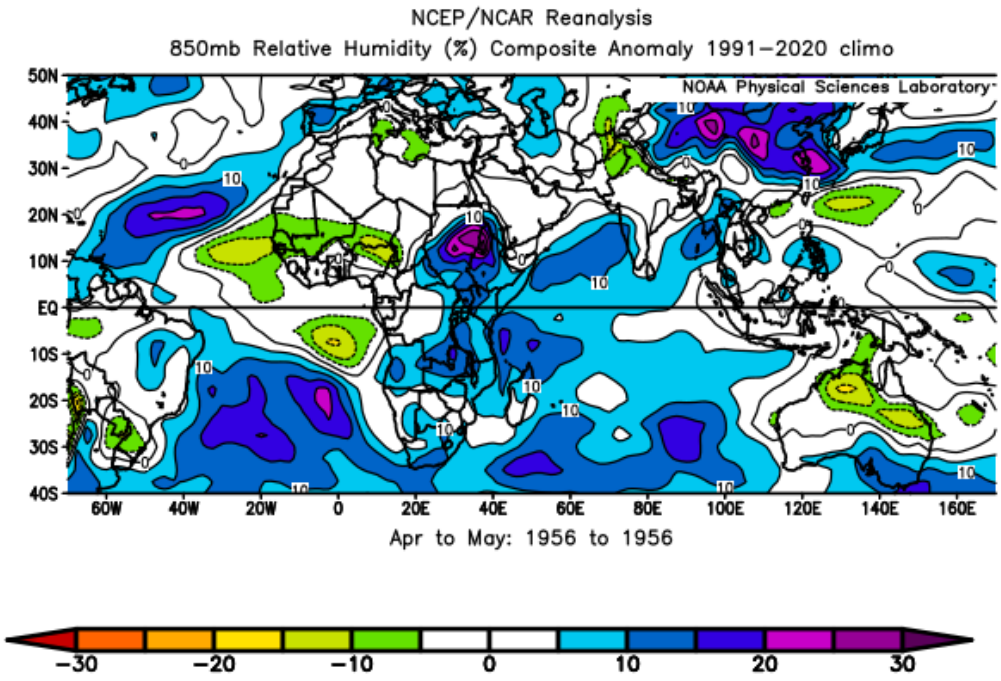

Figure 5. 850 hPa relative humidity (%) composite anomaly, Apr-May, 1956

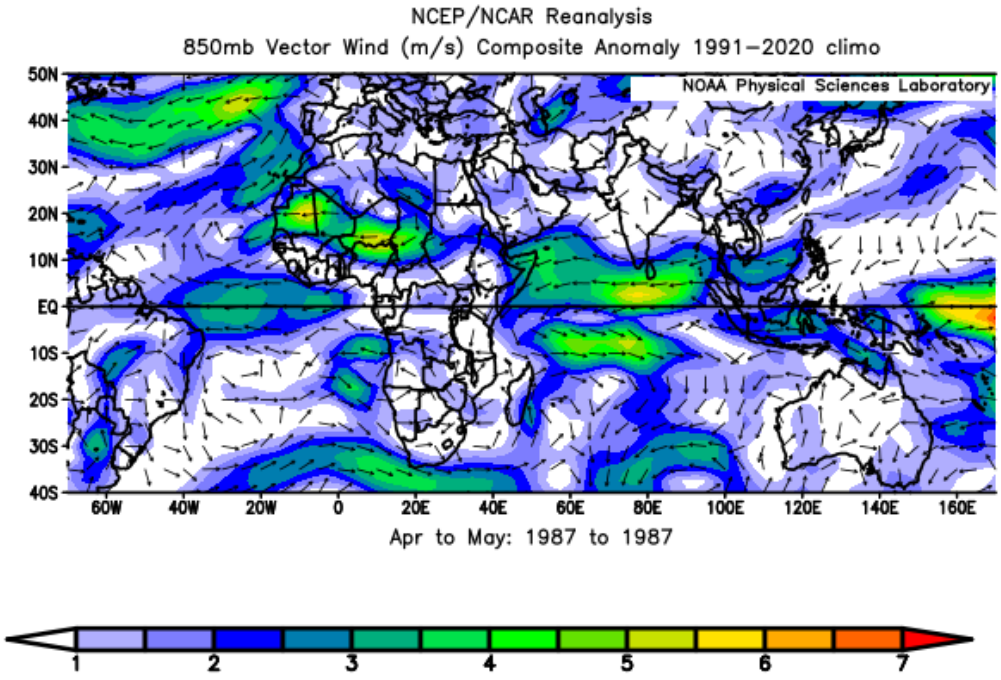

Figure 6. 850 hPa vector wind (meter/second) composite anomaly Apr-May, 1987

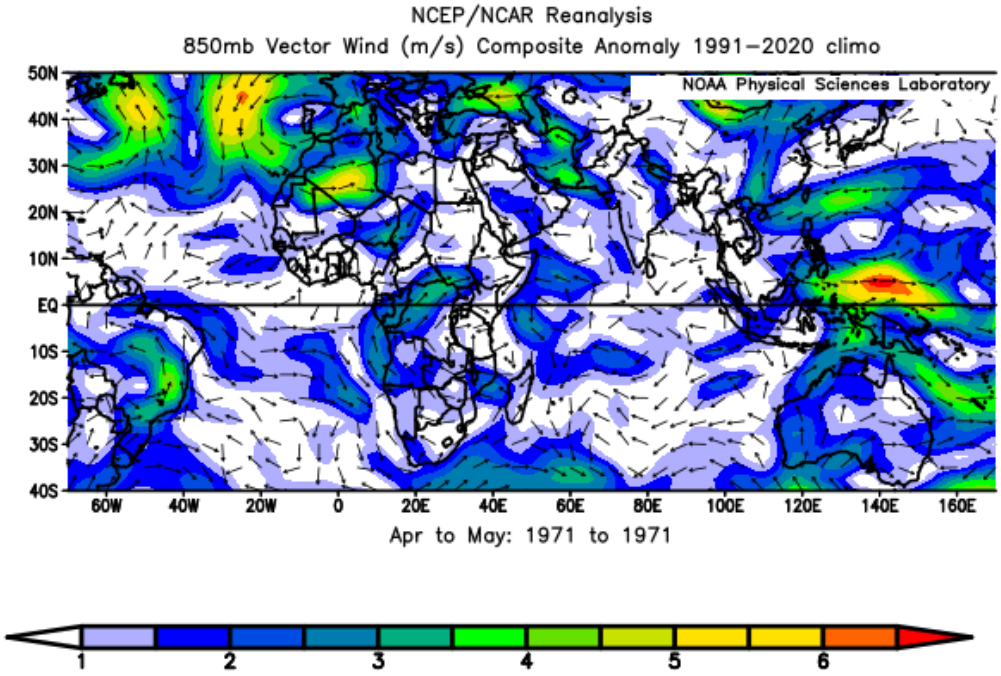

Figure 7. 850 hPa vector wind (meter/second) composite anomaly, Apr-May, 1971

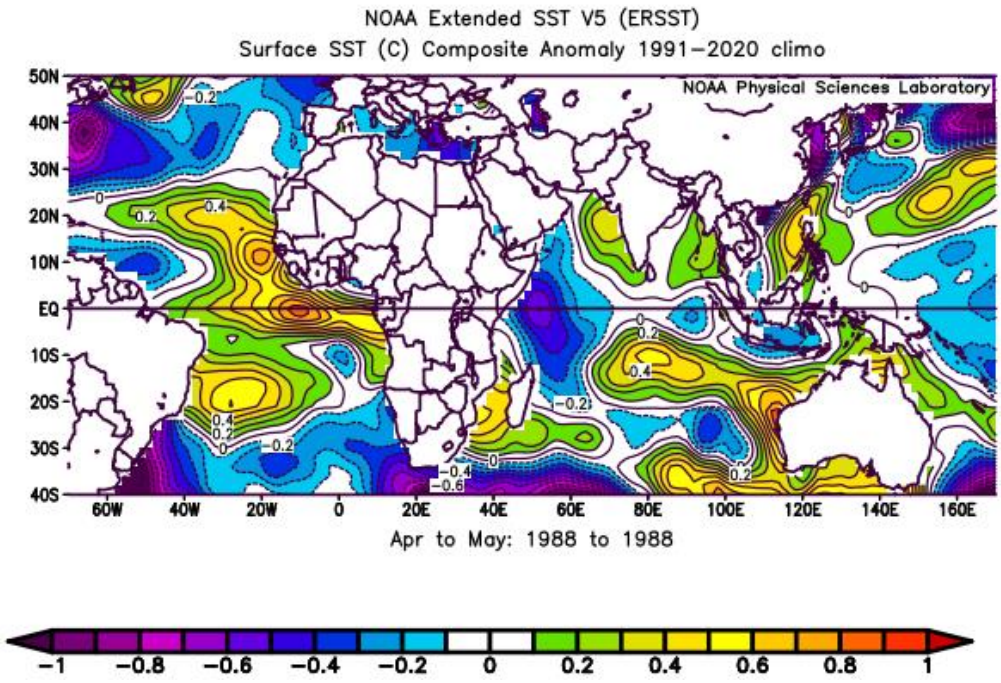

Figure 8. Sea Surface Temperature (Centigrade) composite Anomaly, Apr-May, 1988

In 1971 anti cyclonic flow had been observed south of 20ºN (-0.25) and cyclonic flow north of 20ºN (0.25). As such it did not affect Southern Hemisphere Zonal Westerlies Activity Index and 0 point is given in Figure 7. Sea Surface Temperature over North Atlantic Ocean for the period April-May has been considered up to 20ºN along the coast of North Africa (Table 2). Sea Surface Temperature was observed warm only during 1988 (Figure 8) between the 50 years period 1948-1997 and excess rainfall occurred over India in 1988. Sea Surface Temperature had been observed cold during 22 Years (normal/excess 13 years, below normal 4 years and deficient 5 years) cold and neutral 10 years (normal/excess 8 years and deficient 2 years), warm and neutral 8 years (normal/excess 6 years, below normal 1 year and deficient 1 year), cold and warm 4 years (normal/excess 3 years and deficient 1 year), cold, warm and neutral 4 years (normal/excess 3 years and deficient 1 year) and neutral for 1 year (normal). Sea Surface Temperature for April-May did not suggest any significant impact on normal/deficient rainfall trend over India. As a result Sea Surface Temperature for April-May has not been included in the modified Long Range Forecast under Southern Hemisphere Zonal Westerlies Activity Index.

Data for a period of 50 years (1948-1997) have been used to find the correlation coefficient between All India Monsoon Rainfall (forecast value, Table 2, column 4) and modified Southern Hemisphere Zonal Westerlies Activity Index value (column 3). The correlation coefficient has been found as 0.994, which is highly significant. As such cyclonic/anti cyclonic flow over North Atlantic Ocean below 25ºN/20ºN has been included as a new parameter in the modified Long Range Forecast. In Table 2, data from 1982-1997 have been given for reference**.**

During 27 years period from 1998 to 2024 Sea Surface Temperature had been observed warm for 7 years (normal/excess 6 years and below normal 1 year), cold and neutral 5 years (normal 2 years, below normal 2 years and deficient 1 year), warm and neutral 4 years (normal 3 years and below normal 1 year), cold 3 years (3 years deficient), neutral 3 years (normal/excess 3 years), cold, warm and neutral 3 years (normal, below normal and deficient one year each) and cold and warm 2 years (normal/excess both years) (Table 3). If Sea Surface Temperature is warm/neutral during April-May, it is positive sign for moisture feeding from North Atlantic Ocean during southwest monsoon season. Data from 2015-2024 have been given under Table 3 for reference. Synoptic situations over North Atlantic Ocean along North African coast and points for North Ocean Atlantic Index have been given under column 2. Modified Southern Hemisphere Zonal Westerlies Activity Index covers points given under column 3 for synoptic situations over South Indian Ocean, East Pacific, North Indian Seas and North Atlantic Ocean from 1982-1997 and 2015-2024 under Table 2 and Table 3 respectively.

Table 2. All India Monsoon Rainfall**,** Features in 850 hPa level vector wind, relative humidity, Sea Surface Temperature anomaly fields over North Atlantic Ocean along North Africa coast, Southern Hemisphere Zonal Westerly Activity Index (SHZWAI), forecast All India Monsoon Rainfall (AIMR) during Methodology Development period (1948-1997)

Year (AIMR as % of LPA)	Features in 850 hPa vector wind anomaly over North Atlantic Ocean (NAO) along north Africa coast during April- May up to 25ºN, (NAOI)	Modified SHZWAI : SHZWAI + NAOI	Qualitative and quantitative (as % of LPA) forecast of AMIR	Previous qualitative and quantitative (as % of LPA) forecast of AMIR	Type of forecast correction in AIMR	SST along the west coast of North Africa up to 20ºN
1	2	3	4	5	6	7
1982 (85.5)	ACF, South of 25ºN (-0.5), -Rh	0.5	D 92.6	94.8	PC	C and NL
1983 (113)	ACF, South of 20ºN (-0.25), Rh not matching	2.75	N 102.5	103.6	NC	N L
1984 (95.6)	ACF, South of 25ºN (-0.5), -Rh	2.5	N 101.4	103.6	PC	NL and W
1985 (92.9)	ACF, South of 25ºN (-0.5) -Rh	2	N 99.2	101.4	PC	C
1986 (87.2)	ACF bet 20ºN-10ºN (0.25) , -Rh	-1.25	MD 84.9	86	NC	C
1987 (81.6)	ACF S of 25ºN (-0.5), -Rh	-0.5	MD 88.2	90.4	PC	NL and W
1988 (119.3)	ACF South of 20ºN, (-0.25), -Rh	2.75	N 102.5	103.6	NC	W
1989 (100.9)	ACF bet 25ºN-10ºN, (-0.25), -Rh	1.75	N 98.1	99.2	NC	C
1990 (106.2)	ACF bet 20ºN-10ºN (-0.25), -Rh, CF bet 20ºN-30ºN (0.25), +Rh	2.0	N 99.2	99.2	No change	C
1991 (90.7)	ACF bet 20ºN-10ºN (-0.25), -RH	0.25	D 91.5	92.6	PC	C
1992 (92.3)	ACF bet 20ºN-10ºN (-0.25), -Rh	1.25	BN 95.9	97	PC	C
1993 (99.1)	ACF bet 20ºN -10ºN (-0.25), -Rh	1.75	N 98.1	99.2	NC	NL, W and C
1994 (112.5)	ACF South of 20ºN (-0.25), -Rh	2.25	N 100.3	101.4	NC	NL and C
1995 (98.1)	ACF South of 15ºN (-0.25), -Rh	2.75	N 102.5	103.6	PC	W and NL
1996 (103.4)	ACF South of 20ºN (-0.25) –Rh	3.25	ACTN 104.7	105.8	PC	W and NL
1997 (102.2)	CF South of 15ºN (0.25), +RH	2.25	N 100.3	99.2	PC 78%	C and W

Legend: CF: Cyclonic flow, ACF: Anti cyclonic flow, bet: between, Tr: Trough, ACTN: Active Normal, RH: Relative humidity, cont: Continuous, NOA: North Atlantic Ocean, NOAI: North Atlantic Ocean Index, LPA: Long Period Average, AIMR: All India Monsoon Rainfall, SHZWAI: Southern Hemisphere Zonal Westerlies Activity Index, 'Above Normal (AN)': 104% (110-98%), 'Active Normal (ACTN)': 101% (107-95%), 'Normal (N)': 97% (103-91%), 'Below Normal (BN)': 92% (98-86%), 'Deficient (D)' 88% (94-82%) and 'Markedly Deficient (MD)': 84% (90-78%), PC: Positive change, NC: Negative change, C: Cold, NL: Neutral, W: Warm.

Contribution of North Atlantic Ocean to Indian Summer Monsoon rainfall

During April-May anti cyclonic flow has been observed on 45 occasions, cyclonic flow on 13 and anti cyclonic and cyclonic flow both on 19 occasions during 1948-2024. Using cyclonic and anti cyclonic flow in the modified long range forecast, negative change has been made in 13 cases (26%) of quantitative forecast during 50 years. During 27 years of verification period from 1998-2024, negative change has been made in only one case of quantitative forecast. Contribution from Atlantic Ocean to Indian Summer Monsoon Rainfall is visible in terms of vector winds/relative humidity at 850 hPa geo potential height from June to September. During the monsoon season of 1958, relative humidity is very much marked at 850 hPa level (Figure 9).

Moisture feeding from Atlantic Ocean to Indian Seas is clearly visible in the anomaly of relative humidity at 850 hPa level during 1958 south west monsoon season. It is also visible in the anomaly of 850 hPa vector wind for monsoon season 1958 (Figure 10).

Table 3. Same as Table 2, but for the methodology verification period (1998-2024)

Year (AIMR as % of LPA)	Features in 850 hPa vector wind anomaly over NAO along north Africa coast during April-May up to 25ºN, (NAOI)	Modified SHZWAI: SHZWAI + NAOI	Qualitative and quantitative (as % of LPA) forecast of AMIR	Previous qualitative and quantitative (as % of LPA) forecast of AMIR	Type of forecast correction in AIMR	SST along the west coast of North Africa up to 20ºN
1	2	3	4	5	6	7
2015 (86.0)	ACF bet 5ºN- 25ºN (-0.5), -Rh	-0.5	MD 88.2	90.4	PC	W, NL and C
2016 (97)	CF bet 15ºN-10ºN (0.25) and North of 20ºN, +Rh	2.25	N 100.3	99.2	NC	NL and C
2017 (95)	CF north of 20ºN (0.25), +Rh, ACF bet 15ºN-10ºN (-0.25), (-Rh), (0)	2.0	N 99.2	99.2	No change	W
2018 (91)	CF bet 20ºN-10ºN (0.25), +Rh, ACF South of 10ºN (-0.25), 0 Rh, (0)	1.5	BN 97	97	No change	NL and C
2019 (110)	CF bet 10ºN-25ºN and prominent cross equatorial flow (CEF) South of 10ºN (0.5), +Rh South of 25ºN	4.5	E 110.4	!08	PC	W and C
2020 (109)	CF bet 10ºN and 20ºN and prominent CEF South of 10ºN (0.5), +Rh North of 5ºN	3.5	ACTN 105.8	103.6	PC	W
2021 (99)	CF bet 10ºN-15ºN and ACF South of 5ºN (0), (-Rh)	2.5	N 101.4	101.4	No change	NL
2022 (106)	CF bet 5ºN-15ºN (0.25), +Rh bet 5ºN-20ºN	2.25	N 100.3	99.2	PC	NL
2023 (95)	CF bet 20ºN-25ºN (0.25) +Rh, ACF South of 15ºN (-0.25), (0), -Rh,	2.0	N 99.2	99.2	No change	W
2024 (108)	ACF bet 5ºN-10ºN (-0.25) – Rh CF bet 15ºN-20ºN (0.25), +Rh, (0)	3.0	ACTN 103.6	103.6	No change	W

Legend: CF: Cyclonic flow, ACF: Anti cyclonic flow, CEF: Cross equatorial flow, bet: between, Tr: Trough, ACTN : Active Normal, RH: Relative humidity, cont: Continuous, NOA: North Atlantic Ocean, NOAI: North Atlantic Ocean Index, LPA: Long Period Average, AIMR: All India Monsoon Rainfall, SHZWAI: Southern Hemisphere Zonal Westerlies Activity Index, 'Excess (E) > 110% of normal', 'Above Normal (AN)': 104% (110-98%), 'Active Normal (ACTN)': 101% (107-95%), 'Normal (N)': 97% (103-91%), 'Below Normal (BN)': 92% (98-86%), 'Deficient (D)' 88% (94-82%) and 'Markedly Deficient (MD)': 84% (90-78%), NC: Negative change, PC: Positive change, C: Cold, NL: Neutral, W: Warm.

Cyclonic flow is seen from 30ºN-10ºN along the west coast of North Africa and westerly component of wind is seen from 20ºW along 10ºN up to West coast of India in the anomaly of vector wind from June to September 1958. Above normal, 109.8%, rainfall occurred over India during the south west monsoon season of 1958. Moisture feeding from Atlantic Ocean to Indian Seas has been clearly visible also during 1961 and 2022 monsoon seasons. It is also seen during individual months of Jun-Jul-Aug-Sep. In June 2002, cross equatorial flow is prominent up to 10ºN and east of 25ºW; westerly component of wind is seen along 10ºN reaching Arabian Sea through Somalia coast. Although 2002 was a deficient monsoon year (79.8%) but June rainfall was observed as 109.4%. Position could have been worse, if June rainfall had been observed as deficient. In July 2005 cross equatorial flow is seen prominent up to 5ºN and east of 20ºW. Westerly component of vector wind is seen along 10ºN from 20ºW, crossing Somalia coast and reaching up to 20ºN along the west coast of India. 114.7% of rainfall was recorded over India during the month of July 2005. So, moisture feeding from North Atlantic Ocean also helped in occurrence of +14.7% above normal rainfall over India during the month of July 2005.

The seasonal rainfall during 2012 from June-September over the country as a whole was observed as 93% of its Long Period Average. In June rainfall was recorded as 72% of its Long Period Average, in July 87% of its Long Period Average, in August 101% of its Long Period Average, and in September 112% of its Long Period Average. In Sept 2012, westerly wind component is seen from east of 60ºW south of 15ºN reaching Arabian Sea along 10ºN (Figure 11).

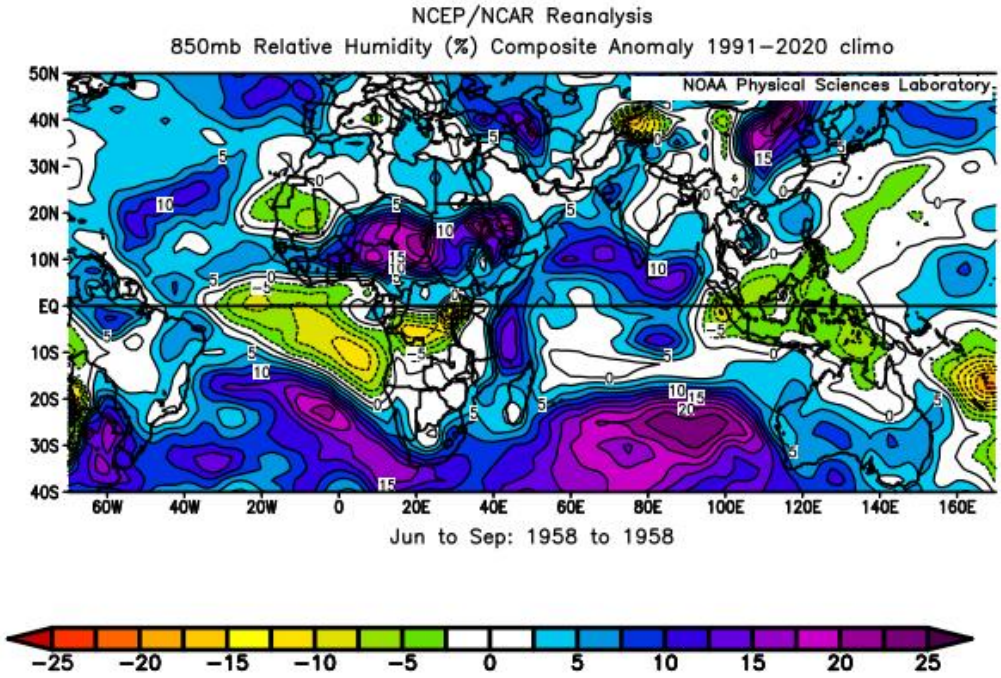

Figure 9. 850 hPa relative humidity (%) composite anomaly, Jun-Sep, 1958

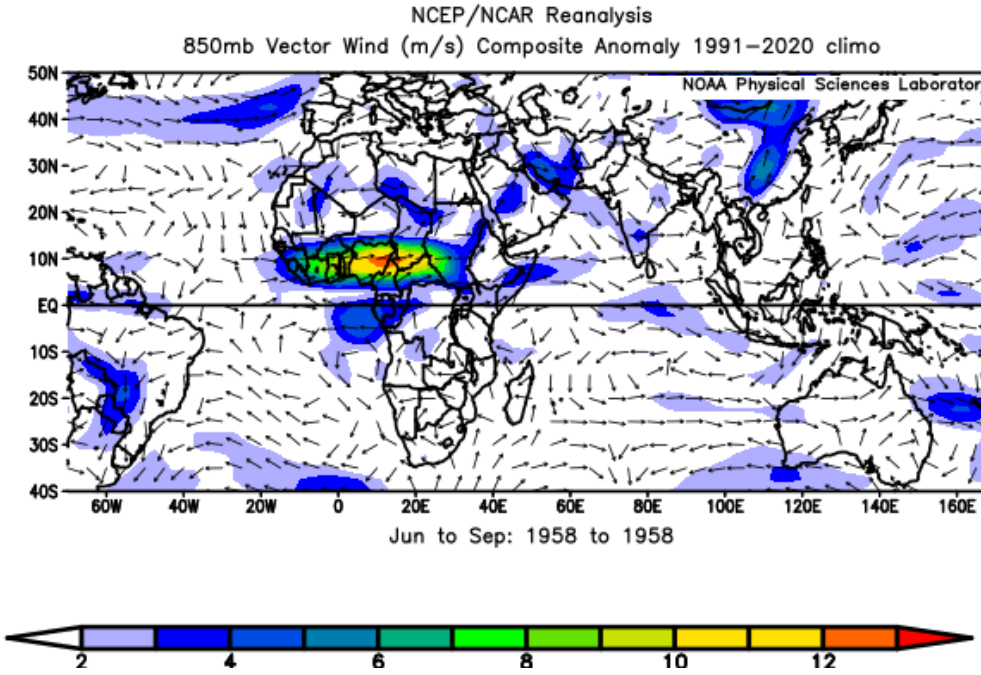

Figure 10. 850 hPa vector wind (meter/second) composite anomaly, Jun-Sep, 1958

Rainfall over the country as a whole during the 2024 southwest monsoon season (June-September) was 108% of its Long Period Average. Monthly rainfall over the country as whole was observed as 89% of Long Period Average in June, 109% of Long Period Average in July, 115% in August, and 112% of Long Period Average in September (IMD, 2024). By the end of May 2024, EL-Nino conditions turned into El Nino-Southern Oscillation neutral conditions and continued to be El Nino-Southern Oscillation neutral till October 2024. In February 2024, the Indian Ocean Dipole conditions weakened from positive to neutral and continued neutral conditions till October 2024 (ESSO, 2024). Even with El Nino-Southern Oscillation (ENSO) and Indian Ocean Dipole neutral conditions, All India Monsoon Rainfall was

observed as above normal during southwest monsoon season. In the month of July 2024, south westerly to westerly winds are seen from east of 60ºW/10ºN to the west coast of North Africa reaching Arabian Sea through along 15ºN and crossing west coast of India and reaching Bay of Bengal along 15ºN (Figure 12).

In the month of August 2024 South westerly to westerly winds are seen from east of 60ºW/10ºN to the west coast of North Africa reaching Arabian Sea along 15ºN and reaching west coast of India along 20ºN. Continuous relative humidity is seen from west coast of North Africa from 10ºN to west coast of India along 20ºN (Figure 13). So, for the month of July and August 2024, moisture feeding from North Atlantic Ocean is seen through vector wind anomaly/relative humidity anomaly at 850 hPa geo-potential height.

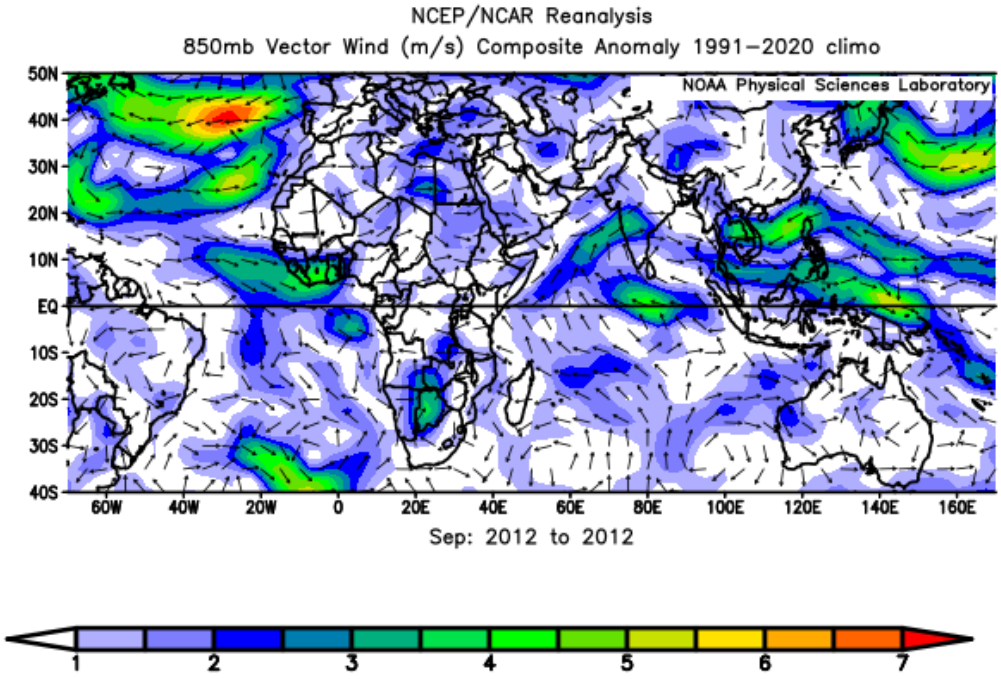

Figure 11. 850 hPa vector wind (meter/second) composite anomaly Sep, 2012

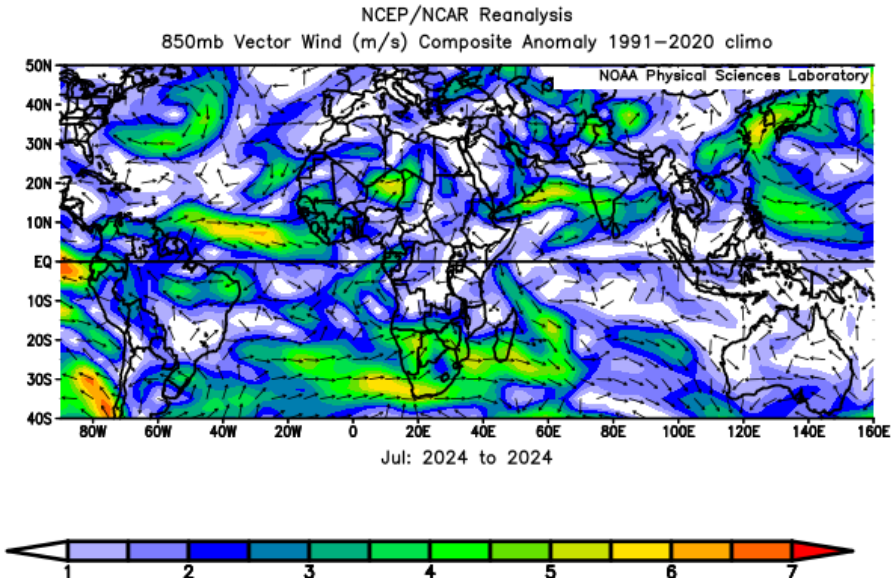

Figure 12. 850 vector wind (meter/second) composite anomaly, Jul 2024

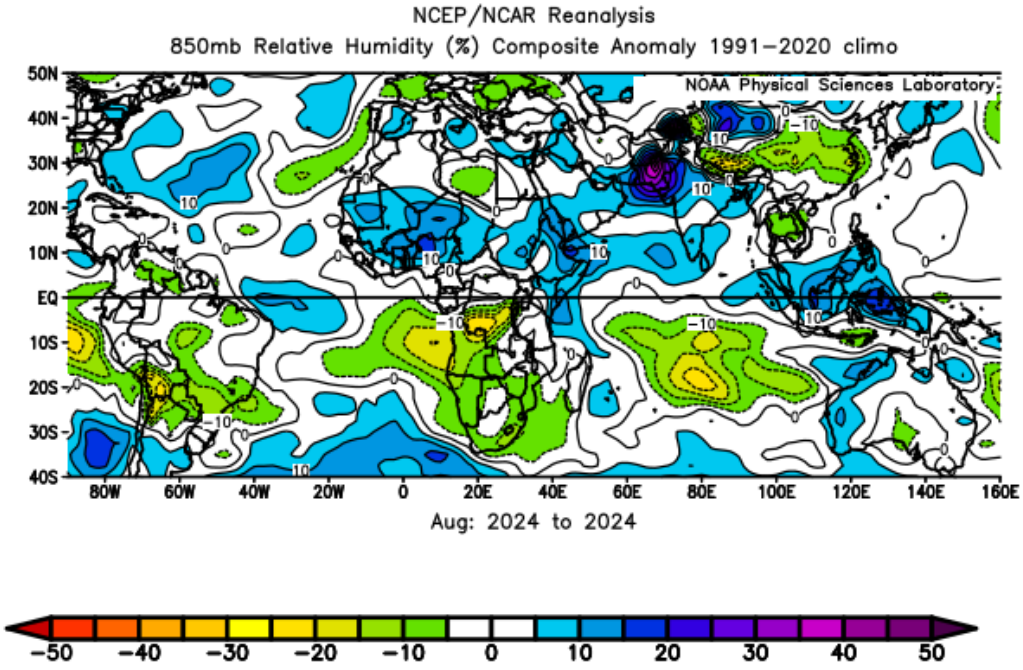

Figure 13. 850 hPa relative humidity (%) composite anomaly Aug 2024

Moisture feeding from North Atlantic Ocean to North Indian seas has been also observed during July 2025 (105%) and September 2025 (115.5%). All India Monsoon Rainfall was observed as 108%, above normal during monsoon season 2025, when El Nino-Southern Oscillation and Indian Ocean Dipole neutral conditions were present. Moisture feeding from North Atlantic Ocean is done during the monsoon season from June to September, depending upon the developed synoptic situation along the west coast of North Africa. During certain months and years, moisture feeding from North Atlantic Ocean may not be visible directly in terms of anomaly of vector winds and relative humidity at 850 hPa level. But its contribution continues during southwest monsoon season, if cyclonic circulation/trough/cyclonic flow is observed along the west coast of North Africa during southwest monsoon season.

CONCLUSIONS

(i) Cyclonic circulation/trough/cyclonic flow observed south of 25ºN of at least 5º latitudinal width along the west coast of North Africa in any months from June-September, helps India Summer Monsoon rainfall.

(ii) Cyclonic (south of 25ºN) and anti cyclonic flow (south of 20ºN) observed in the anomaly of 850 hPa vector wind along the west coast of North Africa for April-May, are useful parameters for calculating quantitative long range forecast.

(iii) Warm/neutral Sea Surface Temperature along the west coast of North Africa south of 20ºN in the anomaly for April-May, is a positive sign for moisture feeding to continue from the North Atlantic Ocean during southwest monsoon season.

(iv) During ENSO and Indian Ocean Dipole neutral conditions, normal rainfall over India is possible with moisture feeding from North Atlantic Ocean, as it happened in 2024 and 2025 monsoon seasons.

ACKNOWLEDGEMENTS

Authors are thankful to India Meteorological Department for the use of monthly/ seasonal rainfall data from 1948-2025 from their website**,** E – MAUSAM and NOAA Earth System Laboratory (U.S.A.) for using their website for the preparation of anomalies of vector wind and relative humidity at 850 hPa and Sea Surface Temperature data from 1948-2025. Authors express sincere thanks to the reviewers for their useful suggestions which significantly improved the manuscript. Authors are also thankful to Dr. Om Prakash Pandey, Chief Editor for his proper suggestions.

Author Credit Statement

Vinod Kumar prepared the manuscript with the help and discussion from M. Satya Kumar.

Data Availability

The data have been prepared from NOAA Earth System Laboratory and rainfall data have been used from IMD publication E-Mausam.

Compliance with Ethical Standards

The authors declare that they have got no conflict of interest and adhere to copyright norms.

References

Athira, K. S., Roxy, M. K., Dasgupta, P., Saranya, J. S., Singh, V. K. and Attada Raju, 2023. Regional and temporal variability of Indian summer monsoon rainfall in relation to El Nino southern oscillation. Scientific Reports, 13, 12643, nature portfolio, 1-13.

Davis, R. E., Hayden, B. P., Gay, D. A., Phillips, W. L. and Jones, G. V., 1997. The North Atlantic Subtropical Anticyclone. J. Climate, 10, 728-744.

ESSO, 2024. Earth System Science Organization (El Nino Southern Oscillation (ENSO) and Indian Ocean Dipole (IOD) Bulletin 1-4.

Goswami, B. N., Madhusoodanan, M. S., Neema, C. P. and Sengupta, D., 2006. A physical mechanism for North Atlantic SST influence on the Indian summer monsoon. Geophys. Res. Lett., 33, L02706, doi. 10: 1029/2005GL024803, 1-4.

IMD, 2024. India Meteorological Department, Salient Features of the 2024 Monsoon Season, 1-15

IMD, 2025. India Meteorological Department (, Subdivision-Wise Rainfall (MM)

Distribution, 1.

Kumar V. and Satya Kumar, M., 2021. Development and movement of waves in zonal westerlies of southern hemisphere and long range forecast of all India monsoon rainfall. J. Ind. Geophys. Union, 25, 66-78.

Li, S., Perlwitz, J., Quan, X. and Hoerling, M. P., 2008. Modelling the influence of North Atlantic multidecadal warmth on the Indian summer rainfall. Geophys. Res. Lett., 35, L05804, doi:10.1029/2007GL032901, 1-6.

Lu, R., Dong, B. and Ding, H., D., 2006. Impact of the Atlantic Multidecadal Oscillation on the Asian summer monsoon. Geophys. Res. Lett., 33, L24701, doi:10.1029/2006GL027655, 1-5.

NOAA, 2025, ENSO: Recent Evolution Current Status and Predictions, 1-32

Rajeevan, M. and Sridhar, L., 2008. Inter-annual relationship between Atlantic sea surface temperature anomalies and Indian summer monsoon. Geophys. Res. Lett., 35, L21704, doi: 10.1029/2008GL036025, 1-7.

Ratna, S. B., Sabeerali, C. T., Sharma, T., Pai, D. S. and Mahapatra, M., 2024. Combined influence of El Nino, IOD and MJO on the Indian Summer Monsoon Rainfall: Case Study for the years 1997 and 2015. Atmosph. Res., 299, 1-15.

Sahsamanoglou, H. S., 1990. A contribution to the study of action centres in the North Atlantic. Int. J. Climatol., 10, 247-261.

Saji, N. H., Goswami, B. N., Vinayachandran, P. N. and Yamagata, T., 1999. A diapole mode in the tropical Indian Ocean. Nature, 401, 360-362.

Yadav, R. K., Srinivas, G. and Chowdary, J. S., 2018. Atlantic Nino Modulation of the Indian summer monsoon through Asian jet. npj Climate Atmosph. Sci., 23, doi: 10. 1038/s41612-018-0029-5, 1-11.

Received on: 21-4-2025; Revised on: 13-1-2026; Accepted on: 15-1-2026

J. Ind. Geophys. Union, 30(3) (2026), 216-227
https://doi.org/10.71122/JIGU.30(3)2026.0022

A global review of cloud seeding techniques for rainfall enhancement

Sanhita Shende[1,2*], Sudarsan Bera[1] and Neelam Malap[1]
[1] CAIPEEX, Indian Institute of Tropical Meteorology, Ministry of Earth Sciences, Pashan, Pune 411008, India
[2]Department of Physics, Savitribai Phule Pune University, Pune, 411008, India
Corresponding Author: sanhitashende23@gmail.com

ABSTRACT

In a climate change scenario, water scarcity is a big problem for the sustainable development of the society. For this reason, searching for unconventional water resources are of utmost importance in water management. In this context, cloud seeding offers a potential option for alternative water resources, particularly in arid and drought-prone regions, such as the rain shadow zones of Western Ghat mountains in India. Cloud Seeding is a weather modification process (i.e., weather is changed or modified by the artificial mechanism), aimed to enhance precipitation by introducing artificial aerosol particles, which serve as ice nuclei or cloud condensation nuclei, into the naturally formed clouds. This report explores the existing cloud seeding techniques across the globe, inclusive of both glaciogenic and hygroscopic seeding methods. It highlights the specific approaches, target clouds, and cloud seeding experiments employed in different countries, including India, China, United States, UAE, Australia, Thailand, Canada, and others. Our study will be useful to the scientific community in planning of any future cloud seeding projects apart from social awareness related to cloud seeding approaches.

Key Words: Cloud seeding, Weather modification, Rain enhancement, Water resources, Cloud physics

INTRODUCTION

In the last few decades, many countries have been exploring cloud seeding technology to overcome the water security problem. However, the main concern is the efficacy of the cloud seeding, which is strongly dependent on the types of clouds formed over the region and the local weather conditions (Kulkarni et al., 2012). Several studies have shown the effective use of hygroscopic cloud seeding over the rain shadow regions (where natural rainfall is very limited) for the rain enhancement purpose (Gayatri et al., 2023; Prabhakaran et al., 2023). For the seeding application, the flares used are of hygroscopic nature that means the aerosol particles released from these flares can be easily activated to cloud droplets and may induce early rainfall by forming larger cloud drops at a lower height (Al Hosari et al., 2021).

Atmospheric aerosols are the tiny particles in solid and liquid phases suspended in the air and have a significant impact on weather, climate, ecology and human health (Kommalapati and Valsaraj, 2009). A fraction of atmospheric aerosols serves as a substrate upon which water vapour can condense to form cloud droplets under supersaturation (SS) conditions (RH >100%) of clouds. These aerosol particles which act as nuclei of water vapour condensation, are called Cloud Condensation Nuclei (CCN) (Mikhailov et al., 2017).

The size and chemical composition of the aerosol particles determine its wetting properties by water vapour; the more soluble a particle is, the lower the value of supersaturation required for it to serve as a CCN (Petters and Kreidenweis, 2008; Pöschl et al., 2009). The ability of an aerosol particle to attract and absorb water vapour from its surrounding environment is known as hygroscopicity. Generally, water soluble particles have higher hygroscopicity and are easier to activate as a droplet. For example, to serve as a CCN at a supersaturation of 1%, particles that are maximally wetted but water-insoluble must have a minimum radius of 0.1 μm, while a soluble particle may serve as CCN at this supersaturation even if their radius at the point of wetting is as low as 0.01 μm (10 times smaller). Most CCNs are a combination of both soluble and insoluble material, known as mixed nuclei (Hudson and Clarke, 1992; Dalirian et al., 2014). The number concentrations of CCN at various levels of supersaturation (0.1 – 1.2%), can be measured using a thermal diffusion chamber known as CCN Counter (Roberts and Nenes, 2005). Small water droplets form over the tiny particles (CCN) at various supersaturation levels in the clouds. Larger size aerosols can be easily activated to droplets, compared to smaller size aerosols with the same material composition. Larger size hygroscopic aerosols such as sea-salt (NaCl) particles with size > 1 μm, are referred to as Giant CCN (or GCCN) and they have high potential to be activated as droplets at a lower supersaturation.

In general, continental origin aerosols lack such giant cloud condensation nuclei (GCCN) due to high contribution from anthropogenic sources that produce mostly sub-micron particles. Continental aerosols, especially in urban city regions, have very high particle number concentration and impact clouds with high droplet number concentration and reduce droplet size, which lead to suppression of warm rain. Under such polluted conditions, where warm rain is suppressed by elevated CCN loading, the introduction of a small concentration of GCCN can modify the cloud microphysics by broadening the droplet size distribution and accelerating the coalescence growth, ultimately enhancing warm precipitation (Jung et al., 2015). This mechanism poses the possibility of weather modification (i.e., rain

enhancement) by introducing artificial CCN with larger size and higher hygroscopicity, such as NaCl, $CaCl_2$, etc.

CLOUD SEEDING

Cloud seeding refers to the method of releasing material known as seeding agents into clouds. These seeding agents act as efficient seed (or nuclei) of droplet or ice formation in the clouds. There are two types of seeding agents, CCN and Ice Nuclei (abbreviated as IN; act as nuclei for ice crystal formation in clod clouds with $T < 0^oC$), which can possibly enhance the amount of precipitation produced. CCN-based (hygroscopic) seeding aims to modify warm-cloud ($T > 0^oC$) processes by enhancing droplet growth in liquid phase, whereas INs are used primarily in cold clouds ($T < 0^oC$), where cloud water is in supercooled liquid phase (i.e., liquid phase of water in subfreezing temperature) or mixed-phase (ice-liquid coexisting). By initiating ice crystal formation of supercooled liquid water droplets, INs enhance the Bergeron-Findeisen process, whereby ice crystals grow at the expense of supercooled water droplets because the saturation vapour pressure over ice, is lower than over liquid water (Pruppacher et al., 1998). The growing ice particles may aggregate them self or rim supercooled drops, forming snowflakes or graupel that fall by the gravitational attraction and melt into raindrops at surface. Sometimes, these seeding agents may initiate precipitation formation in clouds, which are not precipitating by the natural process due to lack of sufficient larger drops that induce collision-coalescence growth of cloud droplets to reach precipitation size drops (in millimeter size). Figure 1 shows a schematic representation of cloud seeding methods. Nucleation is the initial stage in the formation of water droplets or ice crystals in a cloud. Cloud seeding is an aerosol-cloud interaction process that depends on atmospheric conditions such as available water vapour and temperature condition of the clouds. Water droplets are formed when water vapour within a cloud condenses onto tiny aerosol particles known as CCN. Natural aerosols that act as CCN or IN are mineral dust, carbonaceous particles (soot) and sulphate from industries and organics (secondary organic aerosol) from vehicular emission, pollen and biogenic aerosol emission by plants, and sea-salt particles from the ocean etc. However, during the cloud seeding process, artificial aerosols which are more hygroscopic or ice-like structure, are released into the clouds to enhance the growth of water droplets or ice crystals, respectively. These artificial aerosols are chosen with great care for the capability to initiate water condensation or ice crystal formation. The kind of aerosol used varies with the kind of cloud seeding method used. For example, silver iodide (AgI) is used in glaciogenic seeding, while sodium chloride (NaCl) or calcium chloride ($CaCl_2$) are used in hygroscopic seeding (Table 1). The general principle of cloud seeding involves introducing seeding particles into the clouds to alter the microphysical processes and promoting the precipitation formation (either warm or cold clouds).

Cloud seeding operations involve dispersing seeding agents into target clouds using aircraft, drone or artillery. Ground-based generators can also be used (at high altitude sites where clouds are formed close to the ground) to release seeding agents upwind of the target area, allowing the wind to carry the material into the target clouds. Identification of suitable clouds (i.e., 'target') for the seeding is done using Radar observations (on real-time basis). Once a target cloud is seeded, its microphysical changes can be observed using instrumented research aircraft and Radar (Prabhakaran et al., 2023; Konwar et al., 2024).

TYPES OF CLOUD SEEDING

(i) Hygroscopic cloud seeding

Hygroscopic cloud seeding is aimed at accelerating the collision-coalescence of droplets in liquid clouds, ultimately resulting in the formation of larger drops that induce precipitation. Cloud seeding substances are usually composed of larger salt particles (> 0.5 μm) that are dispersed by various modes into the cloud base (Laaksonen and Malilia, 2022). Sodium chloride (NaCl), potassium chloride (KCl), or calcium chloride ($CaCl_2$) is utilized as a seeding agent in warm ($T > 0°C$) cloud seeding, and such a process is referred to as hygroscopic cloud seeding. In this seeding, broadening (widening) of the droplet size spectrum is achieved during the nucleation process by seeding with larger size CCN of 0.5 μm to 3 μm dry diameter which leads condensation growth of larger droplets and thereafter collision-coalescence of droplets are enhanced to increase the efficiency of rain drop formation.

Table 1. Seeding types and corresponding seeding agents, cloud types and physical mechanisms.

Seeding type	Seeding material (agent)	Cloud type	Mechanism
Hygroscopic	NaCl, $CaCl_2$	Warm phase clouds (cloud region with $T > 0\ ^oC$)	Rain enhancement by faster droplet growth by achieving collision-coalescence process
Glaciogenic	AgI, dry Ice	Mixed phase cold clouds (cloud region with $-40^oC < T < 0\ °C$)	Rain enhancement by faster ice crystal growth using seeded IN particles

(ii) Glaciogenic cloud seeding

Convective clouds which grow deeper into the sub-freezing level height (-40°C < T < 0°C) may not be glaciated extensively if sufficient natural IN particles are not present and therefore, produce supercooled (in subfreezing temperature) liquid droplets (Rosenfeld and Woodley, 2000). Such clouds often evolve into mixed-phase clouds, in which supercooled liquid droplets and ice particles (which formed by fewer natural IN particles) coexist over a substantial vertical depth. In the temperature range between 0°C and approximately -40°C, liquid droplets can persist in a metastable state unless frozen by efficient ice nuclei particles (having ice like crystal structure). In glaciogenic seeding (Woodley et al., 2003), IN particles are introduced by seeding to initiate the ice crystal formation of these supercooled liquid drops present in cold cloud regions and precipitation formation occurs by larger ice crystal growth. In deep convective clouds where temperature is subfreezing, the seeding agent commonly employed is silver iodide (AgI) to initiate the ice formation. The crystal structure of AgI, closely resembles that of ice structure, which allows water molecules to readily orient themselves into an ice-like structure on the surface of AgI. When AgI particles come in direct contact of supercooled droplets, it freezes the droplet to form an ice crystal by contact freezing process. These ice crystals once formed are grown further by more water vapour deposition on it and by colliding with other ice crystals or water droplets while falling downward. They also fall down through the warmer cloud regions (T > 0°C) and melt to liquid phase and become raindrops when they reach ground. Glaciogenic cloud seeding is usually applied to summer convective clouds for rain enhancement and hail suppression, and winter orographic clouds for snow fall enhancement.

The effectiveness of AgI as ice nucleating particles, was first shown by Vincent Schaefer in 1946 and Berndt Vonnegut in 1947 respectively (Laaksonen and Malilia, 2022). The crystal structure of AgI is extremely similar to that of hexagonal ice, a concept first put forward as the underlying mechanism of its successful ice nucleation. Dry ice is also used as seeding agent for glaciogenic seeding; however, it is mainly used to generate strong cooling of air pockets through which it passes and thereby initiate the ice nucleation by homogeneous ice nucleation process which occurs at temperature below -40°C. There are different cloud seeding techniques used in various countries depending on various factors like regional climate, geography, and technological advancements. Countries in tropical regions like India, UAE and Thailand, use hygroscopic seeding agents like NaCl or $CaCl_2$, while countries in high latitude regions such as China, USA, Canada, use glaciogenic seeding agents like AgI, dry Ice.

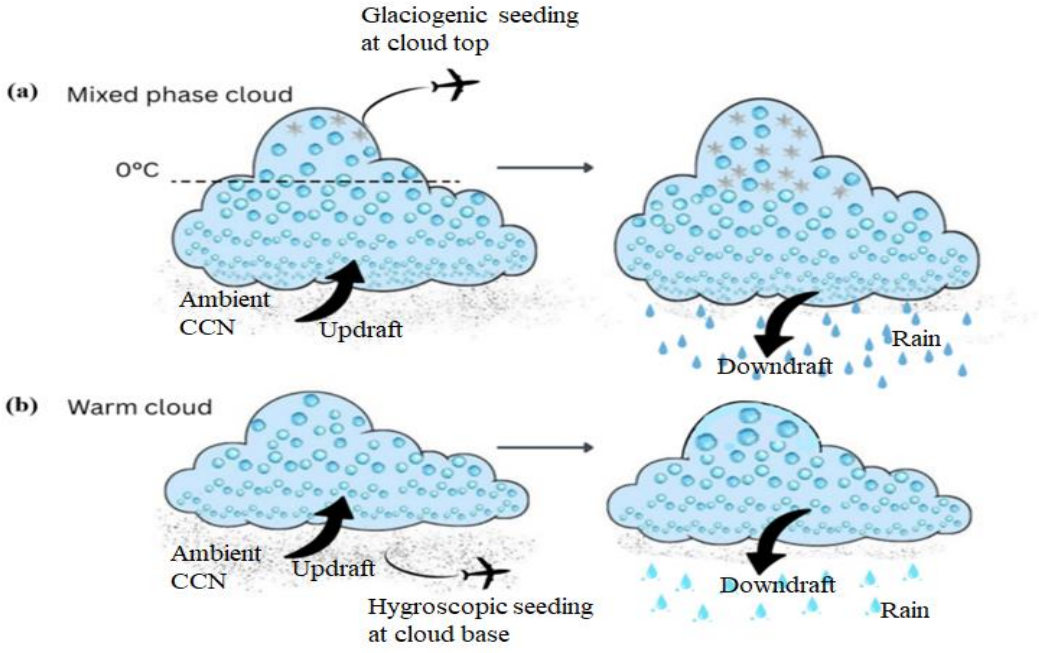

Figure1. Schematic diagram showing **(a)** glaciogenic cloud seeding and **(b)** hygroscopic cloud seeding. The left figure shows the cloud processes during seeding and the right figure indicates cloud processes after seeding. There are aerosol particles (CCN) at the base of the both the clouds, where grey dots represent natural aerosols particles, and black dots represent seeded particles (hygroscopic) by the aircraft. Glaciogenic seeding is done at cloud-top in a mixed-phase cloud, where supercooled liquid water drops exist and AgI seeding particles freeze those liquid drops. In the fig. stars represent the ice-crystals and circles represent the liquid droplets.

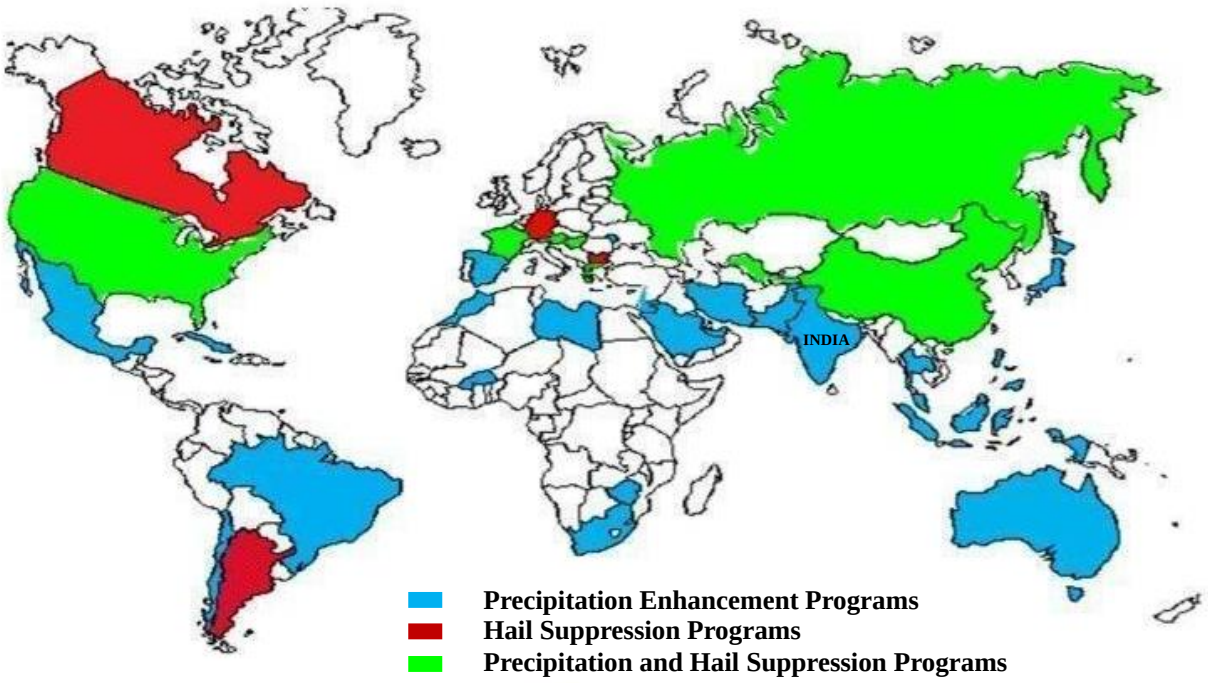

Figure 2. World map showing different countries conducting cloud seeding programs (adopted from Mandous et al., 2006). This map is used for a representative purpose and may not be the actual political map of the world.

CLOUD SEEDING TECHNIQUES: GLOBAL SCENARIO

Cloud seeding technique depends on the local climate and cloud types. Therefore, it varies in different countries. Figure 2 depicts the cloud seeding programs conducted worldwide. The Weather Modification Center at Hebei Province, China, conducted warm cloud seeding experiments on the peripheral cloud system of Typhoon "In-Fa" in the central and south areas of Hebei Province on July 29, 2021 (Yang et al., 2023). Hygroscopic seeding agents such as calcium chloride and potassium chloride were applied in the experiment. The observation indicated that the concentration of large drops (> 50 μm) in the warm clouds of the peripheral cloud system of Typhoon "In-Fa" was enhanced at the expense of smaller droplets due to rapid collision-coalescence. Several strong precipitation centers appeared in the downwind region after the cloud seeding, which indicated the presence of an enhanced coalescence process in the warm clouds (Yang et al., 2023).

Various operational teams in Jiangxi Province examined 71 cloud seeding operations conducted between 2008 and 2014, and statistical analysis suggested precipitation increases of about 20% in some downwind regions following seeding operations (Wang et al., 2019a). Another cloud seeding experiment was conducted over Zhejiang, China during a major international event (on 4th September 2016) held in Hangzhou. The attempt was to reduce the likelihood of rainfall onset by seeding excess concentration of hygroscopic particles in warm clouds to reduce cloud droplet size (Wang et al., 2019b). On the other side, a research team provided the design and implementation of charged particle-based cloud seeding, which is more ecofriendly and cost-effective compared to traditional methods (Wei et al., 2020). The first cloud seeding experiment conducted using negative ions over the northwestern region of China, produced quantitative evaluation results that confirmed the success of the trial in realizing its objective of increasing rainfall in the target area by 20% (Wei et al., 2021).

Similarly, the National Center of Meteorology and Seismology (NCMS, UAE) launched its operational cloud seeding program in 2003, yielding a 23% increase in precipitation annually in seeded areas utilizing radar and rain gauge measurements for assessing the seeding impact (Al Hosari et al., 2021). Long-term studies have compared rainfall data from seeded and non-seeded clouds and have shown significant improvements in storm behavior after seeding agents were released (Al Hosari et al., 2021). A recent study evaluated the impact of cloud seeding on rainfall intensities in Sharjah, UAE and the study found increased

rainfall from 2010 onwards (Almheiri et al., 2021). The UAE Research Program for Rain Enhancement Science, launched by the Ministry of Presidential Affairs, aims to advance scientific research in this field (Al Mazroui and Farrah, 2017). These studies have shown promising results, with a 23% increase in annual surface rainfall over seeded areas and significant enhancements in storm properties, following the conventional practice of inducing hygroscopic flares of natural salt composition (mainly potassium chloride) at the bottom of convective clouds near the updraft core (Al Hosari et al., 2021). Optimizing Cloud Seeding by Advanced Remote Sensing and Land Cover Modification (OCAL) experiment was conducted by the researchers from UAE during 2017-2018. This project focused on optimizing cloud seeding techniques using remote sensing and data collected from advanced Doppler radar systems (Branch et al., 2020).

In fact, cloud seeding has become an increasingly significant part of drought management routines in recent years, as evidenced by the cost-sharing arrangement that has been introduced in the Colorado River Basin, USA which was considered a regional solution to water shortages. This program targeted mountain regions at elevation above 9,000 feet to augment snowpack, resulting in an estimated 10-15% increase in snow water content, translating to significant increases in spring runoff (Griffith et al., 2011). Likewise, a prolonged winter cloud seeding operation in Utah, USA, revealed an average increase of 14.6% in precipitation (Griffith et al., 1997). A 12-year longitudinal study in Peru estimated increases in rainfall between 8% - 15%; the statistical significance was uncertain due to poor experimental design (Howell, 1965). Rainfall Enhancement Projects was also conducted by Texas Weather Modification Association over Texas, USA since 1996, with significant activities noted in 2016. This initiative includes multiple projects across Texas, utilizing both glaciogenic and hygroscopic materials, achieving an average surface precipitation increase of 1.34 inches during the 2016 season (LaRoche et al., 2017).

Apart from these, the Queensland Cloud Seeding Research Program (QCSRP) was conducted by the Queensland Government near Brisbane (southeast Queensland region in Australia) during 2008-2009 wet seasons, with a purpose to enhance rainfall in southeast Queensland due to water shortages. To understand rain enhancement, they included randomized cloud seeding strategy and multi-parameter radar measurements to understand precipitation formation. Initial analyses suggested potential increases in rainfall through hygroscopic seeding, although results were constrained by sample size (Tessendorf et al., 2012). Snowy Precipitation Enhancement Research Project (SPERP) too was undertaken during May 2005 to June 2009 by Snowy Hydro Ltd., to enhance snowfall in the Snowy Mountains during winter cold fronts utilizing glaciogenic static seeding with silver-chloroiodide and a randomized experimental design across 107 experimental units. The Project validated wedding conceptual models through dual-trace chemistry analysis of snowfall (Manton and Warren, 2011). A statistical analysis of 1960-2005 cloud seeding in central Tasmania's hydroelectric catchment area showed increased monthly rainfall during seeding periods. Using a double ratio of target to control rainfall, ten tests revealed a 5-14% increase, with high confidence level. While statistically significant, further cloud microphysics measurements are recommended to confirm the physical basis of the observed rainfall increase (Morrison et al., 2009).

Thailand's Royal Rainmaking Project, initiated by King Bhumibol Adulyadej in the late 1950s in response to drought in the lsan region, began its first artificial rain experiment in 1969. The technique involved dispersing dry ice into clouds to stimulate ice formation and rainfall. In 2018, the project was deployed over Bangkok to combat severe haze caused by ultra-fine dust, using cloud seeding to generate artificial rain and improve air quality. From 1995 to 1998, the Bureau of Royal Rainmaking and Agricultural Aviation (BRRAA), conducted a randomized warm-rain enhancement experiment in northwestern Thailand's Bhumibol catchment area, utilizing a floating single-target design to evaluate the impact of calcium chloride seeding on warm convective clouds. Semi-isolated clouds were randomly assigned to seeded or unseeded groups, with calcium chloride dispersed into cloud updraft regions at a rate of 21 kg km^{-1} per seeding pass of warm convective clouds. The project involved data collection using Doppler radar cloud tracking and, from 1997 onwards, detailed cloud physics measurements via King Air 350 aircraft. Statistical analysis of randomization seeding demonstrated a statistically significant increase in rainfall from seeded clouds, supported by physical measurements (Silverman and Sukarnjanaset, 2000). Besides, randomized cold-cloud seeding demonstration experiments were also carried out during 1991-1998 in the Bhumibol catchment area in Northwestern Thailand. Using the S-band radar, the proportional effects of seeding on Cell Rain Volume was approx. 35%. However, these results did not reach statistical significance (Woodley et al., 2003).

Besides the above examples, some other global experiments include seeding trials over Taiwan, where they have been conducting an ongoing cloud seeding program for more than two decades, primarily for rain enhancement to support

hydroelectric power generation, agriculture, and alleviation of droughts (news reports). They have employed both ground-based silver iodide generators and aerial dispersal techniques (hygroscopic flares) using aircraft. Although some reports indicated possible increases in precipitation, their project is still ongoing and waiting for a conclusion. Recently, severe droughts have increased public demand for the cloud seeding to alleviate water deficiencies. Technologically, Taiwan employs conventional techniques such as silver iodide seeding, and hygroscopic salt seeding, and they are investigating cloud physics and seeding agent improvements to enhance the efficiency.

Weather Modification Inc. (WMI), a cloud seeding agency in Fargo, North Dakota too has conducted a five-year seeding operation (starting from 1996) funded by the Alberta Severe Weather Management Society of Calgary, Alberta. The Alberta Hail Suppression Project in 1996 was operational from June to September. The primary objective of such operations is to limit the destruction caused by hailstorms to crops and urban property, particularly in Calgary and Red Deer. This is done using a C-band weather radar and three dedicated cloud seeding aircrafts, providing continuous coverage. Silver Iodide (AgI) was ejected into clouds by three sources either droppable flares, end-burning flares, or AgI acetone burners (Krauss and Renick, 2021). Silver Iodide flares produced significant ice nuclei, enabling the growth of small and numerous hailstones, which are more likely to melt before hitting the ground, thus limiting the loss to crops and properties. Summer Cumulus Cloud Seeding Experiment was conducted by a research team during 1975-1978, near Yellowknife and Thunder Bay, to assess the microphysical changes in cumulus clouds by seeding. Higher concentrations of ice particles were observed in about 50% of seeded clouds, with approximately 40% producing rain (Isaac et al., 1982).

In Spain, a Precipitation Enhancement Project (PEP) was conducted during 1979-1981 in the upper Duero River Basin of Spain in which the estimated precipitation increase over a 100-km radius of the project area was found to be 10% and 23% on seeding days using two distinct statistical models for precipitation estimation. Overall, a seasonal mean (February–May) increase of 0.75% and 1.8% were reported (Vali et al., 1988). They also concluded that the major contributions to these increases come from cumulus, cumulus-congestus and shallow stratiform clouds.

A seeding trial was also conducted in growing cumulus-congestus clouds over the Asir region of south-west Saudi Arabia (Krauss et al., 2010). They found that clouds seeded with silver-iodide (AgI) flares prior to radar detection showed the most substantial increases in precipitation, with maximum radar reflectivity exceeding 50 dBZ and maximum precipitation flux surpassing 100 m^3/s. In their study, they considered 28 seeded clouds (without any radar echo prior to seeding) versus 43 natural clouds. A consistent positive association was observed between the seeding and maximum radar reflectivity.

Similarly, a long-term cloud seeding program was undertaken in northern Israel spanning for 38 years, which was recently re-evaluated. Initial seeding experiments in the 1960s and 70s suggested significant rainfall increases from cloud seeding. However, later observational studies questioned these findings, possibly due to changing climate conditions. A new, carefully designed randomized experiment (Israel 4, 2013-2020) was conducted, uniquely using forecast rainfall as a control. The results showed a disappointing and statistically insignificant (1.8%) rainfall increase. Consequently, the Israel Water Authority has stopped the operation of cloud seeding in that region. This outcome contrasts sharply with the positive results reported from earlier experiments in the 19th century (Benjamini et al., 2023).

Numerical simulations

Other than the operational or experimental seeding trials, numerical simulations have also become an essential tool for evaluating the effectiveness of cloud seeding and understanding the associated microphysical processes that influenced precipitation. Studies conducted in the Wyoming and Colorado regions of the United States used ensemble simulations with the WRF model to evaluate snow fall enhancement from glaciogenic seeding in winter orographic clouds (Harrold et al., 2026). In another investigation focusing on the North Platte and Little Snake River basins in the United States, atmospheric and hydrological modeling used coupled WRF-WxMod and WRF-Hydro frameworks to quantify the hydrologic impacts of seeding on snowpack and runoff (Dougherty et al., 2026). Numerical simulations of a convective rainfall event in Beijing, China, using the WRF model demonstrated that the seeding effectiveness strongly depends on atmospheric dynamics such as updraft strength, cloud lifetime, and seeding altitude (Hua et al., 2024). Similarly, an ensemble modeling framework using multiple microphysics parameterizations was applied to estimate precipitation enhancement potential in China, highlighting the uncertainty associated with different cloud microphysics schemes (Zhu et al., 2025). Modeling studies conducted in the Yeongdong region of South Korea evaluated airborne seeding experiments through ensemble WRF simulations

combined with observational data, showing measurable changes in precipitation and cloud microphysical properties (Chae et al., 2025). Further numerical investigation of glaciogenic seeding effects on cloud structure and microphysical processes using the WRF model, demonstrated significant increases in ice crystal concentration and enhanced precipitation formation in South Korea (Liu et al., 2025). In addition, aircraft observations and radar measurements were combined with numerical analysis to evaluate microphysical responses to seeding in winter orographic clouds during experiments conducted in the United States, confirming enhanced ice particle production following seeding operations (Xie et al., 2025). These studies collectively demonstrate that the numerical modeling frameworks, particularly those based on mesoscale atmospheric models, provide an effective approach for evaluating cloud seeding efficiency and improving the understanding of precipitation enhancement mechanisms.

INDIAN SCENARIO

India is the home of billions of peoples, and its economy is strongly driven by agricultural productivity. Therefore, the water demand is escalating year after year. Spatial distribution of rainfall over different regions of India during different seasons is shown in Figure 3. This indicates that several regions, especially the rain shadow region of Western-Ghats, lack adequate rainfall required for agriculture activity. From this figure, we can see that the South-West region of India i.e., central Maharashtra and Karnataka states received less rainfall. These states are drought prone, and experience water scarcity. Comparatively, coastal areas receive high rainfall. The North-West region's rainfall is comparatively less over Rajasthan due to desert area.

To provide a solution for agricultural water demand, several state governments in India are demanding rain enhancement by cloud seeding techniques. With its diverse climate and varying rainfall patterns, the Indian government has explored cloud seeding as a potential tool for weather modification, particularly in drought-prone regions like the rain shadow region of Western Ghats Mountains. While effectiveness of seeding varies significantly based on local climate conditions, India's cloud seeding experiments primarily focus on hygroscopic seeding of convective clouds during the monsoon season (June-September). As per Murty et al. (1998), cloud seeding experiment was conducted over inland regions (~100 km from the west coast of India) during monsoon season across multiple years (1973-74, 1976, and 1979-86). Using area randomization, two target regions of 1600 km^2 each, separated by a buffer zone, were seeded with hygroscopic salt particles. Stratocumulus and cumulus clouds were seeded by dispersing 30 kg of salt along a 3 km long flight track at 200-300m above cloud base height. These results showed that he rainfall enhancement strongly depended on cloud thickness and liquid water content, with favorable conditions yielding up to 24% increase in rainfall at the 4% significance level, attributed to accelerated collision-coalescence processes. Since 2003, several Indian states - including Gujarat, Maharashtra, Karnataka, Tamil Nadu and Andhra Pradesh, have attempted operational cloud seeding programs.

Similarly, The Indian Institute of Tropical Meteorology (IITM) at Pune, has conducted extensive research on cloud properties and seeding potential, including the Cloud Aerosol Interactions and Precipitation Enhancement Experiment (CAIPEEX, 2009-2019) project, which demonstrated promising results with hygroscopic seeding, showing rainfall enhancement in specific locations like Solapur district in Maharashtra state. Researchers at IITM Pune have reported that the CAIPEEX experiment, resulted in rainfall enhancement up to 46±13% at certain locations (rain gauge stations) and on average of 18±2.6% over a 100 sq.km area over the rain shadow region near Solapur. Over the two years (2018-2019), scientists at IITM Pune evaluated 276 seeding samples to test the effectiveness of hygroscopic cloud seeding in the monsoon season. A C-band radar located at Solapur is used to monitor the cloud and rainfall properties. The cloud

seeding operation in India faces several challenges, including the need for suitable pre-existing convective clouds, complex dynamics, severe weather alert during operation, air-traffic clearance to reach specific suitable clouds, and limitations during dry and winter seasons when suitable clouds lack. Despite all these limitations, India sees potential in cloud seeding for drought mitigation and strategic applications (Prabhakaran et al., 2023).

CAIPEEX Phase - I

The CAIPEEX phase-I experiment was conducted during the monsoon season (June – September) in the year 2009. The objective of this program was to characterize aerosol-cloud interactions and cloud microphysics properties over various Indian locations with varying meteorological conditions during the monsoon season (Kulkarni et al., 2012). Several flight observations using research aircraft were conducted across Pune, Pathankot, Bengaluru, Hyderabad, Bareilly, and Guwahati (Pandithurai et al., 2012).

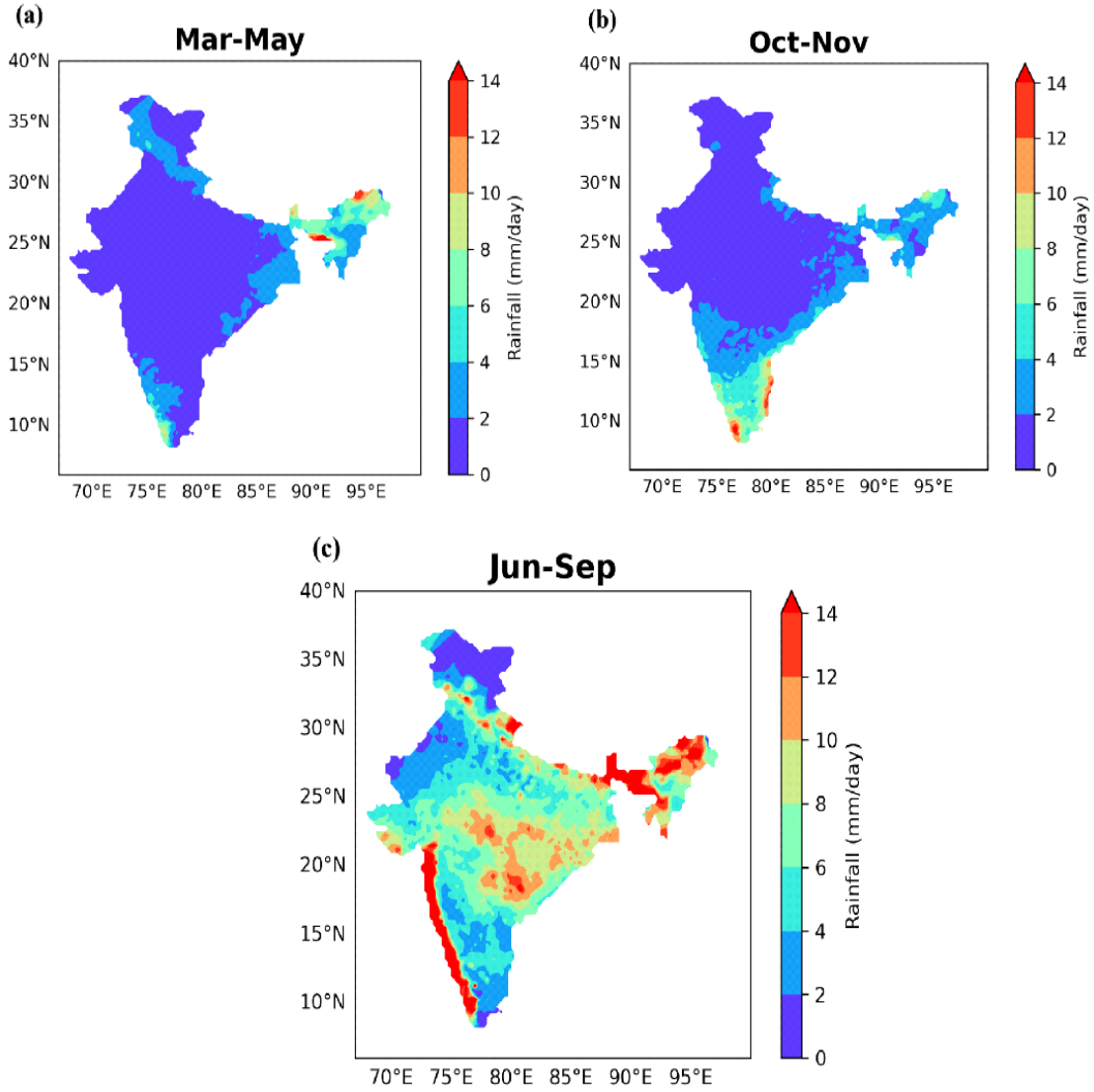

Figure 3. All India daily mean rainfall (in mm/day) in **(a)** Pre-monsoon season, **(b)** Post-monsoon season, and **(c)** Monsoon season during the year 2016-2020. Data source: IMD gridded rainfall data (Pai et al., 2014).

The experiment has collected significant data of vertical/horizontal cloud profiles, cloud and aerosol microphysics, and environmental parameters. This provides a background information of aerosol, clouds, and meteorological properties during monsoon seasons at different places of India which are required to assess the potential of cloud seeding in different Indian regions.

CAIPEEX Phase -II

Based on the results of the Phase-I experiment, phase-II project has focused on randomized seeding trials during the monsoon and post-monsoon seasons of the year 2010 and 2011. Statistical analysis and numerical model simulations were used to evaluate the effectiveness of the seeding experiment. The seeding was carried out using pyrotechnic flares and salt powder. The flares consisted of hygroscopic material (NaCl) for cloud base seeding and glaciogenic material (AgI) for cloud top seeding in the mixed phase clouds ($T < 0^{o}C$). Two aircraft were used, one for the aerosol and cloud microphysics observation called research aircraft (capable for high altitude flying) and another aircraft for flare seeding called seeder aircraft (for cloud base altitude operation). C-band radar was used to track the clouds and rain estimation. Due to insufficient samples, a statistical conclusion was not drawn from the phase-II experiment.

CAIPEEX Phase -III

During phase-III experiment (2014 - 2015), an integrated campaign was conducted over Gangetic Valley (Varanasi, India) region to investigate detailed aerosol-cloud interactions in a highly polluted environments developing deep convective clouds. Flight observations were conducted

over the region to document microphysical properties of aerosol and convective clouds under polluted environment of the Gangetic plains. Some flight observations were also conducted over the rain shadow region near Kolhapur in Maharashtra state during July 2015.

CAIPEEX Phase-IV

The CAIPEEX Phase-IV experiment was conducted during the monsoon season in years 2018-2019. The strategy for hygroscopic seeding is suitable for monsoon clouds over Indian region as monsoon environment develops warm base convective clouds ($T > 0^oC$) with sufficient cloud depth (> 2 km) in the warm region which favors to gain adequate amount of liquid water content in these clouds that can be converted it to rainwater by the hygroscopic seeding. The mixed-phase region ($T < 0^oC$) of the monsoon clouds can also be affected by the cloud base hygroscopic seeding and may induce enhanced rain from the cold clouds as reported by Prabhakaran et al. (2023). The microphysical characteristics of these monsoon convective clouds have been reported in several past papers from the CAIPEEX project (Kulkarni et al., 2012; Bera et al., 2019; Konwar et al., 2024). The phase-IV experiment focused on hygroscopic seeding (Randomization experiment) using $CaCl_2$ flares. Two aircraft were employed for the seeding purpose. Rain shadow regions of Western Ghats (near Solapur district in Maharashtra state), were targeted for the seeding as this region lacks sufficient rainfall required for agriculture activities. A total 276 statistical seeding samples were collected for statistical evaluation of seeding efficacy. A C-band Radar was used for cloud tracking and rain rate measurement. About 80 rain gauge stations were deployed in and around Solapur city to record actual surface rainfall during the seeding experiments. This experiment achieved a statistical rainfall enhancement by 18±2.6% over a 100 sq.km area in the rain shadow region. A detailed report on this experiment is given by Prabhakaran et al. (2023).

Table 2. Summary of cloud seeding experiments in different countries.

Project name (country)	Seeding method	Seeding agents	Purpose	Results	Reference
Hebei Province Typhoon "In-Fa" Warm Cloud Seeding Project (China)	Hygroscopic	$CaCl_2$, KCl	Rain enhancement during typhoon	Enhanced large drops, multiple downwind precipitation centers	Yang et al. (2023)
Jiangxi Province Winter Seeding Operations (China)	Winter glaciogenic and hygroscopic		Rain enhancement	~ 20% increase	Wang et al. (2019a)
Northwest China Charged Particle Seeding Trials (China)	Charged particles	Negative ions	Eco-friendly rain enhancement	20% increase	Wei et al. (2021)
National Center of Meteorology Operational Program (UAE)	Hygroscopic	KCl	Rain enhancement	~23% increase	Al Hosari et al. (2021)
Colorado River Basin Snowpack Augmentation Program (USA)	Glaciogenic	AgI	Snowpack augmentation	10-15% increase	Griffith et al. (2011)
Utah Winter Cloud Seeding Project (USA)	Glaciogenic	AgI	Snowpack augmentation	14.6% increase	Griffith et al. (1997)
Tasmania Hydroelectric Catchment Seeding Program (Australia)	Glaciogenic	AgI	Rain enhancement	5–14% increase	Morrison et al. (2009)
Snowy Precipitation Enhancement Research Project (Australia)	Glaciogenic static seeding	AgI	Snowfall enhancement	Statistically significant	Manton and Watten (2011)
Royal Rainmaking Project (Thailand)	Hygroscopic $CaCl_2$	$CaCl_2$	Rain enhancement, haze reduction	Statistically significant increase	Silverman and Sukarnjanaset (2000)
Taiwan National Cloud Seeding Program (Taiwan)	Ground-based and aerial AgI	AgI	Rain enhancement for agriculture	Mixed/ongoing	
Alberta Hail Suppression Project (Canada)	Glaciogenic	AgI	Hail Suppression	Reduced hailstone size & damage	Krauss and Renick (2021)
Duero River Basin Precipitation Enhancement Project (Spain)	Glaciogenic	AgI	Rain Enhancement	10–23% increase on seeded days	Vali et al. (1988)
Israel 4 Randomized Seeding Trial (Israel)	Glaciogenic	AgI	Rain Enhancement	1.8% increase (not significant)	Benjamini et al. (2023)
CAIPEEX (India)	Hygroscopic	$CaCl_2$	Rain enhancement	18% increase	Prabhakaran et al. (2023)

List of abbreviations and acronyms

Abbreviation/acronyms	Definition
CCN/GCCN	Cloud Condensation Nuclei/Giant Cloud Condensation Nuclei
IN	Ice Nuclei
RH	Relative Humidity
SS	Supersaturation
T	Temperature
NaCl	Sodium Chloride
$CaCl_2$	Calcium Chloride
KCl	Potassium Chloride
AgI	Silver Iodide

Overall, the CAIPEEX project has achieved its objectives of rain enhancement by hygroscopic cloud seeding in warm cumulus monsoon clouds. Further research and seeding trials on cold-cloud seeding of monsoon clouds are expected in near future.

SUMMARY OF CLOUD SEEDING PROJECTS

A summary of various cloud seeding initiatives implemented in different global regions (tropical and high latitude) is provided in Table 2. These projects are categorized by their seeding methodologies, agents used, primary objectives, and outcomes. The results from several cloud seeding projects showed positive outcomes, with a maximum increment in rainfall of ~23% in the UAE region (Al Hosari et al., 2021).

CONCLUSIONS

(1) Global warming and increasing water scarcity have intensified the need for alternate water resources, positioning cloud seeding as a potential solution, although further research is required to optimize its efficacy.

(2) Different countries adopted cloud seeding methods and seeding agents, tailored to their local climatic conditions and cloud types, emphasizing the necessity of region-specific approaches and strategies.

(3) The CAIPEEX-IV seeding experiment over Solapur, India (a rain shadow region) demonstrated feasibility of rain enhancement by hygroscopic cloud seeding, which can be extended to other parts of the rain-shadow regions such as central Maharashtra.

(4) Cloud seeding was also applied for hail suppression purpose in the USA and Europe, with potential relevance for Indian regions, where pre-monsoon hailstorms frequently impact the North-Eastern Himalayan region and Vidarbha (in Maharashtra), causing significant damage to crop and properties.

(5) Future improvements in cloud seeding efficiency depend on developing more efficient seeding agents, advanced radar systems, AI/ML-based weather forecasting and numerical models, and advanced aircraft instrumentation for detailed cloud microphysics study.

(6) This is to be mentioned that although several experiments like CAIPEEX-IV and other international programs, demonstrated that cloud seeding can produce statistically significant rainfall enhancement under suitable microphysical and dynamical conditions, yet its effectiveness remains strongly state-dependent, subject to large natural variability.

Acknowledgement

The authors are grateful to the Indian Institute of Tropical Meteorology (IITM) for providing the opportunity and resources to carry out the research work at IITM Pune campus. This report is part of internship project work of Ms. Sanhita Shende, M.Sc. (Physics), Savitribai Phule Pune University, Pune. We acknowledge that the rainfall data analysed in this paper is taken from the India Meteorological Department gridded rainfall data. We sincerely thank Dr. O. P. Pandey, Chief Editor of the Journal of Indian Geophysical Union (JIGU) and the two anonymous reviewers for their valuable comments that greatly improved the quality of the paper.

Authors credit statement

S. Shende: Data analysis, interpretation, original draft writing; S. Bera: Guidance to the research work, conceptualization, reviewing and editing; N. Malap: Data analysis, reviewing and editing.

Data Availability

IMD gridded rainfall data is available at https://www.imdpune.gov.in/cmpg/Griddata/Rainfall_25_NetCDF.html

Compliance with ethical standards

The authors have no conflict of interest, and they adhere to the copyright norms.

References

Al Hosari, T., Al Mandous, A., Wehbe, Y., Shalaby, A., Al Shamsi, N., Al Naqbi, H., Al Yazeedi, O., Al Mazroui, A. and Farrah, S., 2021. The UAE Cloud Seeding Program: A Statistical and Physical Evaluation. Atmos., 12(8), 1013.

Al Mazroui, A. and Farrah, S., 2017. The UAE seeks a leading position in global rain enhancement research. J. Wea. Mod., 49(1). 10.54782/jwm.v49i1.562

Almheiri, K. B., Rustum, R., Wright, G. and Adeloye, A. J., 2021. Study of Impact of Cloud-Seeding on Intensity-Duration-Frequency (IDF) Curves of Sharjah City, the United Arab Emirates. Water, 13(23), 3363.

Benjamini, Y., Givati, A., Khain, P., Levi, Y., Rosenfeld, D., Shamir, U., Siegel, A., Zipori, A., Ziv, B. and Steinberg, D. M., 2023. The Israel 4 Cloud Seeding Experiment: Primary Results. J. Appl. Met. Clim., 62(3), 317-327.

Bera, S., Prabha, T.V., Malap, N., et al., 2019. Thermodynamics and Microphysics Relation During CAIPEEX-I. Pure Appl. Geophys. 176, 371–388.

Branch, O., Späth, F. and Behrendt, A., 2020. Raw datasets for publication: The new Mountain Observatory of the Project “Optimizing Cloud Seeding by Advanced Remote Sensing and Land Cover Modification (OCAL)” in the United Arab Emirates: First results on Convection Initiation" - Case studies only (5 and 6 Sept 2018). Zenodo. https://doi.org/10.5281/zenodo.4287382

Chae, S., Lee, Y. H., Chang, K. H., Koo, H. J., Ro, Y., Hwang, H. J., Im, Y., Kim B. and Belorid, M., 2025. Effect of Airborne Cloud Seeding on Precipitation through Ensemble Numerical Modeling in the Yeongdong Region of Korea, Asia-Pacific. J. Atmos. Sci., 61(2), 10.

Dalirian, M., Keskinen, H., Ahlm, L., Ylisirniö, A., Romakkaniemi, S., Laaksonen, A., Virtanen, A. and Riipinen, I., 2014. CCN activation of fumed silica aerosols mixed with soluble pollutants. Atmos. Chem. Phys., 15, 3815-3829.

Dougherty, E. M., Gochis, D., Harrold, M., Tessendorf, S. A., Xue, L., Wolff, J. and Geerts, B., 2026. Simulated hydrologic impacts of cloud seeding in the North Platte and little Snake River basins of Wyoming. Water Resources Res., 62(2), e2024WR039383.

Gayatri, K., Prabhakaran, T., Malap, N., et al., 2023. Physical evaluation of hygroscopic cloud seeding in convective clouds using in situ observations and numerical simulations during CAIPEEX. Atmos. Res., 284, 106558.

Griffith, D. A., Thompson, J. R., Risch, D. A. and Solak, M. E., 1997. An update on a winter cloud seeding program in Utah. J. Weath. Mod., 29, 95-99.

Griffith, D. A., Yorty, D. P. and Solak, M. E., 2011. A Winter Operational Cloud Seeding Program: Upper Gunnison River Basin, Colorado. J. Wea. Mod., 43(1), 29–43.

Harrold, M., Tessendorf, S. A., Xue, L., Wolff, J. K., Dougherty, E., Geerts, B., Rodi, A. R. and Gochis, D., 2026. Evaluating the Precipitation Impacts of Cloud Seeding in Southern Wyoming and Northern Colorado using WRF-WxMod® within an Ensemble Modeling Framework. J. App. Met. Clim., e250099.

Howell, W. E., 1965. Twelve Years of Cloud Seeding in the Andes of Northern Peru. J. App. Met., 4, 693-700.

Hua, S., Chen, B., He, H., Chen, Y., Liu, X. E. and Yang, J., 2024. Numerical simulation of the cloud seeding operation of a convective rainfall event occurred in Beijing. Atmos. Res., 304, 107386.

Hudson, J. G. and Clarke, A. D., 1992. Aerosol and cloud condensation nuclei measurements in the Kuwait plume. J. Geophys. Res., 97, 14533-14536.

Isaac, G. A., Strapp, J. W., Schemenauer, R. S. and Macpherson, J. I., 1982. Summer Cumulus Cloud Seeding Experiments near Yellowknife and Thunder Bay, Canada. J. App. Met. Cli., 21(9), 1266-1285.

Jung, E., Albrecht, B. A., Jonsson, H. H., Chen, Y.-C., Seinfeld, J. H., Sorooshian, A., Metcalf, A. R., Song, S., Fang, M. and Russell, L. M., 2015. Precipitation effects of giant cloud condensation nuclei artificially introduced into stratocumulus clouds. Atmos. Chem. Phys., 15, 5645–5658.

Kommalapati, R. R. and Valsaraj, K. T., 2009. Atmospheric aerosols: Characterization, chemistry, modeling, and climate. Vol. 1005. Washington, DC: Amer. Chem. Soc., pp. 1–10.

Konwar, M., Werden, B., Fortner, E. C., Bera, S., Varghese, M., Chowdhuri, S., Hibert, K., Croteau, P., Jayne, J., Canagaratna, M., Malap, N., Jayakumar, S., Dixit, S. A., Murugavel, P., Axisa, D., Baumgardner, D., DeCarlo, P. F., Worsnop, D. R. and Prabhakaran, T., 2024. Identifying the seeding signature in cloud particles from hydrometeor residuals. Atmos. Meas. Tech., 17, 2387–2400.

Krauss, T. W. and Renick, J., 2021. The New Alberta Hail Suppression Project. J. Wea. Mod., 29(1),100-105.

Krauss, T. W., Sinkevich, A. A. and Ghulam, A., 2010. Precipitation Characteristics of Natural and Seeded Cumulus Clouds in the Asir Region of Saudi Arabia. J. Wea. Mod., 42(1), 61–77.

Kulkarni, J. R., Maheskumar, R. S., Morwal, S. B., Kumari, B. P., Konwar, M., et al., 2012. The Cloud Aerosol Interaction and Precipitation Enhancement Experiment (CAIPEEX): overview and preliminary results. Curr. Sci., 102(3), 413–425.

Laaksonen, A. and Malila, J., 2022. Ice nucleation, Nucleation of Water, Editor(s): Ari Laaksonen, Jussi Malila, Elsevier, 2022, Pages 209-248.

LaRoche, K., Ruiz-Columbie, A. and Jennings, J. A., 2017. An Overview of the 2016 Rainfall Enhancement Activities in Texas: A More Intensive Use of Hygroscopic Material. J. Wea. Mod., 49(1), 38–53.

Liu, Z., Yin, Y., Chen, Q., Zou, Z. and Liang, X., 2025. The Response of Cloud Dynamic Structure and Microphysical Processes to Glaciogenic Seeding: A Numerical Study. Atmosphere, 16(12), 1381.

Mandous, A., Abshaev, M., Abshaev, A., Mazroui, A., Muhairi, M. and Bojkov, R., 2006. Achievements in weather modification - uae prize for weather modification, Article: Development of Rocket and Artillery Technology for Hail Suppression, Copyrights © Department Atmospheric Studies, Ministry for Presidential Affairs, p.o.box 4815, Abu Dhabi, UAE.

Manton, M. J. and Warren, L., 2011. A Confirmatory Snowfall Enhancement Project in the Snowy Mountains of Australia. Part II: Primary and Associated Analyses. J. Appl. Met. Clim., 50(7), 1448-1458.

Mikhailov, E. F., Ivanova, O. A., Vlasenko, S. S. et al., 2017. Cloud condensation nuclei activity of the Aitken mode

particles near St. Petersburg, Russia. Izv. Atmos. Ocean. Phys. 53, 326–333.

Morrison, A. E., Siems, S. T., Manton, M. J. and Nazarov, A., 2009. On the Analysis of a Cloud Seeding Dataset over Tasmania. J. App. Met. Clim. 48(6), 1267-1280.

Murty, A. S. R., Selvam, A. M., Devara, P. C. S., Krishna, K., Chatterjee, R. N., Mukherjee, B. K., Khemani, L. T., Momin, G. A., Reddy, R. S., Sharma, S. K. and, Jadhav, D. B., 1998. 11-Year Warm Cloud Modification Experiment in Maharashtra State, India (arXiv: physics/9812046).

Pai, D. S., Rajeevan, M., Sreejith, O. P., Mukhopadhyay, B. and Satbha, N. S., 2014. Development of a new high spatial resolution (0.25 × 0.25) long period (1901–2010) daily gridded rainfall data set over India and its comparison with existing data sets over the region. Mausam, 65(1), 1–18.

Pandithurai, G., Dipu, S., Prabha, T. V., Maheskumar, R. S., Kulkarni, J. R. and Goswami B. N., 2012. Aerosol effect on droplet spectral dispersion in warm continental cumuli. J. Geophys. Res., 117, D16202.

Petters, M. D. and Kreidenweis, S. M., 2008. A single parameter representation of hygroscopic growth and cloud condensation nucleus activity – Part 2: Including solubility. Atmos. Chem. Phys., 8, 6273–6279.

Pöschl, U., Rose, D. and Andreae, M., 2009. Climatologies of cloud related aerosols-Part 2: Particle hygroscopicity and cloud condensation nuclei activity. Clouds in the Perturbed Climate System. 58-72.

Prabhakaran, T., Murugavel, P., Konwar, M., Malap, N., Gayatri, K., Dixit, S., Samanta, S., Chowdhuri, S., Bera, S., et al., 2023. CAIPEEX: Indian Cloud Seeding Scientific Experiment. Bull. Amer. Met. Soc., 104(11), E2095-E2120.

Pruppacher, H. R., Klett, J. D. and Wang, P. K., 1998. Microphysics of clouds and precipitation. Aero. Sci. Tech., 28, 381-382.

Roberts, G. C. and Nenes, A., 2005. A Continuous-Flow Streamwise Thermal-Gradient CCN Chamber for Atmospheric Measurements. Aero. Sci. Tech., 39(3), 206–221.

Rosenfeld, D. and Woodley, W. L., 2000. Deep convective clouds with sustained supercooled liquid water down to -37.5 degrees C. Nature, 25, 405(6785), 440-2.

Silverman, B. A. and Sukarnjanaset, W., 2000. Results of the Thailand Warm-Cloud Hygroscopic Particle Seeding Experiment. J. App. Met., 39(7), 1160-1175.

Tessendorf, S. A., Bruintjes, R., Weeks, C., Wilson, J. W., Knight, C. A., Roberts, R. D., Peter, J. R., Collis, S., Buseck, P. R., Freney, E., Dixon, M., Pocernich, M., Ikeda, K., Axisa, D., Nelson, E., May, P. T., Richter, H., Piketh, S., Burger, R. and McRae, D., 2012. The Queensland Cloud Seeding Research Program. Bull. Amer. Met. Soc., 93(1), 75–90.

Vali, G., Koenig, L. R. and Yoksas, T. C., 1988. Estimate of Precipitation Enhancement Potential for the Duero Basin of Spain. J. App. Met., 27(7), 829–850.

Wang, W., Yao, Z., Guo, J., Tan, C., Jia, S., Zhao, W., Zhang, P. and Gao, L., 2019a. The Extra-Area Effect in 71 Cloud Seeding Operations during Winters of 2008–14 over Jiangxi Province, East China. J. Met. Res., 33(3), 528–539.

Wang, F., Li, Z., Jiang, Q., Wang, G., Jia, S., Duan, J. and Zhou, Y., 2019b. Evaluation of hygroscopic cloud seeding in liquid-water clouds: a feasibility study. Atmos. Chem. Phys., 19, 14967-14977.

Wei, Z., Xue, F., Ming, Z., Wu, Q., Yang, Z., Ma, S., Liang, H., Wang, C., Wang, Y., Xinkun, A., Yang, Y. and Yu, K., 2020. Charged Particle (Negative Ion)-Based Cloud Seeding and Rain Enhancement Trial Design and Implementation. Water, 12(6), 1644.

Wei, Z., Ma, H., Ming, Z., Xue, F., Yu, K., Yang, Y., Ma, S., Wang, C., Pan, Y., Shu, Z., Mu, J., Yang, W. and Yin, X., 2021. Evaluation of the First Negative Ion-Based Cloud Seeding and Rain Enhancement Trial in China. Water, 13(18), 2473.

Woodley, W. L., Rosenfeld, D. and Silverman, B. A., 2003. Results of On-Top Glaciogenic Cloud Seeding in Thailand. Part I: The Demonstration Experiment. J. App. Met., 42(7), 920-938.

Xie, Z., Friedrich, K., Xue, L., Chen, S., Tessendorf, S. A., French, J. R. and Hohman, C. C., 2025. A Case Study of Cloud Microphysical Response to Cloud Seeding in Wintertime Orographic Clouds. J. App. Met. Clim., 64(9), 1249-1270

Yang, W., Fang, B., Zhang, J., Cui, Y. and Hou, S., 2023. Warm cloud seeding experiment of aircraft precipitation enhancement for the northward typhoon In-Fa in China. App. Eco. Env. Res., 21(5), 3887-3894.

Zhu, J., Wang, T., He, H., Liu, X. E., Yang, J., Hou, T., Hu, Z. and Lei, H., 2025. Ensemble forecast of precipitation enhancement potential using multiple microphysics parameterizations. Atmos. Res., 108638.

Received on: 10-11-2025; Revised on 23-03-2026; Accepted on: 29-03-2026

J. Ind. Geophys. Union, 30(3) (2026), 228-240
https://doi.org/10.71122/JIGU.30(3)2026.0023

Seismic wave attenuation in and around Hyderabad granitic region, south Indian shield

M. Srikanth[1*], K. Sivaram[1,2] and V. Pavan Kumar[1,2]
[1]CSIR-National Geophysical Research Institute, Uppal road, Hyderabad 500007.
[2]AcSIR-Academy of Scientific and Innovative Research, Ghaziabad, India.
* Corresponding author: srikanth.geo123@gmail.com

ABSTRACT

We investigate the attenuation characteristics of seismic body waves in the Hyderabad Granitic region (HGR), located in Eastern Dharwar Craton, southern Indian shield, using the coda-normalization method. The analysis is carried out using local earthquake data, recorded by a broadband seismic network of ten stations, installed in and around the HGR. The dataset consists of 30 local earthquakes with magnitudes ranging from 1.4 to 3.9, recorded during the year 2020-2021. Analysis is carried out at five central frequencies 1.5, 3, 6, 12 and 24 Hz for the lapse time window of 40s, to estimate the attenuation parameters for P-waves $(Q_P)^{-1}$ and S-waves $(Q_S)^{-1}$. In this frequency range, the estimated Q_P and Q_S values seem to indicate power-law dependence ($Q \sim Q_0 f^n$), where Q_0 is Q at 1 Hz, and n is the frequency dependence parameter. Q_P values vary from 35 ± 15 to 200 ± 80, while Q_S from 60 ± 10 to 300 ± 150, while 'n' shows minor variations for both P and S waves. The ratios Q_S/Q_P varying from 0.78 to 2.50, indicate variations in crustal properties, including heterogeneity and fracture characteristics. Our study would be of use in the investigation of the regional seismic hazard, seismic wave propagation and crustal heterogeneity.

Keywords: Quality factor Q_P and Q_S, Seismic attenuation, Scattering, Intrinsic absorption, Hyderabad Granitic Region (HGR), Eastern Dharwar Craton, South Indian Shield

INTRODUCTION

The study region of HGR is located in the Eastern Dharwar Craton (EDC) of the southern Indian peninsular shield. According to the seismic zonation map of India (BIS, 2016), this region lies between the seismic zones II and III with low to moderate intraplate seismic activity. Small earthquakes and microtremors associated with the hydrological processes and crustal heterogeneities, have been reported in the numerous recent studies. The HGR is also characterized by active neotectonic processes, with evidence of ongoing uplift at a rate of ~12 mm/year (Catherine and Pandey, 2005), indicating continued crustal deformation The recent installation of broadband seismic networks, has significantly improved the seismic monitoring, enabling a more comprehensive characterization of regional seismicity (Srinagesh et al., 2015). Shallow microtremors in the Hyderabad region, have often been linked to seasonal groundwater recharge following heavy monsoon rainfall, indicating the influence of hydrological processes on local seismicity (Parvin et al., 2021). Most of the seismic events, occur at shallow crustal depths and are often associated with pre-existing fractures and structural discontinuities.

Over the years, various geophysical investigations have been carried out to understand the crustal structure and seismic characteristics of this region. Receiver function modelling studies across the Deccan Volcanic Province and the Eastern Dharwar Craton, have revealed significant variations in crustal thickness and seismic velocity structure within the south Indian shield (Kumar et al., 2020). An earlier seismic attenuation study of Q_P and Q_S was carried out by Baruah et al. (2007) specifically around Jubilee Hills region of the Hyderabad (Telangana, India). Recently, a broadband seismic network consisting of ten stations was deployed by the CSIR-National Geophysical Research Institute, Hyderabad to monitor regional seismicity and investigate crustal structure. Using the acquired data from this network, Mandal et al. (2022) analyzed the moment tensor and source parameters of a rare lower-crustal earthquake (Mw 3.9) that occurred on 25 July 2021 beneath this region. Their results suggest presence of lower crustal attenuation and intraplate deformation. Several significant crustal and mantle discontinuities as well as mantle transition zone discontinuities beneath the HGR have also been discovered by further research using receiver function analysis (Mandal et al., 2024). The performance of broadband seismic stations and the noise levels in the EDC have been assessed by ambient noise analysis (Saha et al., 2024). Shallow shear-wave velocity structure and site response characteristics over this region have been revealed further by site characterisation studies employing Horizontal-to-Vertical Spectral Ratio (HVSR) analysis (Sivaram et al., 2024). Despite these studies, investigations focusing on seismic wave attenuation in the HGR, remain limited. Understanding the attenuation characteristics of seismic waves are directly related to crustal heterogeneities, lithological variations and tectonic features. The current study uses local earthquake data captured by the broadband seismic network to examine the nature of frequency-dependent attenuation properties of seismic body waves in the HGR.

REGIONAL GEOLOGY

The HGR symbolizes the northeastern extension of EDC, which primarily consists of granites and gneisses, together

with some linear and irregular Dharwar schist belts (Chadwick et al., 2000; Jayananda et al., 2000; Vasudev et al., 2000). EDC has undergone multiple tectonic deformations, including kimberlite activity associated with cratonic extension from late to the early Proterozoic period, encompassing the remobilization of crustal blocks and low-pressure metamorphism (Ramam and Murty, 1997). Structural studies have recognized presence of numerous geological features, including fractures, joints, faults and fissures (Murthy and Raghavan, 2002; Krishnamurthy et al., 2003; Singh et al., 2004). Pandey et al., (2002) suggested that the HGR is being neotectonically uplifting possibly due to a major intrusive body situated at sub-crustal depth, leading to changes in river courses and also erosion of several kilometers (~10 km) from its upper crustal column. The HGR exhibits an unusual lithospheric structure, characterized by a thin granitic crust, shallow Moho depth (~32–33 km), and possibly underlying granulitic facies rocks at subsurface depths, indicating significant crustal heterogeneity and thermos-tectonic evolution (Pandey et al., 2002). They also suggest that the cratonic mantle lithosphere beneath HGR is a highly conductive (15 Ωm) hydrous containing seismically anisotropic metasomatised zone between depth of 90 and 100 km, where the estimated temperatures could be in the range of 900–1000 °C. Persistent episodic thermal reactivations during the last 2.6 Ga and continuous uplifting is suggested to have played a major role towards making its crustal column unusual.

DATA

A broadband seismic network was installed and operated by the CSIR - National Geophysical Research Institute, Hyderabad, India, from October 2020 to January 2022 (Figure 1) as a part of seismological project. In Figure 1 and Table 1, we show the locations of the broadband recording stations (as triangles) along with the various lineaments around the studied region. The broadband seismographs consist of Nanometrics make Seismometer Trillium 120QA and Digital data Acquisition System (DAS) CTR4-3S Centaur, coupled with Global Positioning System (GPS). We used continuous waveforms recorded from 10 broadband seismographs. The range of distances between stations vary between 20 to 140 km. Out of the continuously recorded data, spectral analysis of the local earthquakes (~30) with local magnitude ranging from 1.4 to 3.9, recorded by the seismic station data, was performed using seisan software (Ottemoller et al., 2018). The seismic catalogue used in this study is relatively limited in size (~30 events) due to removal of noisy data (Table 2). The dataset is dominated by small-magnitude earthquakes (M_L 1.4-3.9), which can result in lower signal-to-noise ratios, particularly at higher frequencies, thereby affecting the stability of spectral estimates. In addition, the distribution of events in terms of epicentral distance and azimuth is not uniform, which may introduce bias in attenuation estimates. Other limiting factors are that the local site effects at individual stations and variations in wave propagation paths, may also influence the observed amplitudes, contributing to variability in Q_P, Q_S and n values. These factors are reflected in the spread of the estimated attenuation parameters and their influence has been considered qualitatively in the interpretation of the results. The presented estimates are therefore of the first order and need more detailed studies.

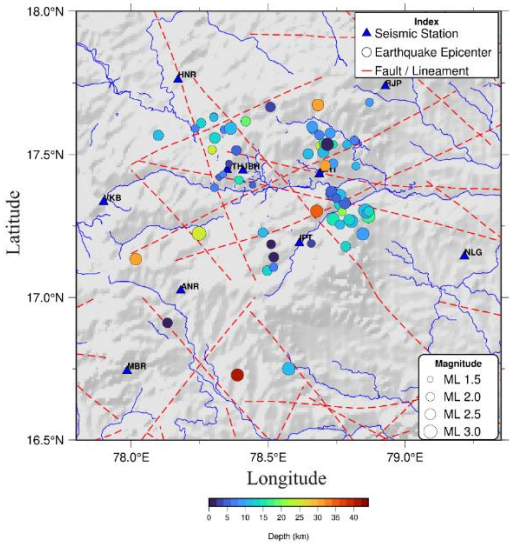

Figure 1. Seismicity map of the Hyderabad Granitic Region (HGR), showing the spatial distribution of earthquake epicenters recorded at the broadband stations (shown as triangles) of the local seismic network. The earthquakes are shown with size (M_L) and also depth (with horizontal color bar).

METHODOLOGY

The Coda-Normalization Method

Attenuation refers to a wave losing energy or becoming weaker as it travels through geological material. This occurs because the wave spreads out, scatters when it encounters irregularities and some of its energy is converted into heat. To quantify how much a wave diminishes, we use the quality factor, Q which indicates how much energy the wave retains compared to what it loses during each cycle. Other terms used to describe seismic attenuation include the attenuation decrement γ, as well as how Q varies with frequency. For the estimation of the quality factor, the single backscattering model proposed by Aki (1969) and Aki and Chouet (1975) is commonly used. According to this model, coda waves are interpreted as the superposition of secondary waves scattered by heterogeneities randomly distributed within the Earth's lithosphere. In this study, the extended coda-normalization method was used to estimate the attenuation of body waves. This method assumes that the coda wave energy is uniformly distributed in the region surrounding the earthquake source. The spectral amplitudes of direct P- and S-waves are normalized by the spectral amplitude of the coda waves, which reduces the effects of instrument gain, source excitation and site amplification. This approach allows us to derive Q_P and Q_S values from a dataset by normalizing the direct P-wave and S-wave spectral amplitudes with the coda-spectral amplitude measured at a set lapse time, approximately twice the direct S-wave travel time from the earthquake's origin time. Yoshimoto et al., (1993) adjusted the body wave component in relation to the coda wave component. The attenuation of P and S waves can be determined from the slope of the least-squares fitting the equations,

$$\left\langle ln\left[\frac{Ap(f,r)r^{\gamma}}{Ac(f,tc)}\right]_{r\pm\Delta r}\right\rangle = \frac{-\Pi f}{Q_P(f)v_p}r + Const(f) \qquad (1)$$

$$\left\langle ln\left[\frac{As(f,r)r^{\gamma}}{Ac(f,tc)}\right]_{r\pm\Delta r}\right\rangle = \frac{-\Pi f}{Q_S(f)v_S}r + Const(f) \qquad (2)$$

where Ap (f, r) and as (f, r) denote the amplitude spectra of direct P- and S-waves at the hypocentre distance r(km). The coda wave spectra, Ac (f, tc) for frequency f, is set at a delay time (tc) at 40 seconds. Vp represents the mean P-wave velocity while Vs denotes the mean S-wave velocity. Q_P and Q_S are the quality parameters for P-wave and S-wave correspondingly. γ is the exponent of geometrical spreading. The values of Q_P and Q_S are derived from the linear regression of $\left\langle \ln\left[\frac{A_p(f,r)r^{\gamma}}{A_c(f,t_c)}\right]\right\rangle_{r\pm\Delta r}$ in relation to hypo central distance r, using the least-squares approach. This represents the mean across numerous events located within a small distance range r±Δr from the station.

To calculate the seismic quality factor, we used the CodaNorm software package, which estimates body-wave attenuation using the coda-normalization method (Predein et al., 2017). In a pre-processing measure, the seismogram was processed through the five consecutive octave frequency bands, utilizing a four-pole Butterworth bandpass filter. The low cut-off and high cut-off bandwidths 1-2, 4-8, 8-16, and 16-32 Hz are applied to the seismogram at central frequencies of 1.5, 3, 6, 12 and 24 Hz. The direct P and S-waves within a 5s interval are analyzed from vertical (Z) and north-south (NS) components, respectively. The P and S-wave arrival times are recorded from the beginning. The coda wave is analyzed using a 20s time window (sd = 20), centered at a lapse time of approximately 40 s (Acoda = 40) from the event origin time. A representative example illustrating the identification of P and S-wave, and coda windows at JBH station, is shown in Figure 2(a). Figure 2(b) shows the band-pass filtered seismograms (8–16 Hz; central frequency 12 Hz) recorded at station JBH.

Table 1. The geographical coordinates of the broadband seismic stations, deployed in the Hyderabad Granitic Region (HGR) for the computation of Q_P and Q_S.

S. No	Station name	Station code	Lat (°N)	Long (°E)	Elevation (m)
1	Annaram	ANR	17.024	78.181	542
2	Vikarabad	VKB	17.33	77.90	574
3	Ghatkesar	GHT	17.431	78.687	386
4	Hatnur	HNR	17.761	78.171	442
5	IIT-Hyderabad	IITH	17.446	78.350	523
6	Ibrahimpatnam	IPT	17.190	78.164	457
7	Jubilee Hills	JBH	17.44	78.408	528
8	Mahbubnagar	MBR	16.742	77.985	426
9	Nalgonda	NLG	17.144	79.217	774
10	Rajapet	RJP	17.738	78.928	400

Table 2. Catalogue of 30 earthquakes with origin time, location, depth, and local magnitude (M_L).

S.No	DATE (YYMMDD)	Origin time HR:MN:SS	Lat (°N)	Lon (°E)	Depth (Km)	Local Mag. (M_L)
1	2020-11-07	12:51:11.5	17.58	78.33	6	1.7
2	2020-11-07	13:08:20.5	17.42	78.32	4.1	1.4
3	2020-11-07	22:33:11.9	17.22	78.48	10.6	2
4	2020-11-08	07:20:43.3	17.22	78.24	24.1	2.9
5	2020-11-11	02:51:00.1	17.41	78.39	14.3	1.8
6	2020-11-11	17:04:59.7	17.32	78.76	13.1	2.2
7	2020-11-14	07:11:32.2	17.58	78.66	8.5	1.9
8	2020-11-14	12:57:02.5	17.61	78.25	12.8	2
9	2020-11-14	13:11:15.5	17.43	78.33	6	1.5
10	2020-11-21	13:42:27.5	17.63	78.3	10.7	1.8
11	2020-12-08	12:55:36.5	17.35	78.74	9.4	1.7
12	2020-12-08	13:33:12.5	17.51	78.29	25.7	1.8
13	2020-12-09	12:06:36.5	17.61	78.41	18.1	2
14	2020-12-11	13:08:53.5	17.3	78.86	12.3	2.1
15	2021-01-10	08:37:43.3	17.56	78.68	7.9	2
16	2021-01-22	07:37:00.3	17.35	78.73	6.9	1.9
17	2021-01-22	08:53:43.3	17.46	78.73	9.7	2
18	2021-02-07	03:11:36.1	17.26	78.8	10.4	2.7
19	2021-02-11	12:51:37.5	17.13	78.01	31.2	2.5
20	2021-02-18	14:01:30.5	17.53	78.7	16	2.1
21	2021-02-27	02:54:14.1	16.75	78.57	10.2	2.7
22	2021-04-12	08:04:04.3	17.09	78.49	12	2.1
23	2021-04-19	13:39:23.5	17.5	78.7	11.8	2.3
24	2021-04-27	08:06:59.3	17.37	78.73	4.7	2.3
25	2021-04-30	03:16:35.1	17.27	78.73	15.7	2.6
26	2021-05-03	08:01:14.3	16.72	78.38	40.2	2.6
27	2021-05-30	07:24:06.3	17.34	78.74	4.6	1.9
28	2021-06-02	13:33:48.5	17.25	78.76	11.7	2
29	2021-06-27	12:58:52.5	17.31	78.86	12	2.1
30	2021-07-25	23:30:53.9	16.17	78.5	35.3	3.9

Here, the upper panels show the raw waveforms (grey) and their RMS envelopes (blue), used for attenuation analysis. This window corresponds to the late coda region, where the wavefield is dominated by multiply scattered energy and is largely free from contributions of direct P- and S-waves. This work considers an average Vp of 6.43 km/s and Vs of 3.66 km/s along with the geometrical spreading exponent $\gamma = 1$ for body wave attenuation (Havskov et al., 1989; Chin and Aki, 1991). The parameter n was obtained by fitting a power-law relation of the form $Q(f) = Q_0 f^n$ in logarithmic space for each bootstrap sample and its uncertainty was derived from the variability of the fitted slope. To minimize the influence of noise and unstable estimates, basic data filtering and consistency checks were applied prior to analysis. Additionally, robust statistical techniques were employed during the estimation process to reduce the impact of outliers and ensure reliable attenuation parameters. To assess the robustness of the estimated attenuation parameters, a bootstrap resampling approach was employed. For each station and frequency band 200 bootstrap realizations were generated by resampling the data with replacement. The quality factor (Q) were estimated using robust linear regression (RLM) for each realization, and the mean and standard deviation were computed from the resulting distributions. The frequency dependence parameter (n) was determined by applying a bootstrap-based linear regression in log-log space between Q and frequency. The mean and standard deviation of the bootstrap estimates were used to quantify the uncertainty in n. The attenuation coefficient (γ) was calculated for each frequency and averaged with its uncertainty represented by the standard deviation. The results indicate that Q values exhibit moderate variability across frequencies, whereas the frequency dependence parameter (n), is relatively well constrained for most stations.

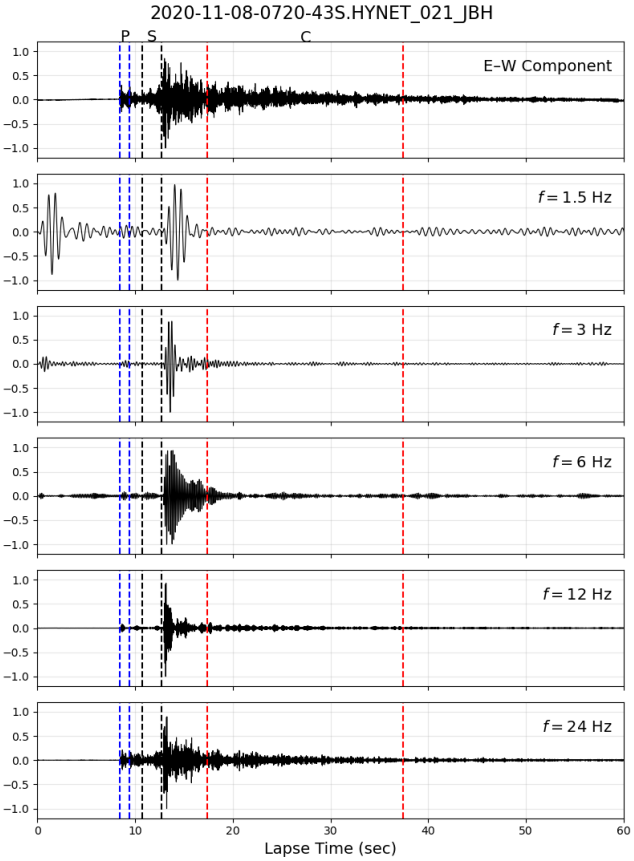

Figure 2 (a). A sample of recorded broadband seismogram and its band-pass filtering at frequencies, 1.5, 3, 6, 12 and 24 Hz at JBH station. An E–W component seismogram is shown in the top. Here dashed–portions P, S, C denote the P-coda, S-coda, and Coda for estimation of Q_P and Q_S from the seismogram.

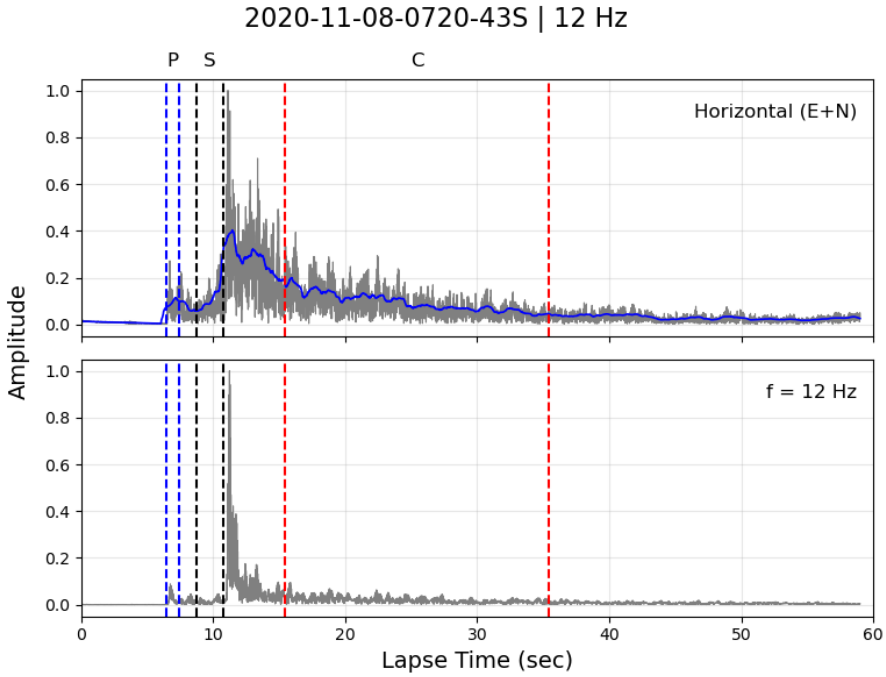

Figure 2 (b). Example of band-pass filtered seismograms (8–16 Hz; central frequency 12 Hz) recorded at station JBH.

The station-wise estimates of Q_P, n and γ along with their uncertainties, while the corresponding frequency-dependent Q_P and Q_S values are given in Tables 3 and 4.The uncertainty bounds (± one standard deviation) are illustrated in Figures 3 and 4 using shaded regions around the estimated curves providing a visual representation of the variability in the attenuation parameters. These uncertainties are estimated independently for each station and reflect the variability inherent in the data and fitting procedure.

RESULTS AND DISCUSSION

Estimation of Q_P and Q_S

Tables 3 and 4 show the estimated Q_P and Q_S values for various frequency bands. The Figure **3** shows that the Q_P values clearly increase with frequency. The Q_P values vary between 358 ± 30 and 9000 ± 3000 at higher frequencies (24 Hz) and between 20 ± 6 and 600 ± 300 at lower frequencies (1.5 Hz). Similarly, Q_S values vary between 46 ± 4 and 900 ± 400 at lower frequencies (1.5 Hz) and between 511 ± 40 and 5000 ± 1500 at higher frequencies (24 Hz). Both Q_P, Q_S values increase with frequency suggesting that seismic waves in the studied area exhibit frequency-dependent attenuation. A regression analysis was performed on normalized wave amplitudes with respect to hypocentral distance across the frequency band 1.5–24 Hz. The selected stations (ANR, GHT, IPT, IITH, IPT, NLG, JBH and RJP) exhibit reasonably consistent linear trends between normalized P and S-wave amplitudes and hypocentral distance across the studied frequency bands, indicating comparatively more stable attenuation behaviour and more reliable estimation of Q_P and Q_S than the remaining stations. The Figure 4 shows linear regression of normalized P-wave and S-wave amplitudes with distance for different frequency bands used for estimating frequency dependent relations of Q_P and Q_S. In Figure 5, station GHT shows low Q_P and a high Q_S/Q_P ratio, indicating stronger attenuation of P-waves relative to S-waves. In contrast, stations ANR, IPT and HNR, exhibit high Q_S values, suggesting lower S-wave attenuation, which is likely to be associated with more homogeneous and less fractured crust, with possible influence from path and site effects. While higher Q values at higher frequencies, indicate less energy loss during wave transmission, comparatively lower Q values at lower frequencies, signal stronger attenuation.

The attenuation characteristics obtained in the present study show broad agreement in terms of general trends with earlier observations reported from the Jubilee Hills region of Hyderabad (Baruah et al., 2007). Nevertheless, a direct quantitative comparison is limited due to differences in methodology, frequency bands and data processing approaches between the two studies. For the majority of stations and frequency bands, a comparison of the data reveals that Q_S values are typically greater than Q_P values. This trend which is frequently seen in attenuation investigations, suggests that S-waves in the crustal medium, undergo less attenuation than P-waves, when the crustal rocks are relatively dry. The spatial variation in attenuation parameters (Q_P, Q_S and n) reflects the influence of regional geology and crustal structure. Stations located near lineaments and fault zones (Figure 1), generally exhibit lower Q_P and higher Q_S/Q_P ratios, indicating enhanced attenuation possibility due to fracturing and scattering. These observations seem to suggest the active neotectonic setting of the HGR, where ongoing uplift at a rate of ~12 mm/year has earlier been reported (Catherine and Pandey, 2005) with highly resistive granitic-gneissic crust below HGR (Singh et al., 2009) which can enhance fracture density. Earlier studies also indicated the complex lithospheric structure and crustal heterogeneity beneath HGR (Pandey et al., 2002 among others). Stations within stable crustal blocks usually show higher Q values and lower n, indicating more homogeneous and competent conditions.

The attenuation patterns are broadly consistent with the crustal thickness variations reported by Mandal et al. (2024), where structurally complex or thicker crust exhibits stronger frequency-dependent attenuation. For example, GHT shows low Q_P and high Q_S/Q_P, indicating localized heterogeneity, whereas IPT and JBH exhibit higher Q_S values, suggesting relatively less attenuating and more competent crust. Overall, the results highlight the role of geological structures and crustal heterogeneity in controlling seismic attenuation.

Frequency dependence relation of Q

From regression analysis, we observed the power-law frequency dependence relations of the Q_S and Q_P at the seismic stations, which are presented in Table 5 and 6, respectively. The attenuation parameters follow the empirical relation $Q(f) = Q_0 f^n$, where Q_0 represents the quality factor at 1 Hz and 'n' denotes the frequency dependence parameter. Figure 5 illustrates the spatial distribution of Q_P (color-coded) and Q_S (represented by symbol size) at the seismic stations, where the reported values correspond to Q_0 at a reference frequency of 1 Hz. The Q_P values vary significantly across the study region, ranging from low values at stations such as GHT (~35) and VKB (~40), to high values at JBH (~180) and RJP (~200). Similarly, Q_S values also exhibit considerable variability, with lower values at VKB (~60) and JBH (~140) and higher values at ANR (~300) and IPT (~220).

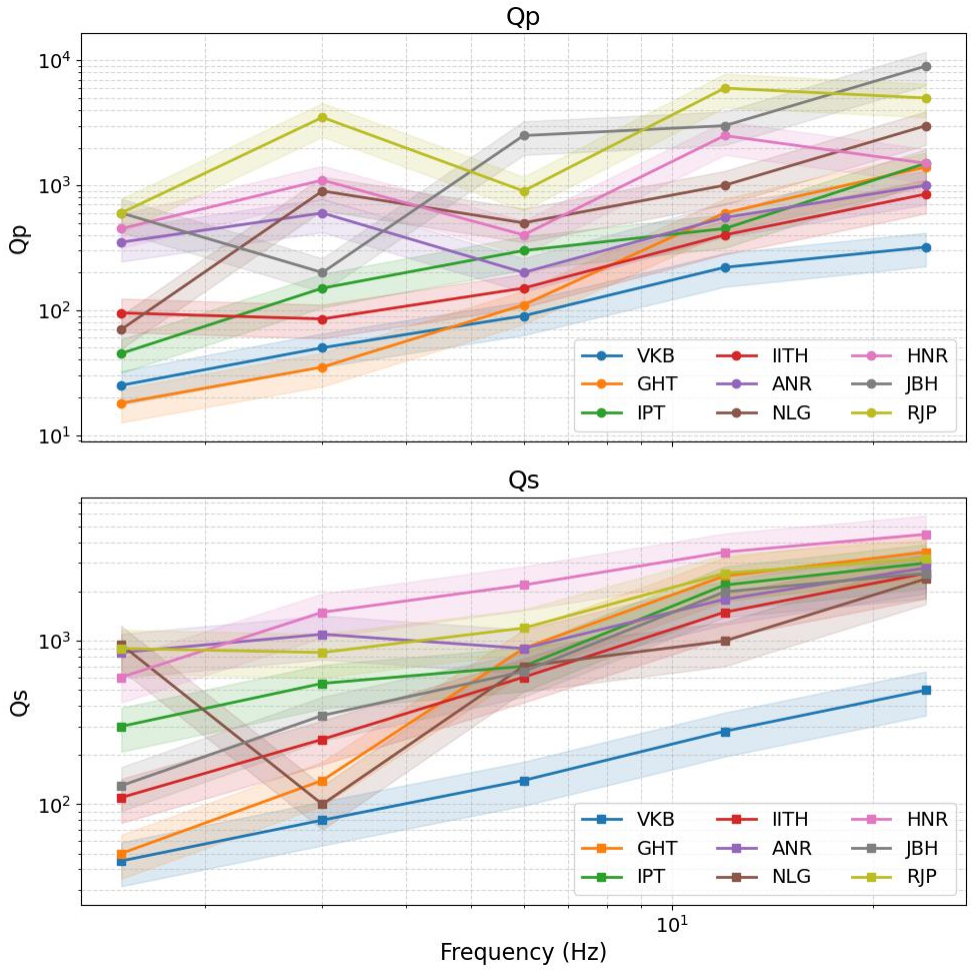

Figure 3. Plot of estimated Q_P and Q_S for different frequencies for all stations. Both Q_P and Q_S indicate power-law frequency dependence. Lines denote Q values and shaded bands represent ± uncertainty.

Table 3. Estimated P-wave quality factor (Q_P) values for different frequency bands (1.5-24 Hz). The values are expressed as mean ± standard deviation, with 95% Confidence Interval (in parentheses).

S.No	Station	Q_P (1.5Hz)	Q_P (3 Hz)	Q_P (6 Hz)	Q_P (12 Hz)	Q_P (24 Hz)
1	VKB	27 ± 3 (21-33)	49 ± 5 (39-59)	91 ± 8 (75-107)	234 ±20 (195-273)	358±30 (299-417)
2	GHT	20 ± 6 (8-32)	34 ± 12 (10-58)	120 ± 80 (0-277)	560 ±250 (70-1050)	1500±700 (128-2872)
3	IPT	45 ± 12 (21-68)	165 ± 80 (8-322)	320 ± 150 (26-614)	405 ±90 (229-581)	1600±700 (228-2972)
4	IITH	95 ± 40 (17-173)	85 ± 60 (0-203)	165 ± 40 (87-243)	400±100 (204-596)	870±250 (380-1360)
5	ANR	380 ± 150 (86-674)	650±200 (258-1042)	220 ± 80 (63-377)	620±150 (326-914)	1030±250 (540-1520)
6	NLG	70 ± 30 (11-129)	900±600 (0-2076)	500 ± 300 (0-1088)	1000±500 (20-1980)	2800±1200 (448-5152)
7	HNR	480 ± 200 (88-872)	1100±500 (120-2080)	420±150 (126-714)	2500±1000 (540-4460)	1400±500 (420-2380)
8	JBH	600±250 (110-1090)	200±150 (0-494)	2700±800 (1132-4268)	3100±900 (1336-4864)	9000±3000 (3120-14880)
9	RJP	600 ± 300 (12-1188)	2800 ±1500 (0-5740)	900±300 (312-1488)	5700±2000 (1780-9620)	5300 ± 2000 (1380-9220)

The Table 3 shows estimated Q_P values vary in the range from 20 ± 6 to 9000 ± 3000. Stations HNR and RJP show relatively higher Q_P values compared to stations such as GHT, VKB and IPT which exhibit lower values. Table 4 shows estimated Q_S values for different frequency bands (1.5-24 Hz). Similarly, Table 5 shows frequency dependence parameter n that varies between 0.39 ± 0.32 and 1.62 ± 0.29. Among the stations, GHT and JBH exhibit relatively higher (n) values, indicating stronger frequency dependence, while lower values at stations like ANR and HNR, indicate weaker dependence on frequency.

The attenuation coefficient (γ) which represents the rate of decay of P-wave energy with distance, varies between 0.0014 ± 0.0004 and 0.0282 ± 0.0028. Higher values of (γ) observed at stations such as VKB and GHT, suggest relatively stronger attenuation, possibly associated with increased crustal heterogeneity or localized structural complexities, whereas lower values at stations like RJP indicate, comparatively weaker attenuation. Similarly, Table 6 shows the estimated values range of Q_S between 46 ± 4 and 5000 ± 1500. Stations like HNR and RJP shows relatively higher Q_S values, while GHT and VKB exhibits the lowest Q_S values among the stations. The frequency dependence parameter n for varies between 0.34 ± 0.52 and 1.95 ± 0.87. Stations such as ANR and GHT exhibit higher (n) values, indicating stronger frequency dependence, while lower values at stations like HNR, suggest relatively weaker dependence on frequency. The relatively higher values of (γ) observed at VKB and NLG stations suggest stronger attenuation, likely associated with increased crustal heterogeneity, whereas, lower values at HNR, IPT and ANR stations, indicate comparatively stable and less attenuating geological conditions.

A comparison of the results indicates that the frequency dependence parameter (n) for S-waves is generally higher than that for P-waves, suggesting stronger frequency-dependent attenuation for S-waves. The frequency dependence parameter (n) provides insight into attenuation mechanisms, where lower values indicate weak frequency dependence associated with relatively homogeneous, dry and mechanically stable crust, dominated by intrinsic absorption. In contrast, higher n values reflect strong frequency dependence due to enhanced scattering from small-scale heterogeneities such as fractures and faults. The spatial variation of the QS/QP ratio across the study region is depicted in Figure 5 using a color scale, which range from 0.78 to 2.50. The ratio is lowest at JBH (0.78) and highest at GHT (2.20) and ANR (2.50). In Tables 3-6, the lower bounds of the 95% C.I in some cases approach non-physical values due to large uncertainties.

Table 4. Estimated S-wave quality factor (Q_S) values for different frequency bands (1.5-24 Hz). The values are expressed as mean ± standard deviation (±1σ), with 95% Confidence Interval (in parentheses).

S.No	Station	Q_S (1.5Hz)	Q_S (3 Hz)	Q_S (6 Hz)	Q_S (12 Hz)	Q_S (24 Hz)
1	VKB	46 ± 4 (38-54)	85 ± 7 (71-99)	149 ± 12 (125-173)	290 ± 22 (247-333)	511 ± 40 (433-589)
2	JBH	130 ± 20 (91-169)	350 ± 50 (252-448)	600 ± 80 (443-757)	1800 ± 300 (1212-2388)	2600 ± 400 (1816-3384)
3	IITH	110 ± 30 (51-169)	250 ± 60 (132-368)	500 ± 100 (304-696)	1500 ± 300 (912-2088)	3000 ± 800 (1432-4568)
4	ANR	800 ± 300 (212-1388)	1200 ± 500 (220-2180)	900 ± 300 (312-1488)	2000 ± 700 (626-3374)	3000 ± 1000 (1040-4960)
5	NLG	900 ± 400 (116-1684)	100 ± 40 (22-178)	600 ± 250 (110-1090)	1000 ± 400 (216-1784)	2500 ± 900 (734-4266)
6	IPT	300 ± 100 (104-496)	550 ± 150 (255-845)	700 ± 200 (308-1092)	2500 ± 800 (932-4068)	3500 ± 1200 (1148-5852)
7	GHT	50 ± 20 (11-89)	150 ± 50 (52-248)	1000 ± 300 (412-1588)	3000 ± 900 (1236-4764)	4000 ± 1200 (1648-6352)
8	RJP	800 ± 300 (212-1388)	800 ± 250 (310-1290)	1200 ± 400 (412-1988)	3000 ± 900 (1236-4764)	4000 ± 1200 (1648-6352)
9	HNR	500 ± 200 (108-892)	1500 ± 500 (520-2480)	2500 ± 800 (932-4068)	4000 ±1200 (1648-6352)	5000 ± 1500 (2060-7940)

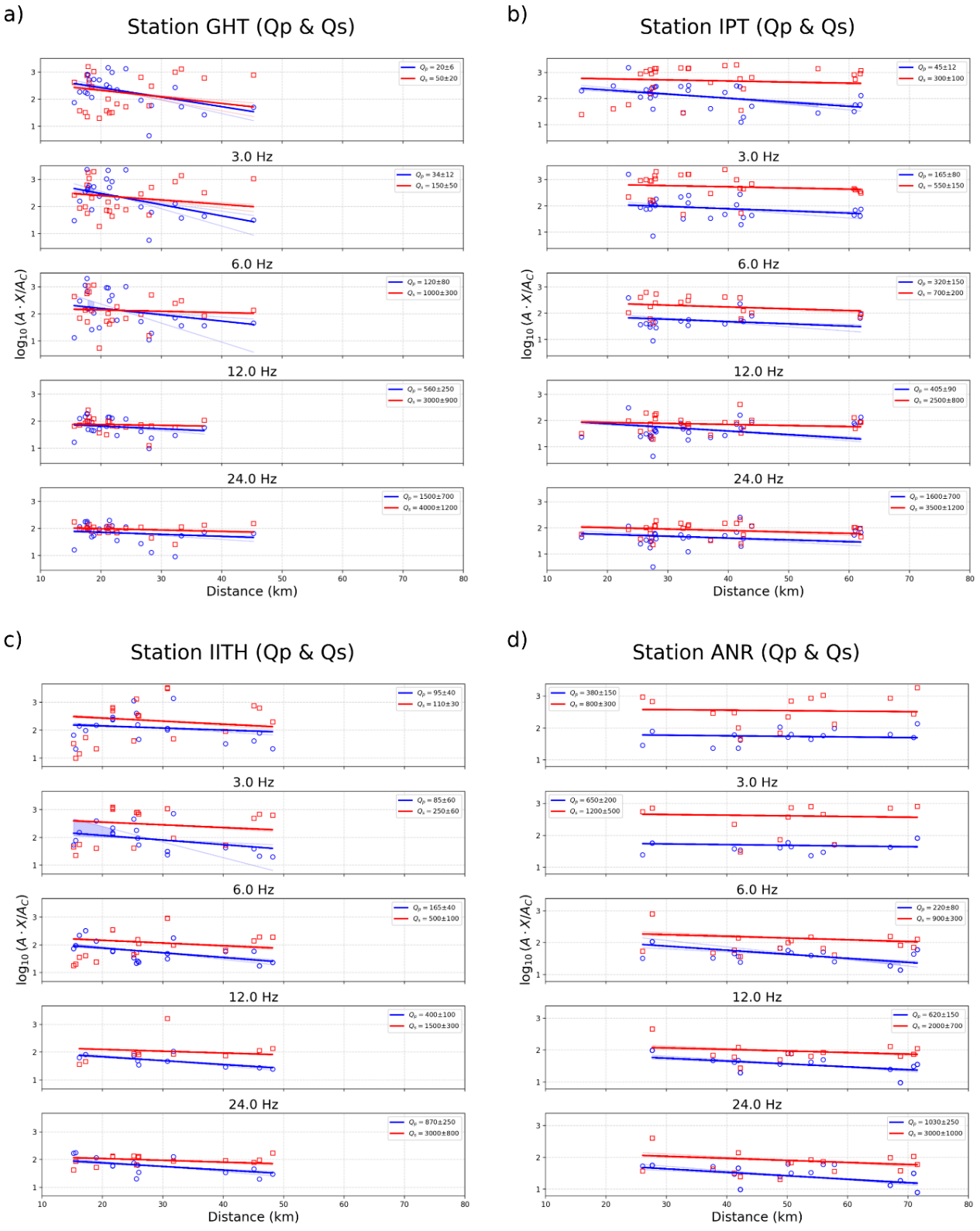
a)
Station GHT (Qp & Qs)
3.0 Hz
6.0 Hz
12.0 Hz
24.0 Hz
log10 (A · X/AC)
Distance (km)
b)
Station IPT (Qp & Qs)
c)
Station IITH (Qp & Qs)
d)
Station ANR (Qp & Qs)

(continued..)

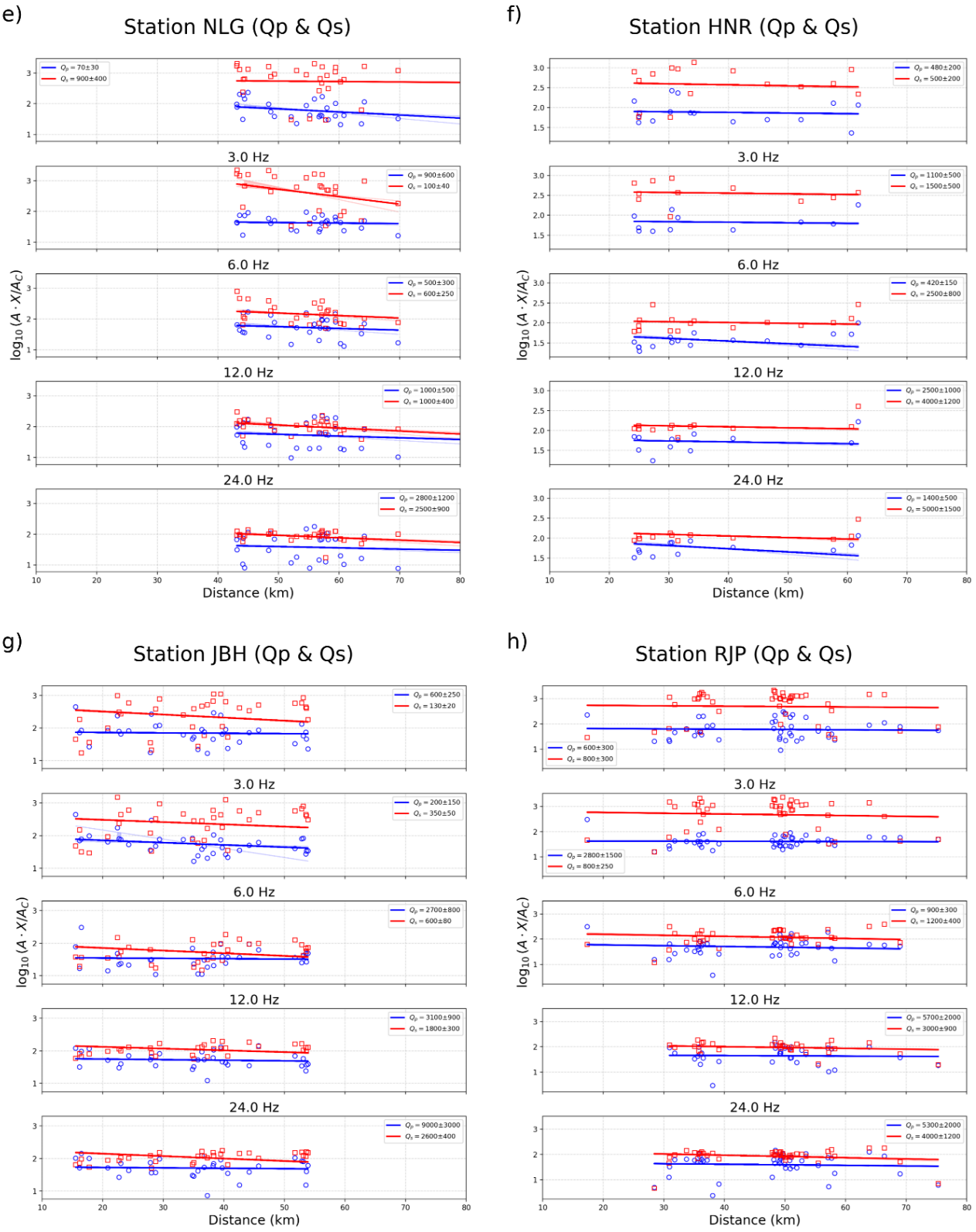

Figure 4. Linear regression of normalized P-wave and S-wave amplitudes with distance for different frequency bands used to estimate frequency dependent relations for Q_P and Q_S for the (a) GHT, (b) IPT, (c) IITH, (d) ANR, (e) NLG, (f) HNR, (g) JBH, (h) RJP seismic stations.

Table 5. The Station-wise attenuation parameters including Q_P value Q_0 (quality factor at 1 Hz), frequency dependence parameter (n), and attenuation coefficient (γ). The values are expressed as mean ± standard deviation, with 95% Confidence Interval (in parentheses).

S.No	Station	Q_0 (1 Hz)	n	γ
1	VKB	40 ± 10 (20-60)	0.98 ± 0.07 (0.84-1.12)	0.0282 ± 0.0028 (0.0227-0.0337)
2	GHT	35 ± 15 (6-64)	1.62 ± 0.29 (1.05-2.19)	0.0260 ± 0.0143 (0-0.0540)
3	IPT	100 ± 30 (41-159)	1.11 ± 0.24 (0.64-1.58)	0.0108 ± 0.0037 (0.0036-0.0180)
4	IITH	95 ± 30 (36-154)	0.87 ± 0.27 (0.34-1.40)	0.0150 ± 0.0046 (0.0060-0.0240)
5	ANR	120 ± 50 (22-218)	0.39 ± 0.32 (0-1.02)	0.0073 ± 0.0042 (0-0.0155)
6	NLG	110 ± 40 (32-188)	1.23 ± 0.29 (0.66-1.80)	0.0057 ± 0.0027 (0.0004-0.0110)
7	HNR	140 ± 60 (22-258)	0.45 ± 0.48 (0-1.39)	0.0038 ± 0.0026 (0-0.0089)
8	JBH	180 ± 60 (62-298)	1.44 ± 0.33 (0.79-2.09)	0.0037 ± 0.0029 (0-0.0094)
9	RJP	200 ± 80 (44-356)	1.11 ± 0.35 (0.42-1.80)	0.0014 ± 0.0004 (0.0006-0.0022)

Table 6. The estimated Q_S value (Q_0) at 1 Hz, frequency dependence parameter (n), and attenuation coefficient (γ) for each station. The values are expressed as mean ± standard deviation, with 95% confidence intervals (in parentheses).

S.No	Station	Q_0 (1 Hz)	n	γ
1	VKB	60 ± 10 (40-80)	0.87 ± 0.02 (0.83-0.91)	0.0319 ± 0.0040 (0.0241-0.0397)
2	GHT	80 ± 30 (21-139)	1.90 ± 0.24 (1.43-2.37)	0.0059 ± 0.0049 (0-0.0155)
3	IPT	220 ± 70 (83-357)	1.51 ± 0.15 (1.22-1.80)	0.0021 ± 0.0009 (0.0003-0.0039)
4	IITH	150 ± 60 (32-268)	1.60 ± 0.44 (0.74-2.46)	0.0113 ± 0.0058 (0-0.0227)
5	ANR	300 ± 150 (6-594)	1.95 ± 0.87 (0.25-3.65)	0.0027 ± 0.0024 (0-0.0074)
6	NLG	200 ± 100 (4-396)	1.45 ± 0.43 (0.61-2.29)	0.0130 ± 0.0067 (0-0.0261)
7	HNR	250 ± 120 (15-485)	0.34 ± 0.52 (0-1.36)	0.0013 ± 0.0007 (0-0.0027)
8	JBH	140 ± 40 (62-218)	1.35 ± 0.18 (1.00 -1.70)	0.0099 ± 0.0037 (0.0026-0.0172)
9	RJP	180 ± 70 (43-317)	1.51 ± 0.32 (0.88-2.14)	0.0025 ± 0.0010 (0.0005-0.0045)

These values were constrained to zero to ensure meaningful interpretation. The ratio is near or higher than unity in the majority of sites, suggesting that S-waves are attenuated less than P-waves. The spatial heterogeneity of the HGR's crustal structure is reflected in the change in the QS/QP ratio among the stations. In general, our results seem to support the findings of unusual lithospheric structure beneath the HGR, Eastern Dharwar craton, south India (Pandey et al. 2002; Catherine and Pandey, 2005, Singh et al., 2009). We limited our analysis to the freely available software "CodaNorm" (https://github.com/ElsevierSoftwareX/SOFTX-D-15-00038). Our results are thus first-order evaluations. Due to the limited earthquake dataset, we did not estimate scattering and intrinsic attenuation, which can be attempted in future studies with denser network and high S/N data. Also, other complimentary estimation methods like Multiple Lapse Time Window Analysis (MLTA) can further be attempted in due course.

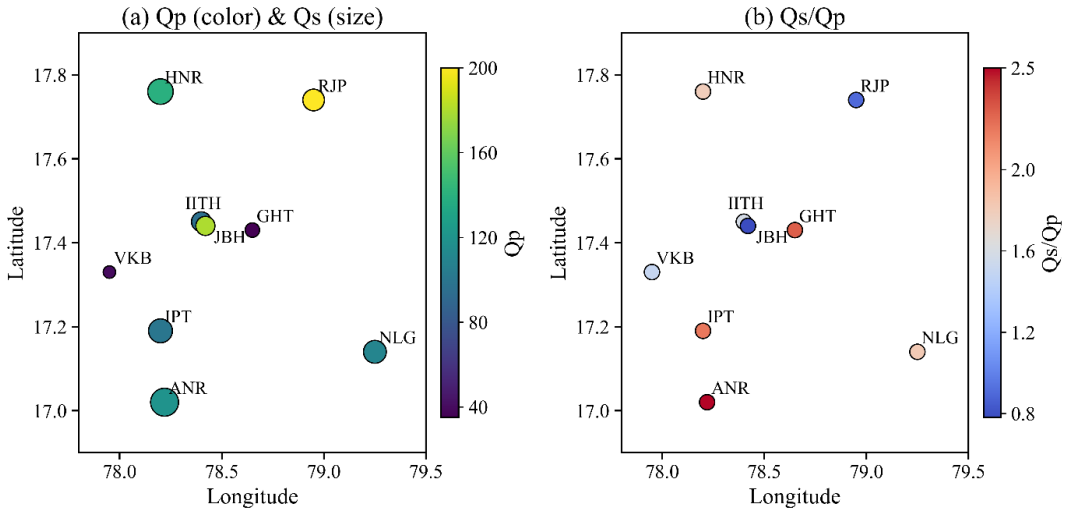

Figure 5. Spatial distribution of seismic attenuation parameters across the study area. **(a)** Q_P values are represented by the color of the symbols, while Q_S values are indicated by the size of the symbols. Red colors correspond to higher Q_P (lower attenuation) and larger symbols represent higher Q_S. **(b)** Spatial variation of the Q_S/Q_P ratio, shown using a color scale. Higher Q_S/Q_P values indicate relatively increased shear-wave attenuation compared to compressional waves, often associated with crustal heterogeneity, whereas lower values suggest more competent and less heterogeneous rock formations. The observed spatial variations highlight significant crustal heterogeneity within the region.

CONCLUSIONS

This study used the coda-normalization method applied to ~30 local earthquake records to examine the attenuation properties of seismic waves in the Hyderabad Granitic region, located in southern India. The seismic quality factors for P-waves (Q_P) and S-waves (Q_S) were investigated in the frequency range of 1.5-24 Hz. In absence of detailed attenuation studies, the findings provide a first-order frequency-dependent attenuation behaviour of seismic waves in the studied area. In the power-law regression ($Q \sim Q_0 f^n$), Q_P values vary from 35 ± 15 to 200 ± 80, while Q_S from 60 ± 10 to 300 ± 150, while 'n' have shown slight variations for both P and S waves. The Q values at stations like HNR and RJP are comparatively higher, whereas those of stations like GHT and VKB are lower, suggesting regional differences in crustal attenuation. Similarly, the frequency-dependence parameter n, ranges between 0.39 ± 0.32 and 1.62 ± 0.29 for Q_P, and from 0.34 ± 0.52 and 1.95 ± 0.87 for Q_S, indicating that S-waves have greater frequency dependence over P-waves. Additionally, the attenuation coefficient (γ) which represents the rate of decay of wave energy with distance, the P-wave γ values varies between 0.0014 ± 0.0004 to 0.0282 ± 0.0028 and S-wave γ between 0.0013 ± 0.0007 and 0.0319 ± 0.0040. Overall, our study indicates the HGR is heterogeneous at many stations with relatively dry rock nature.

Acknowledgements

Authors are grateful to the Editor and the anonymous reviewers for their valuable suggestions to improve the quality of the manuscript. We acknowledge the Director of CSIR-NGRI, Hyderabad, for his encouragement and permission to publish this work (vide ref No.Ngri/Lib/2026/38). The Project MLP-6401-28(PK) supported this work. Funding was provided by CSIR-NGRI, Hyderabad, India, Grant No (MLP-7008-28(PK).We also acknowledge the use of the freely available software "CodaNorm" (https://github.com/ElsevierSoftwareX/SOFTX-D-15-00038; last accessed December 2025) for computation of Q_P and Q_S. Data processing was done using the Seisan software, while mapping has been done using GMT.

Authors credit statement

M. Srikanth: Designing the workflow for data processing and analysis, writing; K. Sivaram: Conceptualization and designing the overall workflow, editing, rewriting, overall supervision, and seismic data acquisition; V. Pavan Kumar: supervision for this study.

Data availability

Data will be made available on request to Director, CSIR-NGRI, India.

Compliance with ethical standards

The author declares that there are no conflicts of interest regarding the publication of this paper.

The authors declare no use of AI tools in writing this Manuscript. They adhere to copyright norms

REFERENCES

Aki, K., 1969. Analysis of the seismic coda of local earthquakes as scattered waves. J. Geophys. Res., 74,615-74631.

Aki, K. and Chouet, B., 1975. Origin of coda waves: Source, attenuation, and scattering effects. J. Geophys. Res., 80, 3322-3342.

Baruah, S., Hazarika, D., Gogoi, N.K. and Raju, P.S., 2007. The effects of attenuation and site on the spectra of microearthquakes in the Jubilee Hills region of Hyderabad, India. J. Earth Syst. Sci., 118,1-12.

BIS, 2016. Bureau of Indian Standards (BIS) 2016. IS 1893 (Part 1): Criteria for earthquake resistant design of structures. Bureau of Indian Standards, New Delhi, India

Catherine, J.K. and Pandey, O.P., 2005. Differential uplift between Hyderabad and Bangalore geotectonic blocks of Eastern Dharwar Craton, South India. J. Geol. Soc. India, 65, 493–496.

Chadwick, B., Vasudev, V.N. and Hegde, G.V., 2000. The Dharwar craton, southern India: Interpretation of oblique convergence in the late Archean. Precamb. Res., 99, 295–314.

Chin, B.H. and Aki, K., 1991. Simultaneous study of source, path, and site effects on strong ground motion during the Loma Prieta earthquake. Bull. Seismol. Soc. Am., 81, 1859–1884.

Havskov, J., Malone, S.D. and Crosson, R.S., 1989. Coda Q for the state of Washington from local earthquakes. Bull. Seismol. Soc. Am.,79, 691–701.

Jayananda, M., Peucat, J.J., Chardon, D., Krishna Rao, B., Fanning, C.M. and Corfu, F., 2000. 3.35–3.30 Ga juvenile crust formation in the eastern Dharwar craton, southern India. Precamb. Res., 99, 43–60.

Krishnamurthy, P., Suryaprakash Rao, P. and Raghavan, V., 2003. Lineament analysis and tectonic significance in parts of the Eastern Dharwar Craton, south India. J. Geol. Soc. India, 61, 679–688.

Kumar, S., Gupta, S., Kanna, N. and Sivaram, K., 2020. Crustal structure across the Deccan Volcanic Province and Eastern Dharwar Craton in the south Indian shield using receiver function modelling. Phys. Earth Planet. Inter., 305, 106543. https://doi.org/10.1016/j.pepi.2020.106543.

Mandal, P., Saha, S., Kumar, S., Gupta, S., Biswas, R., Kumar, S., Sivaram, K., Prasad, B.N.V., Dixith, M.S., Prathigadapa, R., Singh, B. and Madhusudan, S., 2022. Modelling of moment tensors and source parameters of the 25 July 2021 rare lower crustal Hyderabad (India) earthquake of Mw 3.9. Pure Appl. Geophys., 179, 993–1010.

Mandal, P., Gupta, S., Sivaram, K., Kumar, S., Kumar, S., Biswas, R., Prathigadapa, R., Prasad, B.N.V. and Dixith, M.S., 2024. Imaging of different crustal and mantle discontinuities below the Hyderabad region on the Eastern Dharwar Craton. Pure Appl. Geophys., 181, 109–125.

Murthy, K.S.R. and Raghavan, V., 2002. Lineament analysis and its significance in understanding the tectonic framework of the Hyderabad granitic terrain, Andhra Pradesh, India. J. Geol. Soc. India, 59, 551–560.

Ottemöller, L., Voss, P.H., and Havskov, J. (2018). SEISAN: Earthquake analysis software for seismology, Version 11.0.

Pandey, O.P., Agrawal, P.K. and Chetty, T.R.K., 2002. Unusual lithospheric structure beneath the Hyderabad granitic region, eastern Dharwar craton, south India. Phys. Earth Planet. Inter.,130, 59-69.

Parvin, S.S., Naresh, B., Vijaya Raghavan, R., Solomon Raju, P., Suresh, G., Srinagesh, D. and Surinaidu, L., 2021. Source parameters of shallow microtremors induced by seasonal groundwater recharge in Hyderabad, southern Peninsular India. J. Geol. Soc. India, 97, 1073–1079.

Predein, A., Korn, M. and Scherbaum, F., 2017. Seismic attenuation studies using coda normalization and their implications for crustal heterogeneity. Geophys. J. Int., 210, 1082–1096.

Ramam, P.K. and Murty, V.N., 1997. Geology of Andhra Pradesh. Geol. Soc. India, Bangalore, 278 pp.

Saha, S., Biswas, R., Mandal, P., Vengala, P.K., Dixith, M.S. and Prasad, B.N.V., 2024. Evaluation of the Hyderabad network's broadband seismic stations for characterizing ambient noise in the Eastern Dharwar Craton, southern India. J. Earth Syst. Sci., 133, 24. https://doi.org/10.1007/s12040-023-02231-w.

Singh, A.P., Mishra, D.C. and Kumar, A., 2004. Lineament analysis and tectonic interpretation of the granitic terrain in parts of the Eastern Dharwar Craton, south India. J. Geol. Soc. India, 63, 73-82.

Singh, S.B., Ashok Babu, G. and Veeraiah, B., 2009. Thinning of granitic-gneissic crust below uplifting hyderabad granitic region of the eastern Dharwar craton (south Indian shield): Evidence from AMT/CSAMT experiment. J Geol Soc India, 74, 697–702.

Sivaram, K., Mandal, P., Biswas, R., Prasad, B.N.V., Dixith, M.S. and Madhusudhan, S., 2024. Site characterization and shallow shear velocity through HVSR measurements around the Hyderabad Metropolitan Region, India. J. Geol. Soc. India, 100, 953-963.

Srinagesh, D., Chadha, R.K., Raju, P.S., Suresh, G., Vijayaraghavan, R., Sarma, A.N.S., Sekhar, M. and Murty, Y.V.V.B.S.N., 2015. Seismicity studies in eastern Dharwar craton and neighbouring tectonic regions. J. Geol. Soc. India, 85, 419-430.

Vasudev, V.N., Chadwick, B. and Hegde, G.V., 2000. Structure and evolution of the eastern Dharwar Craton, southern India. Precamb. Res., 99, 81-97.

Yoshimoto, K., Sato, H. and Ohtake, M., 1993. Frequency-dependent attenuation of P and S waves in the Kanto area, Japan, based on the coda normalization method. Geophys. J. Int., 114, 165-174.

Received on: 12-03-2026; Revised on 06-04-2026; Accepted on: 08-04-2026

GUIDE FOR AUTHORS

The Journal of Indian Geophysical Union (JIGU), a SCI Journal published bimonthly by the Indian Geophysical Union (JIGU), is an inter disciplinary journal from India that publishes high-quality research in earth sciences with special emphasis on the topics pertaining to the Indian subcontinent and the surrounding Indian Ocean region. The journal covers several scientific disciplines related to the Earth sciences such as solid Earth Geophysics, geology and geochemistry, apart from marine, atmosphere space and planetary sciences. J-IGU welcomes contributions under the following categories :

*Research articles, short notes and students section reporting new findings, results, etc.

*Review articles providing comprehensive overview of a significant research field.

In addition, JIGU also welcomes short communications, after communications and report on scientific activity, book reviews, news and views, etc.

The manuscript should be submitted electronically as a single word format (.doc file) including the main text, figures, tables, and any other supplementary information along with the signed "Declaration Letter". The manuscript should be submitted by email (jigul1963@ gmail.com) to the Chief Editor.

After acceptance of the manuscript the corresponding author would be required to submit all source files (text and Tables in word format) and figure in high resolution standard (*.jpg, *.tiff, *.bmp) format. These files may be submitted to JIGU as a single *.zip file along with the "Copyright Transfer Statement".

IMPORTANT INFORMATION

Ethics in publishing; J-IGU is committed to ensuring ethics in publication and takes a serious view of plagiarism including self-plagiarism in manuscripts submitted to the journal, Authors are advised to ensure ethical values by submitting only their original work and due acknowledgement to the work of others used in the manuscript. Authors must also refrain from submitting the same manuscript to more than one journal concurrently, or publish the same piece of research work in more than one journal, which is unethical and unacceptable. Editor of JIGU is committed to make every reasonable effort to investigate any allegations of plagiarism brought to his attention, as well as instances that come up during the peer review process and has full authority to retract any plagiarized publication from the journal and take appropriate action against such authors if it is proven that such a misconduct was intentional.

Similarly, Editor and Reviewers are also expected to follow ethical norms of publishing by ensuring that they don't use any unpublished information, communicated to them for editorial or review purpose, in their own research without the explicit written consent of the author. They are also expected to keep manuscript' data/ observations/ any other information related to the peer review confidential to protect the interest of the authors. Reviewers should refrain from reviewing the manuscripts in which they have conflicts of interest resulting from competitive, collaborative, or other relationships or connections with any of the authors, companies, or institutions connected to the manuscript.

Conflict of interest

All authors are requested to disclose any actual or potential conflict of interest including any financial, personal or other relationships with other people or organizations within three years of beginning the submitted nor that could inappropriately influence, or be perceived to influence, their work.

Submission declaration

Submission of a manuscript implies that the work has not been published previously and it is not under consideration for publication elsewhere, and that if accepted it will not be published elsewhere in the same or any other form, in English or in any other language, without the written consent of the publishers. It also implies that the authors have taken necessary approval from the competent authority of the institute/organization where the work was carried out.

Copyright

After acceptance of the manuscript the corresponding author would be required to sign and submit the "Copyright Transfer Statement".

MANUSCRIPT PREPARATION

The corresponding author should be identified (include E-mail address, Phone/Mobile number). Full affiliation and postal address must be given for all co-authors.

Abstract:

An abstract of not more than 300 words must be included.

Text:

The manuscript should be structured to include a front page containing the title, Author(s) name, affiliation and address of the institute, where the work was carried out, and 5-to-6 Key words. Author(s) present address, if different from the above mentioned address, may be given in the footnote. The corresponding author should be identified with an asterisk and his/her email ID should be provided. This page should be followed by the main text consisting of Abstract, Introduction, Methods/ Techniques/ Area description, Results, Discussion, Conclusions, Acknowledgements, and References. Tables and Figures with captions should be inserted at the end of main text. It should not be inserted in the body of the text.

Figures/ Illustrations:

figures should be provided in camera-ready form, suitable for reproduction (which may include reduction) without retouching. Figures in high-resolution (at least 300 dpi) standard formats (*.jpg, * tiff, *.bmp) are acceptable. Figures should be numbered according to their sequence in the text. References should be made in the text to each figure. Each figure should have a suitable caption.

Tables:

Authors should take note of the limitations set by the size and layout of the journal. Table should not exceed the printed area of the page. They should be typed on separate sheets and details about the tables should be given in the text. Heading should be brief. Large tables should be avoided and may be provided as supplementary information, if required.

Equations:

Equations should be numbered sequentially with Arabic numerals and cited in the text. Subscripts and Superscripts should be set off clearly.

Equation writing software that presents each equation as an object in MS Word will be accepted. Style and convention adopted for the equations should be uniform throughout the paper.

References:

All references to publications cited in the main text should be presented as a list of references in order following the text and all references in the list must be cited in the text. References should be arranged chronologically, in the text. The list of references should be arranged alphabetically at the end of the paper.

References should be given in the following form:

Kaila, K.L., Reddy PR., Mall D.M., Venkateswarlu, N., Krishna V.G. and Prasad, A.S.S.S.R.S., 1992, Crustal structure of the west Bengal el eon deep seismic sounding investigations. Geophys. J. Int., 1,45-66.

REVIEW PROCESS:

All manuscripts submitted to the journal are peer-reviewed. It is advisable to send the contact details of 4 potential reviewers along with the manuscript to expedite the review process. Editor has the option to select reviewers from the list or choose different reviewers. The review process usually takes about 3 months. All enquiries regarding the manuscript may be addressed to the Chief Editor.

GALLEY PROOF:

Technical editing of manuscripts is performed by the editorial board. The author is asked to check the galley proof for typographical errors and to answer queries from the editor. Authors are requested to return the corrected proof within two days of its receipt to ensure uninterrupted proceedings The editor will not accept new material in proof unless permission from the editorial board has been obtained for the addition of a "note added in proof". Authors are liable to be charged for excessive alterations to galley proof.

PUBLICATION CHARGES:

There are no page charges for publication. The corresponding author will receive a soft copy (pdf format) of his/her published article. Should the author desire to purchase reprints of his/her publication, he/she must send the duly signed Reprint Order Form (accompanies the galley proof and contains price details) along with the corrected galley proof to the Editor. The reprint charges must be paid within one month of sending the Reprint Order Form.

Any payment related to printing or purchase of reprints should be made in the form of a Demand Draft in the name of Treasurer, Indian Geophysical Union, payable at Hyderabad.

You may download the pdf file from:
http://iguonline.in/journal/instructions.php